NEUTRON SPECTROSCOPY DEVELOPMENT IN TENSIONED METASTABLE FLUID DETECTORS

by

Anthony Sansone

A Dissertation

Submitted to the Faculty of Purdue University

In Partial Fulfillment of the Requirements for the degree of

Doctor of Philosophy

School of Nuclear Engineering

West Lafayette, Indiana

May 2021

THE PURDUE UNIVERSITY GRADUATE SCHOOL
STATEMENT OF COMMITTEE APPROVAL

Dr. Rusi Taleyarkhan, Chair
School of Nuclear Engineering

Dr. Shripad Revankar
School of Nuclear Engineering

Dr. Robert Bean
School of Nuclear Engineering

Dr. Hany Abdel-Khalik
School of Nuclear Engineering

Dr. James Schweitzer
School of Health Sciences

Dr. Brian Archambault
School of Nuclear Engineering

Dr. Thomas Grimes
School of Nuclear Engineering

Approved by:
Dr. Seungjin Kim

ACKNOWLEDGMENTS

I would first like to acknowledge my mentor, and Major Professor Rusi Taleyarkhan, for his guidance and support. Thank you to committee members Drs Revankar, Schweitzer, Bean, Abdel-Khalik, Archambault, and Grimes. Furthermore, thank you to past and present colleagues at the Metastable Fluid Research Laboratory Dr. Brian Archambault, Dr. Tom Grimes, Dr. Alex Hagen, Dr. Nathan Boyle, Dr. Jeff Webster, and others; your efforts are greatfully acknowledged. Assistance and flexibility provided by the staff of Purdue Univeristy's Radiological and Environmental Management is greatly appreciated. Thank you to the staff at Oak Ridge National Lab Dr. Zane Bell, Dr. Michael Wright, and Gomez Wright. Funding for this project was supplied by Purdue University, Sagamore Adams Labs LLC, and the Department of Energy.

TABLE OF CONTENTS

LIST OF TABLES

LIST OF FIGURES

ABBREVIATIONS

ATMFD	acoustically tensioned metastable fluid detector
BSS	bonner sphere spectrometer
CDF	cumulative distribution function
CFR	code of federal regulations
CCDF	complementary cumulative distribution function
CTMFD	centrifugally tensioned metastable fluid detector
CSDA	continuous slowing down approximation
DETC	deposition energy threshold for cavitation
DFP	decafluoropentane
DFP-TMB-M	decafluoropentane-trimethylborate-methanol
FOM	figure of merit
$H^*(10)$	ambient dose equivalent
HDPE	high density polyethylene
ICRP	international commission on radiation protection
ISO	international standards organization
MFARL	metastable fluid advanced research lab
MCNP	monte carlo n particle code package
MCNPP	MCNP-PoliMi code package
NCRP	national commission radiation protection
ORNL	oak ridge national laboratory
OUAL	ohio university edward's accelerator laboratory
LET	linear energy transfer
SDD	superheated droplet detector
SRIM	stopping range of ions in matter code package
TOF	time of flight
TMFD	tensioned metastable fluid detector
TRIM	transport range of ions in matter code package

ABSTRACT

This dissertation describes work conducted in pursuit of interests in adapting Tension Metastable Fluid Detectors (TMFDs) for dosimetry-related applications with the specific intent of engineering a neutron ambient dose spectrometer. TMFDs possess several characteristics desirable for neutron spectrometry, including high efficiencies, complete blindness to gamma and beta radiation, and tailorable-threshold response functions. Prior spectroscopic work with TMFDs, aptly named Single Atom Spectroscopy (SAS), was constrained to a specific subset of detection fluids who's composition includes hydrogen and only one other higher Z element (e.g. hydrocarbons), where only one element is assumed capable of initiating a cavitation detection event (CDE). The present work alleviates these restrictions, enabling spectroscopy in detection fluids with multiple constituent elements.

Simulating the detector's response predicates knowledge of the energy necessary for radiation induced nucleation, which has been theoretically derived with nucleation theory for superheated fluids, but remains unbeknownst for tensioned metastable states. This limitation was overcome using MCNPX-PoliMI to model the spatial recoil nuclei spectra from isotope sources and coupled with SRIM to generate the ion energy deposition probability density within a critical length scale of each interaction event. Thereafter, the energy deposition threshold necessary to generate a detection event, and corresponding response matrix, was derived empirically by solving for the solution curve that minimizes the residual difference between the measured and simulated count rates.

The accuracy of the derived response matrix was evaluated through comparisons with a ^{6}LiI Bonner Sphere Spectrometer in which, for ^{252}Cf and ^{239}PuBe/^{241}AmBe isotope source neutron spectra, the two systems offered results within ±10% of each other for ambient equivalent fluences on the order of 100 μRem/hr fields. Notably, when under ultra-low (10 μRem/hr) fields the Bonner spectrometer and other traditional detectors proved impractical. In contrast, the TMFD system was capable of resolving underlying spectral features and corresponding ambient dose rates within ±5% of MCNP predictions.

1. INTRODUCTION

This dissertation provides a technical summary of the work conducted in pursuit of interests in adapting Tension Metastable Fluid Detectors (TMFDs) for dosimetry-related applications. with the specific intent of engineering an ambient equivalent dose monitor. Enablement of such capability predicated leveraging the ability of TMFD's to nonlinearly tailor their radial-dependent efficiency through systematic variation in tension states as a means of generating response function vectors. Combined together, these response vectors form a system of equations utilized for unfolding the ambient neutron energy spectrum.

1.1 Relevant Fundamentals Underpinning the Motivation For Neutron Spectroscopy in Dosimetry

To better understand the motivation underlying this project it is first beneficial to understand how dose rates from exposure to external neutron radiation fields are computed using information about the radiation's intensity and energy spectrum. First, we must define select radiological quantities originally defined by the International Commission on Radiation Protection (ICRP). The ICRP makes the distinction between operational quantities and protection quantities.

Protection quantities include equivalent dose H and effective dose E. The equivalent dose shown in eq. (1.1) weights the absorbed dose D with a quality factor dependent on the relative biological effectiveness of radiation R in a specified tissue T, which roughly can be described to relate the ionization density of different types and energies of incident radiation. The energy dependence of the quality factor is most significant for neutrons. The ICRP has gone through several revisions on how this dependence is defined, which are shown in fig. 1.1. Depending on the granularity of information available about the spectrum's energy dependence, the assigned weighting factor and therefore the equivalent dose can vary significantly. Importantly, 10 CFR 835 mandates that a constant weighting factor of 20 be assumed when spectral data are insufficient to identify the energy of the neutrons [1]. Therein lies the motivation for spectroscopic capability in a radiation dosimeter.

$$H_{T,R} = \sum_R w_r D_{T,R} \tag{1.1}$$

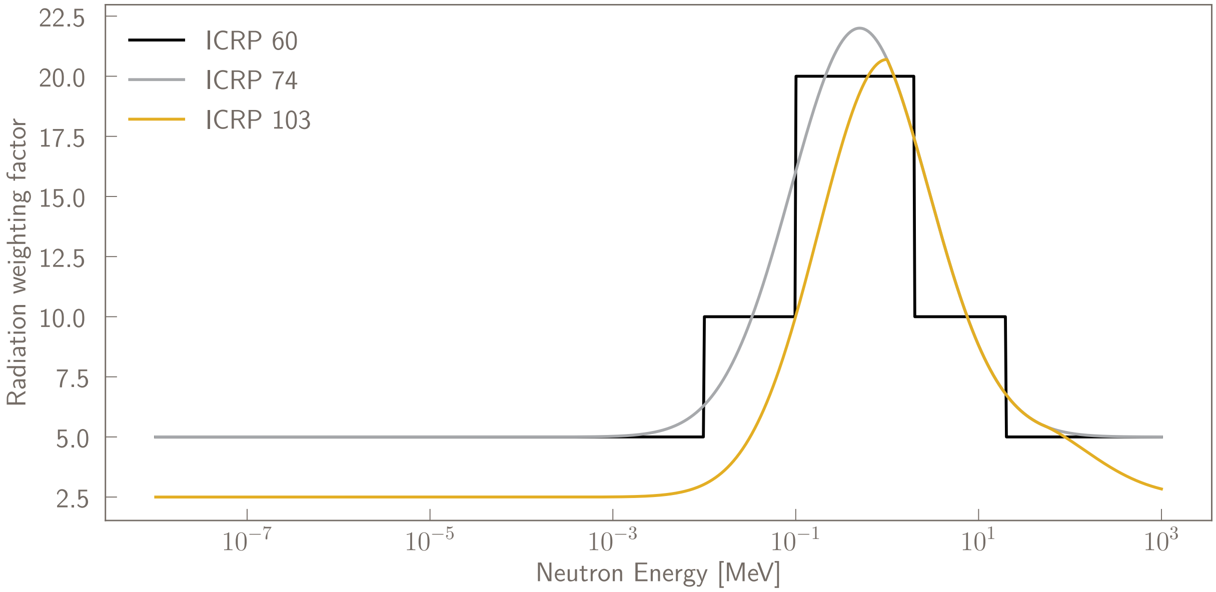

Figure 1.1. Revisions of the ICRP definition of the radiation weighting factor w_r for neutrons versus neutron energy [2].

The other protection quantity, effective dose, is shown in eq. (1.2) where w_T is the tissue weighting factor for the tissue in organ T, accounting for the fact that certain organs have a higher propensity for damage in an equivalent radiation field of type R. Effective dose is categorized as a protection quantity because it is used to determine conformance with numerical limits and action levels in radiation protection standards. However, protection quantities are only theoretical in nature as it is not possible to physically measure the distribution of energy deposition throughout different organs in the body. For compliance purposes, operational quantities are introduced.

$$E = \sum_{T} w_T H_T \tag{1.2}$$

Operational quantities are designed to be measurable in principle and can be used to determine the properties of radiation fields for compliance with regulatory standards. The specific properties that are actually measurable include the radiation field intensity and energy distribution, though the latter requires a detector intrinsically capable of inferring energy information. To set operational limits, a functional relationship must exist to map spectral energy and intensity to effective dose in the body. The ICRP established this relationship using Monte Carlo methods with standardized monoenergetic radiation fields to simulate the energy deposition as a function of depth in a water phantom. The results of these simulations establish a set of energy dependent weighting coefficients quantifying effective dose per unit flux.

Operational quantities are further subdivided into categories for area monitoring or personnel monitoring, defined as the ambient dose equivalent $\mathrm{H}^{*}(\mathrm{d})$ and personal dose equivalent $\mathrm{H}_{\mathrm{p}}(\mathrm{d})$, respectively. For area monitoring of strongly penetrating radiation, the ICRP recommends the use of the ambient dose equivalent, $\mathrm{H}^{*}(\mathrm{d})$ at 10 mm (commonly referred to as $\mathrm{H}^{*}(10)$) to estimate the whole-body dose. Using the ICRP recommended values, the total dose rate of a given radiation field is found from the dot product of the fluence vector discretized in energy space with the weighting coefficient vector as seen in eq. (1.3).

$$E = \sum_{i=1}^{i=N} \phi\left(E_i\right) H^{*}\left(E_i\right) \tag{1.3}$$

1.2 Shortcomings of Conventional Rem-Meter Dosimeters

The intent of this section is to summarize the differences between a spectrometer and a common dosimeter with regards to ambient dose monitoring. In general, a spectrometer can function as a dosimeter but a dosimeter cannot perform spectroscopy. The incentive for spectroscopic capability in a neutron survey instrument is driven by factors such as: the allowable tolerance in the computed dose rate, the time investment required for the estimated dose to converge within the desired tolerance window, and the extensibility of that accuracy as a function of spectrum shape. A spectrometer will exhibit limited dependence on spectrum shape relative to a typical dosimeter, where the accuracy of the computed dose is a function of the accuracy and resolution of the energy and intensity information inferred from measurements. The additional accuracy gained through spectrometry unfortunately comes at the expense of required acquisition time.

To avoid potential ambiguity, the term "rate meter" or "rem meter" will be used interchangeably as a reference to common dosimeters that do not possess spectroscopic capabilities. The term rate meter is chosen as a moniker as a literal reference to the way in which the dose rate is computed. Specifically, the linear relationship between the detector count rate and the dose rate, e.g. 3 counts per second per millirem per hour. That is, the number of detections per second that is to be expected from exposure to a 1 mRem/hr field.

Calculation of a rate meter's dose conversion constant requires knowledge of the instrument's response function. The concept of the response function, shown as R in eq. (1.4) will be elaborated on in later chapters, but for the present discussion can be thought of as the number of detection events per unit flux. The conceptual similarities between the units of the response function and the $\mathrm{H}^{*}(10)$ dose conversion coefficients should now be evident. Integration of eq. (1.4) over all N energy bins yields the total count rate. Similarly, the ambient equivalent dose rate is found by integration of eq. (1.3) over all energies. The quotient of the two quantities then represents the counts recorded per unit time per unit dose rate. Furthermore, by equating eq. (1.3) and eq. (1.4), it is apparent that a rate meter can not accurately estimate the $\mathrm{H}^{*}(10)$ dose unless the ratio of the response function and $\mathrm{H}^{*}(10)$ weighting coefficient vectors is constant with respect to neutron energy or if the dependence can be accounted for through knowledge of the neutron spectrum. Thus, the design basis for any rem meter is to produce an instrument who's response function is in close agreement with the contours of the fluence-to-ambient dose equivalent conversion function. Despite decades of research, so far it has proven impossible to do so.

$$\dot{C} = \sum_{i=1}^{i=N} \phi\left(E_i\right) R\left(E_i\right) \tag{1.4}$$

On account of the fact that rem meters are engineered to reproduce the $H^*(10)$ as closely as possible, it is no surprise that the current industry-standard devices are fundamentally similar in design, containing a thermal neutron detector encased in a combination of boron or cadmium, lead or tungsten, and a heavily hydrogenated material such as high density polyethylene. In most instrument designs, colloquially known as Andersson-Braun type in reference to the author's pioneering work in the 1960s, approximately 20 lbs of moderator material are necessary to tune the response curve to the desired shape. Spallative materials like tungsten are necessary to improve the response above 8 MeV but at the expense of added weight. Furthermore, as a consequence of the moderation requirement, the intrinsic detection efficiency can be as low as 0.05% and the angular dependence of the detector can influence the computed dose rate by as much as 30%. Later variants of the original design, now commercialized, include the SNOOPY, LINUS, NRD, and WENDI [3]–[7].

The response of select rem meters relative to the fluence to ambient dose equivalent conversion function is shown in fig. 1.2. The detector responses are in closest agreement with the conversion function for neutron energies of 50 keV to 10 MeV. This is by design as the weighting factors increase by a factor of 30 over this energy range and is consequently relevant for the moderated fission spectra encountered in the power industry. Nevertheless, the average error in the thermal and fast regions ranges from 20-50% to hundreds of percent in the epithermal region. In spite of the obvious deviations, rem meters are still capable of measuring the ambient dose rate within acceptable tolerance, albeit with a few caveats. Inherent deviations from the conversion function can be mitigated by calibrating the instrument with a well-characterized, traceable spectrum such as bare ^{252}Cf. Operation in a radiation field different than the calibration spectrum will incur error. Thus, rem meters have the most utility for purposes of routine verification.

The right axis in fig. 1.2 displays the the ratio of the ICRP fluence-to-dose coefficients relative to the N(ational)CRP report 38 recommended values. Published in 1971, NCRP report 38 served as the reference standard for many years. Consequently, rem meters were engineered to imitate these fluence-to-dose conversion function. The ICRP coefficients have steadily become the reference standard following the release of report 26 in 1977 and report 60 in 1991. Variations between the two standard's coefficients are seen to be as high as ± 25% at thermal and epithermal energies and up to 50% between 100 keV and 1 MeV. These differences equate to approximately a 15% change in the standard dose rate for a bare ^{252}Cf spectrum. In 2007, amendments to the 10 CFR 835 mandated the ICRP system of dosimetry be adopted. The impact of this change was unique to each rem meter each design. In comparison, the effect on spectrometers is minimal because the measured fluence does not change, only the way it is weighted in computation of the dose.

The above discussion is not meant to be overly critical of rem meters or debate their utility. Their are many scenarios that simply do not warrant the required time and financial investment to employ a spectrometer. Nevertheless, documentation of their limitations is an effective prelude of the incentive to develop the capability for neutron spectroscopy in TMFDs.

1.3 Overview of Spectrometer Systems

Dosemeters used to measure radiation fields should be designed to measure the ICRU operation quantities. As such, it can be concluded that the universal accuracy of any ambient dose monitor is ultimately constrained by the information ascertained from the detector's output about the underlying neutron spectrum. The manor in which spectral information can be inferred is specific to each class of detector and it's fundamental detection mechanism. These systems share a commonality in their capability to distinguish, albeit with different resolutions, the cumulative energy deposition of ionizing radiation originating from neutron interactions in the detection volume. In any case, the the energy of these charged particles must be related to the corresponding neutron energies. The spectral information possible to ascertain from the detector output alone is limited at best. As a consequence, conformance

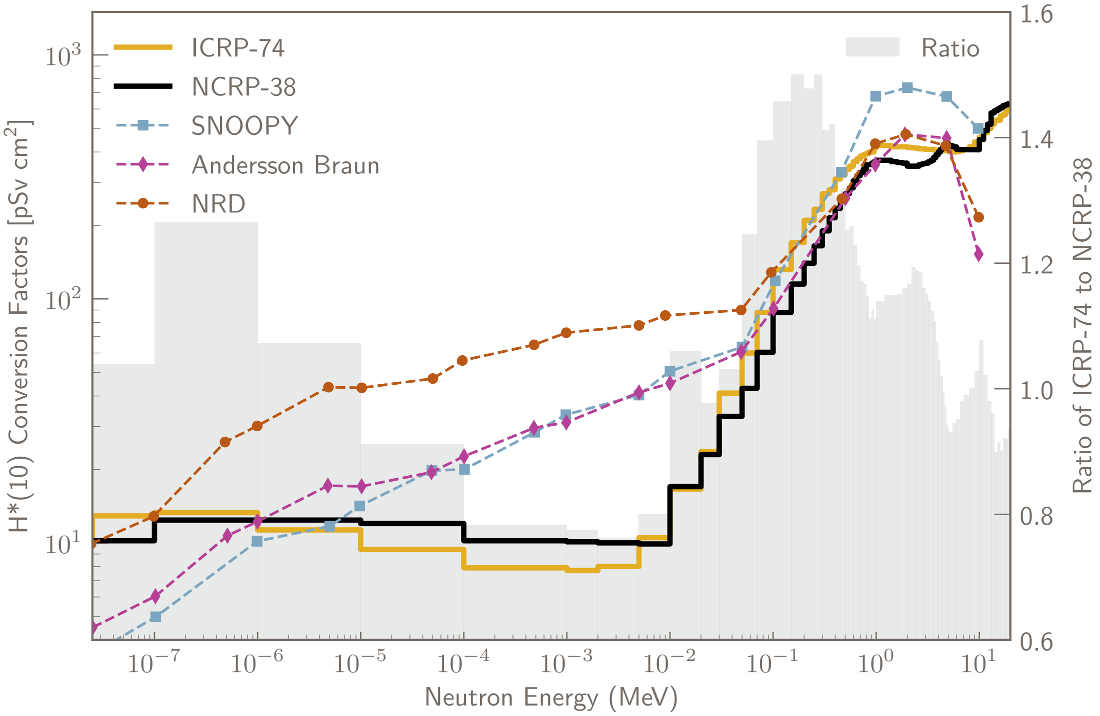

Figure 1.2. Comparison of the H*(10) ambient dose equivalent coefficients between NCRP38 and ICRP74. Responses of common rem balls are also shown to illustrate their regions of inaccuracy.

with limits set for the ambient dose equivalent operation quantity requires the neutron spectrum to be mathematically “unfolded” from the detector response.

The detector classes historically employed as survey instruments include proportional counters , scintillators, and superheated droplet detectors. Proportional counter and scintillation based spectrometers are designed around two interaction mechanisms: exothermic charged particle production reactions or elastic scattering.

Charged particle production-based detectors e.g. $^3\mathrm{He(n,p)}^3\mathrm{H+Q(Q = 764\,keV)}$ produce an electrical signal with an amplitude proportional to the sum of the neutron energy and Q value of the production reaction. Gas-filled proportional counters utilizing this mechanism often use ^{3}He as a fill gas while scintillation-based detectors typically use ^{6}Li. The inverse relationship between cross section and energy necessitates the use of spherical or cylindrical moderating materials external to the detection volume. These systems are nominally referred

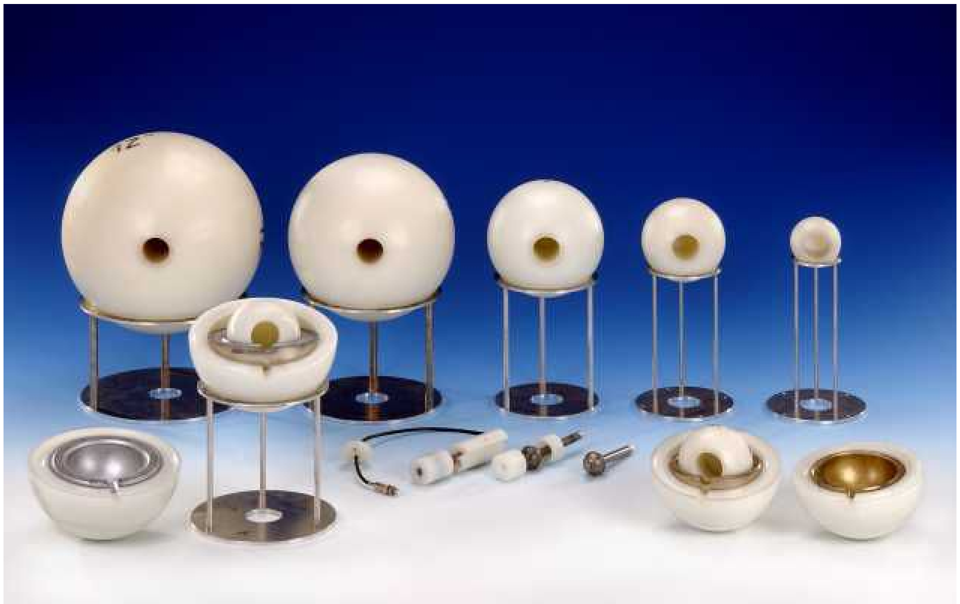

Figure 1.3. Example of a bonner sphere spectrometer system developed at the Physikalisch-Technische Bundesanstalt in Germany [8]

to as Bonner sphere spectrometers [9]. An example of a well-known ^{3}He Bonner spectrometer system, developed at Physikalisch-Technische Bundesanstalt and shown in fig. 1.3, contains 12 moderating spheres from 3.5 to 18 inches in diameter. Downscattering the neutron spectrum to thermal energies is advantageous in the fact that these systems are sensitive to the entire spectrum of neutron energies. However, this advantage is inherently countered by a corresponding poor energy resolution for fast energies, where the dose equivalent per unit fluence is about 30 times higher. Furthermore, the low efficiency and weight of the larger moderating spheres limits the feasibility of this system in certain industrial environments [10].

The other class of proportional counters and scintillation detectors utilizes elastic scattering and subsequent production of recoil protons in the hydrogenated detection medium. Proportional counters commonly employ H_2 or CH_4 as a fill gas. Gas-filled proportional counters have high (on the order of a few percent) energy resolution, a near isotopic response, and are usable in high thermal and epithermal fields because of their low efficiency. The major disadvantage of these systems is the limited energy range which they have spectroscopic utility, which is only about 10 keV to 1.5 MeV [11]. At higher energies the track length of the recoil proton becomes significant relative to the detector's dimensions, at which point the effects of partial energy depositions become relevant. In practice, geometric limitations in the workplace and quality assurance challenges constrain manufacturers from simply designing larger detection volumes [9].

Scintillation-based spectrometers can use either a liquid or solid (plastic or crystal) detection medium such as NE213 or BC501A stilbene, which absorb and then later emit the energy deposited by neutron-induced recoil nuclei in the form of light. The emitted light is collected and amplified to create a proportional voltage that is then fed into a multichannel analyzer. Spectroscopic information can be simulated to reproduce the multichannel analyzer output because of the functional relationship that exists between recoil energy deposition and light (voltage) output in scintillating materials. The light output is dependent on the form of incident radiation (i.e. neutron versus photon) and recoil nuclei. For the case of proton recoils, the light output exhibits a quadratic or exponential non-linearity as a function of ion energy. The detector response functions are composed of the multi-channel pulse height spectra produced by monoenergetic sources. One advantage of multichannel unfolding is that the unfolded spectra are generally independent of the unfolding algorithm and do not require *a priori* information because the deconvolution produces a unique solution within the bounds of counting statistics [12].

Spectrometry in mixed (neutron and photon) fields can be problematic for scintillators if the light pulses produced by incident neutrons cannot be discriminated from those produced by photons. Discrimination between neutron and photon events is possible on account of differences in the excitation decay time constants, which increases with the linear energy transfer. In general, scintillation-based systems have the highest utility for neutrons above 1 MeV. However, the discriminatory capability of scintillation spectrometers, in regards to both waveform integration and pulse-pileup rejection, has benefited significantly with advancements in digitizers and signal processing. With gigabit digitization rates, simultaneous analysis of the pulse shape for discrimination and pulse height for spectrometry are possible [13], [14]. In the case of measurements with accelerator sources, such as for experimental measurement of the detector's response function, time-of-flight gating can be used to achieve excellent photon discrimination and energy resolution.

Figure 1.4. ROSPEC rotating spectrometer incorporating 6 proportional counter detectors [15].

Table 1.1. Characteristics of each detector in the ROSPEC system [15].

Detector	Radius [cm]	Fill Gas	Pressure [kPa]	Energy Range
^{3}He (bare)	2.54	^{3}He/Kr	83	0.01 eV - 1 eV
^{3}He (boron)	2.54	^{3}He/Kr	216	1 eV - 50 keV
SP2-1	2.54	H_2	76	50 keV - 250 keV
SP2-4	2.54	H_2	400	50 keV - 250 keV
SP2-10	2.54	H_2	1000	400 keV - 1.5 MeV
SP6	2.54	CH_4/Ar	500	1.2 MeV - 5.0 MeV

The system shown in fig. 1.4, known as ROSPEC and produced by Bubble Technology in Canada, utilizes a combination of ^{3}He, H_2, and CH_4 proportional counters to unfold spectral information from 0.01 eV to 5 MeV. Characteristics of the individual proportional counters are shown in table 1.1. Bubble Technology sells an additional unit known as the Simple Scintillation Spectrometer that interfaces with the ROSPEC base unit for determining spectroscopic information over the range of 4-17 MeV. Both proportional counter and scintillation spectrometers utilize multichannel analyzers in their electronic circuitry, where the entire spectrum of individual channel count rates are used as input to the unfolding package in what is known algorithmically as multi-channel unfolding. Counting statistic requirements impose an operational disadvantage on multichannel detector architectures. Specifically, inadequate statistics in the high-energy region of the exponentially decreasing proton recoil spectrum has a tendency to manifest as strong oscillations in the unfolded spectrum. Consequently, measurements of lower dose rate fluence fields will inherently require a proportionately longer time investment. Nevertheless, the main disadvantage of the otherwise state of the art ROSPEC system, however, is the significant financial investment required.

The final class of spectrometers are comprised of superheated droplet detectors (SDD). Unlike the prior classes, the detection mechanism of SDDs is not based on some variant of charge or light collection. Rather, charged recoil nuclei nucleate submicroscopic vapor cavities inside the superheated droplets. If the submicroscopic cavities reach a critical threshold diameter, the expansion process becomes irreversible, and the cavity rapidly grows (within microseconds) to a macroscopic size. The radiation-induced nucleation process is characterized by threshold energies which depend on the fluid composition, operating temperature, and pressure. The different parameterizations of the operating conditions coupled with the thermodynamic properties of the emulsion fluid, which is typically a halocarbon, are unified with respect to neutron sensitivity equivalency using the non-dimensional quantity reduced superheat.

Bubble detectors have been a mainstay option in the field of neutron dosimetry for several decades due to their high sensitivity, dose equivalent response, and complete insensitivity to photons [16]. Two classes of systems are found: a passive system known as the bubble damage spectrometer which uses an array of detectors, and an active system comprised of one or more detectors known as the bubble interactive neutron spectrometer. In the passive system, each detector unit has a designated threshold (at 20 °C) of sensitivity to the spectral fluence. Deviations from the reference temperature introduce errors in the response matrix through variations in the energy thresholds and overall sensitivity, restricting their applicability to temperature controlled environments. The bubble interactive neutron spectrometer actively controls the detector(s) state of reduced superheat to achieve the thresholds necessary for unfolding, effectively removing the problem of environmental temperature variations. Active control over the state of metastibility also allows the detection threshold to be tailored for specific use cases. Bubble formation from neutron interactions are detected acoustically and analyzed with an onboard microprocessor [17].

The response functions are nested in quasi-lethargic intervals and are characterized by sharp thresholds exhibiting sensitivity to fast energies only, with a practical operating range of 0.1-10 MeV [18]. Thus, the detector's responses are nearly orthogonal, a very attractive feature for spectrometry. Without explicit *a priori* information, the spectral resolving power of the response functions is approximately 20-30%. As a consequence, the unfolded spectra inherently have relataively high uncertainties. However, because the adjacent energy groups are negatively correlated, the uncertainty associated with integral fluence quantities, e.g. dose equivalent, is only on the order of 5-10%. Though the efficiency of SDD systems like the bubble interactive neutron spectrometer is higher than that of proportional counter spectrometers, their maximum data acquistion rate is constrained by the long (60 ms) duration of the acoustic signals generated by the droplet vaporization and computational time associated with signal analysis and anticoincidence discrimination. As a consequence, the intrinsic maximum detection rate is on the order of 10 s^{-1}. For 1 MeV neutrons, this would equate to a maximum sustainable fluence rate of on the order of $10^4 \, \frac{\mathrm{n}}{\mathrm{cm}^2\,\mathrm{s}}$ [17].

1.4 Dissertation Overview and Objectives

This section provides an overview of the various objectives of this dissertation which ranged from deriving neutron spectroscopy information using conventional spectrometers as a baseline reference but also, with the aide of monte-carlo techniques, for tensioned metastable fluid detectors.

The key objectives pertaining to TMFD-based investigations were:

1. Establishment of a baseline reference of accuracy using a conventional bonner sphere spectrometer for comparative purposes with the CTMFD.

2. Development of a simulation model for TMFDs extensible beyond pure hydrocarbons and capable of integrating energy deposition from multiple recoil ion species and or isotopes. That is, to develop TMFD based multi-atom spectroscopy (MAS)

3. Development of a geometrically independent response matrix for TMFDs using monte-carlo-based monoenergetic neutron sources from 100 keV to 14 MeV.

4. Successfully unfold neutron spectra from data taken with TMFDs using templates of a priori spectral-shape information and subsequently estimate the $H^*(10)$ neutron dose.

5. Extend TMFDs for also enabling sensitivity to neutrons below 100 keV using borated fluids to estimate the dose contribution from thermal and epithermal regions of the fluence spectrum.

6. Independently evaluate the CTMFD's dosimetric and spectroscopic capabilities against the baseline reference Bonner sphere spectrometer

2. BACKGROUND ON TMFDS AND PAST WORK ON NEUTRON SPECTROSCOPY

2.1 Tension Metastable Fluid Detector Background Information

Detection of radiation using metastable fluids is based on the principle that nuclear particles can deposit enough energy to weaken the fluid's intermolecular bonds such that explosive phase change will occur on a localized scale. Assuming the fluid is in a sufficiently high state of metastability, the induced localized boiling can then manifest itself on a macroscopic (visible) scale. The application of metastable fluids for nuclear particle detection is almost solely associated with superheated droplet detectors (SDD), where the state of metastability is attained through thermal superheat.

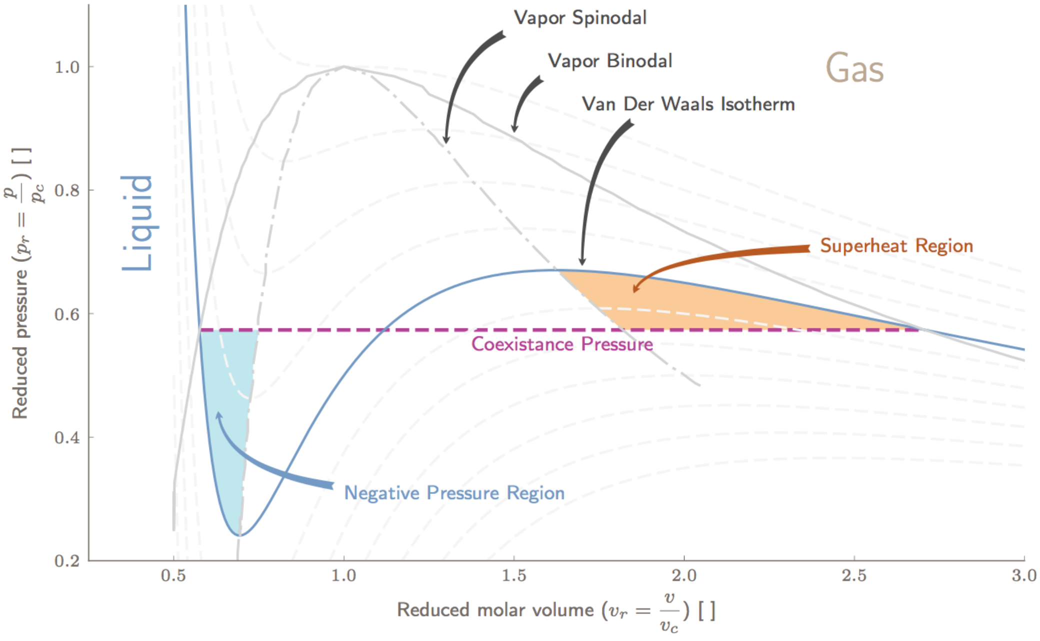

Figure 2.1. Van Der Waal's isotherm for water at $T_r = {}^{T}/_{T_c} = {}^{7}/_{8}$

Tensioned metastable fluid detectors use a converse methodology from SDDs to place fluids into metastable states. As shown in fig. 2.1, following a fluid down its isotherm and passing into the vapor dome creates a coexistance of both vapor and fluid. In most cases, the fluid follows Maxwell's line of coexistance pressure. However, it is possible in two regions, labeled as metastable on fig. 2.1, to add or subtract pressure and not induce phase change. The left-most metastable region is analogous to inducing negative pressure in a liquid below its boiling point that is at equilibrium with its vapor. Disparate from vacuum pressure, negative pressure in fluids is exactly analogous to tension in solids [19] and is often called "tensile" pressure.

In regards to practical operational considerations, TMFDs have an implicit advantage over SDDs as the rate with which a fluid can be placed in a metastable state is constrained by the speed of sound, as opposed to the thermal diffusivity. Presently, TMFD systems employ two distinctly different designs based on the method with which tensioned metastable states are attained. The simpler of the two designs utilizes centrifugal force, and served as the primary apparatus used in the data presented herein. A schematic of the CTMFD is shown in fig. 2.2. The detector consists of a diamond shaped glass piece connected at one end to a glass bulb, which comprises the detectors sensitive volume, and to a variable speed motor at the other end. As the motor rotates the apparatus about its centerline axis, centrifugal force drives the liquid up the arms. Since the void space above the elbow bend balances the internal pressure, zero net liquid motion is observed, effectively allowing the centrifugal force to counteract the intermolecular forces and thereby inducing a state of tension.

The pressure in the fluid as the glass is rotating can be found by applying an energy balance along the axial centerline in the form of the well-known Bernoulli equation. Parametrically, the realized pressure varies as a function of the fluid density, rotational speed, and the radial distance from the axial centerline. Save for small changes from temperature effects, the density and "radius" are effectively fixed prior to operation. The operator, via specification of the negative pressure(rotational frequency), can tailor the detector's sensitivity to nuclear particles in real time. The Bernoulli equation is shown in eq. (2.1), where P_{neg} is the negative pressure at the radial centerline, ρ is the fluid density, f is the rotational frequency in $\frac{rot}{s}$, r_m is the distance between the centerline and the air cavity/fluid interface in the upper arms, and P_{amb} is the ambient pressure.

$$P_{neg} = 2\pi^2 \rho f^2 r_m^2 - P_{amb} \tag{2.1}$$

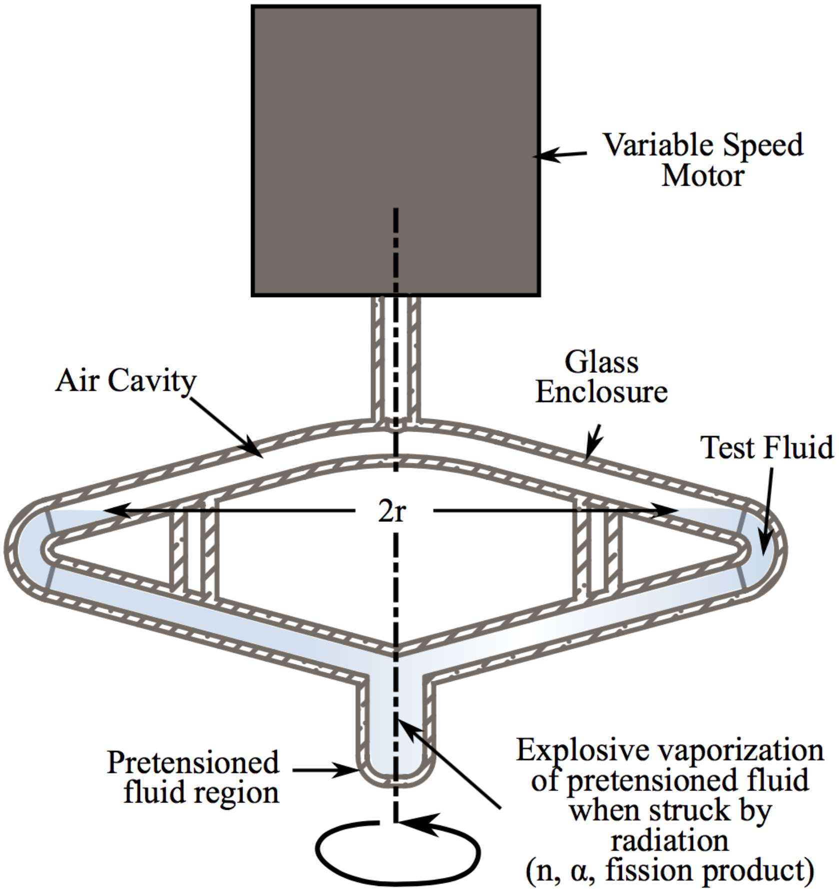

Figure 2.2. Schematic diagram of a CTMFD system

The quantitative criterion for determining whether a localized energy deposition event will trigger mechanically stable vapor cavity is known as the critical radius. The critical diameter d_c is defined in equation form in eq. (2.2), where σ represents the surface tension of the detection fluid and P_{amb} and P_{neg} represent the ambient pressure and negative pressure of the fluid, respectively. For a given ambient liquid pressure, if a radiation interaction generates a vapor cavity that does not satisfy the critical radius criteria, the cavity will collapse back into the liquid. Conversely, cavities that do meet the criteria will reach mechanical equilibrium within microseconds.

$$d_c = 2r_c = 2\left(\frac{2\sigma}{P_{amb} - P_{neg}}\right) \tag{2.2}$$

2.2 Mathematical Basis for the CTMFD Response Function

One of the fundamental challenges addressed in this work is answering the question of, for a given degree of metastability, how much energy must be deposited by a recoil ion to create a vapor cavity that satisfies eq. (2.2). This deposition requirement has been theoretically derived for SDDs using thermal spike theory [20]. However, such a theoretical treatment has been proven inapplicable for tension metastable states [21]. If the amount of energy (deposited) needed to make a stable vapor cavity was known for each pressure, developing a response matrix for the detector would be trivial. Without the threshold information, the detector's response function must be determined empirically. Further complication is induced by the fact that, at present, the information output by the detector following a successful detection event is binary or scalar in nature. That is, there is no detector operation mode analogous to a multichannel analyzer, which gives differential energy deposition information; nor is there a way to ascertain the pressure(location) at which the critical-sized cavity originated. Thus, the current problem is composed of trying to solve a system of equations using one known parameter, the scalar count rate at each centerline pressure, and two unknown vector parameters: the energy deposition thresholds(which is pressure dependent) and the differential count rate at each pressure in the detection volume. To draw analogy to conventional scintillation detectors, the problem would be equivalent to simulating a response matrix without knowing the functional relationship between energy deposition and light output and constraining that the magnitude of the light output varies with the distance from the detectors centerline

If the detector's sensitivity was homogeneous across the entire volume, the lack of detection location information would be of no consequence, and the detector's response reading

C_p, i.e. total counts measured while operating at a centerline pressure p_c, to a polyenergetic fluence $\phi(E)$ with N energy groups, could be mathematically defined as shown in eq. (2.3).

$$C_{p_c} = \int_{E_0}^{E_n} R_{p_c}(E)\phi_E(E)\, dE \tag{2.3}$$

Note that, in the discretized form necessary for transformation into a linear matrix, the quantity $R_p(E)$ is actually the group averaged response function as shown in eq. (2.4), to the group fluence shown in eq. (2.5).

$$R_{p_c,n} = \frac{\int_{E_n}^{E_{n+1}} R_{p_c}(E)\phi_E(E)\, dE}{\int_{E_n}^{E_{n+1}} \phi_E(E)\, dE} \tag{2.4}$$

$$\phi_n = \int_{E_v}^{E_{v+1}} \phi_E(E)\, dE \tag{2.5}$$

The functional form of eq. (2.3) resembles that of a mathematical convolution $M(E) = R(E) * \phi(E)$, meaning the detector response $C(E)$ is the result of the response function $R(E)$ being folded with the fluence function $\phi(E)$. For a detector with a non-homogenous sensitivity like the CTMFD, the response function needs to be integrated across the pressure distribution in the detector. Thus, each differential pressure segment has a unique sensitivity to the fluence spectrum $\phi(E)$ and the final scalar detector response is the resulting summation of the counts recorded by all of the pressures in the detector volume, as shown in eq. (2.6).

$$C_{p_c} = \int_{P(r=0)}^{P(r=r_m)} dP \int_0^\infty R_{p_c}(P(r), E)\phi_E(P(r), E) dE \tag{2.6}$$

2.3 Single Atom Spectroscopy Overview

The baseline work in neutron spectroscopy with TMFDs was first investigated by Grimes [21], who developed a solution methodology, known as Single Atom Spectroscopy (SAS) to empirically estimate the deposition energy thresholds for cavitation. To prove the validity of the empirical methodology, the problem was simplified even further by looking only at hydrocarbon fluids, specifically, heptane, under the assumption that the linear energy transfer (LET) of hydrogen was too low to nucleate a stable vapor cavity and register as a detection event. As such, it is then only necessary to model the energy deposition from carbon recoils. Fundamentally, despite the ability for more total energy to be deposited onto hydrogen via elastic scattering with neutrons, the more energetic hydrogen ions cannot nucleate as readily as the lower energy carbon ions due to their much lower LET. Therefore, the onset of sensitivity to the carbon recoils will occur at negative pressures much closer to vacuum than the onset of sensitivity to hydrogen. This is a justifiable assumption as the experimental data used for unfolding was taken at pressures just above the detection threshold of each source.

$$\alpha = \left(\frac{A-1}{A+1}\right)^2 \tag{2.7}$$

Using the collision data from MCNPX-PoliMi code model simulations, the collision events were discretized (binned) in 0.1 bar radial increments from the detector centerline, Each radial bin (pressure) has its own recoil-ion spectrum in deposition-energy event-frequency space, from which the theoretical count rate is calculated from. An example of a hypothetical frequency-recoil distribution for a CTMFD operating at a centerline pressure of 4.7 bar is shown in figure fig. 2.3. For a specific deposition energy threshold for cavitation (DETC), E_T, the expected contribution to the total count rate from events occurring only in the local radial bin corresponds to the intersection of the distribution curve with the line perpendicular to E_T. In the context of this example, assume that the DETC for the 4.3-4.4 bar region is 40 keV, 30 keV for 4.4-4.5 bar, 20 keV for 4.5-4.6 bar, and 10 keV for 4.6-4.7 bar. Examining the 4.4 bar curve shown in figure fig. 2.3, there were a total of 6150 events which deposited at least 40 keV. Similarly, the predicted count totals for the 4.5, 4.6, and 4.7 bar curves would be 7500, 17650, and 16400 counts, respectively. The total number of detection-inducing events across all regions would then be 47,700. This number can be converted to an experimental count rate $\dot{C}_{exp}$ using eq. (2.8), where C_{mcnp} is the number of predicted cavitation-inducing events, NPS_{mcnp} is the total number of particles simulated by MCNP, and $\dot{S}$ is the intensity in neutrons/second of the physical source.

$$\dot{C}_{exp} = \frac{C_{mcnp}}{NPS_{mcnp}}\dot{S} \tag{2.8}$$

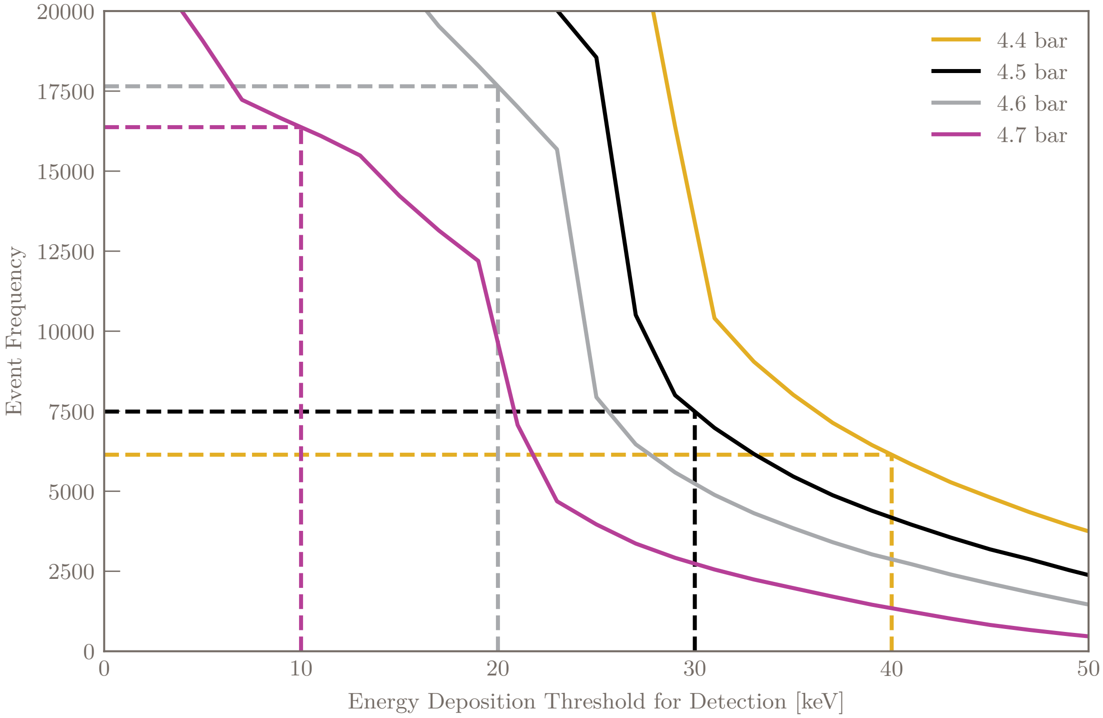

Figure 2.3. Cumulative frequency distribution of energy depositions by recoil ions inside each radial pressure bin

The solution procedure begins at the pressure at which a non-zero count rate above background is recorded. For the particular PuBe isotope source and heptane-filled CTMFD used by Grimes [21], this pressure threshold equated to a centerline pressure of 4.4 bar. All of the radial segments equating to 4.3 bar and below, shown in gold in fig. 2.4, are assumed to have zero contribution to the total count rate. Under the assumption that there are no other “active” pressure regions, the energy deposition threshold that minimizes the difference between the MCNP predicted counts (in the green radial bin of figure fig. 2.4) and experimental count rates can be directly solved for. For the next centerline pressure of 4.5 bar, the number of predicted counts in the 4.3-4.4 bar region (second inner-most black ring) is constrained by requiring the same energy threshold be used as solved for in the prior 4.4 bar centerline case. The threshold in the center-most gray region is adjusted such that the total counts from all ”active” pressure regions minimizes the difference with the experimental count rate.

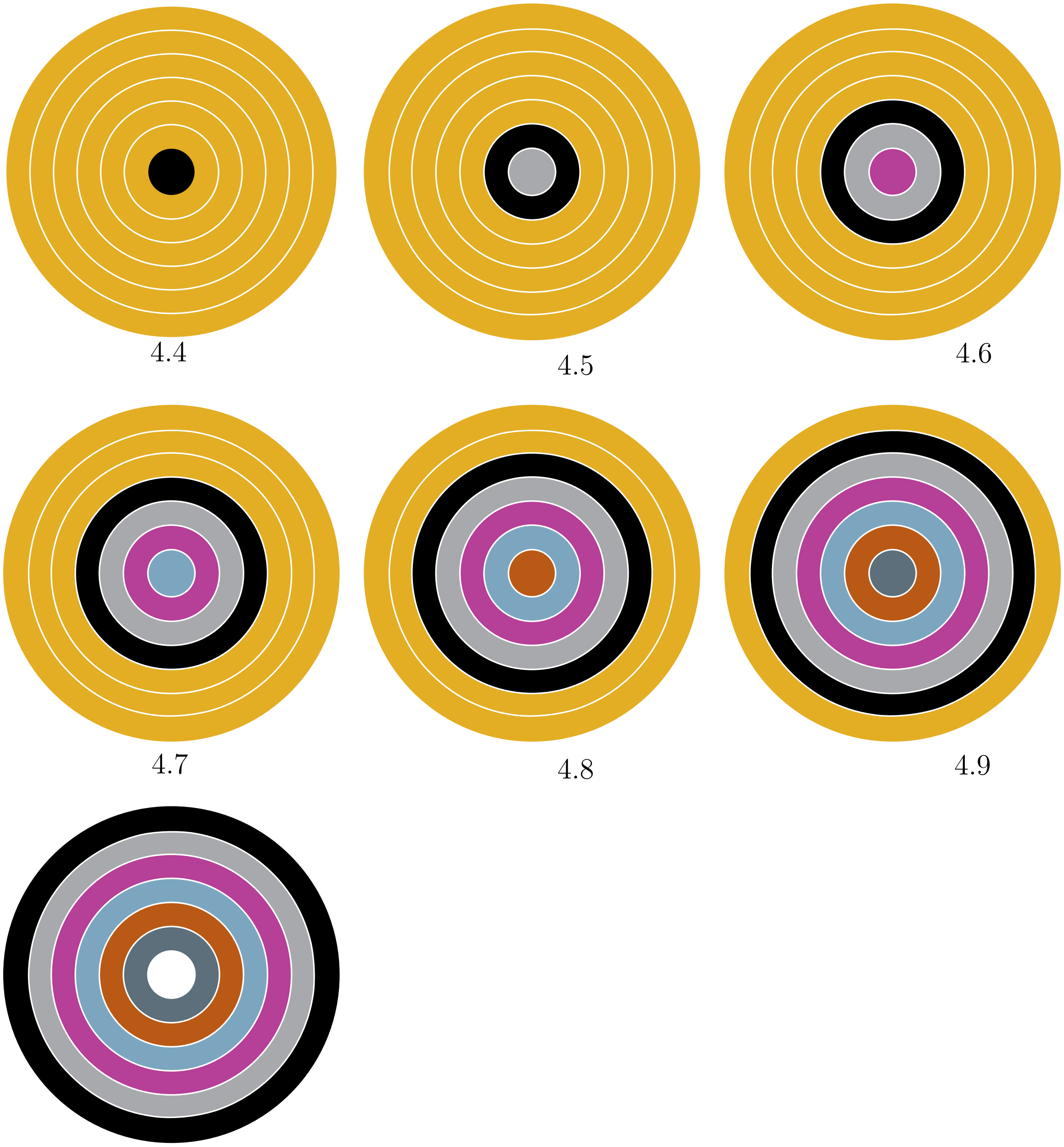

4.4 4.5 4.6

4.7 4.8 4.9

5.0

Figure 2.4. Discretization of the radial pressure gradient, where the colors represent regions of equal threshold

This solution concept of “equal” DETC thresholds across different radial bins and centerline pressures is illustrated in figure fig. 2.4. Notice how the color of each central region propagates outward as the centerline pressure is increased, indicating the DETC should remain the same as calculated in the previous centerline pressure case. Thus, only a single new energy threshold is calculated for each centerline pressure. In practice, the concept of this iterative procedure was best applied using a system of equations, where the entire DETC solution vector is solved for simultaneously.

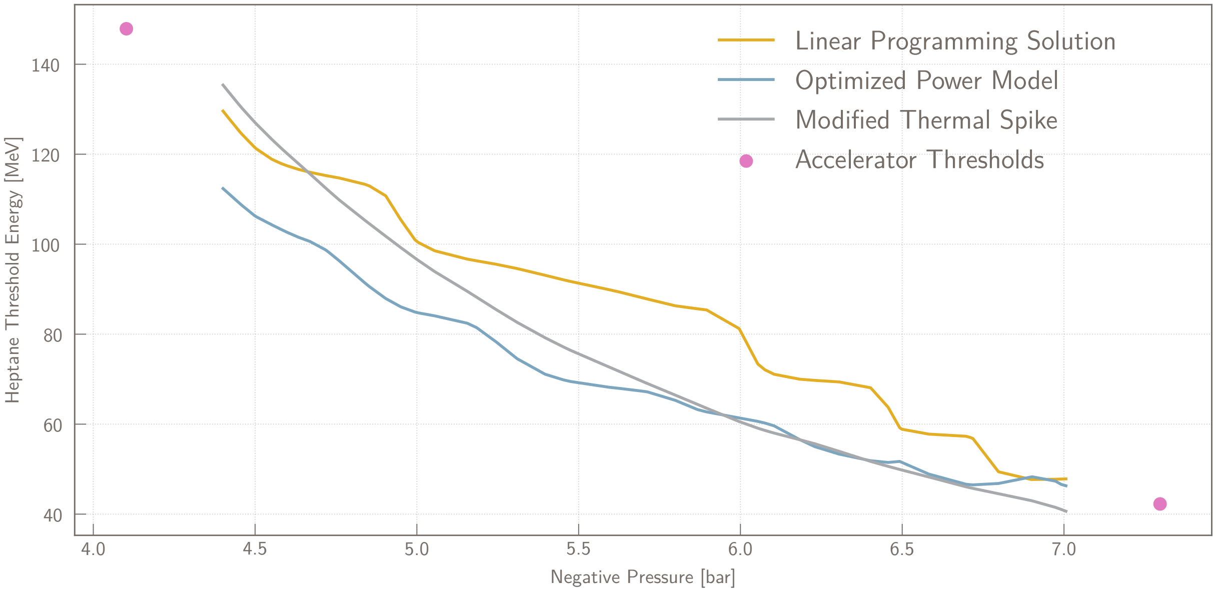

Figure 2.5. Solution curve, obtained using the Single Atom Spectroscopy method, representing the amount of energy that a recoil ion must deposit inside a critically-sized vapor cavity in heptane [21].

2.4 Need for Extending the SAS Unfolding Methodology to Multi-Atom Fluids, Resulting in MAS

While the work by Grimes [21] was instrumental in developing spectroscopic capabilities for TMFDs, there are several areas needing further investigation to make TMFD technology field applicable. The most prominent action items are to make the empirical methodology for TMFD response matrix development independent of the surrounding geometry and extensible to multi-atom fluids.

2.4.1 Advantages of Using Decafluoropentane as a Detection Fluid

Except for niche applications outside the scope of this thesis, TMFDs have, at the present time, adopted a fluid known as DecaFluoroPentane (DFP) as their detection fluid of choice. DFP is a fluorocarbon with chemical formula $C_5F_{10}H_2$. The presence of both carbon and fluorine violates the methodology of Single Atom Spectroscopy and there are several reasons meriting development of a multi-atom method for DFP rather than adopting heptane or another hydrocarbon variant.

From a practical standpoint DFP is ideal as it has all zeros on the National Fire Protection Association Scale of Material Hazards; meaning it is non-reactive, poses almost no exposure risk, and is non-flammable. This is an important consideration for widespread adoption of TMFD technology

DFP's chemical composition and high density of 1.6 g/cm^3 is advantageous from a neutronics standpoint due to the inverse relationship between mean free path and volumetric number density. As a point of comparison, the density of other applicable organic fluids (e.g. acetone, heptane) is typically 0.6-0.8 g/cm^3. Though DFP's molecular weight at 252 g/mol is higher than that of organic fluids, the effect is mostly offset by the high density such that the interaction efficiency is approximately equivalent. The primary advantage DFP has over organic fluids is actually its relative *absence* of hydrogen atoms. As mentioned earlier, the LET of proton recoils is simply too low to nucleate a stable vapor cavity and every interaction with a hydrogen atom is essentially a wasted energy deposition event. Conversely, the large atomic fluorine composition is highly beneficial for TMFDs due to its high LET. As a point of reference, the ^{252}Cf weighted, macroscopic cross section for DFP is approximately 0.2 cm^{-1} and approximately 0.08 cm^{-1} for acetone when neglecting hydrogen interactions.

From a thermofluid dynamics standpoint, DFP has low values of viscosity, surface tension, boiling temperature, and latent heat of vaporization. The low surface tension allows the fluid to properly wet the detector surfaces, thereby preventing spurious cavitations, which register as false-positive detection events. As inferred from eq. (2.2), lowering the surface tension reduces critical bubble size constraint, and thereby reduces the amount of vapor that a traversing recoil ion must generate from localized boiling. Finally, the low enthalpy of vaporization and boiling temperature means less energy is required to induce phase change; i.e. a recoil ion will generate more vapor per unit linear energy transfer. All of these factors equate to DFP having a high intrinsic efficiency for fast neutron detection.

2.4.2 Shortcomings of Heptane

Looking at the DETC curve for heptane in figure fig. 2.5, it can be seen that the deposition energy threshold at 7 bar is approximately 500 keV. Using the α parameter defined in eq. (2.7), the minimum neutron energy that can deposit 500 keV on a carbon nucleus via elastic scatter can be back calculated. Assuming there are no partial energy depositions, that is, the max energy recoil nucleus will deposit all of its energy over the length scale of a critical diameter, the minimum energy neutron that could be detected would be 1.76 MeV. From a neutron dosimetry standpoint, especially for fission spectra for which the most probably emission is approximately 0.8 MeV, this is an unacceptable lower bound for industrial field applications.

2.4.3 Geometrically Independent Response Matrices

In order to develop a field portable dosimeter, it is necessary to develop a response matrix that is independent of the surrounding geometry. The SAS response matrix was developed to be applicable to the specific CTMFD and surrounding geometry where the experimental measurements were conducted; that is, neutron albedo from the surrounding geometrical structures is built into the detector's response. In this approach, the unfolded spectrum represents the fluence spectrum emitted by the source itself. However, for a field usable spectrometer/dosimeter, it is necessary to unfold the fluence spectrum at the immediate location outside the detector to best estimate the dose personnel might receive at that particular location regardless of the number and location of sources. The later approach allows for the use of the $H^*(10)$ ambient fluence to dose conversion factors for any arbitrary fluence spectrum. More details regarding response matrix development is discussed in later chapters.

3. SOURCES AND SPECTRUMS USED IN MAS EXPERIMENTS

This chapter provides an overview of the sources and geometry utilized during the array of experiments conducted throughout the scope of this work. A comprehensive summary of the isotope neutron sources is given as an introduction to the sources of variability and uncertainty in isotope-source spectra. The importance of prefacing this information prior to the presentation of data results cannot be understated. The assumed intensity and energy spectrum of the sources described herein are taken as the reference standard for comparisons with unfolded spectrum and simulation results. As a consequence, any inaccuracy or uncertainty in the assumed values will unavoidably be propagated through the data used in simulations of the detector response matrices.

3.1 Californium-252 Source Characterization

One of the two main sources used for this unfolding work was a ^{252}Cf spontaneous fission source from Isotope Products Laboratories (current part number CS730240500M), a subsidiary company of Eckert & Ziegler. The nature of the source material is a californium-nitrate compound deposited in a ceramic matrix. The active element of the source is doubly-encapsulated in a standardized 3024 stainless steel capsule, 6 mm in diameter and 10 mm in height. The source data sheet, containing pertinent information about the isotopic composition, initial activity, and calibration date is shown in figure fig. 3.1. Note that, while note shown in the data sheet, the manufacturer product catalog specifies a 15% uncertainty in the initial activit

3.1.1 Estimation of the Californium-252 Source Intensity

The neutron source intensity is a crucial piece of information for the proposed spectroscopy procedures outlined in this work. The importance of source intensity is partially illustrated by equation eq. (2.8), which illustrates how MCNP results are scaled to obtain physical countrate estimates. Allowing the source intensity to remain as an independent variable adds an additional degree of dimensionality to the parameterization matrix used to

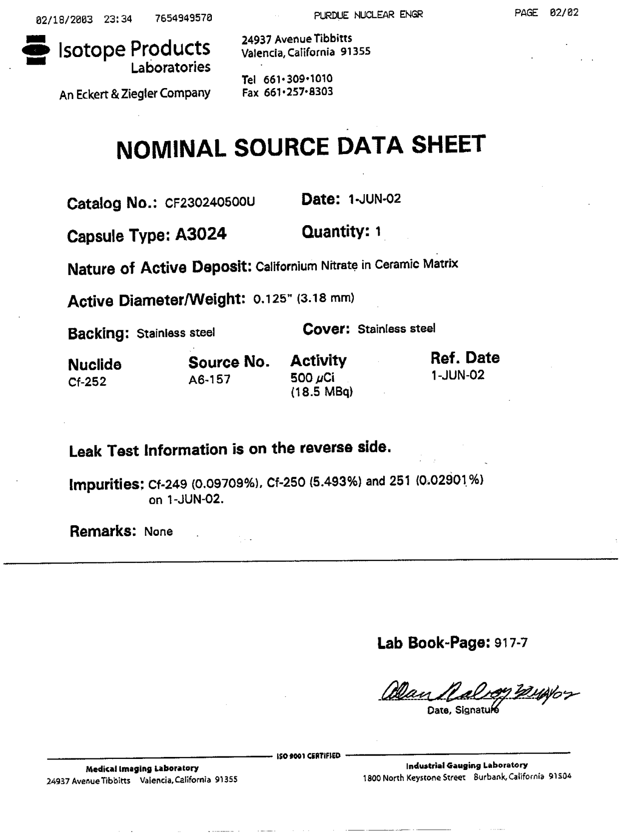

02/18/2003 23:34 7654949570 PURDUE NUCLEAR ENGR PAGE 02/02

Isotope Products
Laboratories
An Eckert & Ziegler Company

24937 Avenue Tibbitts
Valencia, California 91355

Tel 661•309•1010
Fax 661•257•8303

NOMINAL SOURCE DATA SHEET

Catalog No.: CF230240500U **Date:** 1-JUN-02

Capsule Type: A3024 **Quantity:** 1

Nature of Active Deposit: Californium Nitrate in Ceramic Matrix

Active Diameter/Weight: 0.125" (3.18 mm)

Backing: Stainless steel **Cover:** Stainless steel

Nuclide	Source No.	Activity	Ref. Date
Cf-252	A6-157	500 μCi (18.5 MBq)	1-JUN-02

Leak Test Information is on the reverse side.

Impurities: Cf-249 (0.09709%), Cf-250 (5.493%) and 251 (0.02901%) on 1-JUN-02.

Remarks: None

Lab Book-Page: 917-7

Date, Signature

ISO 9001 CERTIFIED

Medical Imaging Laboratory
24937 Avenue Tibbitts Valencia, California 91355

Industrial Gauging Laboratory
1800 North Keystone Street Burbank, California 91504

Figure 3.1. Manufacturer data sheet containing pertinent information about the ^{252}Cf source used in experiments at MFARL

estimate the DETC curve, as will become evident in later chapters. As such, this section describes the approach taken to estimate the true source intensity based on the limited source information shown in figure fig. 3.1.

The international standards organization (ISO) 8529 [22], [23] reference document on radiation sources requires that the source strength of a ^{252}Cf source be corrected for radioactive decay on a day-to-day basis. ISO 8529 further states that the standard uncertainty in the ^{252}Cf half-life is 0.5% to 0.7%. The uncertainty in the ^{252}Cf half-life alone equates to a relative uncertainty in the intensity of approximately 1% after two half-lives. It is assumed that the uncertainty in the half-lives of the other relevant isotopes is at least as large as the ^{252}Cf uncertainty; therefore, it is recommended that ^{252}Cf sources undergo recalibration every 5 years.

In addition to the ISO 8529 recommendations, other work has shown that ^{252}Cf sources do not decay exactly with the half-life of the ^{252}Cf isotope, uncertainty included [24]–[26]. Rather, the sources decay according to an effective half-life due mainly to the contributions of ^{248}Cm and ^{250}Cf. ^{248}Cm will be present from the α decay branch of ^{252}Cf and ^{250}Cf will be present as an impurity artifact of the transmutation chain. Roberts and Jones [24] analyzed several sources from the National Physical Laboratory, which had average compositions (in atom percent) of 16.8% ^{250}Cf and 83.2% ^{252}Cf, and found that a 20 year old source which had not been calibrated for 5 years could underestimate the intensity by 4%. Considering a reasonable margin of error for compliance with the H*(10) dose is only 20%, it seems important to evaluate the isotopically corrected intensity to prevent unnecessary introduction of error into the dose estimation.

Since the ^{252}Cf source used in this work has not been re-calibrated since its original manufacturer-specified calibration date, the current estimate has to the use the isotopics specified in the data sheet of figure fig. 3.1. It is assumed that the impurities are listed in atom percent. The specific activity $\hat{A}$, in bequerels per gram $\left[\frac{Bq}{g}\right]$, of a radioisotope is given by equation eq. (3.1), where λ is the radioactive decay constant, N_a is Avagadro's number, and M is the isotope's molar mass.

$$\hat{A} = \lambda \frac{N_a}{M} \tag{3.1}$$

The total specific activity $\hat{A}_{tot}$ of a ^{252}Cf source, with an isotopic composition in weight percent, w, identical to that of the source used in this work, is then given by equation eq. (3.2). The amount of source material initially present in the ceramic matrix can then be found by dividing the initial activity, in Becquerels, by the source's specific specific activity as shown in equation eq. (3.3).

$$\hat{A}_{tot} = N_a \left(w_{249} \frac{\lambda_{249}}{M_{249}} + w_{250} \frac{\lambda_{250}}{M_{250}} + w_{251} \frac{\lambda_{251}}{M_{251}} + w_{250} \frac{\lambda_{252}}{M_{252}} \right) \tag{3.2}$$

$$m_0 = \frac{A_0}{\hat{A}_{tot}} \tag{3.3}$$

To estimate the total neutron emission rate as a function of time we can treat each isotope as a separate source and sum over all isotopic contributions. For the Cf isotopes initially present, the neutron emission rate per second $\dot{I}$ of isotope i can be calculated using the familiar first-order radioactive decay law and accounting for the spontaneous fission branching ratio per decay, κ_{SF_i}, and the average neutron yield per fission, ν, as shown in equation eq. (3.4).

$$\dot{I}_i = \nu_i \kappa_{SF_i} \hat{A}_i m_i e^{-\lambda_i t} \tag{3.4}$$

The present analysis also takes into account the buildup and decay of ^{248}Cm. The time dependence of the ^{248}Cm contribution is treated by solving the Bateman equation. The subscripts p and d shown in equation eq. (3.5) correspond to the parent isotope (^{252}Cf) which decays by α decay with a branching ratio κ_α to the daughter isotope (^{248}Cm) which further decays by spontaneous fission with a branching ratio κ_{SF}.

$$\dot{I}_d = \nu_d \kappa_{SF_d} \kappa_{\alpha_p} \hat{A}_p m_{0_p} \frac{\lambda_d}{\lambda_d + \lambda_P} \left(e^{-\lambda_p t} - e^{\lambda_d t} \right) \tag{3.5}$$

The decay trend is represented visually in fig. 3.2

3.2 ^{241}Amerecium-Berrylium (AmBe) Source Characterization

In order to make sure the CTMFD's empirical response function was not overfit to a single spectrum shape, data were also taken with a 10mCi ^{241}AmBe (α,n) isotope source, which has a characteristically harder neutron spectrum. The ^{241}AmBe source is in the form of a Troxler moisture-density gauge. Due to the age of the instrument, the manufacturer could not provide a source datasheet or any details about the instrument's construction or manufacturing. The lack of detailed information makes using this source's spectrum as a calibration reference somewhat problematic.

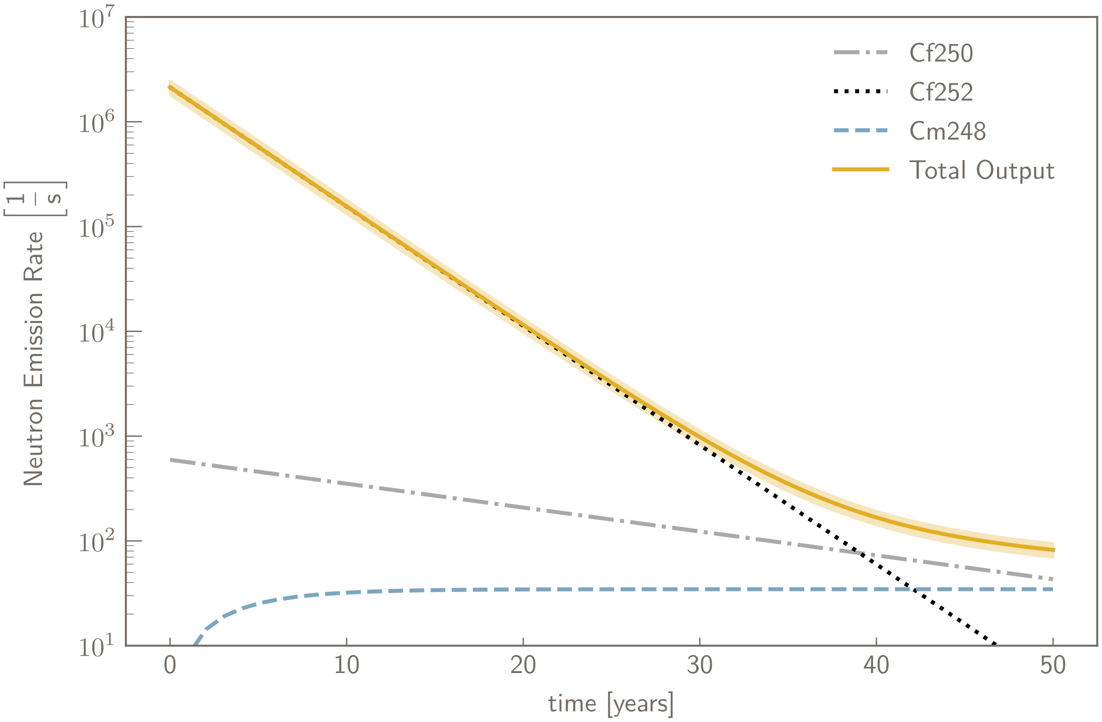

Figure 3.2. Time-dependent intensity of a ^{252}Cf source with an isotopic composition similar to the source used in this work after accounting for the contributions from ^{248}Cm and ^{250}Cf. Deviation of the intensity from the pure ^{252}Cf begins to occur after approximately 25 years

3.2.1 Inherent Uncertainties in Isotope Sources

In contrast to a spontaneous-fission source like ^{252}Cf, the neutron spectrum from (α,n) sources have significantly more variability in both the spectrum shape and intensity. The inherent variability can be attributed to a multitude of factors, including: the manufacturer's knowledge of the radioactive material's characteristics e.g. material density, oxidation characteristics, initial mass of the radioactive isotope, and granulometry of the oxide crystals.

Spectral Shape Variations

The size distribution of the amerecium-oxide crystal clusters has a particularly pronounced effect on each source's spectrum. Alpha particles from ^{241}AmBe are born with a monoenergetic spectrum at energies of 5.48574 MeV and 5.44298 MeV with branching ratios of 85.2 and 12.8, respectively [9], but undergo some amount of energy loss inside the ^{241}AmO$_2$ crystal cluster before interacting with the beryllium, such that the beryllium atoms are subject to a spectrum of alpha energies, rather than two distinct energies.

The effect of cluster radius on the spectrum shape as derived using the SOURCES4C code package [27] is illustrated in fig. 3.3. It can be seen that the width's of the spectrum peaks are a strong function of the cluster size. The reference spectrum was taken from ISO 8529-1 as the standard spectrum to use for ^{241}AmBe sources, though with understanding that the spectrum does not represent an absolute reference of accuracy.

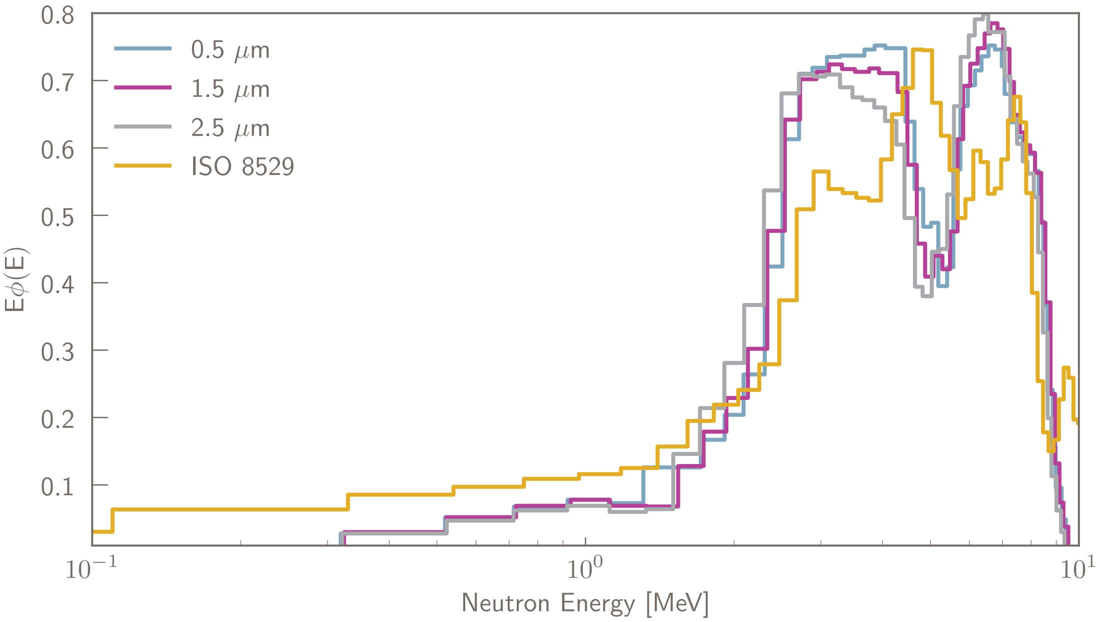

Figure 3.3. SOURCES4C calculation of theoretical neutron spectra from an ^{241}AmBe source with varying crystal cluster sizes.

Spectral shape variations also arise as artifacts of the source size and Be:^{241}Am atomic composition ratio. A high ratio of Be:^{241}Am is analogous to an infinitely thick target approximation, where every α particle is fully stopped inside the Be material. Large ratios inherently imply larger physical dimensions which, in conjunction with beryllium's affinity as a neutron moderator, will increase the relative fraction of neutrons below 2 MeV [28].

Spectral Intensity Variations

The cluster radius also influences the overall yield through the $Be(\alpha, n)$ differential cross section. In general, the higher the alpha energy the greater the neutron yield. Larger cluster sizes result in softer α spectra as they experience what is analagous to continuous energy deposition self-shielding and subsequently yield a lower neutron output. This effect is illustrated in figure fig. 3.4.

Estimates for the alpha-to-neutron conversion yield vary widely across literature. Theoretical and experimental measurements of thick-target neutron yields are in the range of 50-90 neutrons per million alphas. The most frequently used estimate is about 2.2x10^6 neutrons per second per curie or about 59 neutrons per million alphas [9], [28]–[30]. Using this value, the Troxler ^{241}AmBe source used in this work would have an estimated intensity of about 2.2x10^4 neutrons per second.

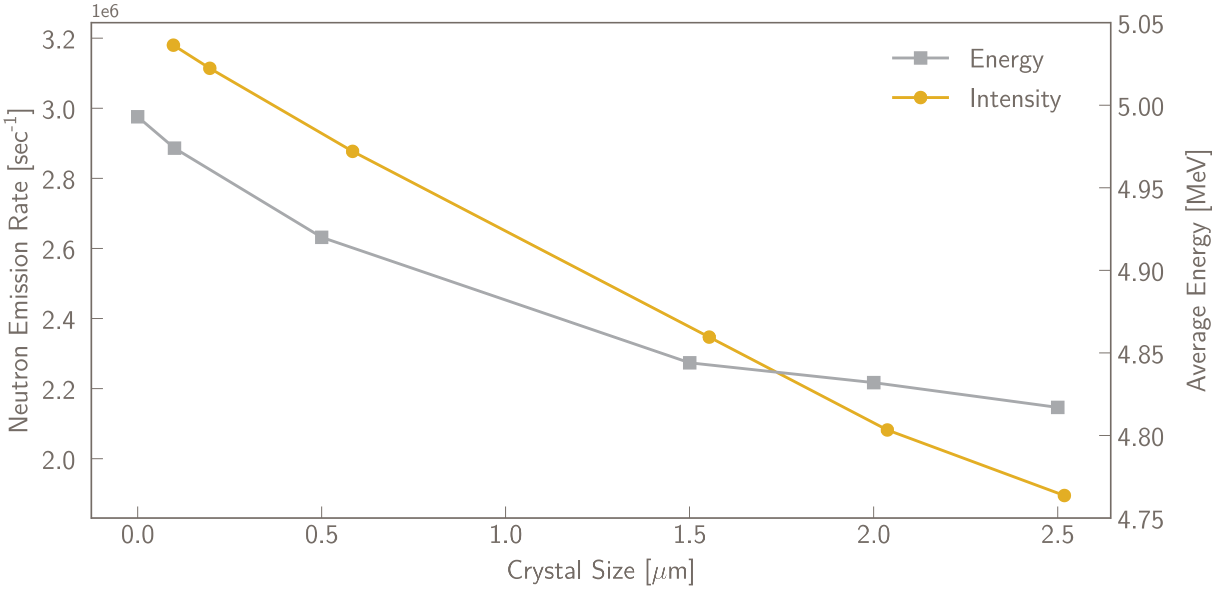

Figure 3.4. Estimation of the neutron yield as a function of crystal diameter and the corresponding average alpha energy.

3.3 Geometric Considerations for MCNP Modeling of Experiments

Two options existed for where experiments should be conducted. The first option was an open geometry where the only predominant source of neutron albedo would be the concrete floor. While a geometry with minimal room-return would be ideal, the inability to take long datasets limited its attractiveness. Without a sufficient number of detection events, count rate trends could be susceptible to statistical fluctuations. The other option was a small enclosed room 4 meters long, 2.5 meters wide, and 6 meters tall. The proximity of the detector to the room walls meant room return could not be assumed to be negligible. However, access restrictions to the room meant data could be taken over an extended time period. This ability to remove susceptibility to statistical fluctuations was deemed of greater importance than minimizing room return as long as the room features could be adequately translated to the MCNP model.

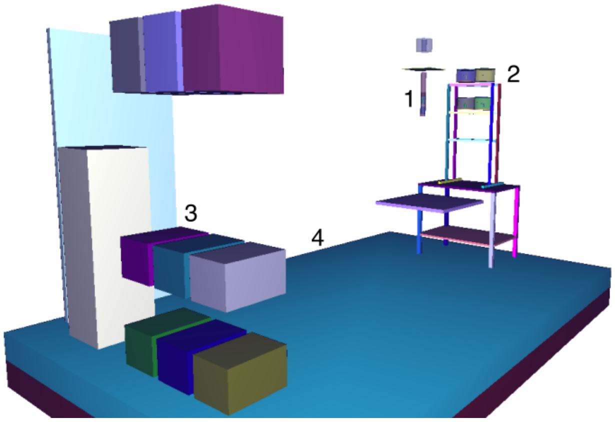

Figure 3.5. MCNP model of the lab geometry used in experiments with unmoderated sources. The structures and walls enclosing the room are not shown for visual clarity. The numbers in the image correspond to the following: (1) Source drop tube, (2) CTMFD detector panel, (3) Storage (hydrogenous shielding), (4) Concrete floor

The "true" flux present at the detector surface was estimated using an F4 flux tally in MCNP model. For experiments with the CTMFD, the tally volume was represented using parallelpiped macrobody located inside the acrylic detector enclosure. The dimensions of the cell volume were 14 cm long, 14 cm wide, and 9 cm tall. While, the actual physical volume of the CTMFD is much less than the volume of the tally cell, these dimensions were specifically selected to encompass both the detector bulb and arms. Thus, the tally represents the spatial average flux that the detector arms experience as they spin about their axis of rotation.

For experiments with the ^{6}LiI based Bonner spheres, hereafter referred to as LiI BSS, the “true” flux present at the LiI BSS detector surface was represented by tallying the flux inside the 2 inch Bonner sphere, where the cell material card was changed from polyethylene to air. It was assumed that the spatial variation in the flux would be negligible relative to the energy resolution of each detector, thereby making the exact choice of the tally volume’s dimensions arbitrary in nature.

3.3.1 Impact of Room Scattering on the Spectra Used for Calibrating Detector Response Functions

The relative contribution of neutron albedo to the flux spectrum at the detector face can be estimated in MCNP by “voiding” all of the cells representing physical structures in the room. Note that the detector enclosure, source encapsulation cells were left unchanged as they would be present in both the open room and closed room geometries. The Cf and AmBe spectra, shown in fig. 3.6, depict the spectra at the CTMFD detector with the sources at a distance of 300 cm. This distance corresponds to the maximum source-to-distance case used in experiments with either detector system and consequently the case with the highest albedo contribution. Also the case where the simulation results are most susceptible to bias introduced by uncertainty in transcribing physical geometrical nuances to a simplified MCNP geometry.

Room return increases the integral fluence by 37% and 40% for ^{241}AmBe and ^{252}Cf. The impact of albedo on the fluence energy spectrum is not constant between sources on account of the spectra having different average neutron energies. These differences can be quantified by comparing the cumulative integral fluence totals as a function of energy. First, the spectra are first normalized to remove intensity differences. The cumulative integral fluence is calculated using eq. (3.6) and shown by the gold and gray curves in fig. 3.7. The effect becomes more evident when comparing the ratio of the cumulative totals in each energy bin shown on the right-hand axis. The slope of the black curve effectively illustrates the rate (with respect to energy) that neutrons born with higher energies are down scattered into lower energy bins from collisions in the room geometry.

$$\hat{\phi} = \frac{\int_0^{E_i} \phi(E)dE}{\int_0^{E_{max}} \phi(E)dE} \tag{3.6}$$

Because neutron room return decreases as the source-to-detector distance decreases, the slope of the black curve in fig. 3.7 will vary for the same source at different distances. Conceptually, the consequences of this effect will become more evident during the discussions in section 7.3 regarding the equivalence of measurements with overlapping pressures but taken at different sources. This discussion becomes irrelevant if the response calibration measurements could be taken in a low-scatter room. Alternatively, a more cost effective option is to acquire or construct a device known as a scatter cone, which is designed specifically for the purpose of isolating contributions from room scattering.

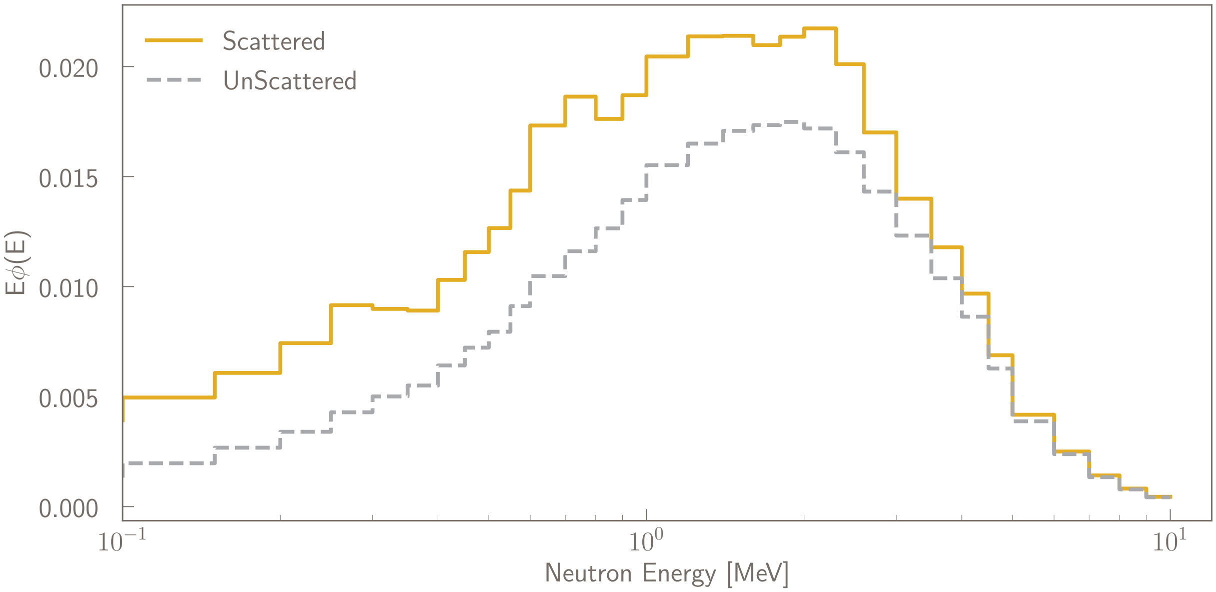

(a) ^{252}Cf

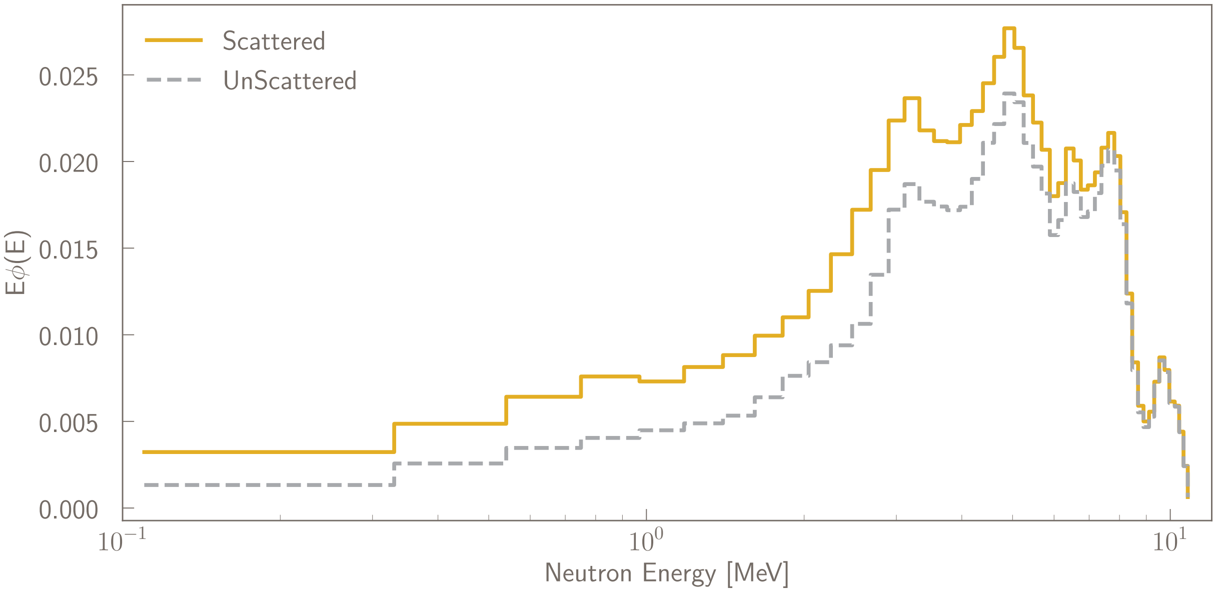

(b) ^{241}AmBe

Figure 3.6. Comparison of the albedo contribution from room structures in the closed geometry to a free-in-air spectrum at a source to detector distance of 300 cm.

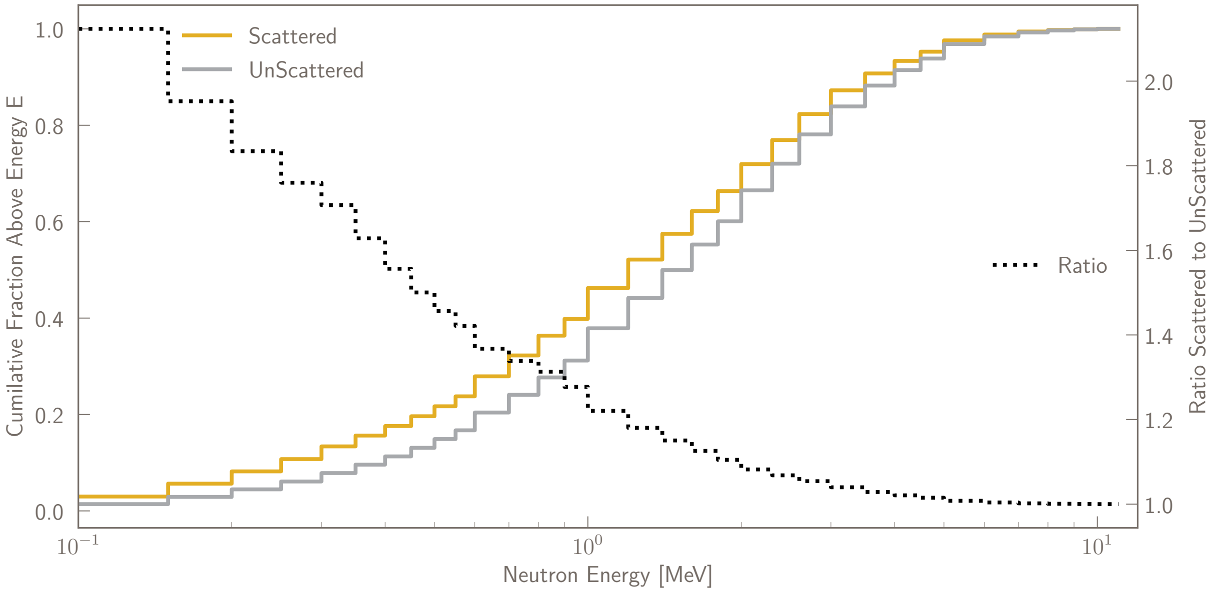

(a) ^{252}Cf

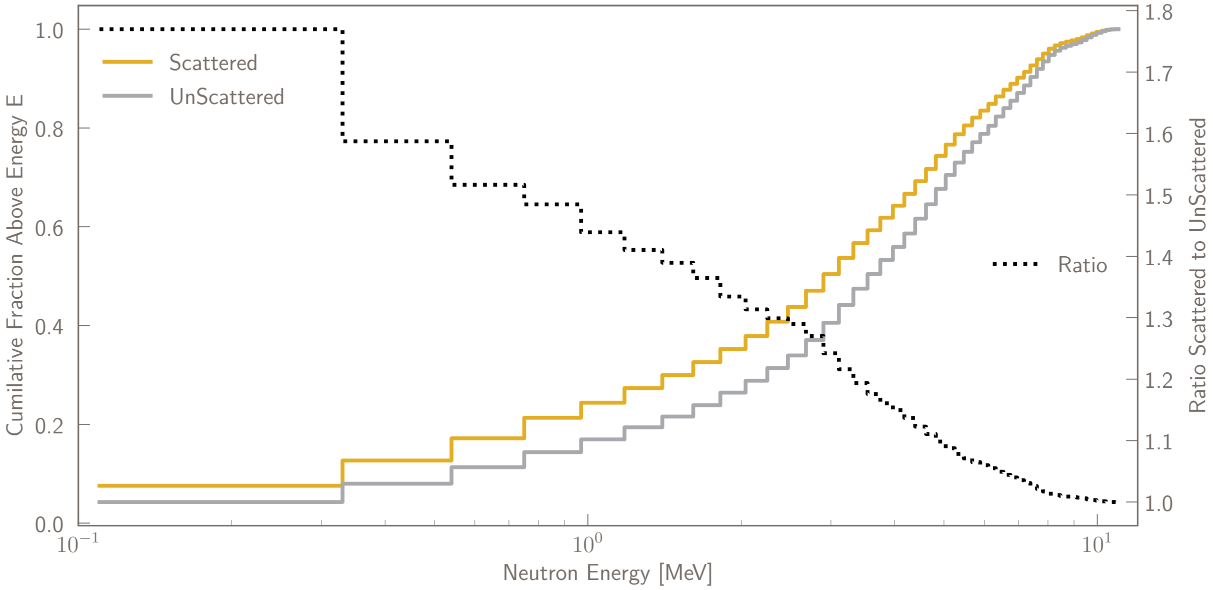

(b) ^{241}AmBe

Figure 3.7. Cumulative fluence totals as a function of neutron energy for the spectra from fig. 3.6 as an alternative representation for quantifying the influence of room return.

4. BENCHMARK UNFOLDING WITH BONNER SPHERE SPECTROMETERS

Measurements were also taken with a bonner sphere type spectrometer to serve as a baseline performance comparison for the CTMFD's spectroscopic capabilities. Given the vast amount of research and development experience on bonner sphere type spectrometers throughout the industry, most of the assumptions and model design choices in this work were based on information reported in literature. The details of these choices are outlined in this chapter.

4.1 MCNP Model for the ^{6}LiI Bonner Sphere Spectrometer

The particular BSS variant (Ludlum Measurements Inc. Model 42-5) used in this work uses a ^{6}LiI scintillation crystal as its thermal neutron detector. Dimensions of the detector were taken from a combination of the product manual and literature references by groups who physically deconstructed detectors to validate their models. A radiograph of the detector, taken by Sarchiapone et. al and reported in [31], is shown in fig. 4.1. The corresponding geometry in MCNP is shown in fig. 4.2.

As specified in the product manual, the scintillation crystal is rectangularly shaped, 4 mm in diameter and 4 mm in height. Crystal densities ranging from 3.494-4.08 g cm^{-3} have been reported in literature. A density of 3.494 g cm^{-3} was chosen for the simulations in this work as it seemed to be the most frequently adopted value. For the material composition of the crystal, the mass fractions (in weight percent) of the ^{6}Li, ^{7}Li, and ^{127}I atoms were selected as 4.36x10^{-2}, 1.80x10^{-1}, and 9.546x10^{-1}, respectively.

The bonner sphere set contains high density polyethylene spheres (HDPE) of 2, 3, 5, 8, and 10 inches in diameter. The density of HDPE was taken as 0.95 g cm^{-3}. The $S(\alpha,\beta)$ thermal scattering cross section corrections were used for materials which had libraries available: aluminum and HDPE.

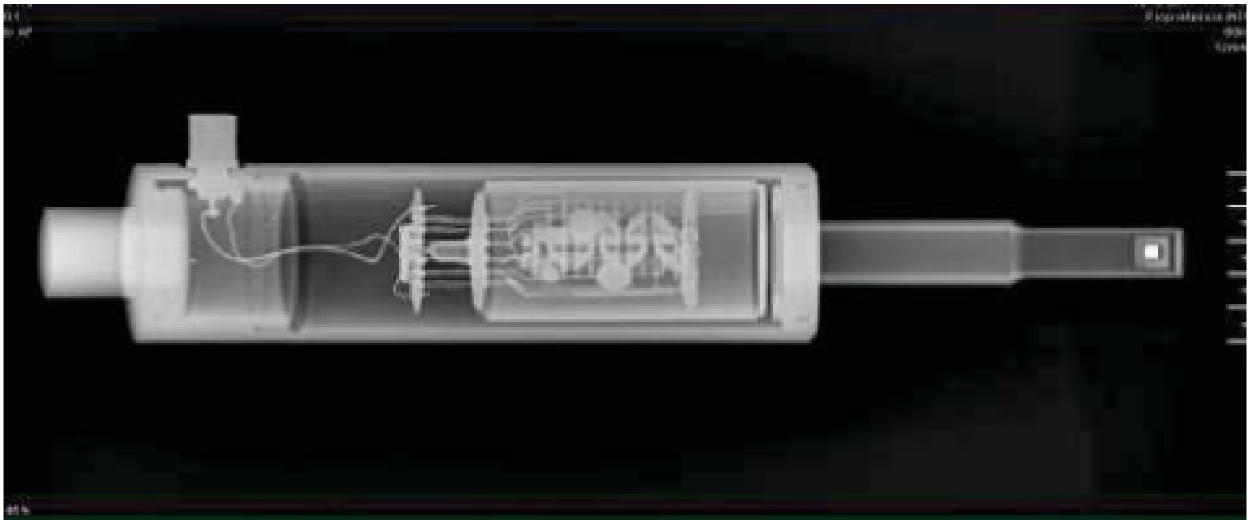

Figure 4.1. Radiograph of the LiI detector

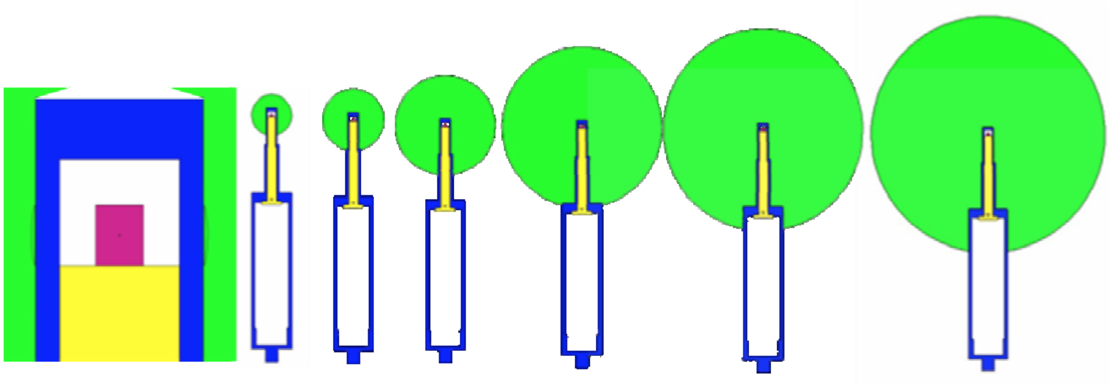

Figure 4.2. MCNP representation of the LiI detector and the different bonner ball sizes

4.2 Calculation of the ^{6}LiI Response Matrix

When simulating the BSS response matrix the detector must be fully "illuminated" by the monoenergetic source and there must be zero spatial gradient in the flux field intensity at the detector face. Without this specification, the anisotropy of the flux field could introduce an artificial angular dependency in the computed response, which cannot be easily unfolded. When a detector's dimensions (i.e. the bonner sphere diameter) are comparable to the source to detector distance, the neutron flux intensity will vary across the sphere's surface. At large distances, however, the fluence field can be approximated by a plane wave as shown in fig. 4.2.

This assumption serves as the basis for simulating a detector's response to a monoenergetic neutron source.

4.2.1 Methodological Modeling Considerations and Output Normalization

Simulation of a plane wave in MCNP was accomplished using a rectangular surface source 32 cm wide and 48 cm tall. The width of the source is was chosen to be slightly greater than the diameter of the 12 inch bonner sphere to satisfy the requirement that the detector is fully illuminated. The reason the height dimension is greater than 32 cm is to account for neutrons which might scatter off the acrylic light pipe and into the bonner ball. Inclusion of the light pipe makes the detector asymmetrical and thereby introduces an angular dependence into the detector's response. It was suspected that this effect would be insignificant for fast neutrons but potentially important for epithermal neutrons. Particularly, for neutrons which have scattered off the ground and are traveling upwards into the detector.

Response matrix simulations for BSS are often done with a circular surface source with a cross sectional area (diameter) identical to each bonner ball. However, this approach does not allow for secondary effects from the rest of the LiI detector's body. In the approach adopted here, the rectangular surface source's area is larger than the bonner ball. Thus there will be some fraction of neutrons which will miss the detector entirely and that fraction will increase as the bonner ball size decreases. Though the source area was left constant, the number of particles simulated necessary to achieve statistical convergence varies as a function of neutron energy, i.e. cross section. As a consequence, it is necessary to apply a scaling factor to normalize the MCNP output across all bonner sphere diameters.

Conceptually, a detector's response can be thought of as its effective area, similar to how the barn (with units of cm^2) is used to represent nuclear cross sections. A more simplistic interpretation is that a detector's response is the number of counts recorded per unity flux. Normalization of the MCNP output is achieved using eq. (4.1) where R is the detector's response in cm^2, C_{mcnp} is the total number of thermal capture events in the LiI crystal during the simulation, N_{mcnp} is the total number of neutron histories simulated, and A_s is the surface area of the source. The right-most side of eq. (4.1) is included since MCNP automatically normalizes its tally results by N_{mcnp}.

$$R = \frac{C_{mcnp}}{N_{mcnp}/A_s} = \left(\frac{C_{mcnp}}{N_{mcnp}}\right) A_s \tag{4.1}$$

4.2.2 Response Matrix Energy Binning

The binning of the response matrix was chosen to encompass all energy bin edges seen in the ISO spectra for the Cf and AmBe sources for neutron energies below 100 keV. For energies above 100 keV, the bins are set to be 100 keV wide, up to 15 MeV. This degree of fast energy discretization is unnecessary given that the BSS response is smooth and the archetype's inherently coarse energy resolution. However, the extra data points provide flexibility for re-binning purposes and allows for an equivalent comparison to the CTMFD's fast energy response. Response matrices of BSS systems published in literature commonly have between 30 and 50 energy bins, are usually equally wide in lethargy space, and contain about four bins per decade in energy.

4.2.3 Response Matrix Simulation Results

The response matrices calculated with MCNP in this work are in close agreement with recent studies found in literature [32]–[35]. This is to be expected as the MCNP model used in this work was built using dimensions and compositions reported in other studies. The accuracy of the BSS in measuring dose rates will largely be a function of the calibration factor used for agreement between experimentally recorded values and simulation predictions. A certain degree of over-prediction should be expected as MCNP cannot account for light loss photomultiplier tube inefficiencies and photon contamination. The next section will discuss the experiments used to calibrate the BSS used in this work.

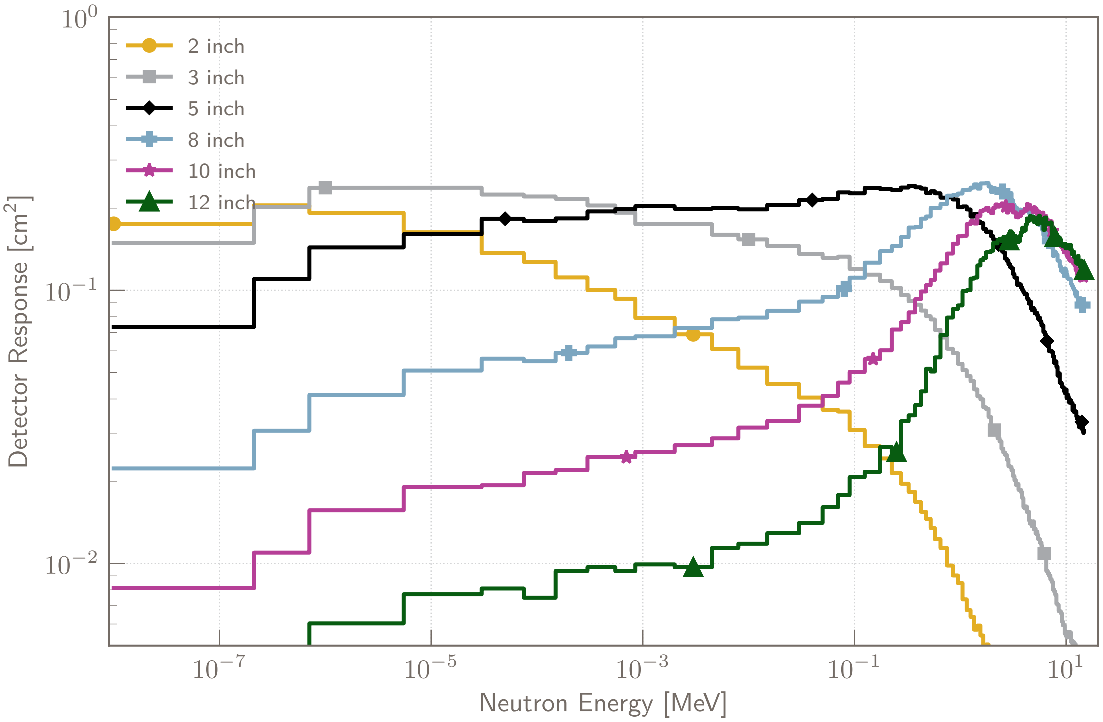

Figure 4.3. Response matrix of the ^{6}LiI detector for each bonner ball as calculated with MCNP6.

4.3 Comparison Between Experimental and MCNP Code ModelCount Rates

To verify the correctness of the MCNP simulated response matrix. Measurements were taken in the closed room geometry shown in fig. 3.5 with bare ^{241}AmBe and ^{252}Cf sources using a source to detector distance of 50 cm. The MCNP model of the closed room geometry was used to generate fluence tallies and count rate predictions. Ideally, the hypothetical detector inefficiencies that MCNP cannot simulate can be accounted for by comparing measured count rates to predicted rates, and determining a proportional constant that scales the predictions to match experiments. Unfortunately, this proved problematic as the MCNP predictions are a function of the true source intensity; which, as discussed in section 3.2, is somewhat ambiguous.

Comparison data of the measured and simulated count rates for the ^{252}Cf and ^{241}AmBe sources are shown in table 4.1 and table 4.2, respectively. In each instance MCNP over predicts the count rate, as expected, though the degree of over prediction is inconsistent between ^{252}Cf and ^{241}AmBe. This is counterintuitive as photomultiplier tube effects, gamma contamination, etc. cannot explain the dependency on ball size and spectrum type. While surprisingly sparse, references to differences between MCNP predictions and experimental measurements do exist in the literature [32], [36]. Both of these papers report on the experimental response to monoenergetic accelerator sources and are frequently referenced in the literature field of bonner sphere spectrometry. Mares et. al [32] reports a 28% difference between simulation and experiment. Alevra et. al [36] even reports a strong dependency on ball size, observing a 25% difference between the 2 inch and 12 inch spheres. Interestingly, Alevra also presents data from identical experiments with 3 different Bonner systems utilizing ^{3}He detectors. The associated calibration constants were found to be independent of the ball diameter for the ^{3}He systems. These results suggest that the ball-diameter dependency is unique to the ^{6}LiI system.

Table 4.1. Comparison between the count rates measured in the closed room geometry to those predicted by MCNP for the ^{252}Cf source.

Ball Diameter	**Experiment** $\left[\text{min}^{-1}\right]$	**MCNP** $\left[\text{min}^{-1}\right]$	**Ratio**
2	1.56 ± 0.02	2.02 ± 0.01	0.77
3	4.83 ± 0.05	6.99 ± 0.01	0.69
5	12.63 ± 0.11	19.00 ± 0.03	0.67
8	13.21 ± 0.11	20.65 ± 0.04	0.64
10	9.65 ± 0.10	15.32 ± 0.03	0.63

Possible explanations for the ratio differences between the ^{252}Cf and ^{241}AmBe sources are that the adopted source intensities are incorrect and or the MCNP model of the room geometry is incorrect. To investigate the possibility of geometric modeling errors all count rates were normalized by the summation of the count rates in all spheres. If the geometry was modeled incorrectly enough to significantly vary the flux spectrum then the normalized count distribution from experiment versus MCNP should differ accordingly.

Values for the normalized count rates are shown in table 4.3. The ^{252}Cf experiment and MCNP ratios show negligible differences in all but the 2 inch sphere, though this is not

Table 4.2. Comparison between the count rates measured in the closed room geometry to those predicted by MCNP for the ^{241}AmBe source.

Ball Diameter	Experiment $\left[\text{min}^{-1}\right]$	MCNP $\left[\text{min}^{-1}\right]$	Ratio
2	0.92 ± 0.02	0.69 ± 0.02	1.38
3	2.87 ± 0.04	2.28 ± 0.05	1.26
5	8.20 ± 0.09	6.97 ± 0.09	1.18
8	10.54 ± 0.10	9.61 ± 0.10	1.10
10	8.70 ± 0.09	8.56 ± 0.09	1.02

concerning due to the innate difficulties associated with modeling thermal neutrons [37]. Larger discrepancies exist in the ^{241}AmBe data. The fact that the ^{252}Cf data matches so well implies that geometric modeling errors are not the source of the problem. It is possible, and likely probable, that the ISO recommended ^{241}AmBe spectrum differs from the source spectrum used in these experiments. However, it is clear that the spectrum shape is not the dominant contributor to the discrepancies between table 4.1 and table 4.2.

Table 4.3. Comparison between the normalized count rates measured in the closed room geometry to those predicted by MCNP. Count rates are normalized by the sum of the counts in all spheres.

Diameter	Norm. Count Rate		Exp/MCNP Ratio	
	Cf	AmBe	Cf	AmBe
2	0.037	0.029	1.180	1.239
3	0.115	0.092	1.056	1.133
5	0.302	0.263	1.016	1.058
8	0.315	0.337	0.977	0.986
10	0.230	0.279	0.962	0.914

The more plausible explanation behind the count rate ratio differences is an incorrect estimate of the ^{241}AmBe source intensity. The average count rate ratio for ^{252}Cf is 0.68, acceptably similar to the 0.72 ratio reported by Mares et. al. In contrast, the average ratio for ^{241}AmBe is 1.19. It would appear logical to expect the average ^{241}AmBe ratio would be close to the ^{252}Cf average ratio, i.e. 0.68. The MCNP predicted count rates in table 4.2 are calculated using the ISO recommended source intensity of 2.2x10^6 neutrons per second per curie. In order to reduce the ^{241}AmBe average count rate ratio from 1.19 to 0.68 the assumed source intensity has to be increased to 3.8x10^4; which, according to fig. 3.4, is higher than the maximum possible theoretical yield for the listed 10 mCi activity.

Though the ^{252}Cf intensity is known with a reasonable degree of confidence, it cannot be used as a reference point to calibrate the ^{241}AmBe intensity. Even if the source intensities were identical, the different spectrum shapes will register different count rates in the same detector. The effect of spectrum shape can theoretically be accounted for by passing the different spectra through a detector's response matrix and taking the ratio of the responses. However, this approach would require more accurate knowledge of the ^{241}AmBe spectrum's shape than is currently available.

In theory, ^{239}PuBe and ^{241}AmBe sources would have a similar spectra, so any intensity difference should scale a detectors response proportionately. In reality, the calibration is more complicated. ^{239}PuBe sources still suffer from the same manufacturing-induced variability as ^{241}AmBe and also have the added complication of a non-negligible fission contribution. Nevertheless, two additional measurements were taken using a 1 Ci ^{239}PuBe source. The first measurement was a direct count rate comparison (without unfolding) using the ^{6}LiI detector and the 5, 8, and 10 inch bonner spheres. The sources were placed within a few centimeters of each sphere to minimize scattering contributions from objects in the room. The second measurement was a dose rate comparison using a Fuji NSN3 gas proportional counter type dosimeter.

The data for the direct count rate comparison is shown in table 4.4. The average proportionality ratio of all three spheres indicates that the ^{239}PuBe intensity is a factor of 80 times greater than the ^{241}AmBe source. The dose rate measurements with the Fuji NSN3 in table 4.5 similarly indicate an intensity ratio of approximately 80. Table 4.6 contains a parametric tabulation of what the ^{241}AmBe intensity equate to based on an assumed ^{239}PuBe intensity and an 80:1 ratio. Unfortunately, a traceable intensity calibration or information on the isotopic composition of the ^{239}PuBe is not available. However, a previous colleague conducted similar proportionality-based measurements with a calibrated 3 Ci ^{241}AmBe source and a liquid scintillation detector, the results of which indicated a ^{239}PuBe intensity of approximately 2.2x10^6 neutrons/second. Based on this number and the average ratios in table 4.4 and table 4.5, the 10 mCi Troxler ^{241}AmBe intensity is approximately 2.8x10^4 neutrons/second. This number is assumed for the remainder of the work herein.

Table 4.4. Count rate proportionality measurements from 1 Ci ^{239}PuBe and 10 mCi ^{241}AmBe sources with a ^{6}LiI detector

Diameter	**Count Rate [cps]**		
	AmBe	PuBe	Ratio
5	0.79	63.96	80.77
8	1.26	99.17	78.47
10	1.19	97.51	81.68
Avg			80.31

Table 4.5. Dose rate proportionality measurements from 1 Ci ^{239}PuBe and 10 mCi ^{241}AmBe sources with a Fui NSN3 Dosimeter

Distance [cm]	**Dose Rate**			**Ratio**		
	Cf	AmBe	PuBe	Cf	AmBe	PuBe
25	0.407	0.434	36.436	0.938	1	83.92
50	0.107	0.120	9.985	0.892		83.26
100	0.031	0.036	2.743	0.841		74.38
Avg				0.899		80.52

Table 4.6. Calculated AmBe intensity as a function of PuBe intensity using the count rate proportionality measurements in table 4.4

^{239}PuBe Intensity (1 Ci)	1.80e6	2.00e6	2.20e6	2.40e6
Diam	**AmBe Intensity (10 mCi)**			
5	2.23e4	2.48e4	2.72e4	2.97e4
8	2.29e4	2.55e4	2.80e4	3.06e4
10	2.20e4	2.45e4	2.69e4	2.94e4
Avg	2.24e4	2.49e4	2.74e4	2.99e4

4.4 Spectrum Unfolding Results Using the ^{6}LiI Bonner Sphere Spectrometer

All unfolding is conducted with the Oak Ridge National Laboratory (ORNL) based Radiation Safety Information Computational Center (RSICC) distributed UMG 3.3 code package which incorporates the GRAVEL and MAXED unfolding algorithms. MAXED was originally developed to apply the maximum entropy principle to the unfolding of neutron spectrometric measurements [38]. The approach followed in MAXED has several features that make it attractive: it permits inclusion of *a priori* information in a well-defined and mathematically consistent way, the algorithm used to derive the solution spectrum is based on arguments that originate in information theory, and the solution spectrum is a non-negative function that can be depicted in closed form. This last feature permits the use of standard methods for the sensitivity analysis and propagation of uncertainties of MAXED solution spectra, which is incorporated via the use of the included IQU code package [39].

The main inputs into the MAXED unfolding package include: the response matrix of each detector, their measured count rate, and the uncertainty in each measurement. MAXED's roots in information theory require the user supply *a priori* information about the solution form. From a mathematical standpoint, the algorithm is maximizing the entropy of a probability distribution (spectrum) by iteratively perturbing the distribution prior. During each iteration, the algorithm "learns" new information, i.e. gains entropy, about the true form of the solution based on the entropy expression (eq. (4.2)) of the current solution and the default distribution. Thus, since the entropy S is a function of the shape of the default spectrum, the accuracy of the output solution will also carry a dependence on the accuracy of the starting spectrum.

$$S = \sum_i \left\{ \phi_i ln \left(\frac{\phi_i}{\phi_i^{def}} \right) + \phi_i^{def} - \phi_i \right\} \tag{4.2}$$

Another feature worth mentioning is MAXED's option to automatically scale the magnitude of the default spectrum. The default spectrum is normalized prior to unfolding. After the deconvolution, the normalized solution spectrum is multiplied by a proportional constant to preserve spectrum's intensity. This scale factor, computed by MAXED, corresponds to the value that minimizes the χ^2 of the default spectrum. Admittedly, this feature is mainly only of importance to this work because of the calibration uncertainties discussed in section 4.3. In consideration of field-practical operation where the intensity of the fluence field is likely unknown, it is recommended that this feature be turned on. However, any inaccuracy in the magnitude of response functions will consequently be represented as a bias in the total fluence/dose.

This recurrent issue with the response magnitude is further illustrated in fig. 4.4. The spectra shown in the figure are the result of unfolding the experimental data in table 4.2 and table 4.1 using the response matrix in fig. 4.3. The purple curve in each subfigure corresponds to the neutron spectrum simulated by MCNP. The MCNP result is used for the default spectrum because it represents the best guess of the true spectrum shape. The black, gold, and blue curves are the result of multiplying the response functions by the various calibration factors reported above. The response matrix yielding the black curve was multiplied by unity (no calibration factor). The gold curve was generated by multiplying the response functions by the vector of ball-dependent calibration factors. Finally, the response functions yielding the blue curve were multiplied by a scalar constant, computed from the mean of the vector of ball-dependent calibration factors.

The shape of the unfolded spectra in fig. 4.4 very closely resemble the MCNP-predicted spectrum. Differing only in magnitude implies that the response function curves are approximately correct and the problem is related to normalization of the matrix. This is supported by the discussion in the prior section regarding the normalized count rate data in table 4.3.

Table 4.3 contains data from one the MAXED output files. The quantity $\frac{C_{unf}-C_{meas}}{C_{meas}}$ is the fractional percent difference between the predicted and measured count rates, where the predicted counts are computed by folding the output spectrum with the detector response matrix. The quantity $\frac{C_{unf}-C_{meas}}{\sigma_{meas}}$, commonly known as the “Z-score”, is the ratio of the count rate difference to the measurement uncertainty. Values greater than unity indicate that the count rate difference is greater than the 1 sigma uncertainty implied by counting statistics. The information in these tables has proven useful over the course of this work. Specifically, it has been found that when inaccuracies are present in the unfolded spectrum, it is often the case that one or more of the count rates has a Z-score greater than unity.

Integral quantities for the unfolded fluence and dose rate are shown in table 4.8. The Lit_{avg} calibration factor yields the result closest to MCNP, predicting a dose rate within -12% of MCNP for ^{252}Cf and 14% for ^{241}AmBe. The MCNP dose rate is taken as the standard of accuracy. Therefore, the Lit_{avg} calibration factor will be used for the remainder of this work.

4.4.1 Impact of *A Priori* Spectrum on the Unfolded Result

A catalog of common spectrum shapes was assembled to study the influence of the guess spectrum shape on the unfolded result. At present, the library consists only of spectra from typical isotope sources, most of which were taken from ISO 8529. Figure 4.5 and fig. 4.6 contain unfolded spectra for each guess case using measurement data from ^{252}Cf and ^{241}AmBe, respectively. The gold curve is the unfolded spectrum using the guess shape corresponding to the same source used to record the data. The alternate color curve is the result of using one of the non-ideal guess spectra in the library.

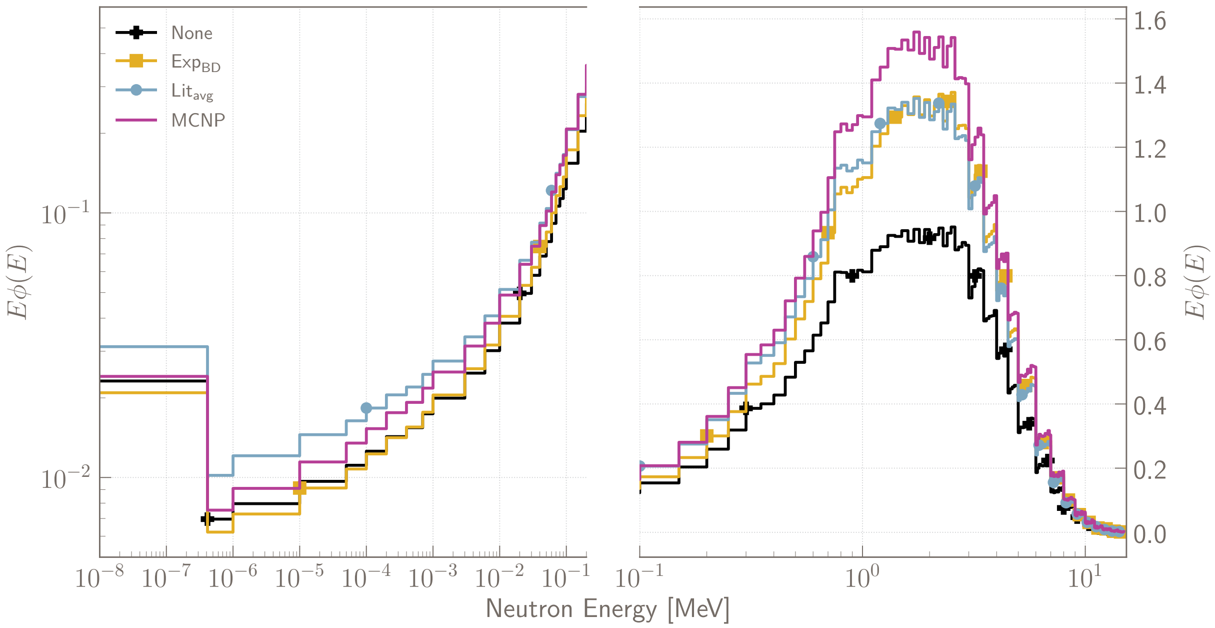

(a) ^{252}Cf

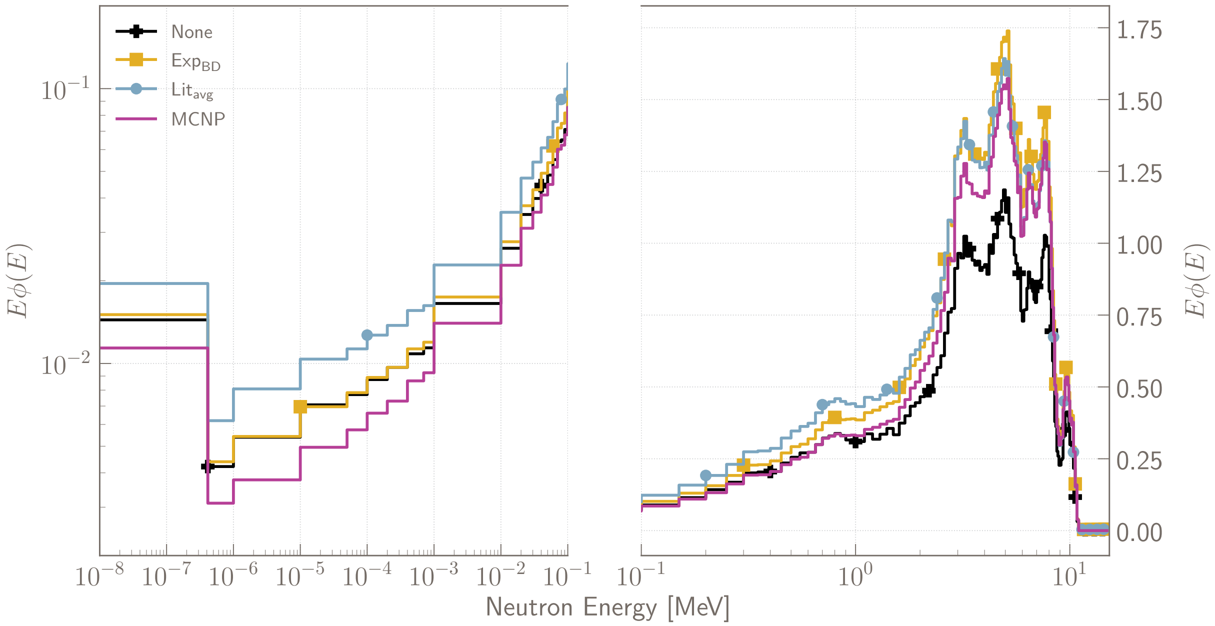

(b) ^{241}AmBe

Figure 4.4. BSS unfolded spectra comparison against MCNP using the various calibration factors. The true spectrum (purple), as simulated by MCNP, is used as the starting guess.

Table 4.7. Comparison of the measured versus calculated count rates for the different calibration factor options. The predicted count rates are calculated in MAXED by passing the guess and unfolded spectra through the detector response matrix.

(a) ^{252}Cf

		Guess		**Unfolded**	
	Diam	$\frac{C_{unf}-C_{meas}}{C_{meas}}$	$\frac{C_{unf}-C_{meas}}{\sigma_{meas}}$	$\frac{C_{unf}-C_{meas}}{C_{meas}}$	$\frac{C_{unf}-C_{meas}}{\sigma_{meas}}$
None	2	0.253	18.6	-0.020	-1.48
	3	0.406	36.9	-0.007	-0.64
	5	0.506	58.8	0.001	0.15
	8	0.553	65.1	0.005	0.53
	10	0.582	55.4	0.015	1.45
	Avg.	0.460	47.0	0.010	0.85
Exp_{BD}	2	0.175	12.9	-0.013	-0.92
	3	0.188	17.1	0.004	0.38
	5	0.182	21.2	0.012	1.34
	8	0.159	18.7	0.005	0.56
	10	0.128	12.2	-0.014	-1.38
	Avg.	0.166	16.4	0.009	0.92
Lit_{avg}	2	-0.098	-7.2	-0.020	-1.49
	3	0.012	1.1	-0.008	-0.74
	5	0.084	9.8	0.002	0.20
	8	0.118	13.9	0.005	0.64
	10	0.139	13.2	0.014	1.34
	Avg.	0.090	9.0	0.010	0.88

Table 4.7. Comparison of the measured versus calculated count rates for the different calibration factor options. The predicted count rates are calculated in MAXED by passing the guess and unfolded spectra through the detector response matrix.

(b) ^{241}AmBe

		Guess		**Unfolded**	
	Diam	$\frac{C_{unf}-C_{meas}}{C_{meas}}$	$\frac{C_{unf}-C_{meas}}{\sigma_{meas}}$	$\frac{C_{unf}-C_{meas}}{C_{meas}}$	$\frac{C_{unf}-C_{meas}}{\sigma_{meas}}$
None	2	-0.122	6.6	-0.001	-0.08
	3	0.016	-1.2	-0.006	-0.44
	5	0.108	9.6	0.007	0.62
	8	0.169	17.4	-0.015	-1.59
	10	0.244	23.2	0.015	1.38
	Avg.	0.132	11.6	0.009	0.82
$\mathrm{Exp}_{\mathrm{BD}}$	2	-0.176	-9.5	-0.032	-1.71
	3	-0.169	-12.1	-0.009	-0.61
	5	-0.130	-11.5	0.005	0.42
	8	-0.128	-13.2	-0.012	-1.21
	10	-0.113	10.8	-0.002	-0.23
	Avg.	0.143	11.4	0.012	0.84
$\mathrm{Lit}_{\mathrm{avg}}$	2	-0.368	-19.8	-0.001	-0.06
	3	-0.292	-20.8	-0.007	-0.48
	5	-0.202	-17.9	0.006	0.54
	8	-0.159	-16.3	-0.015	1.55
	10	-0.104	-9.9	0.015	1.44
	Avg.	0.225	17.0	0.009	0.813

Table 4.8. Comparison of the unfolded spectra fluence and dose rate versus MCNP as a function of the calibration factor.

(a) ^{252}Cf

	Fluence $\frac{n}{cm^2 s}$			**Dose** $\frac{mRem}{hr}$		
	Total	Fast	Thermal	Total	Fast	Thermal
MCNP	1.791	1.596	0.194	0.215	0.213	1.50e-3
None	1.193 ±1.9e-2	1.033 ±1.4e-2	0.160 ±4.8e-3	0.138 ±1.9e-3	0.137 ±1.8e-3	1.211e-3 ±3.2e-5
Exp_{BD}	1.547 ±1.7e-2	1.385 ±1.4e-2	0.162 ±3.5e-3	0.187 ±1.8e-3	0.186 ±1.8e-3	1.278e-3 ±2.3e-5
Lit_{avg}	1.652 ±2.1e-2	1.431 ±1.6e-2	0.221 ±5.4e-3	0.191 ±2.1e-3	0.190 ±2.0e-3	1.643e-3 ±3.5e-5

(b) ^{241}AmBe

	Fluence $\frac{n}{cm^2 s}$			**Dose** $\frac{mRem}{hr}$		
	Total	Fast	Thermal	Total	Fast	Thermal
MCNP	1.128	1.040	8.781e-2	0.146	0.145	7.601e-4
None	0.970 ±4.7e-2	0.865 ±3.7e-2	0.105 ±1.1e-2	0.120 ±5.0e-3	0.119 ±4.9e-3	7.601e-4 ±6.9e-5
Exp_{BD}	1.285 ±7.8e-3	1.173 ±6.2e-3	0.112 ±1.6e-3	0.164 ±8.6e-4	0.163 ±8.5e-4	8.311e-4 ±9.2e-6
Lit_{avg}	1.344 ±4.4e-2	1.198 ±3.4e-3	0.146 ±1.0e-2	0.166 ±4.7e-3	0.165 ±4.6e-3	1.055e-3 ±6.5e-5

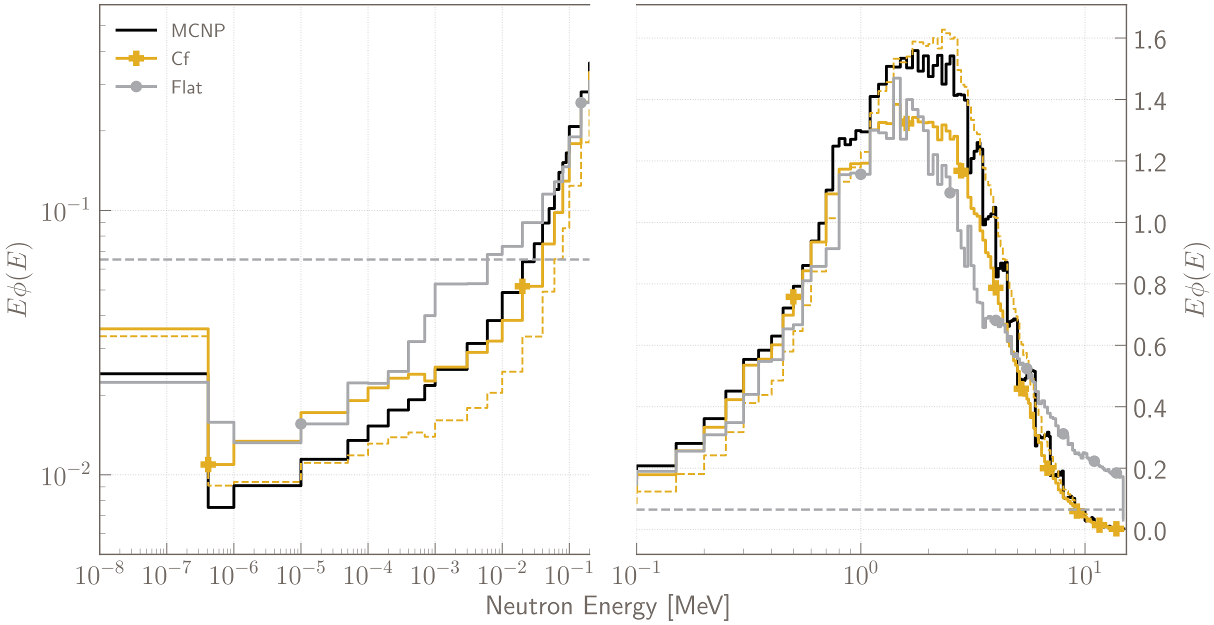

(a) Flat guess (in lethargy space)

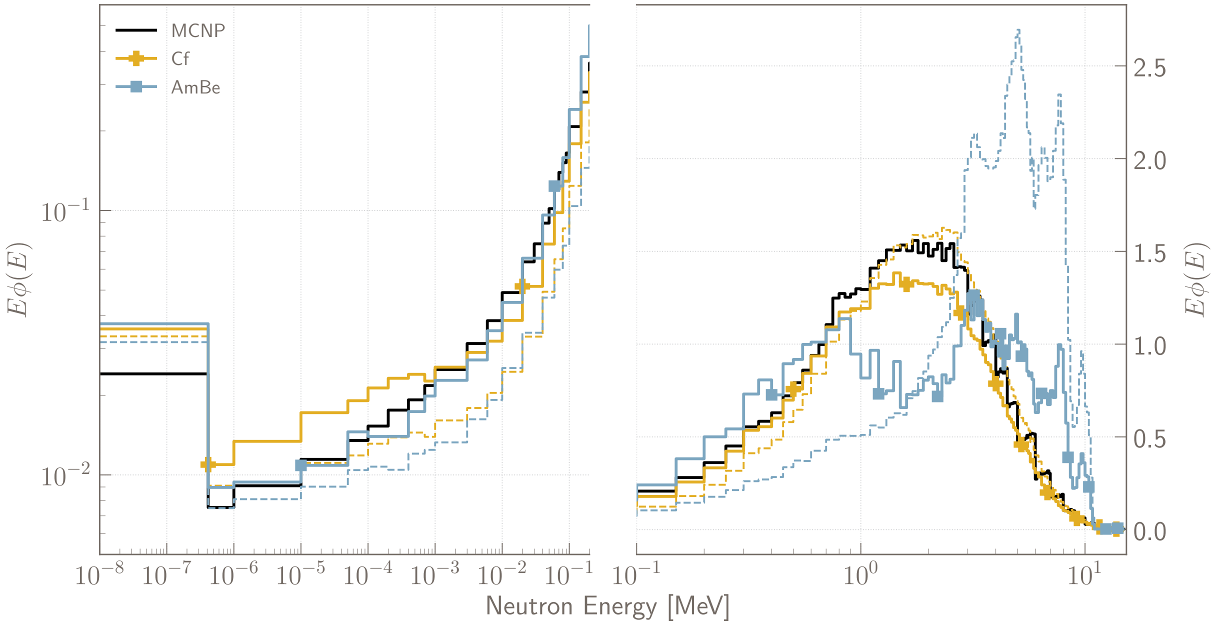

(b) ^{241}AmBe guess

Figure 4.5. Unfolded spectra using Cf measurement data for different guess spectrum template shapes. Guess spectra are depicted by dashed curves.

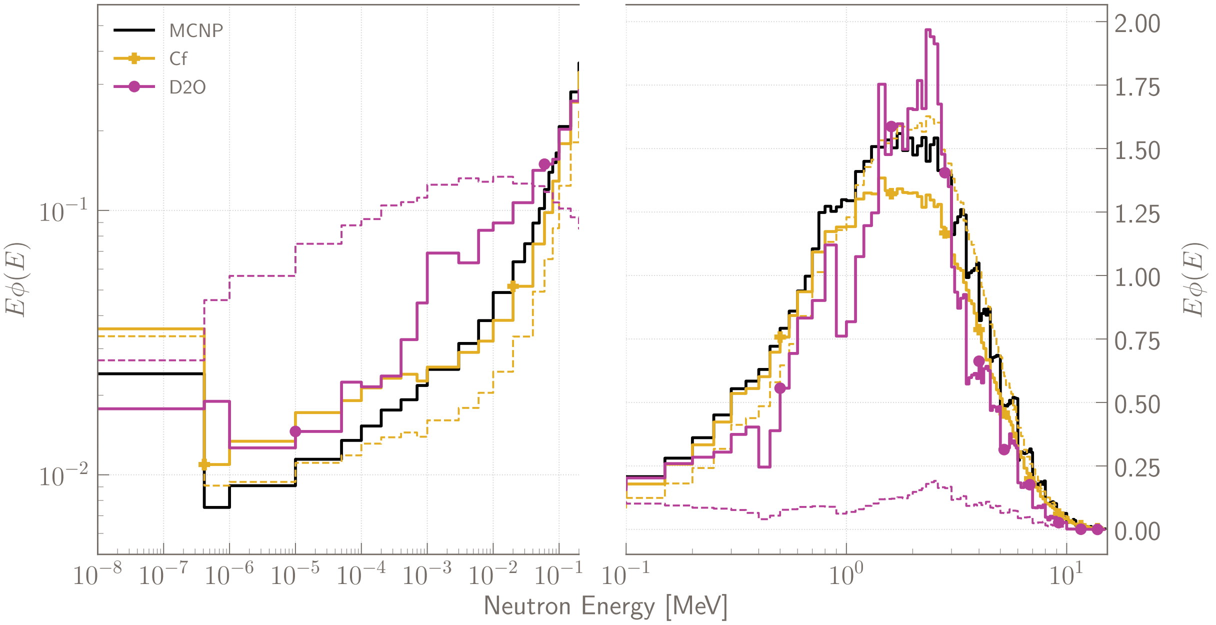

(c) D_2O guess

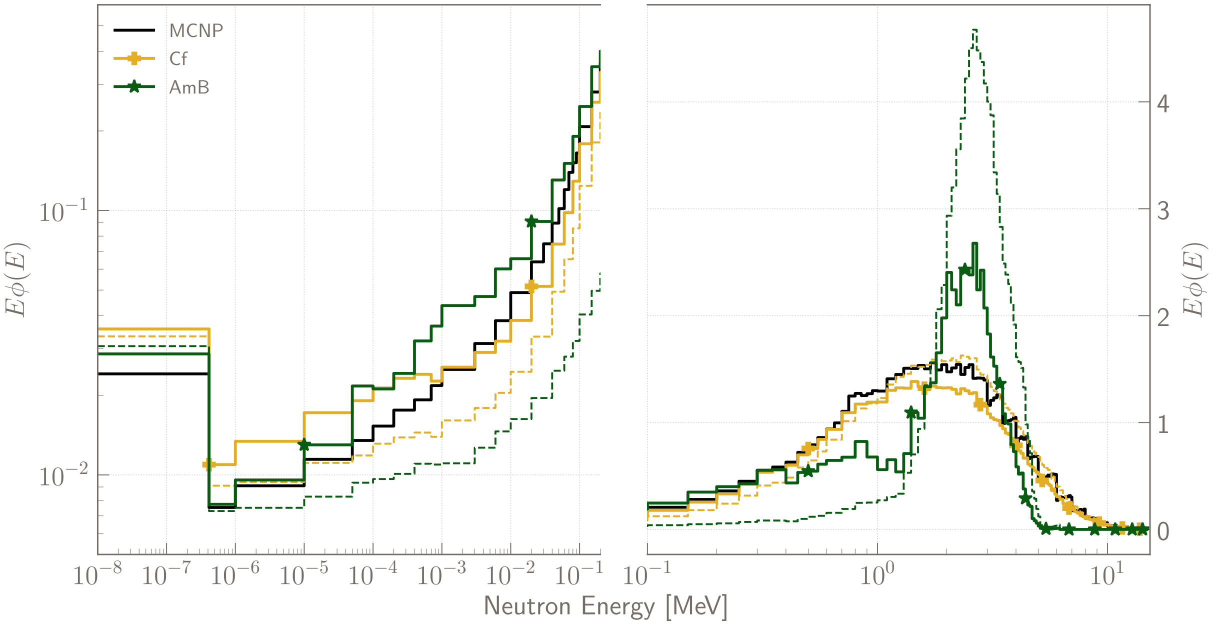

(d) ^{241}AmB guess

Figure 4.5. Unfolded spectra using Cf measurement data for different guess spectrum template shapes. Guess spectra are depicted by dashed curves.

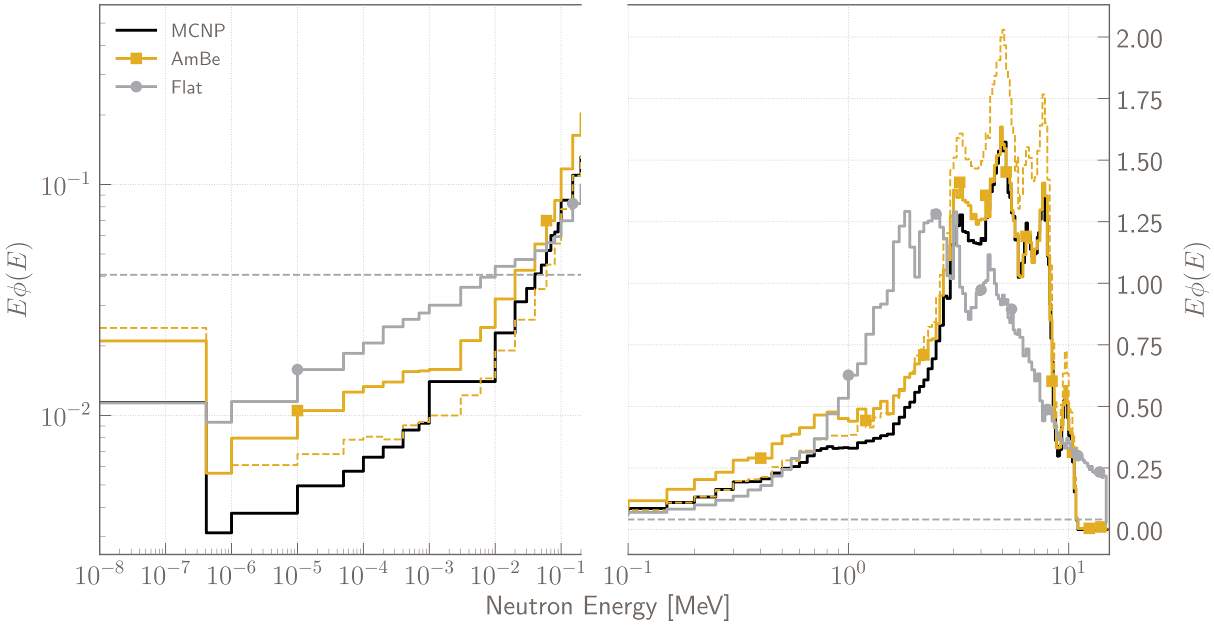

(a) Flat guess (in lethargy space)

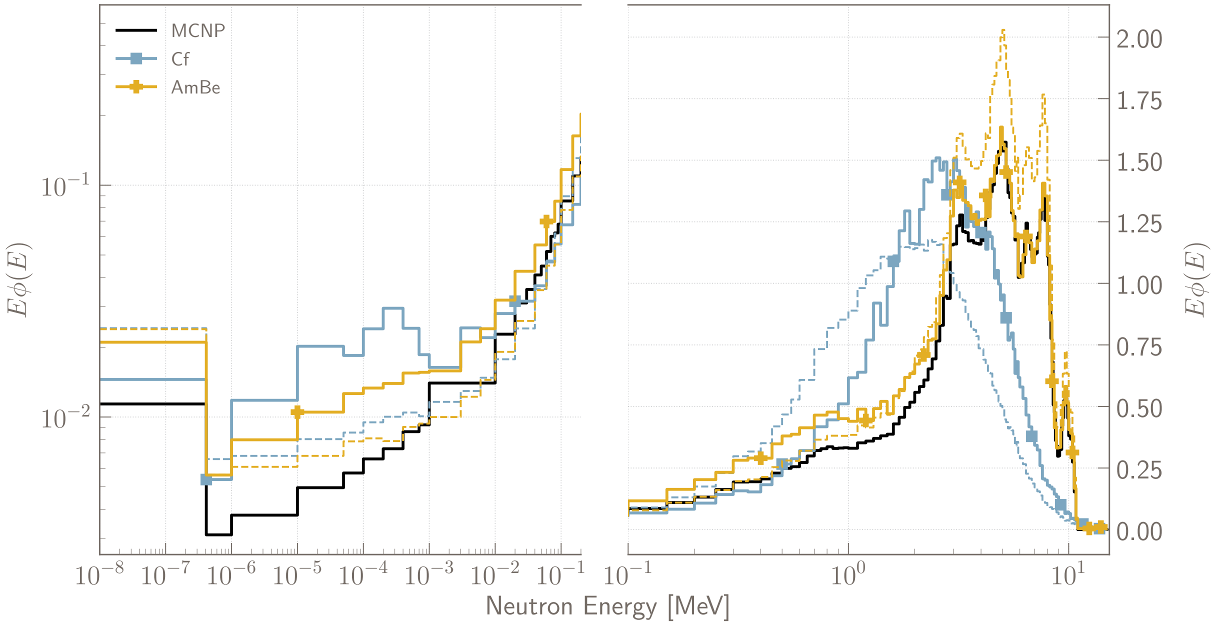

(b) ^{252}Cf guess

Figure 4.6. Unfolded spectra using AmBe measurement data for different guess spectrum template shapes.Guess spectra are depicted by dashed curves.

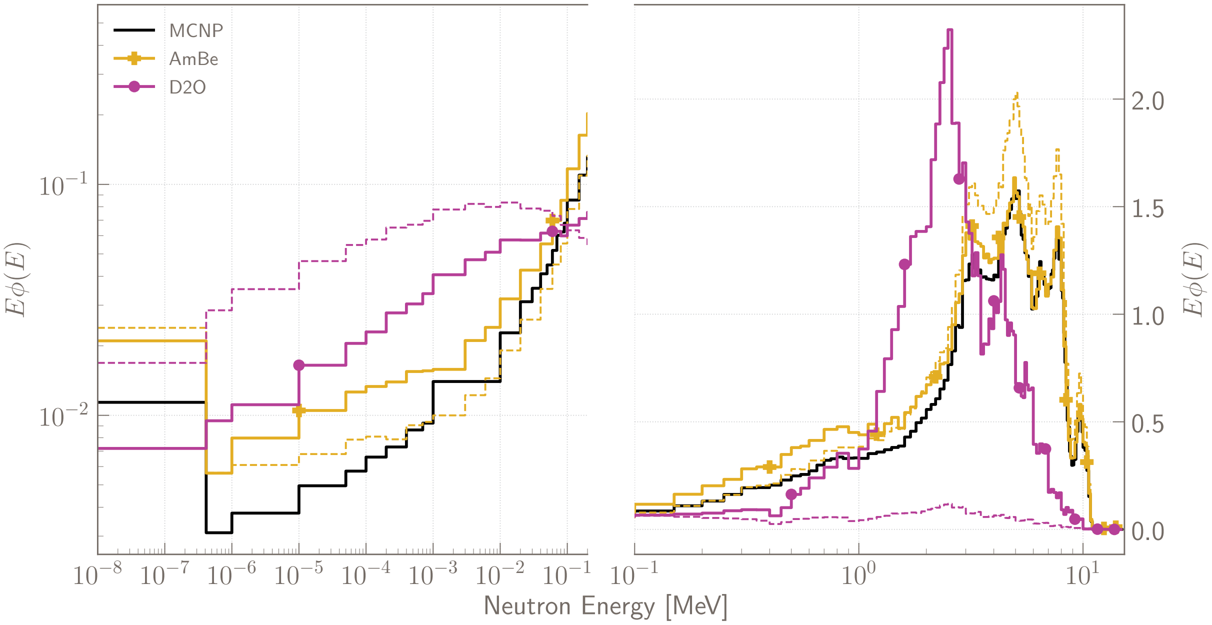

(c) D_2O guess

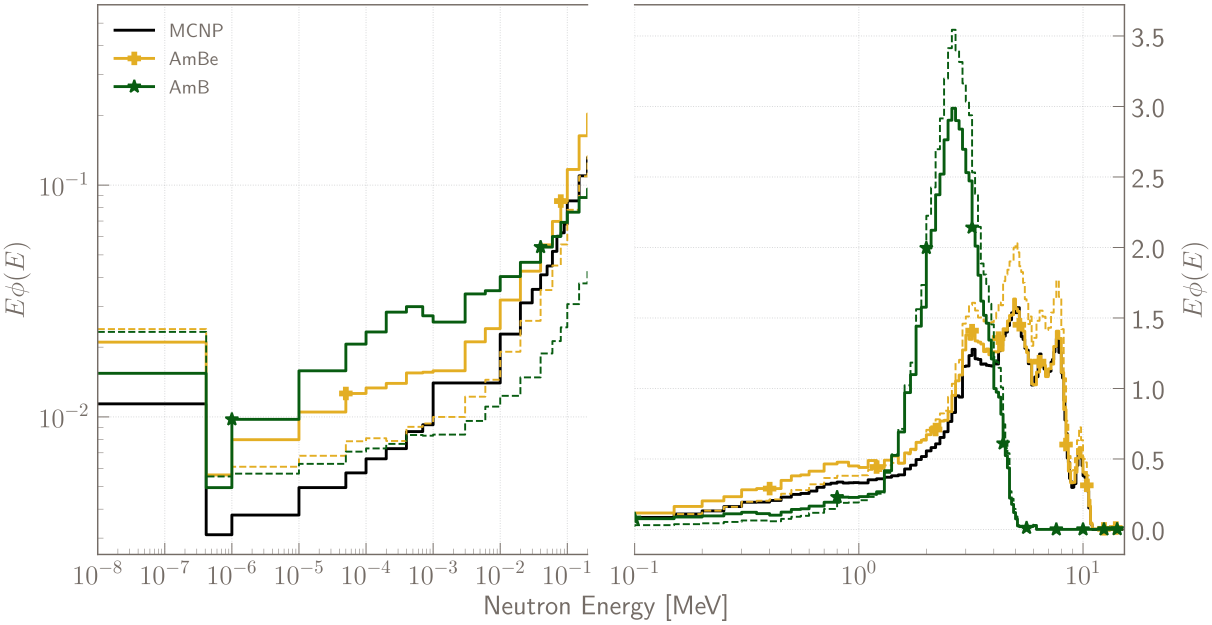

(d) ^{241}AmB guess

Figure 4.6. Unfolded spectra using AmBe measurement data for different guess spectrum template shapes. Guess spectra are depicted by dashed curves.

5. EMPIRICAL MODELING FRAMEWORK FOR PREDICTING CAVITATION EVENTS IN TMFDS

This chapter introduces the main software packages used in this work and gives a brief overview of the software's typical output. Discussions are provided on what information is extracted from each data file, and how that information is fed into various analyses routines.

5.1 Monte Carlo Simulations for Mapping Neutron Interactions to Recoil Nuclide Energies

As introduced in section 2.3, monte carlo software can be used to simulate, and later extract, the spatial collision event locations inside the CTMFD, effectively removing the need to deconvolve the locations of the detection events measured in experimentation. Similar to Grimes [21], the MCNP custom variant known as MCNPX-PoliMi (MCNPP) was adopted for this work. MCNPP is advantageous over traditional MCNP because of its deterministic handling of particle interactions. Whereas traditional MCNP would randomly sample the double differential cross section to determine a neutron's energy after an elastic collision, MCNPP actually implements momentum and energy conservation. This makes MCNPP useful for simulating a detector's actual response on an event-by-event basis, as opposed to on average. The default information made available in a MCNPP output file is shown in table 5.1. More information on MCNPP's capabilities can be found in the software's manual [40].

5.1.1 Processing of Event Positional Information

The x and y event coordinates of each event (column xxx and yyy) were converted into a radial distance r_i from the centerline (x_0, y_0) using $\sqrt{(x-x_0)^2+(y-y_0)^2}$. The axial location is not relevant as their is no pressure gradient in the axial direction. For a given

Table 5.1. Information contained in the MCNP PoliMi output file and corresponding column headers.

Column Name	Description
nps	Starting event id number
npar	Particle identification number
ipt	Particle type (neutron, photon, electron)
ntyn	Collision type (elastic, inelastic, capture, etc.)
ntxs	Target nucleus ZAID identification or material number
ncl	Cell number where reaction occurred
EnReCo	Energy deposited in the collision (MeV)
tme	Time of the interaction (shakes)
xxx	X location of the interaction
yyy	Y location of the interaction
zzz	Z location of the interaction
wgt	Weight of the incident particle
ngen	Generation number (in a fission chain) of incident particle
nsca	Number of scatterings from birth of incident particle
ncode	Reaction number of event indicating (n,n'), (n,2n'), etc.
erg	Doppler broadened energy of incident particle

centerline pressure P_c, and meniscus radius r_0, the local pressure at which the event occurs at is calculated with eq. (5.1).

$$P(r_i) = (P_c(r=0) - P_{amb}) * \frac{(r_0 - r_i)^2}{r_0^2} + P_{amb} \tag{5.1}$$

Since the CTMFD is a sealed system, and a vacuum is pulled on the CTMFD prior to operation, the term for P_{amb} in eq. (5.1) needs to be adjusted. The current operating procedure is to pull the air cavity above the liquid in the CTMFD to $P_{amb} = 27$ inHg. The air cavity will then equilibrate until the partial pressure of the DFP vapor reaches its vapor pressure. The ambient pressure (in Pascals) is then defined as $P_{amb} = 1.01325e5 - P_{vac} + P_{vap}$. The vapor pressure of DFP was taken as $P_{vap} = 26385$ Pa [41].

The local pressure from eq. (5.1) is used to calculate the critical diameter size of a vapor bubble using eq. (2.2). It is important to note that the value for the pressure P_{neg} in eq. (2.2) must be the local pressure $P(r_i)$ of the collision event from eq. (5.1), not the centerline pressure.

5.1.2 Handling Particle Production Reactions in MCNP-PoliMi

The recoil nucleus energy (column EnReCo) and isotope number (column nxs) is used to calculate the energy that the given nucleus would deposit in the critical diameter calculated with eq. (2.2). The details of the energy deposition calculation will be discussed in later sections. The recoil nucleus energy correctly accounts for the neutron-nucleus interaction kinematics. For inelastic scattering interactions, the code also deterministically calculates the valid recoil nucleus, secondary photon, and secondary neutron energy as the excited nucleus decays to its ground state. These considerations are crucial to properly simulate the response of a TMFD with DFP because of the large relative atomic composition of fluorine and the large number of inelastic level states.

These conservation of energy and momentum for elastic and inelastic interactions are implicitly handled by the code and require no special configuration options. In order to correctly handle particle production reactions, the 4th option on the MCNPP RPOL data card needs to be set to 1. Without this option, the MCNPP data file will only contain the ZAID code of the parent nucleus (struck by the neutron) and the total energy deposited by all fragments. When the 4th entry is set to 1, the data file will contain the ZAID and recoil energy of each individual daughter product. The energy deposition inside a critical diameter is then handled for each daughter nucleus separately.

For example, consider the (n, α) reaction on oxygen. If the struck nucleus' ZAID is 8016, the fragments' ZAID numbers are 2004 and 6013; if the struck nucleus is 8000, they are 2004 and 6000. In this case the carbon residual nucleus has surely mass number greater or equal to 13, in contrast to the convention adopted in MCNP's material specification, in which 6000 means carbon natural, i.e. almost all 6012. The cross sections for the reactions accounted for in this analysis can be found in fig. 5.1.

5.2 Description of SRIM Monte Carlo Code for Ion Transport

Simulating the energy deposition of the recoil ions generated by MCNPP was accomplished using the Stopping Range of Ions in Matter (SRIM) monte carlo code. SRIM was chosen over other computational packages due to its rich treatment of the physics of ion

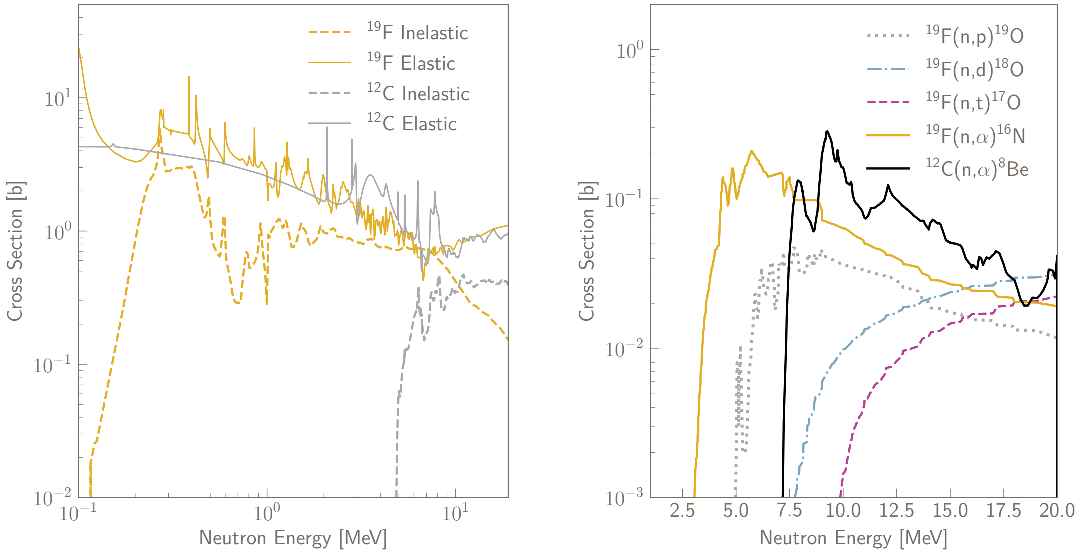

(a) Elastic and inelastic scattering

(b) Charged particle production

Figure 5.1. ^{19}F and ^{12}C cross sections relevant to modeling the response of TMFDs using DFP as a detection fluid

energy deposition, including that of heavy ions. The free software can calculate stopping powers with an average accuracy of about 5% overall, 6% for heavy ions, and better than 2% for high energy light ions and offers an optional library of experimental data supporting the accuracy of its calculations. In addition to stopping power and range calculations, the software, being a monte carlo based package, has the capability to output energy and position information about each ion transported in the simulation. This feature was used heavily throughout the work described in this chapter.

A T(transport)RIM simulation can be run through a graphical user interface, or through batch mode using a TRIM.IN file. An example of the user interface and the corresponding TRIM.IN file is shown in fig. 5.2. Most of the inputs are self explanatory and have been discussed in earlier chapters, namely the properties of the ion and target (DFP).

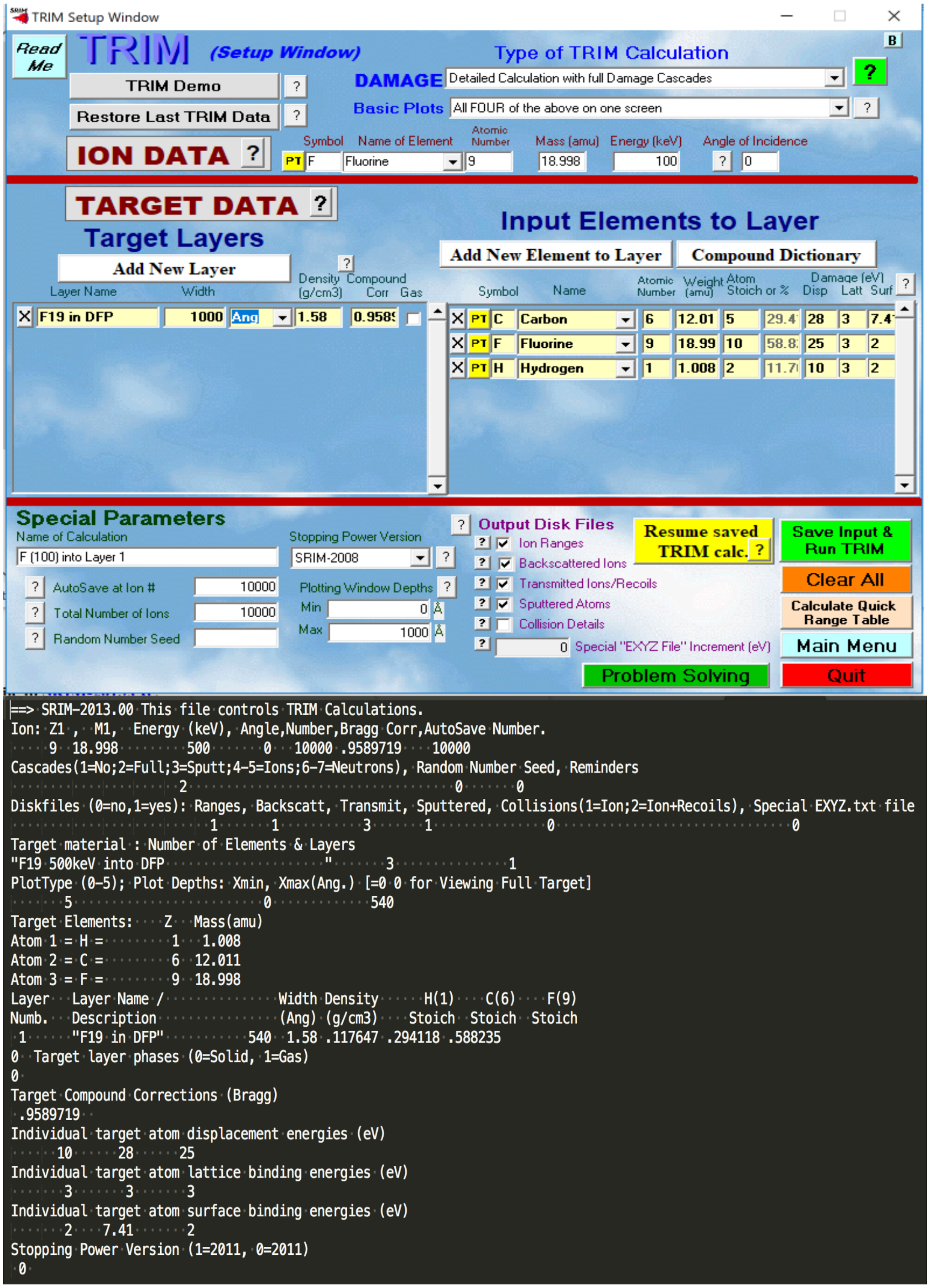

Type of TRIM Calculation
DAMAGE: Detailed Calculation with full Damage Cascades
Basic Plots: All FOUR of the above on one screen

Symbol	Name of Element	Atomic Number	Mass (amu)	Energy (keV)	Angle of Incidence
F	Fluorine	9	18.998	100	0

Layer Name	Width		Density (g/cm3)	Compound Corr	Gas
F19 in DFP	1000	Ang	1.58	0.958	☐

Symbol	Name	Atomic Number	Weight (amu)	Atom Stoich or %		Damage (eV) Disp	Latt	Surf
C	Carbon	6	12.01	5	29.4	28	3	7.4
F	Fluorine	9	18.99	10	58.8	25	3	2
H	Hydrogen	1	1.008	2	11.7	10	3	2

Name of Calculation: F (100) into Layer 1
Stopping Power Version: SRIM-2008
AutoSave at Ion #: 10000
Total Number of Ions: 10000
Random Number Seed:
Plotting Window Depths: Min 0 Å, Max 1000 Å

☑ Ion Ranges
☑ Backscattered Ions
☑ Transmitted Ions/Recoils
☑ Sputtered Atoms
☐ Collision Details
0 Special "EXYZ File" Increment (eV)

```
==> SRIM-2013.00 This file controls TRIM Calculations.
Ion: Z1 ,  M1,  Energy (keV), Angle,Number,Bragg Corr,AutoSave Number.
     9  18.998        500      0  10000 .9589719   10000
Cascades(1=No;2=Full;3=Sputt;4-5=Ions;6-7=Neutrons), Random Number Seed, Reminders
                      2                                   0       0
Diskfiles (0=no,1=yes): Ranges, Backscatt, Transmit, Sputtered, Collisions(1=Ion;2=Ion+Recoils), Special EXYZ.txt file
                          1       1           3      1               0                                0
Target material : Number of Elements & Layers
"F19 500keV into DFP                     "      3              1
PlotType (0-5); Plot Depths: Xmin, Xmax(Ang.) [=0 0 for Viewing Full Target]
       5                         0             540
Target Elements:    Z   Mass(amu)
Atom 1 = H =        1   1.008
Atom 2 = C =        6  12.011
Atom 3 = F =        9  18.998
Layer   Layer Name /               Width Density     H(1)    C(6)    F(9)
Numb.   Description                (Ang) (g/cm3)    Stoich  Stoich  Stoich
 1      "F19 in DFP"           540  1.58 .117647 .294118 .588235
0  Target layer phases (0=Solid, 1=Gas)
0
Target Compound Corrections (Bragg)
 .9589719
Individual target atom displacement energies (eV)
      10      28      25
Individual target atom lattice binding energies (eV)
       3       3       3
Individual target atom surface binding energies (eV)
       2    7.41       2
Stopping Power Version (1=2011, 0=2011)
 0
```

Figure 5.2. User interface for setting up a TRIM calculation manually (top) or in batch mode (bottom)

The type of TRIM calculation should be set to “detailed calculation with full damage cascade”. This enables tracking of secondary recoil ions generated by the primary ion (originating from the neutron interaction). The secondary ions can then subsequently generate ternary recoils. Up to this point, all discussion related to energy deposition inside a critically-sized vapor cavity has been in relation to the primary ion. The importance of secondary recoils will be discussed in later sections.

The “compound correction” field next to the density parameter in fig. 5.2 is related to the difference in stopping power in elemental materials and compounds composed of the same element. Stopping in compounds is reasonably well compensated for by using Bragg’s rule, which states that the stopping power in a compound can be estimated as a linear combination of the stopping power of individual elements. The accuracy of Bragg’s rule is limited because the energy loss to the electrons in any material depends on the detailed orbital and excitation structure of the matter, and any differences between elemental materials and the same atoms in compounds will cause Bragg’s rule to become inaccurate.

SRIM applies a correction factor to the Bragg rule based on a more recent theory known as the Core and Bond (CAB) approach which states that stopping powers in compounds can be predicted using the superposition of stopping by atomic “cores”, which are relatively independent of the ion velocity, and then adding the stopping due to the bonding electron. Because of the nature of how electrons are shared in covalent bonds, the CAB approach applies adjustments based on the type of atomic bound e.g. single, double, carbon-carbon, carbon-oxygen, etc. By inspecting the chemical structure of DFP, shown in fig. 5.3, it can be seen that there are 4 C-C single bonds, 10 C-F single bonds, and 2 C-H single bonds. The final correction factor calculated by SRIM is 0.959. While a 4% difference is relatively insignificant, this correction should be kept under consideration in future endeavors exploring other candidate detection fluids outside of DFP.

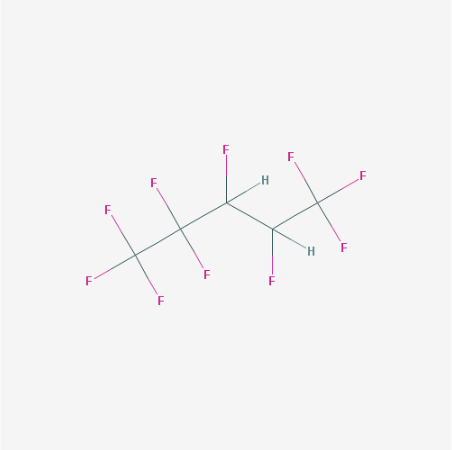

Figure 5.3. Schematic of the chemical structure of a DFP molecule, used for calculating the correct stopping power in a compound versus an elemental material

5.3 Continuous Slowing Down Approximation Approach for Modeling Recoil Nuclide Energy Deposition

Charged particle energy losses are often calculated using an approximation known as the Continuous Slowing Down Approximation (CSDA). When a charged particle interacts with matter it loses energy as a result of interactions in which a small amount of energy is lost to neighboring electrons and nuclei. The loss to each neighboring particle is small enough relative to the primary ion's energy that the process can be approximated as continuous the rate of energy loss at every point along the track and is assumed to be equal to the total stopping power. Thus, the range of a particle and the medium's stopping power are closely related, and can be defined as shown in eq. (5.2).

$$R(E) = \int_0^{E_0} \frac{dE}{S_{tot}(E)}\, dE \tag{5.2}$$

The stopping power in DFP for the relevant recoil ions seen in the MCNPP simulations are shown in figure fig. 5.4. Because range and stopping power are interrelated by eq. (5.2), the energy deposited over a discrete distance, e.g. a critical diameter length, can be cleverly calculated through interpolation of a range table, as is common practice.

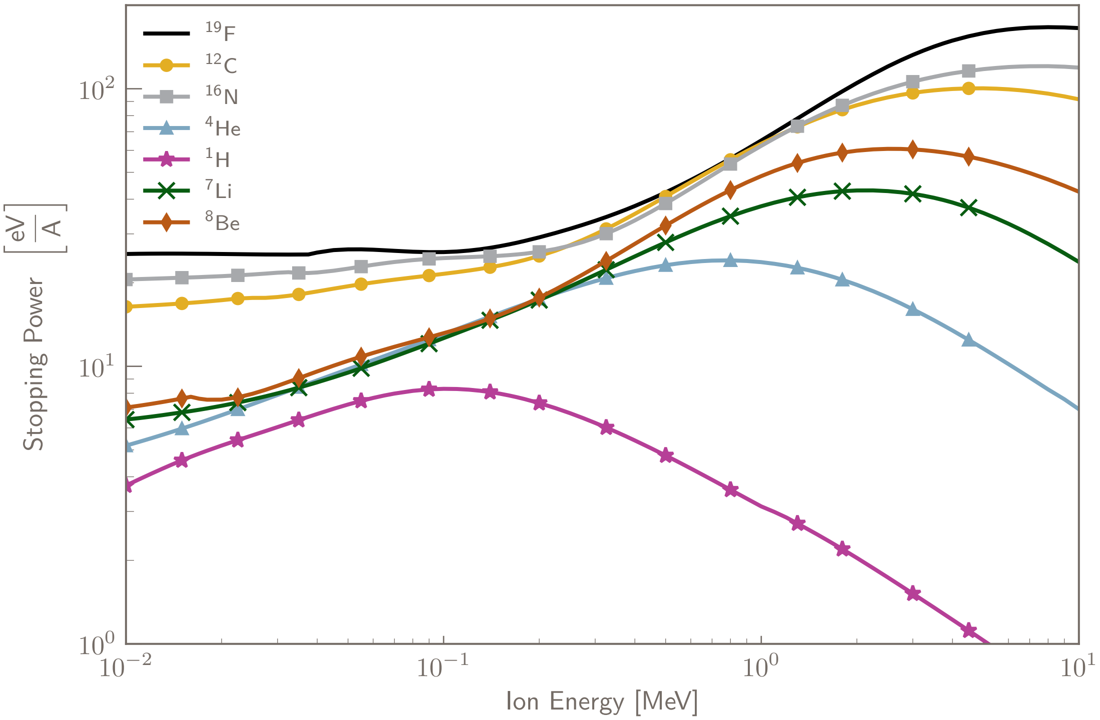

Figure 5.4. Stopping power of the various ions relevant to the neutron interactions encountered in DFP.

However, in this work we have opted to perform the energy deposition calculations through a numerical integration of the stopping power. The critical diameter is divided into 100 equidistant segments and the energy deposited inside each segment is simply the stopping power multiplied by the segment length as shown in eq. (5.3). After each segment the ion's energy is updated and the stopping power for the next segment is re-interpolated.

$$dE_{tot} = \sum_{i=1}^{n=100} \left(\frac{dE}{dx}(E)\right)_i dx \tag{5.3}$$

The reasoning behind the more laborious approach is the regime change observed around 100 keV as the dominant contributor to the stopping power alternates from electronic stopping to nuclear stopping. Ion energies on the order of 100 keV are frequently seen from neutron interactions. The range of these ions is also on the same order of magnitude as the critical diameter length.

Using the continuous slowing down approximation as the method of calculation for energy deposition has a few important implications for predicting the response of TMFDs. Mainly, the implications are a result of the deterministic nature of the CSDA which neglects statistical fluctuations in energy losses, such as are typical in stopping power regimes governed by nuclear stopping. With the CSDA, determination of whether a given recoil ion will induce a detection event is a binary conditional. The ion either deposits an amount of energy greater than the DETC value, resulting in a detection event, or the vapor cavity collapses back into the bulk fluid.

It was hypothesized that this binary-type approach for predicting the detector's response could be problematic, as the average value of a statistical distribution is not necessarily indicative of the mode of that distribution. It is well known that the Bethe-Bloch formula describes the average energy loss of charged particles when traveling through matter. Fluctuations of energy loss by ionization of a charged particle in a thin layer of matter are, however, described by a Landau (or Laundau-Vavilov) distribution [42], [43]. The Landau probability density function (distribution) resembles a Gaussian distribution with a long upper tail; the tail being a consequence of infrequent collisions that have a small probability of transferring large amounts of energy. These rare collision events shift the mean energy loss into the tail of the distribution. The mean of the energy loss ($\frac{dE}{dx}$) given by the Bethe equation is not representative of energy losses by individual particles [44], which is exactly what is being attempted with the MCNPP output data. The most probable energy loss, corresponding to the maximum value of the Landau distribution function, is better suited for the task at hand.

5.4 Stochastic Distribution Fitting of Ion Energy Deposition for Probabilistic Estimation of Cavitation Likelihood

The effects of energy straggling can be accounted for using the "Transmitted Ions/Recoils" option seen in the "Output Disk Files" section in figure fig. 5.2. The functionality outputs select statistics about any ion that exits the layer width window. The output file contains a unique nps number for the given history, the ZAID of the ion, the energy, the (x,y,z) coordinate, and the directional cosign velocity vector at its point of exit from the layer window. This functionality is commonly employed for analysis of radiation therapy proton beams to calculate various parameters like energy-distribution, position-distribution (beam-profile), angular-distribution, momentum-distribution, etc. Based on the results of this statistical analysis, further manipulation with the particle set is possible, such as filtering particles exceeding a certain threshold of a given parameter.

An example depicting the ion energy straggling is shown in fig. 5.5. The primary ions are shown in red in the left figure and the secondary recoil chains are shown in the right figure. The different colors represent the different recoil nuclei. An example probability density distribution of the exiting ion energies is shown in fig. 5.6. Subtracting the energy of each bin in the distribution from the ion's initial energy yields the energy deposited by that ion.

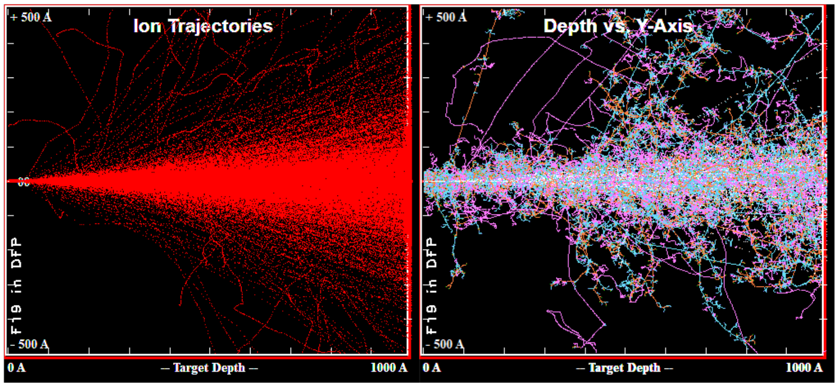

Figure 5.5. Trajectories of primary ions (left) and secondary recoils (right) in a 1000 A layer of DFP.

Ultimately, the aim of the distribution analysis is to yield an estimate for the probability that an ion of a given energy deposits an amount of energy greater than or equal to the DETC inside the layer width, which necessarily must be fixed to the 1-dimensional length of a critically sized vapor cavity. In statistics, the integral of a probability density distribution is known as a cumulative distribution function (CDF). Physically, the value of the CDF at a specific point x can be thought of as the probability that x will take a value less than or equal to y. Taking the compliment of the CDF yields the complementary cumulative distribution function (CCDF), also known as the survival or reliability function. The survival function

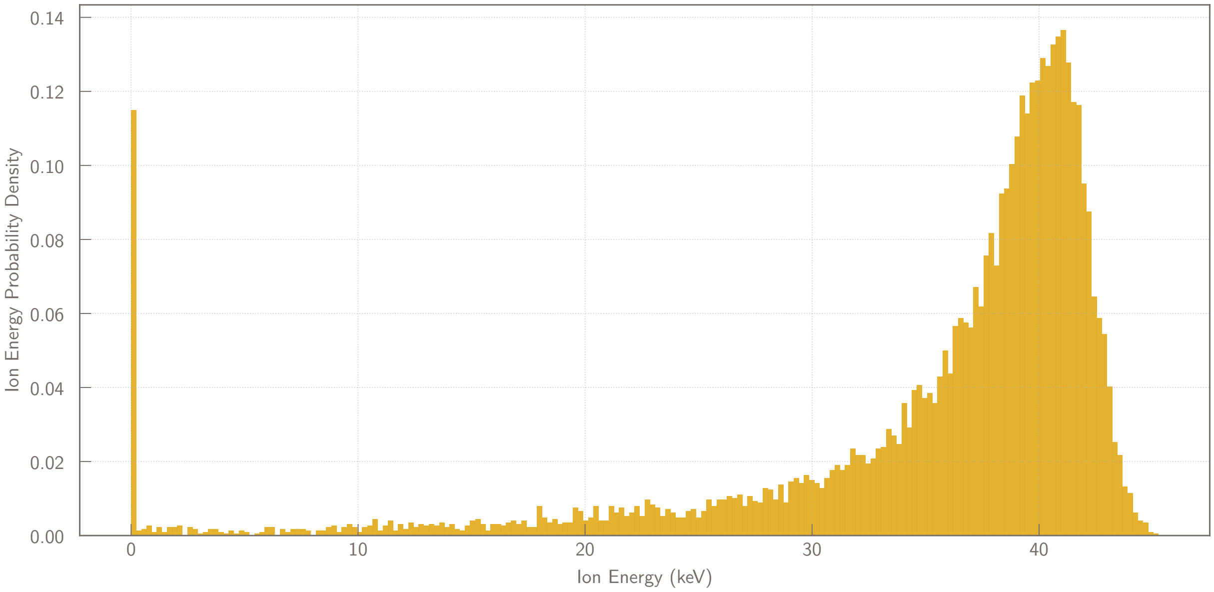

Figure 5.6. Probability density distribution of the primary ^{19}F ion's energies as they exit the layer window. The incident ion energy is 50 keV and the layer width is 540 angstroms (approximately 10 bar in DFP).

represents the probability that the random variable will "survive" (the value of the function is greater than zero) beyond a specified time. In the scope of modeling a TMFD's response, the idea of "surviving" takes the context of depositing a specified amount of energy before exiting the layer window.

The resultant CCDF from the ion exit energy probability density distribution of fig. 5.6 is shown in fig. 5.10. The gold curve (left axis) can be seen to closely follow the shape of the probability density histogram (right axis). The large peak seen at 50 keV corresponds to ions that deposited all their energy inside of the layer. The CCDF probability of detection function is compared against the binary detection probability in fig. 5.8. In this instance, the DETC has been hypothetically set at the same value as the energy a 50 keV ^{19}F ion can deposit over a length of 540 angstroms using the CSDA. Whereas the CSDA method predicts 100% of 50 keV ions would generate a detection event, the stochastic CCDF predicts approximately only 25% the ions will deposit enough energy to generate a detection.

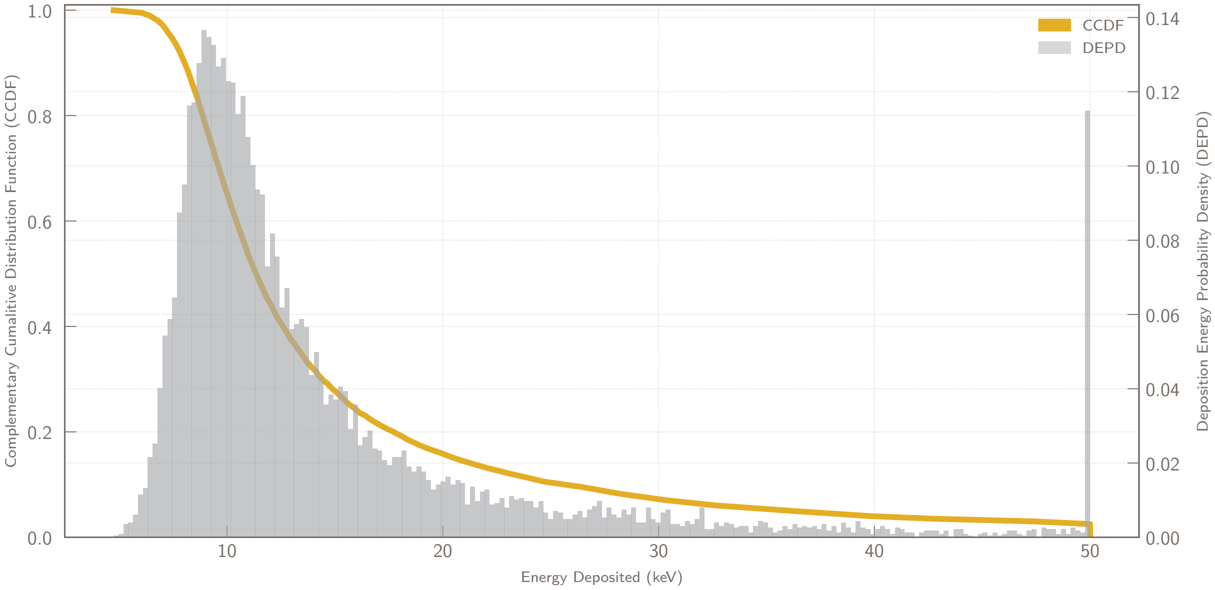

Figure 5.7. Resultant complimentary cumulative distribution function, representing the probability that an ion will generate a detection event, constructed from the information given in the TRANSMIT.TXT file for the case of 50 keV ^{19}F ions incident in a layer of DFP 540 angstroms wide.

5.5 Effect of Secondary Recoils on the Probability of Detection

In most basic treatments of classic dosimetric cavity theory, the amount of dose a thin cavity receives from a fluence field is a function of the amount of charge generated by ionization inside that cavity. More complex treatments address the issue of additional charge generation inside of the thin cavity by secondary charged particles and δ-rays. The additional charge generation misrepresents the true "ionization power" of the external fluence field. Though the Bragg-Gray, Spencer-Attix, and Burlin theory treatments are not directly applicable to the scenario of recoil ions depositing their energy in a critical diameter, useful corollaries can still be drawn from principles behind the theories. Namely, the concept of energy deposition by secondary particles.

The ion exit energies shown in fig. 5.6 merely represent the amount of energy the primary ion gave up inside a critical diameter, not the amount of energy that was absorbed

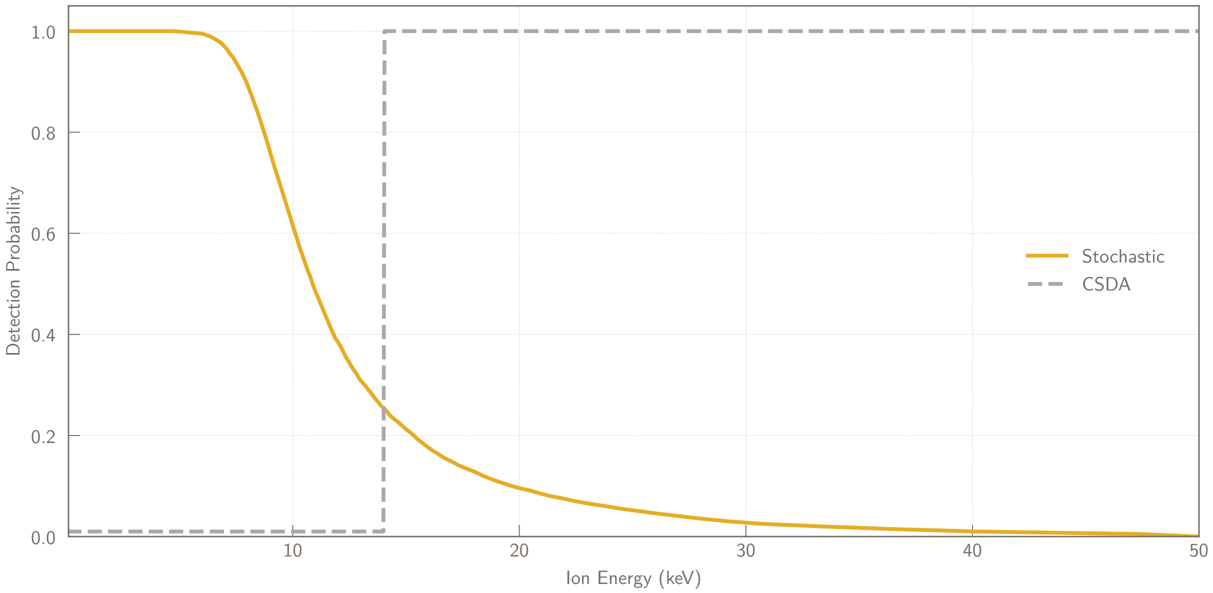

Figure 5.8. Comparison between the binary CSDA and the stochastic energy straggling detection probability functions

in the critical diameter. In order for the primary ion to generate a detection event, the metastable fluid itself must absorb the energy to subsequently undergo phase change. Thus, any secondary recoil ions generated must also give up their energy in the critical diameter; or rather, additional treatment is necessary to correct for the secondary recoils which leave the critical diameter with some nonzero energy.

The numerous secondary recoil tracks exiting the geometry window in the right-most image of fig. 5.5 illustrate that additional treatment is necessary. Information about the energy of secondary recoils as they exit the geometry is contained in the TRANSREC.txt output file. The “Ion Numb” column in the output file identifies the source particle history number which generated the recoil cascade. For each source history the total energy of all secondary recoils exiting the window is subtracted from the energy lost by the source ion, yielding the net energy lost inside the geometry. For example, in fig. 5.9, the source ion (history number 6) exits the geometry with 23.44 keV of energy and thus gives up 26.56 keV of its initial 50 keV of energy. Six ions of the resulting recoil cascade leave the geometry with a total of 3.2 keV. The net energy deposited is therefore 23.36 keV.

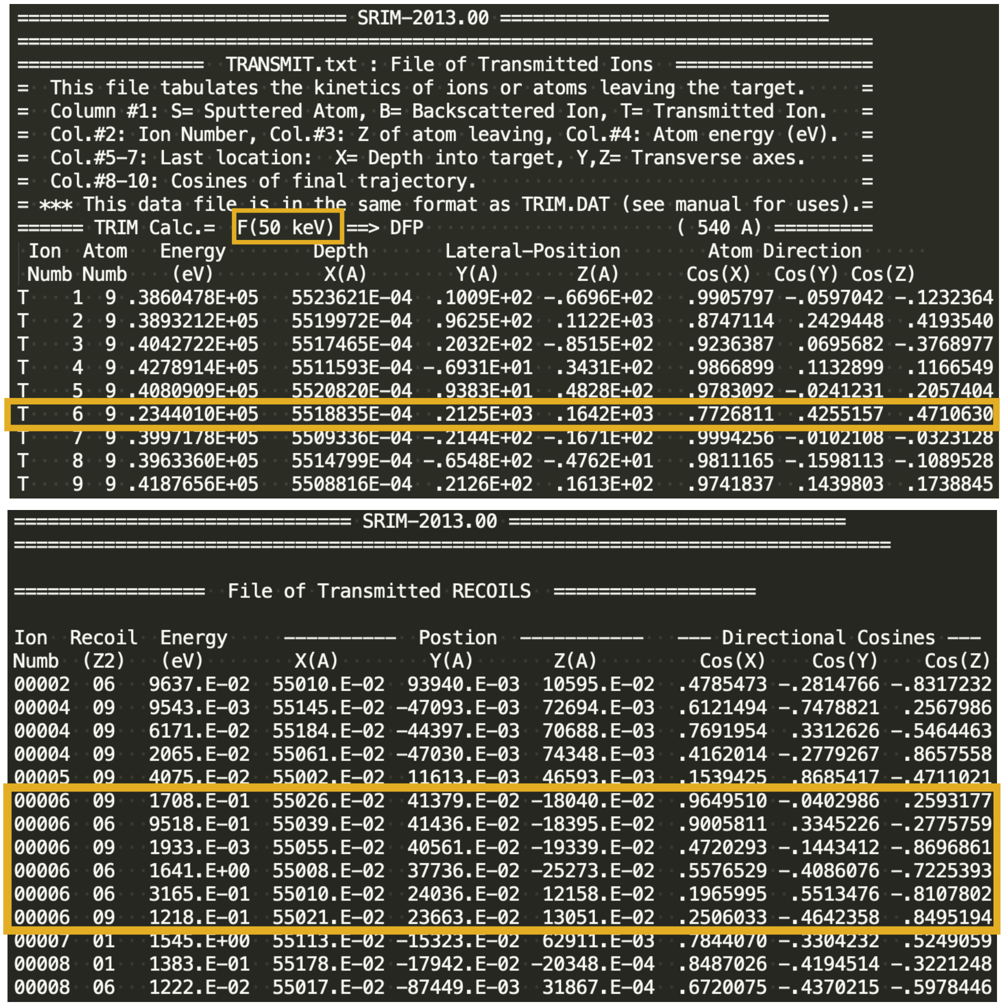

```
============================== SRIM-2013.00 ==============================
==========================================================================
=================  TRANSMIT.txt : File of Transmitted Ions  ==================
=  This file tabulates the kinetics of ions or atoms leaving the target.     =
=  Column #1: S= Sputtered Atom, B= Backscattered Ion, T= Transmitted Ion.   =
=  Col.#2: Ion Number, Col.#3: Z of atom leaving, Col.#4: Atom energy (eV).  =
=  Col.#5-7: Last location:  X= Depth into target, Y,Z= Transverse axes.     =
=  Col.#8-10: Cosines of final trajectory.                                   =
= *** This data file is in the same format as TRIM.DAT (see manual for uses).=
====== TRIM Calc.=  F(50 keV) ==> DFP                     ( 540 A) =========
 Ion  Atom   Energy        Depth       Lateral-Position        Atom Direction
 Numb Numb    (eV)          X(A)         Y(A)       Z(A)      Cos(X)  Cos(Y) Cos(Z)
T    1  9 .3860478E+05   5523621E-04  .1009E+02 -.6696E+02   .9905797 -.0597042 -.1232364
T    2  9 .3893212E+05   5519972E-04  .9625E+02  .1122E+03   .8747114  .2429448  .4193540
T    3  9 .4042722E+05   5517465E-04  .2032E+02 -.8515E+02   .9236387  .0695682 -.3768977
T    4  9 .4278914E+05   5511593E-04 -.6931E+01  .3431E+02   .9866899  .1132899  .1166549
T    5  9 .4080909E+05   5520820E-04  .9383E+01  .4828E+02   .9783092 -.0241231  .2057404
T    6  9 .2344010E+05   5518835E-04  .2125E+03  .1642E+03   .7726811  .4255157  .4710630
T    7  9 .3997178E+05   5509336E-04 -.2144E+02 -.1671E+02   .9994256 -.0102108 -.0323128
T    8  9 .3963360E+05   5514799E-04 -.6548E+02 -.4762E+01   .9811165 -.1598113 -.1089528
T    9  9 .4187656E+05   5508816E-04  .2126E+02  .1613E+02   .9741837  .1439803  .1738845
```

```
============================== SRIM-2013.00 ==============================
==========================================================================


=================  File of Transmitted RECOILS  ==================

Ion  Recoil  Energy     ----------  Postion  -----------   --- Directional Cosines ---
Numb  (Z2)    (eV)        X(A)        Y(A)       Z(A)        Cos(X)     Cos(Y)    Cos(Z)
00002  06   9637.E-02  55010.E-02  93940.E-03  10595.E-02  .4785473 -.2814766 -.8317232
00004  09   9543.E-03  55145.E-02 -47093.E-03  72694.E-03  .6121494 -.7478821  .2567986
00004  09   6171.E-02  55184.E-02 -44397.E-03  70688.E-03  .7691954  .3312626 -.5464463
00004  09   2065.E-02  55061.E-02 -47030.E-03  74348.E-03  .4162014 -.2779267  .8657558
00005  09   4075.E-02  55002.E-02  11613.E-03  46593.E-03  .1539425  .8685417 -.4711021
00006  09   1708.E-01  55026.E-02  41379.E-02 -18040.E-02  .9649510 -.0402986  .2593177
00006  06   9518.E-01  55039.E-02  41436.E-02 -18395.E-02  .9005811  .3345226 -.2775759
00006  09   1933.E-03  55055.E-02  40561.E-02 -19339.E-02  .4720293 -.1443412 -.8696861
00006  06   1641.E+00  55008.E-02  37736.E-02 -25273.E-02  .5576529 -.4086076 -.7225393
00006  06   3165.E-01  55010.E-02  24036.E-02  12158.E-02  .1965995  .5513476 -.8107802
00006  09   1218.E-01  55021.E-02  23663.E-02  13051.E-02  .2506033 -.4642358  .8495194
00007  01   1545.E+00  55113.E-02 -15323.E-02  62911.E-03  .7844070 -.3304232  .5249059
00008  01   1383.E-01  55178.E-02 -17942.E-02 -20348.E-04  .8487026 -.4194514 -.3221248
00008  06   1222.E-02  55017.E-02 -87449.E-03  31867.E-04  .6720075 -.4370215 -.5978446
```

Figure 5.9. TRANSMIT.TXT and TRANSREC.TXT output files shown as reference for how net energy deposition is calculated

The amount of energy given to a secondary recoil affects the likelihood that it can escape the geometry window with some nonzero energy. The larger the energy transfered in the collision, the greater the likelihood of escape. Thus, secondary recoils affect the net energy deposition the most when the source ion energy is low and the stopping regime is dominated by collisional(nuclear) versus electronic stopping. The magnitude of this effect is illustrated in fig. 5.10. The dashed lines represent the survival function when net energy deposition is accounted for while the solid lines consider only the difference of the primary ions initial and exit energy. At 500 keV the collisional stopping power of ^{19}F ions in DFP constitutes only 7% of the total stopping power, compared to 47% at 50 keV. Examining the two survival functions for the 50 keV case, it can be seen that the dashed line begins to diverge from its solid counterpart as a consequence of the higher frequency of large energy transfer collision events.

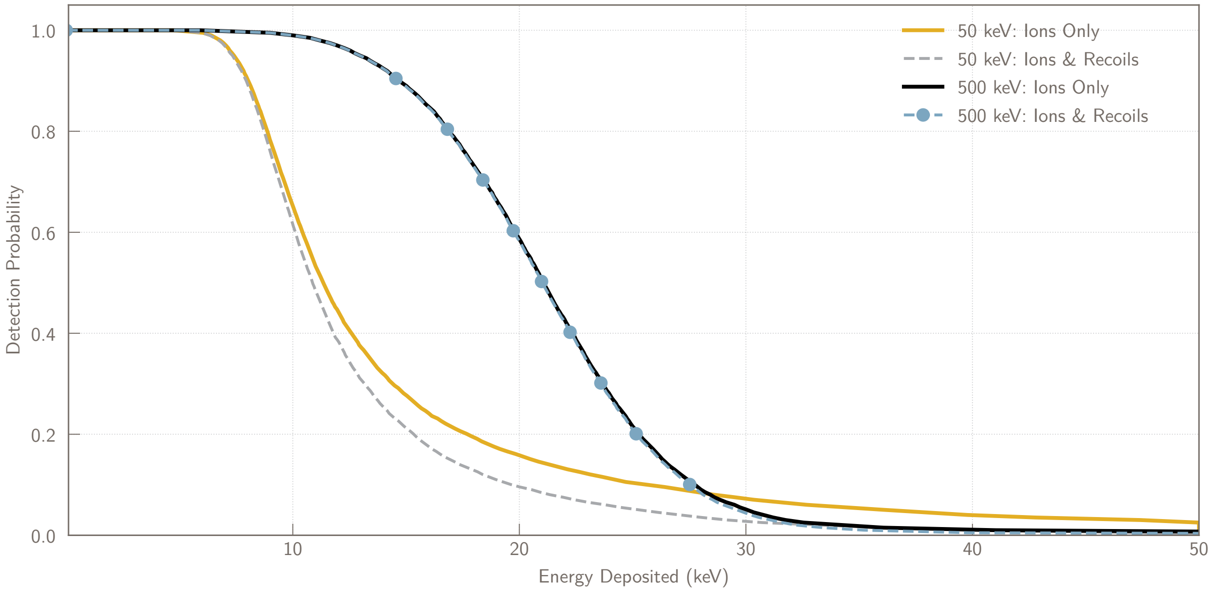

Figure 5.10. Examples of the survival function for 50 keV and 500 keV ^{19}F ions in a 540 angstrom layer of DFP illustrating the effect of tracking energy deposition of secondary recoil ions on the shape of the cumulative distribution function.

5.6 Procedure for Evaluating Detection Probabilities from MCNPP Output Files

In order to apply the probabilistic approach to detection probability to each event in a MCNPP output file, a procedure needed to be developed to construct a CDF for any arbitrary combination of ion ZAID, recoil energy, and critical diameter size. A monte carlo simulation based approach using SRIM was selected over development of an analytical solution using the Landau distribution function. The Landau distribution is known to exhibit inaccuracies for small thicknesses [44]. Furthermore, without proper equipment, the only way to evaluate the accuracy of such a custom model would be to use simulation packages.

The difficulty in using SRIM to solve the problem at hand is that the simulation data is discretized in the energy and width parameter spaces. Running a specific simulation for every event in a MCNPP output file is impractical as some of the files analyzed are composed of hundreds of thousands of events. Rather, a three dimensional parametric matrix of combinations (i.e. ZAID, recoil energy, and geometry width) was developed to serve as a database. The CCDF of any specific combination of nuclei, energy, and width encountered in a MCNPP output file could then be inferred by interpolating between the results in the SRIM simulation database. Interpolation is done using a Lagrange polynomial of the first order.

Currently, the database contains simulation results for the following nuclei: ^{19}F, ^{12}C, ^{16}N, ^{4}He, and ^{1}H. Though (n,p), (n,d), and (n,t) reactions produce different isotopes of oxygen, it has not yet been included in the database. It was decided that the validity of the probabilistic approach to detection probability would be evaluated before additional computational resources were devoted to special cases. Furthermore, the total percentage of nuclei resulting from any of the production reactions shown in section 5.1.2 was found to rarely exceed 5%. The majority of that 5% are (n,α) reactions, which are accounted for with the ^{16}N and ^{4}He simulation results.

In regards to the energy and geometry width parameter spaces, the database contains results for widths ranging from 400 A (13.66 bar) to 3000 A (1.6 bar). Future work should extend this range down below 1.0 bar. However, because of the inverse relationship between pressure and critical diameter size, this would have almost doubled the computational time requirement. As such, it was again decided that the validity of this model should be evaluated before investing the additional resources. The range of ion energies in the database is isotope dependent. For ^{19}F, ^{12}C, and ^{1}H the upper bound is set by the maximum energy a 15.3 MeV neutron (the maximum energy in the response matrix) can deposit on the particular nuclei from an elastic scatter. For ^{16}N and ^{4}He the bounds are set using momentum and energy conservation kinematics of the (n, α) reaction. In total, these bounds equate to thousands of individual SRIM simulations for each isotope.

An example of how the database of SRIM results is used to infer the CCDF of an arbitrary case is shown in fig. 5.11. To gage the accuracy of the interpolation procedure, the arbitrary case shown here was chosen to be the same as a case that already exists in the database: ^{19}F ions with energy $\mathrm{E_f}$=55 keV and a geometry width $\mathrm{W_f}$=550 A. From inspection of fig. 5.11c, the interpolation procedure described below yields very good agreement to the simulation results:

1. Parse the database to find the two energies, $\mathrm{E_1}$ and $\mathrm{E_2}$, that bound the ion energy of interest, $\mathrm{E_f}$. For each energy, find the two width cases, $\mathrm{W_1}$ and $\mathrm{W_2}$, that bound the width of interest, $\mathrm{W_f}$. This should yield results from four simulation cases.
2. Using equation eq. (5.4), interpolate the two widths, $\mathrm{W_1}$ and $\mathrm{W_2}$, to the final width $\mathrm{W_f}$ for the left bound energy case, $\mathrm{E_1}$. The interpolated CCDF is shown in fig. 5.11a.
3. Using equation eq. (5.5), interpolate the two widths, $\mathrm{W_1}$ and $\mathrm{W_2}$, to the final width $\mathrm{W_f}$ for the right bound energy case, $\mathrm{E_2}$. The interpolated CCDF is shown in fig. 5.11b.
4. Using equation eq. (5.6) and the resulting interpolated CCDFs from the prior two steps, ($\mathrm{E_1}$, $\mathrm{W_f}$) and ($\mathrm{E_2}$, $\mathrm{W_f}$), interpolate to final energy, $\mathrm{E_f}$. The interpolated CCDF is shown in fig. 5.11c.

$$P(E_1, W_f) = \left(\frac{P(E_1, W_2) - P(E_1, W_1)}{W_2 - W_1}\right)(W_f - W_1) + P(E_1, W_1) \tag{5.4}$$

$$P(E_2, W_f) = \left(\frac{P(E_2, W_2) - P(E_2, W_1)}{W_2 - W_1}\right)(W_f - W_1) + P(E_2, W_1) \tag{5.5}$$

$$P(E_f, W_f) = \left(\frac{P(E_2, W_f) - P(E_1, W_f)}{E_2 - E_1}\right)(E_f - E_1) + P(E_1, W_f) \tag{5.6}$$

5.7 Methodological Comparisons between the Probabilistic Detection Model and Superheated Droplet Detector Literature

To the best of knowledge, the approach of simulating the probability density distribution of energy deposition as a function of recoil ion energy (for purposes of metastable fluid detector, e.g. superheated droplet, response matrix development) is unique to this work. The uniqueness, however, does not imply that the approach is without merit. The simulated probability density distribution shown in fig. 5.10 strongly resembles the Laundau-Vavilov theoretical distribution [42]–[44].

The main reason the methodology outlined here for TMFDs differs from SDDs is that Seitz's thermal spike theory is not extensible to tensioned metastable states; therefore, the energy deposition necessary to create a stable vapor cavity remains an independent variable. The probabilistic detection model was designed with this fact in mind. In the example CCDF shown in fig. 5.10, the horizontal axis (independent variable) is the amount of energy an ion deposits and the dependent variable represents the fraction of ions that deposit the specified energy. In essence, the current model slightly rephrases the question without actually changing the meaning of the independent variable. The original question of "what fraction of ions will deposit at least "x" keV of energy?" becomes "if the energy threshold is set to "x" keV, what is the probability that an ion deposits an amount of energy greater than the threshold?".

In contrast, SDDs use the energy deposition threshold from Sietz's thermal spike theory as an absolute point of reference to build their theoretical framework around. The first distinct difference is that the length scale L_c over which an ion can deposit its energy is not explicitly defined as the diameter of a critical sized vapor cavity like in eq. (2.2). The critical length scale is actually scaled by an empirically determined constant b as shown in eq. (5.7). The semi-empirical assumptions underlying this factor originated from analysis that found that the track length with which the highest LET ion deposited the required amount of energy had to be greater than the length predicted by eq. (2.2). It was surmised that the vapor cavity may initially extend along the charged particle track before quickly acquiring a spherical shape [45]. Values for the constant b have been reported in the range of 4-18, depending on the temperature of operation and the type of radiation being detected [46], [47], i.e. neutron induced recoils versus alpha emitter decay.

$$L_c = b\left(\frac{2\sigma}{P_{vap} - P_{amb}}\right) \tag{5.7}$$

Another notable difference is related to the efficiency of detection and can be considered a hybrid of the CSDA and probabilistic approaches described in this work. The SDD model recognizes that the binary conditional treatment of detection probability is not appropriate due to statistical fluctuations in energy deposition. The model still uses the mean stopping power to calculate the energy deposition E_{dep} as shown in eq. (5.8). The probability $P(E_{dep}, E_{th})$ that an ion, assuming the deposited energy is greater than or equal to the threshold energy E_{th}, will induce a phase transition is governed by the sigmoidal shape function shown in eq. (5.9). The function implies that the probability of detection increases as the ratio $\frac{E_{dep}}{E_{th}}$ increases. The empirical fit parameter a describes the observed steepness of the energy threshold. The larger the value of a, the sharper the threshold is defined. Reported values of a range from 1-10 depending on the radiation particle type, particle energy, and superheated fluid [46], [48].

$$E_{dep} = \frac{dE}{dx} L_c \tag{5.8}$$

$$P(E_{dep}, E_{th}) = 1 - exp\left[a\left(1 - \frac{E_{dep}}{E_{th}}\right)\right] \tag{5.9}$$

In summary, SDD response models differ from TMFDs in that they contain empirical coefficients where the value of the coefficient was determined based on what yielded the best agreement between simulation and experiment. Each coefficient fit is implicitly based on knowledge of the energy threshold. It is not practical to implement these empirical fitting factors at this time because the energy threshold is not known.

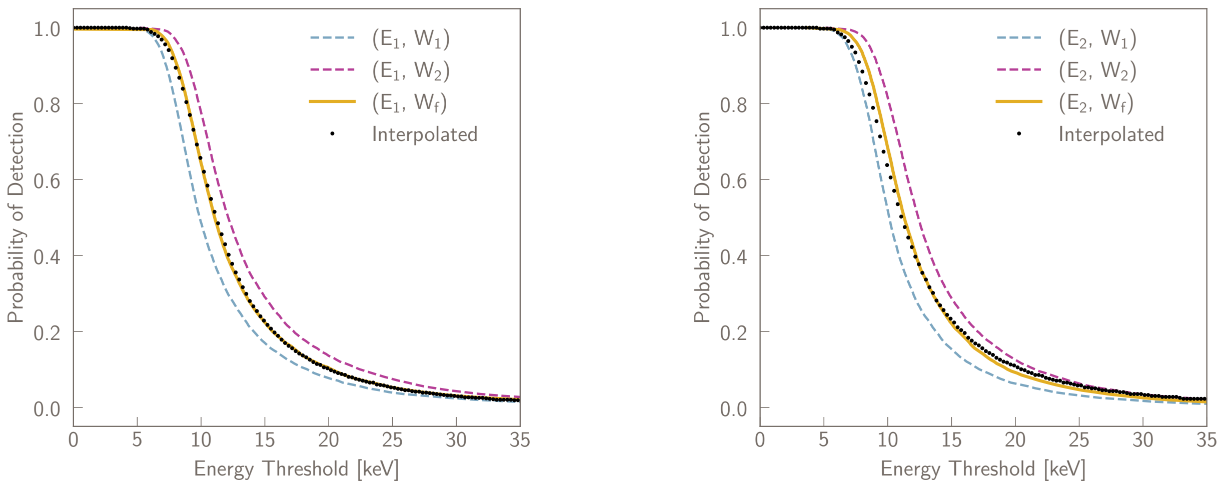

(a) Width interpolation of lower bound energy E_1=50 keV to width W_f using the bounding widths W_1=500 A and W_2=600 A

(b) Width interpolation of upper bound energy E_2=60 keV to width W_f using the bounding widths W_1=500 A and W_2=600 A

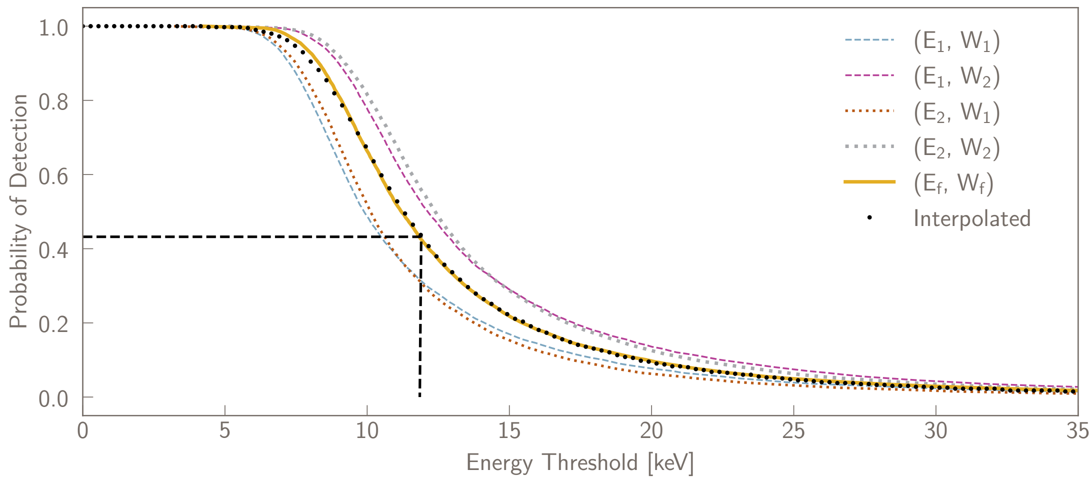

(c) Energy interpolation to the final case (E_f, W_f) using the prior width interpolations (E_1, W_f) and (E_2, W_f)

Figure 5.11. Example interpolation procedure to estimate the survival function shape for the case of ^{19}F ions with energy E_f=55 keV in a W_f=550 A medium of DFP. The interpolated shape (black dots) is compared against an equivalent case SRIM simulation (solid gold line).

6. INVESTIGATION OF NEUTRON ENERGY DETECTION THRESHOLDS USING MONOENERGETIC SOURCES

This chapter discusses experiments using monoenergetic neutron sources from a Van de Graaff accelerator. The count rates obtained at the various neutron energies are curve-fitted to provide estimates for the pressure thresholds which CTMFDs first become sensitive to a given neutron energy. Finally, an estimate for the deposition energy threshold for cavitation is computed using the insights obtained from these experiments.

6.1 Importance of Establishing Neutron Energy Detection Thresholds

As described in section 2.3, the prior work by Grimes established that the DETC curve takes the parametric form of a power curve $E_T = Ax^N$. chapter 7 outlines the procedure for optimization of the “A” and “N” coefficients. One conclusion that can be drawn from the data in chapter 7 is that their does not appear to be a single set of “A” and “N” coefficients that accurately model the CTMFD’s response across all neutron energies. As such, the set of experiments discussed in this chapter were devised to place constraints on which “A” and “N” coefficients are valid.

It should be noted that at the time of these experiments, the probabilistic detection model introduced in chapter 5 had yet to be developed. In fact, it was the insights retained from these monoenergetic source experiments that prompted the initial investigation of the probabilistic method over the CSDA model. One implication of the CSDA’s binary conditional representation of detection probability is that a distinct relationship should exist between neutron energy and the pressure at which detection first becomes possible. This relationship is governed by the recoil ion that deposits the most energy over the critical length scale.

The negative pressure thresholds for 2.5 and 14.1 MeV neutrons have been measured at MFRL by Archambault et. al [49] using D-D and D-T accelerator sources. The amount of energy an elastically scattered ^{12}C or ^{19}F recoil ion can deposit at the pressure threshold is shown in table 6.1. Note that neutron background contamination makes it difficult to definitely identify the exact threshold. To account for this uncertainty, the energy deposition

Isotope	Carbon	Flourine
Neutron Energy [MeV]	14.1	
Max Recoil Energy [MeV]	4.005	2.679
Negative Pressure [bar]	**Energy Deposited [keV]**	
0.75	344.18	412.52
0.80	333.98	400.82
0.85	324.36	389.76
0.90	315.29	379.30
0.95	306.70	369.38
Neutron Energy [MeV]	2.5	
Max Recoil Energy [MeV]	0.710	0.475
Negative Pressure [bar]	**Energy Deposited [keV]**	
2.65	79.17	63.50
2.70	78.10	62.64
2.75	77.07	61.81
2.80	76.06	60.99
2.85	75.07	60.20

Table 6.1. Comparison of the max energy that D-D and D-T neutrons can transfer to ^{12}C and ^{19}F recoil nuclei after an elastic scattering event and their subsequent energy deposition over a critical diameter length scale

is tabulated for a range of pressures which encapsulate the true threshold. Using the CSDA model model for 2.5 MeV neutrons, ^{12}C recoil ions deposit more energy over the critical length scale than ^{19}F despite having a lower LET; therefore, ^{12}C ions define the threshold. Conversely, the threshold at 14.1 MeV is defined by ^{19}F. The D-D and D-T statepoints imply that the energy deposition threshold for detection should lie within 412.52-369.38 keV for a pressure threshold in the range 0.75-0.95 bar and 63.50-60.20 keV for a pressure threshold in the range of 2.65-2.85 bar. Using the power law formulation for the DETC curve, any combination of "A" and "N" coefficients which predict an energy threshold outside of those two ranges can be rejected.

Since each monoenergetic threshold measurement further constrains the solution space for the DETC curve, it was theorized that with enough measurements the remaining uncertainty in the DETC curve could be deduced using simulation alone. Once the DETC curve is known, the CTMFD response matrix could be simulated with relative ease, thereby avoiding the costly and time consuming approach of having to experimentally measure the full response matrix of the detector. In summary, the goal of the experiments described herein was as follows: verify the 2.5 MeV pressure threshold, measure at least two more pressure thresholds for neutron energies between 2.5 and 14.1 MeV, and obtain a threshold measurement as close to 100 keV (the lower bound of the CTMFD response matrix) as realistically achievable.

6.2 Facility Description: Ohio University Edward's Accelerator Lab

Access to monoenergetic neutrons was provided by Ohio University Accelerator Laboratory (OUAL). The facility is home to a Model T-11 4.5-MV tandem pelletron van de Graff accelerator. Maximum beam current available on target is on the order of 80 uA [50], depending on which material is being used. Multiple target options are available, including: ^{2}H, ^{2}H, ^{3}H, ^{7}Li, and ^{9}Be. Multiple ion sources are available as well, including, ^{2}H, ^{2}H, and ^{15}N. Several reactions can be used with the various combinations of ion source and target material. Each reaction has its advantages and disadvantages as a neutron source depending on the range of neutron energies desired, energy resolution, and intensity [51].

Because of time limitations, it was necessary to avoid switching ion sources. While the ^{3}H(p,n)^{3}He reaction has a high neutron yield and is capable of producing neutrons over the desired range of 100 keV to approximately 8 MeV, the issue of radioactive contamination made it impractical for a scoping study such as this one. The ^{9}Be(p,n)^{9}B reaction, which has a Q value and threshold energy of 1.850 MeV and 2.057 MeV, respectively, was chosen by the accelerator operator as the next best option. The other reaction candidates have low breakup reaction thresholds which contaminate the spectrum with high energy neutrons. Other ^{9}Be proton reactions also exist that produce neutrons directly or indirectly, though none of them produce neutrons of higher energy and their cross-sections are comparatively small. However, as seen in fig. 6.2, the downside of the ^{9}Be(p,n)^{9}B reaction is a relatively small yield for neutrons below 500 keV.

One way to compensate for the small cross section is to increase the proton energy and look for neutrons emitted at angles other than 0°. This technique is possible through the use of a beam swinger, shown in fig. 6.1b, located at the end of the ion beam. In its nominal position the ion beam meets the target material at a right angle to the original beam trajectory. This beam swinger can be rotated around the original beam direction to any angle between -4°and +180°. The relationship between the accelerated ion energy, neutron energy, and angle of emission is given by eq. (6.1).

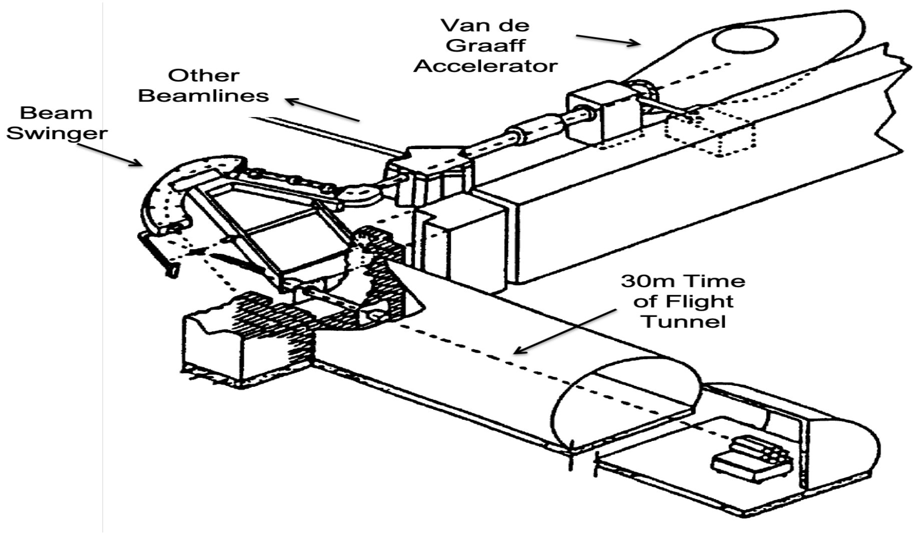

(a) Schematic of the accelerator facility

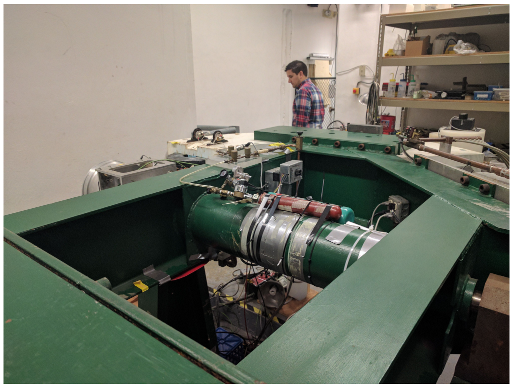

(b) Beam swinger controlling which neutron emission angle enters the collimator

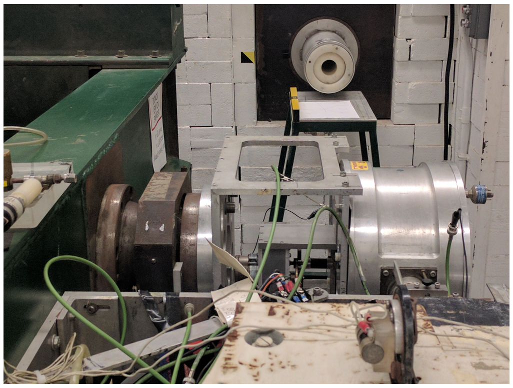

(c) View from the target emission line into the collimator

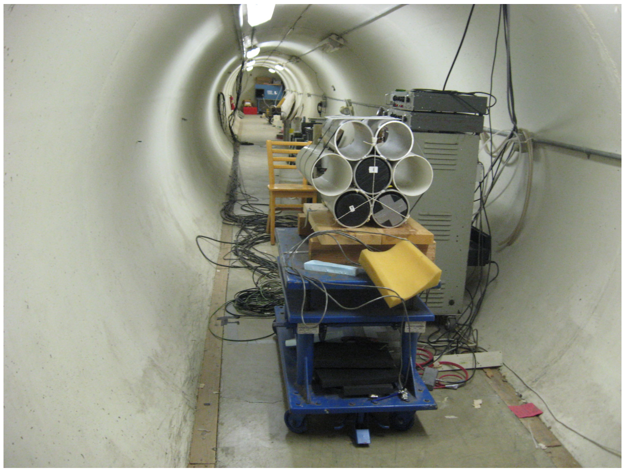

(d) View down the time of flight tunnel

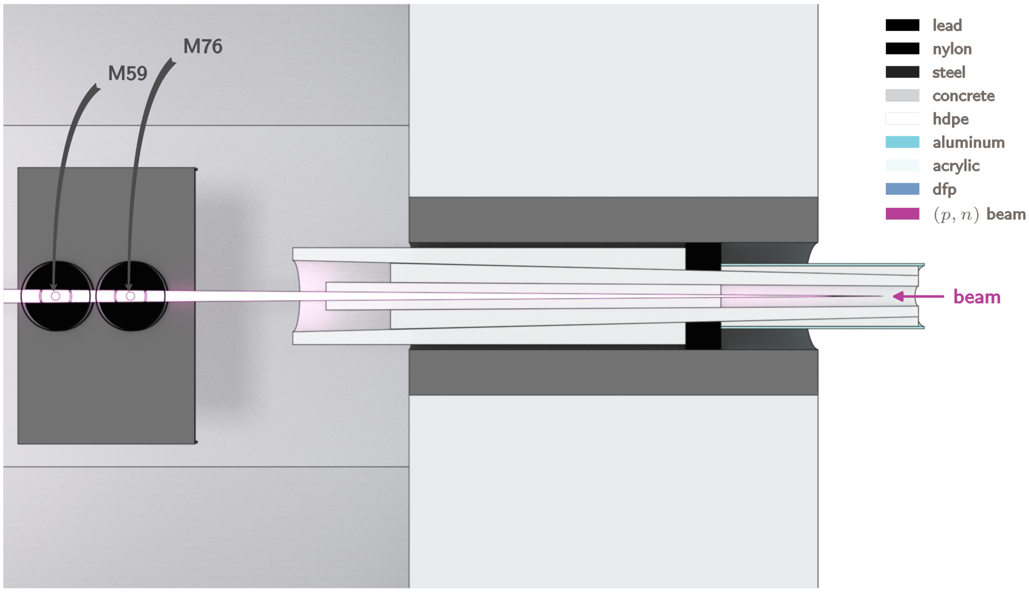

(e) Schematic of the CTMFD arrangement in the time of flight tunnel

Figure 6.1. Images of the accelerator facility.

$$Q = E_n\left(1 + \frac{M_n}{M_{B^9}}\right) - E_a\left(1 - \frac{M_n}{M_{B^9}}\right) - \frac{2}{M_{B^9}} cos\theta\sqrt{M_p M_n E_p E_n} \tag{6.1}$$

Energy contamination from neutrons emitted at other angles is limited by the collimator shown in fig. 6.1c. The collimator consists of a tube protruding from the shielding wall 50 cm long, made of polyethylene, and encased in an aluminum jacket with an outer diameter of 14.5 cm and an inner diameter of 5 cm. The tube juts out of a shielding wall made of concrete and inlaid with more paraffin tube that is 150 cm thick. On the other side of the collimator is a 30 m long time of flight (TOF) tunnel, which is shown in fig. 6.1d. The TOF tunnel is approximately 2 m in in diameter, made of concrete, and approximately 1 m underground to minimize neutron background.

Figure 6.1e shows the arrangement of the two 16 cm^3 CTMFDs used in the experiment. Both detectors were placed in the direct line of the beam at the immediate exit of the collimator tube into the TOF tunnel. The detector, labeled as "M76" in fig. 6.1e, will attenuate some of the flux away from the "M59" detector. This, however, is inconsequential to a threshold measurement because only neutrons at the endpoint energy should be detectable.

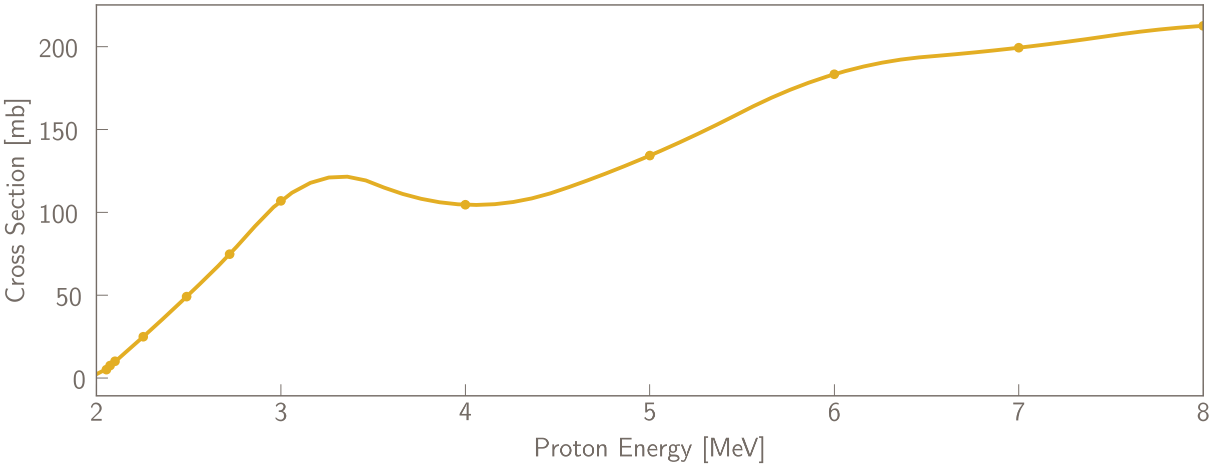

Figure 6.2. Angle-integrated cross section for the ^{9}Be(p,n)^{9}B reaction

6.3 Experimental Count Rates and Curve Fitting Procedures for Threshold Estimation

In a perfectly ideal experiment, a pressure detection threshold would behave as a step function, where just below the threshold the detector could operate indefinitely without recording an event. Once the operating pressure is increased to just above the threshold, the detector would saturate. The radial pressure gradient in the detection volume implies that, when just above the threshold, only a small fraction of the volume can be considered sensitive and thus detections will only be observed in the immediate proximity of the centerline. As a consequence, a large neutron fluence is necessary to observe steep increases in count rates from incremental changes in the centerline pressure.

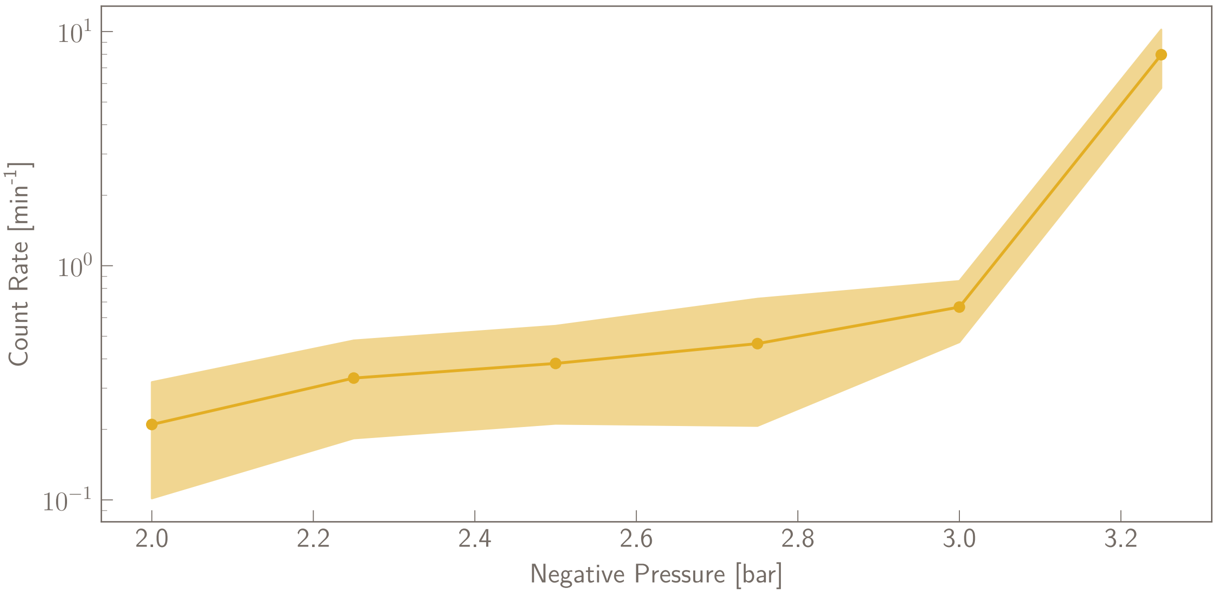

Figure 6.3. Count rate data for a threshold measurement from a 5x10^7 neutrons/second D-D accelerator source at MFRL using the 16 cm^3 CTMFD "M76" at a distance of 1 m.

Figure 6.3 shows count rate data for a threshold measurement from a D-D accelerator source at MFRL using the 16 cm^3 CTMFD "M76", the same detector shown in fig. 6.1e. The D-D source had an intensity of 5x10^7 n/s and the source to detector distance was 1 meter, which equates to a flux of approximately 400 n/s/cm^2. The count rate remains almost flat up to 3.0 bar, whereafter it increases by a factor of 12 at 3.25 bar. The flat plateau before 3.0 bar is an artifact of tritium buildup inside the accelerator target. Though relatively small in magnitude, the contamination of 14.1 MeV neutrons prevents the count rate from decreasing asymptoticly at the threshold [49]. Nevertheless, the observed trend illustrates a procedure for identifying a pressure threshold: Begin by operating at a pressure where the detector is nearing saturation. Once identified, incrementally decrease the operating pressure. If the count rates are not rapidly decreasing, it is likely that the operating pressure is too far above the threshold pressure. Continue incrementally decreasing the pressure until the count rate approaches the level of background. The slope of the count rate curve between background and saturation will be indicative of the source intensity.

Table 6.2. Accelerator beam parameters for each neutron energy

Neutron Energy [MeV]	**Proton Energy** [MeV]	**Emission Angle** [°]	**Beam Current** [nA]	**Differential Cross Section** [mb]	**Differential Neutron Yield** [n/min/sr]
0.207	2.499	150	100	4.78	9.854e5
0.245	2.205	0	300	1.42	7.211e5
0.357	2.745	150	225	3.35	1.715e6
0.527	2.745	0	100	7.50	1.517e6
0.754	2.670	0	100	8.16	1.805e6
1.050	2.961	0	100	8.88	2.164e6
1.361	3.257	0	95	7.97	2.005e6
1.767	3.655	0	100	10.86	3.163e6
2.527	4.406	0	100	41.44	1.407e7
3.936	5.806	0	100	10.40	4.414e6
6.136	8.000	0	100	7.81	4.280e6

Threshold measurements were taken at each of the neutron energies shown in table 6.2. The corresponding proton energy, angle of emission, and proton beam current are also included. The differential cross section and neutron yield are calculated using the computer code DROSG-2000 [52]. DROSG-2000 is a computational tool made specifically for two-body neutron producing reactions. The tabulated cross sections and neutron yields are for the specific angle of emission. The code does not calculate the neutron yield for a specific target geometry. Rather, the yield is normalized for a target thickness that results in a 10 keV neutron energy spread at an angle of 0°. Thus, this number may not be representative of the actual source intensity emitted from the Be target geometry at OUAL, yet is still a useful point of reference for the relative intensity differences between the different neutron energies

The corresponding count rate measurements for each neutron energy in table 6.2 are shown in fig. 6.4 and fig. 6.5. Each set of count rates has been curve-fit using variance-weighted non-linear least squares regression. The regression fit takes the functional form of a power law $\dot{C} = A(p_{neg})^N$. The curve-fit is extrapolated to pressures outside of the measurement range to illustrate whether the count rate curve appears asymptotic.

Asymptotic behavior is evident for neutron energies above 1 MeV and distinctly absent for energies below 1 MeV. The extrapolated curve fits even appear to intersect each other at energies below 750 keV. Such behavior conflicts with the CSDA model, which predicts a monotonic relationship between neutron energy and pressure threshold. A lower neutron energy should have a correspondingly higher pressure threshold. An explanation for this behavior will be discussed later in this chapter.

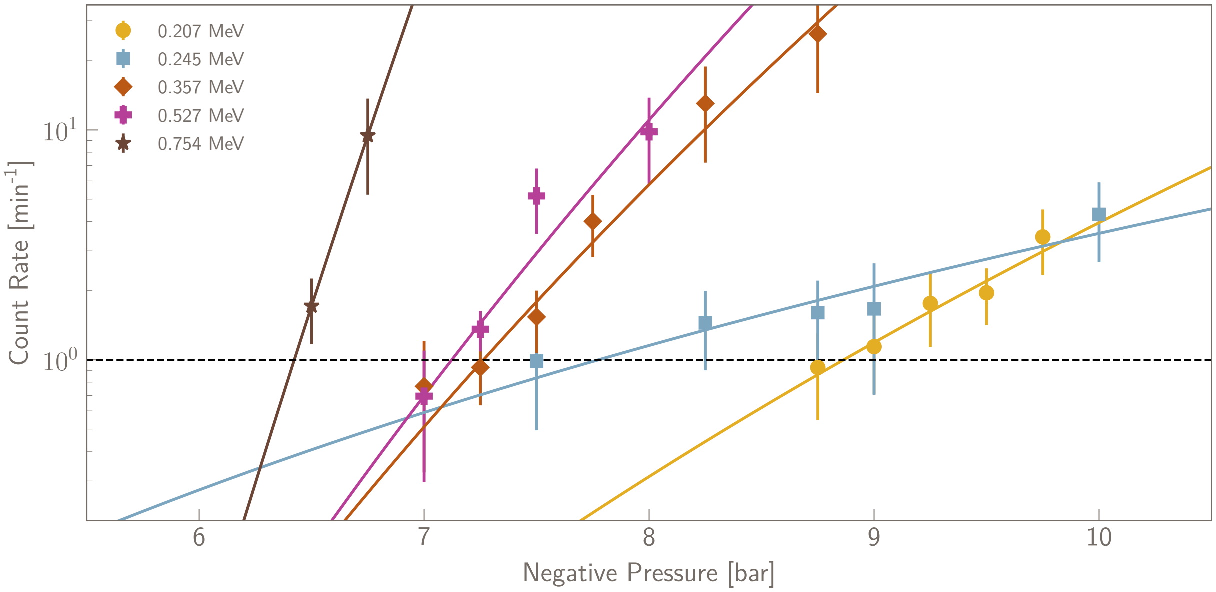

Figure 6.4. Curve fits to the count rates obtained for neutron energies below 1 MeV.

6.3.1 Corrections to the Initial Threshold Estimates

It is worth noting that the decision, made by the accelerator operator, to use the ^{9}Be(p,n)^{9}B reaction was not decided prior to the experiments at OUAL. The cross section and neutron yield data in table 6.2 were found retrospectively while analyzing the experimental data. The drop off in the reaction cross section below 3 MeV (proton energy) was found to be too large to support a neutron fluence capable of producing a step-like response

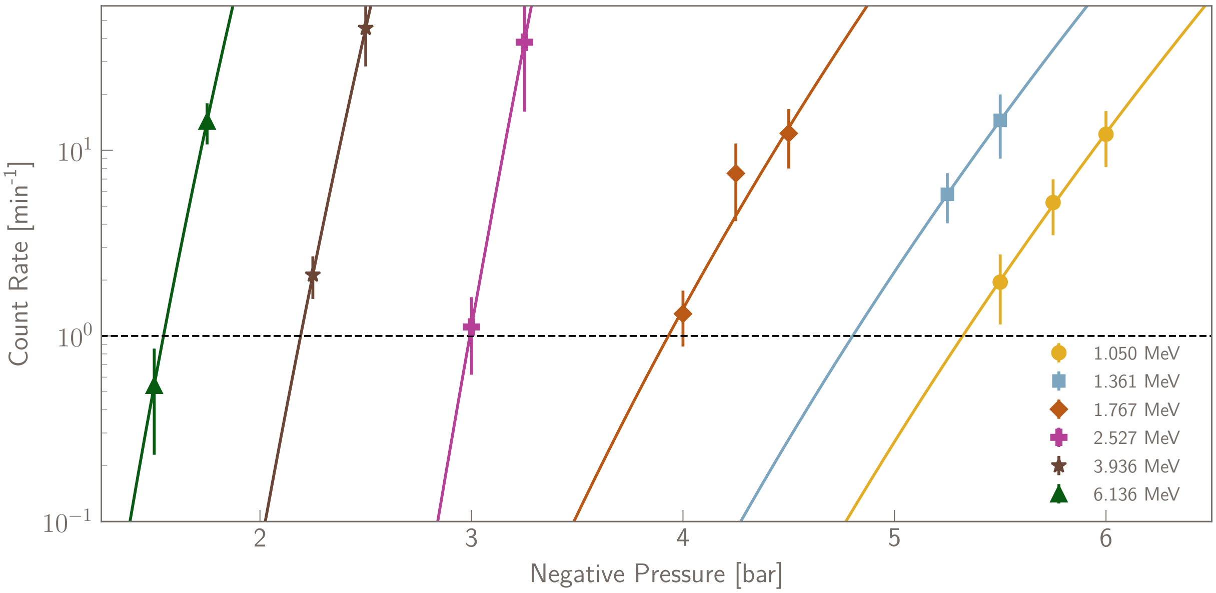

Figure 6.5. Curve fits to the count rates obtained for neutron energies above 1 MeV.

in count rates. As a consequence, time constraints made it necessary to implement an ad-hoc definition of the pressure threshold after data acquisition had already begun. A decision was made to define the threshold as the pressure that yielded a count rate of approximately 1 cpm or lower.

One inherent problem with affixing the threshold to a specific count rate is that count rate is intensity dependent. To compensate for this intensity dependence, the “A” coefficients of each curve fit was normalized by the corresponding neutron yield in table 6.2 and then scaled to a constant value, taken as the average yield from all measurements. The original and adjusted threshold estimates are shown in table 6.3.

A plot of the adjusted threshold pressures as a function of neutron energy is shown in fig. 6.6. A distinguishable feature of the pressure threshold-neutron energy relationship is that two sets of regression lines are necessary to fit the data. The intersection of the two slope regimes occurs approximately at a neutron energy of 0.84 MeV and a pressure of 6.2 bar. The exact mechanism responsible for this is unclear.

Table 6.3. Power fit parameters for the measured countrates and resultant estimates of the pressure threshold at each neutron energy

Neutron Energy [MeV]	Proton Energy [MeV]	A Coefficient	N Coefficient	Estimated Threshold [bar]	Adjusted Threshold [bar]
0.207	2.499	1.607e-17	11.397	8.75	7.962
0.245	2.205	4.592e-11	5.030	8.50	7.211
0.357	2.745	1.328e-22	18.165	7.50	7.001
0.527	2.745	1.509e-24	20.689	7.25	6.855
0.754	2.670	1.591e-43	45.240	6.75	6.336
1.050	2.961	2.587e-22	21.005	5.75	5.213
1.361	3.257	1.840e-20	19.712	5.25	4.679
1.767	3.655	1.404e-18	19.097	4.00	3.919
2.527	4.406	7.029e-29	44.125	3.25	3.019
3.936	5.806	2.853e-17	29.044	2.25	2.213
6.136	8.000	2.288e-11	21.256	1.75	1.562

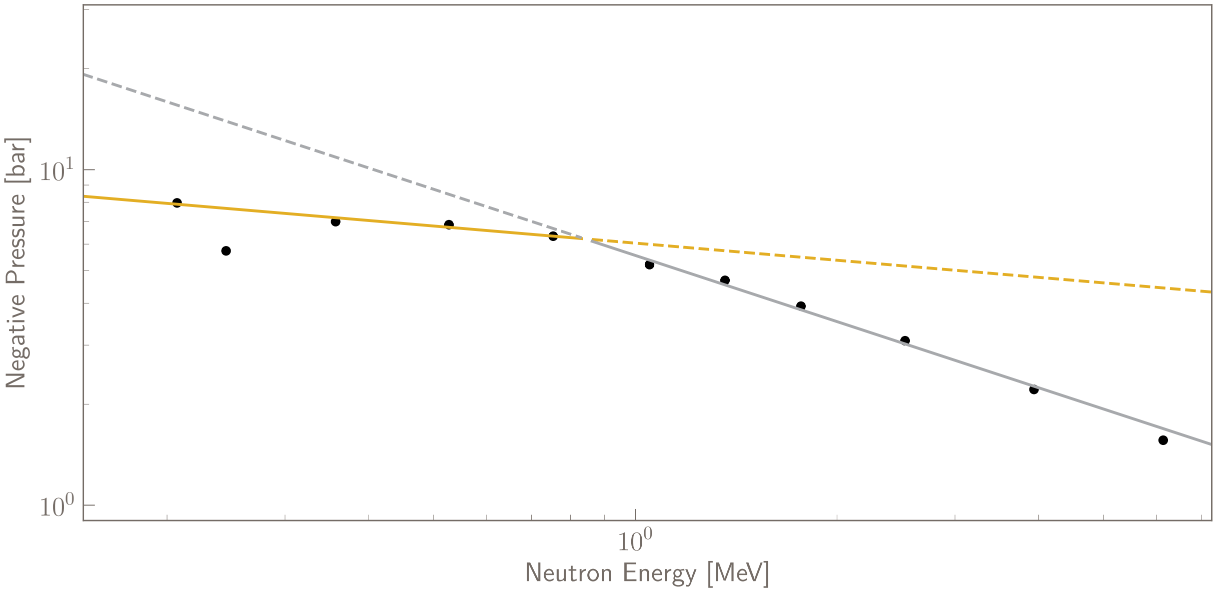

Figure 6.6. Power fits to the adjusted pressure thresholds measured using monoenergetic sources.

It is plausible that the ad-hoc redefinition of the pressure threshold as a function of count rate resulted in an inaccurate estimate of the true threshold, even after correcting for intensity variations. The lack of prior knowledge about the decreasing source intensity for neutron energies below 750 keV is reflected in the number of measurements (pressures) in each of the count rate curves in fig. 6.4. The overlap in the 357 and 527 keV count rate curves and the plateau-like behavior in the 207 and 245 keV curves made it very difficult to identify the threshold. This ambiguity is irreconcilable without more data at lower pressures. Nevertheless, it is almost certain that the gray regression line in fig. 6.6 is not accurate over the entire energy range; thereby implying the need for the second regression fit shown in gold. The point in contention is what the slope of the gold line should be.

6.4 Mapping the Relationship Between Neutron Energy and Pressure Threshold to Deposition Energy Necessary for Cavitation

As discussed in section 6.1, the CSDA's binary representation of detection probability allows the deposition energy threshold for cavitation to be predicted if the relationship between neutron energy and pressure threshold is known. The solid regression lines in fig. 6.6 are discretized into a sufficient number of ordered pairs: (neutron energy, pressure threshold). For each ordered pair, neutron energy is mapped to ^{12}C and ^{19}F recoil ion energy using the max transferable energy from an elastic scatter event. Threshold pressure is converted to a length scale using eq. (2.2). Finally, energy deposition is calculated using eq. (5.3). Results are shown in fig. 6.7.

The deposition energy threshold for cavitation is set by which ion, ^{12}C or ^{19}F, deposits the greater amount of energy. The two energy deposition curves intersect in two places: approximately 243 keV and 21 keV, corresponding to neutron energies of 9.55 and 0.84 MeV and pressure thresholds of 1.26 and 6.22 bar, respectively. ^{19}F defines the thresholds outside the range of 1.26 and 6.22 bar and ^{12}C defines the threshold within. Interestingly, the intersection of the two ion deposition curves at 6.22 bar occurs at the same pressure as the intersection of the two regression fits in fig. 6.6. This implies the reason for the change in slope of the regression fit is the transition from ^{12}C recoil ions defining threshold to ^{19}F.

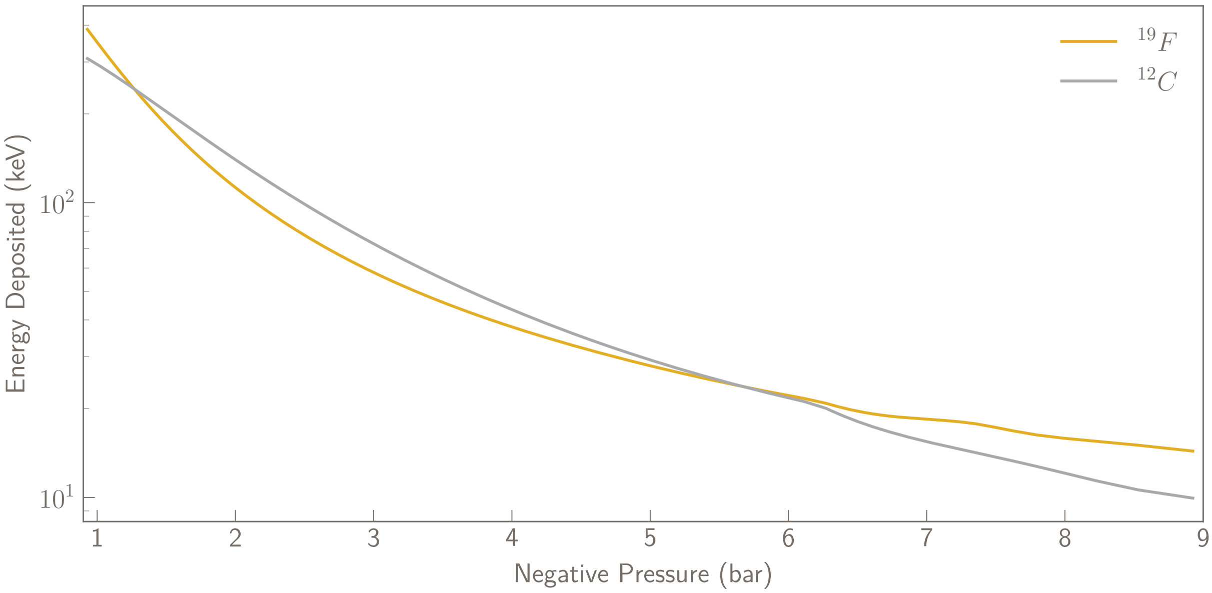

Figure 6.7. Estimates for the max energy a ^{12}C or ^{19}F recoil ion can deposit inside a critical-sized vapor cavity for the neutron energies and corresponding pressure thresholds from the curve fits in fig. 6.6.

6.5 Threshold Analysis Using the Probabilistic Detection Model

Each of the neutron energy and pressure threshold cases were also analyzed with the probabilistic detection mode. Inference of the DETC curve is not possible with this model due to the probabilistic nature of an ion's energy deposition. Useful insights can still be deduced, such as which ion is responsible for defining the thresholds.

A SRIM simulation has been run for each neutron energy and pressure threshold combination in table 6.3. The resulting detection probability estimates as a function of threshold energy are shown in fig. 6.8. Each subfigure displays the probability estimate with and without taking into account net energy deposition, which was first introduced in section 5.5. The dashed vertical lines represent the CSDA average energy deposition and the solid circular marker coincides with the intersection of the CSDA line with the detection probability curve. This intersection occurs within the probability range of 0.2-0.4 for every case shown. Thus, only 20-40% of the ions actually deposit an amount of energy greater than or equal to CSDA average, substantiating the concerns expressed in section 5.3 about the validity of using the average, as opposed to the most probable, value of the energy deposition distribution.

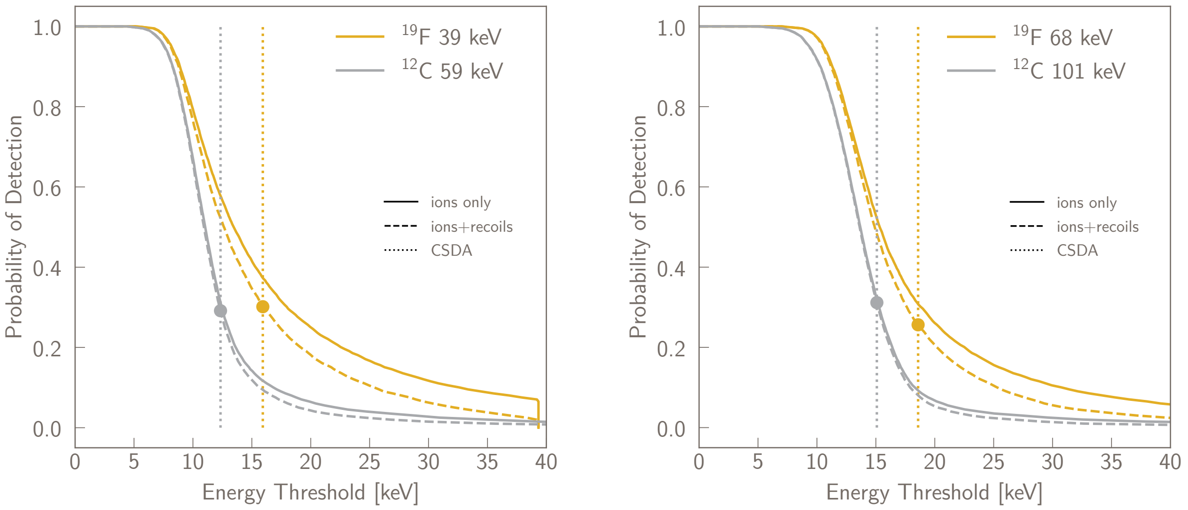

(a) E_n=0.207 MeV, P_{neg}=7.962 bar

(b) E_n=0.357 MeV, P_{neg}=7.211 bar

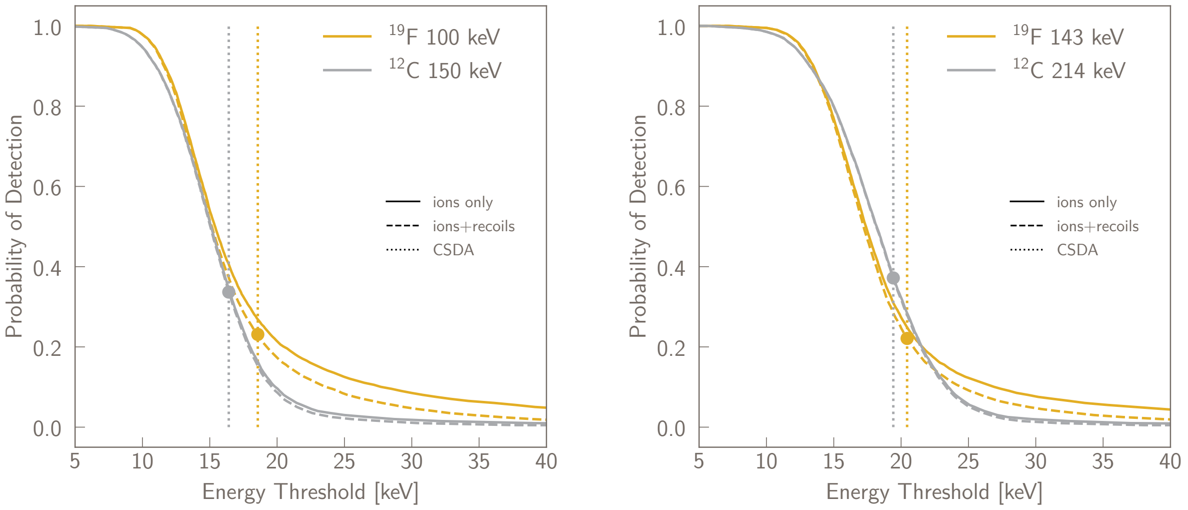

(c) E_n=0.527 MeV, P_{neg}=6.855 bar

(d) E_n=0.754 MeV, P_{neg}=6.336 bar

Figure 6.8. Corresponding detection probability curves for each neutron energy case in table 6.3.

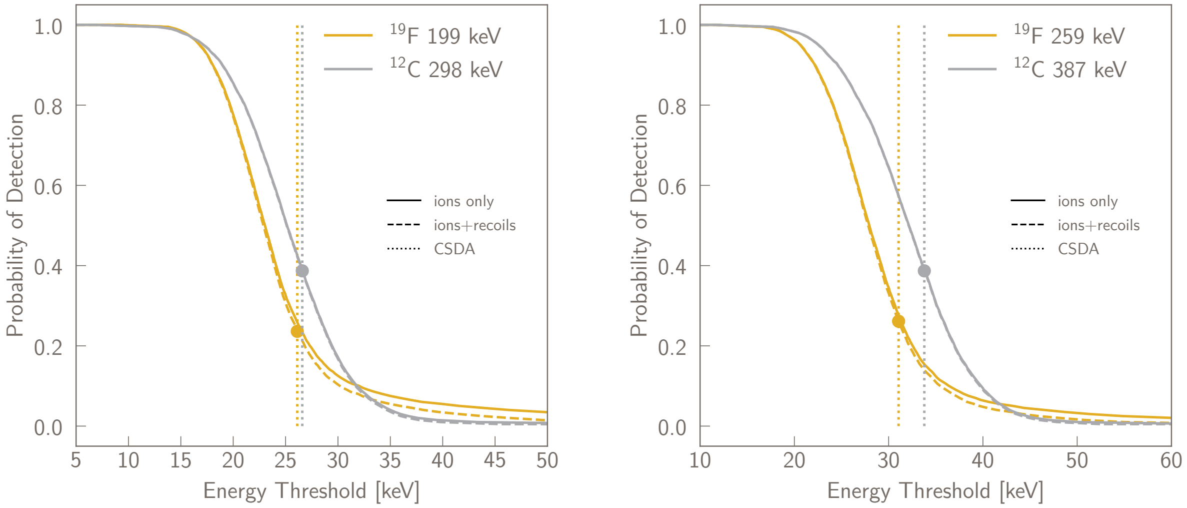

(e) E_n=1.050 MeV, P_{neg}=5.213 bar

(f) E_n=1.361 MeV, P_{neg}=4.679 bar

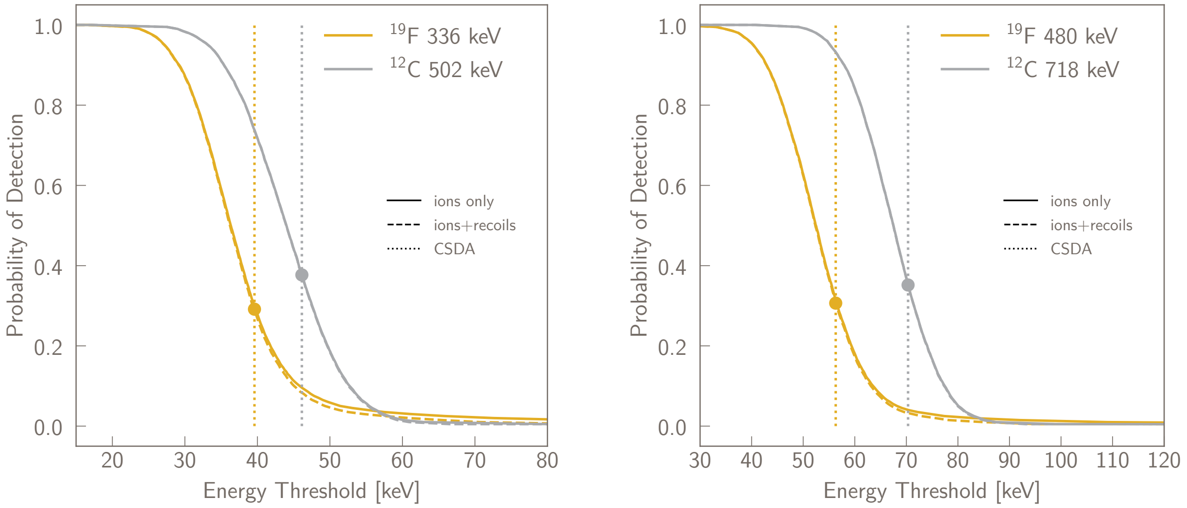

(g) E_n=1.767 MeV, P_{neg}=3.919 bar

(h) E_n=2.527 MeV, P_{neg}=3.019 bar

Figure 6.8. Corresponding detection probability curves for each neutron energy case in table 6.3.

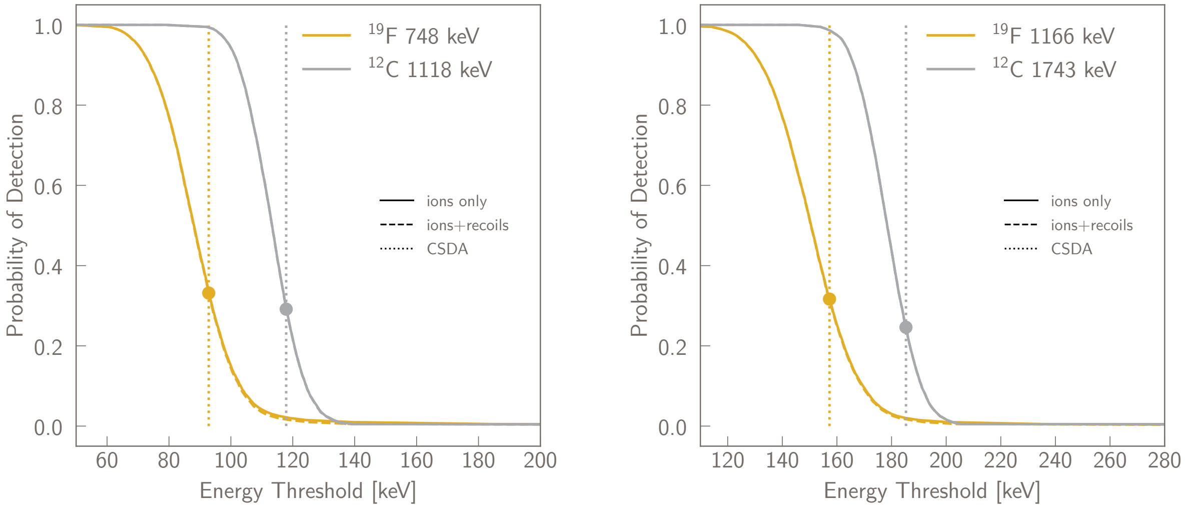

(i) E_n=3.936 MeV, P_{neg}=2.213 bar

(j) E_n=6.136 MeV, P_{neg}=1.562 bar

Figure 6.8. Corresponding detection probability curves for each neutron energy case in table 6.3.

For a given neutron energy, the position of the ^{19}F detection probability curve with respect to the ^{12}C curve is a rough indication of the relative contribution of each ion to the measured count rate. At higher neutron energies, for example 1.767 MeV and above, the ^{19}F and ^{12}C curves are well separated, with ^{12}C having a higher propensity to generate a detection event. The converse is true for neutron energies of 357 keV and below. The 754 keV case is of interest because the detection probability curves are similar. This similarity partially validates the hypothesis that the observed slope change of the regression fits in fig. 6.6 is an artifact of a change in which recoil ion is defining the threshold. The CSDA model predicts that ^{19}F defines the threshold at pressures of 6.22 bar and above, whereas the probabilistic model indicates that both ions contribute to the count rate. The similarity in the detection probability curves, however, does not imply that ^{19}F and ^{12}C contribute equally to the total count rate, as a consequence of differences in their respective macroscopic cross sections.

6.5.1 MCNP Modeling of a CTMFDs Theoretical Response at the Pressure Threshold

While beneficial from a conceptual standpoint, the detection probability curves shown in fig. 6.8 have limited utility for validating the accuracy of the pressure thresholds in table 6.3. To validate the measured count rates through simulation a detailed MCNP model of the OUAL facility would need to be developed. Proton transport through the Be target would need to be modeled to get an accurate estimate of the emitted neutron spectrum, which is not truly monoenergetic. In reality, accelerator source spectra are only quasi-energetic on account of the fact that the accelerated ions experience differing amounts of energy loss inside the target material before undergoing capture. In regards to neutron transport, the MCNP model would need to include the beam swinger, collimator, shielding wall, and the TOF tunnel. Unfortunately, the detailed dimensions necessary to make such a model were unavailable.

A simplified MCNPP model can still provide useful insights about a CTMFD's response at the pressure threshold. The geometric details of the model are identical to that used for calculating the CTMFD's response matrix, which is described in section 8.1. Given the simplicity of the model, the scope of analysis of the detector's response was limited to two areas: the radial distribution of detection events through the detection volume and the relative contribution of ^{19}F and ^{12}C to the total count rate. Furthermore, only two of the eleven neutron energies were analyzed. The 2.527 MeV threshold was of interest for comparison with the D-D accelerator data taken at MFRL. The 0.754 MeV threshold was included to further investigate the slope change of the regression fits in fig. 6.6.

All analyses were done using the probabilistic detection model. In order to estimate the count rate it is first necessary to select the "A" and "N" coefficients that define the deposition energy threshold for cavitation as a function of pressure. The coefficients used in this analysis were selected from table 7.2 based on the optimization procedure discussed in chapter 7. The table displays values for three datasets, corresponding to source-to-detector distances of 50, 100, and 200 cm. The optimized coefficients are further parameterized by a "cut factor". The significance of this cut factor is introduced below.

The radial distribution of counts within the detection volume can aid in identifying how far the estimated pressure thresholds are from the true value. As mentioned earlier, when just above the threshold, detections should only be observed in the immediate proximity of the centerline. Increasing the centerline pressure above the threshold has the effect of increasing the fraction of the detection volume that will be sensitive to neutrons. While analyzing the radial count distributions for these experiments, it was noted that detection events were not localized about the centerline, but were predicted throughout the entire volume. In fact, the probabilistic model did not predict the existence of any threshold behavior whatsoever, a result that is in direct conflict with the D-D and D-T threshold statepoints measured by Archambault et. al [49].

Analysis of the detection events occurring far from the centerline revealed that the each event had a low (<5%) probability of detection. This is a consequence of sampling the long tail region of the detection probability curve, which extends out to the full energy of the ion. The existence of the tail region is supported by SRIM simulations (see fig. 5.6 and fig. 5.10) as well as the theoretical Landau distribution. It was postulated that the high energy (transfer) collisions responsible for the tails existence do not contribute to heating the fluid as efficiently as electronic stopping. Within the current computational framework of the probabilistic model, the only way to preserve the existence of thresholds is to disregard events that sample the tail of the detection probability curve. Any event with a detection probability below a specified cut point is automatically assigned a probability of zero. An example of what the detection probability curve curve would look like with a 20% cut factor is shown in fig. 6.9. This approach, however, introduces the challenge of determining what fraction of the distribution should be truncated.

The radial distribution of counts within the detection volume for the 2.527 MeV and 0.754 MeV cases are shown in fig. 6.10 and fig. 6.11, respectively. The distributions are further separated by isotope to identify the relative contributions of ^{19}F versus ^{12}C. The gold line represents the shape of the radial distribution without truncating any fraction of the detection probability curve while the gray and blue lines are the result of truncating events with probabilities less than 10% and 20%, respectively.

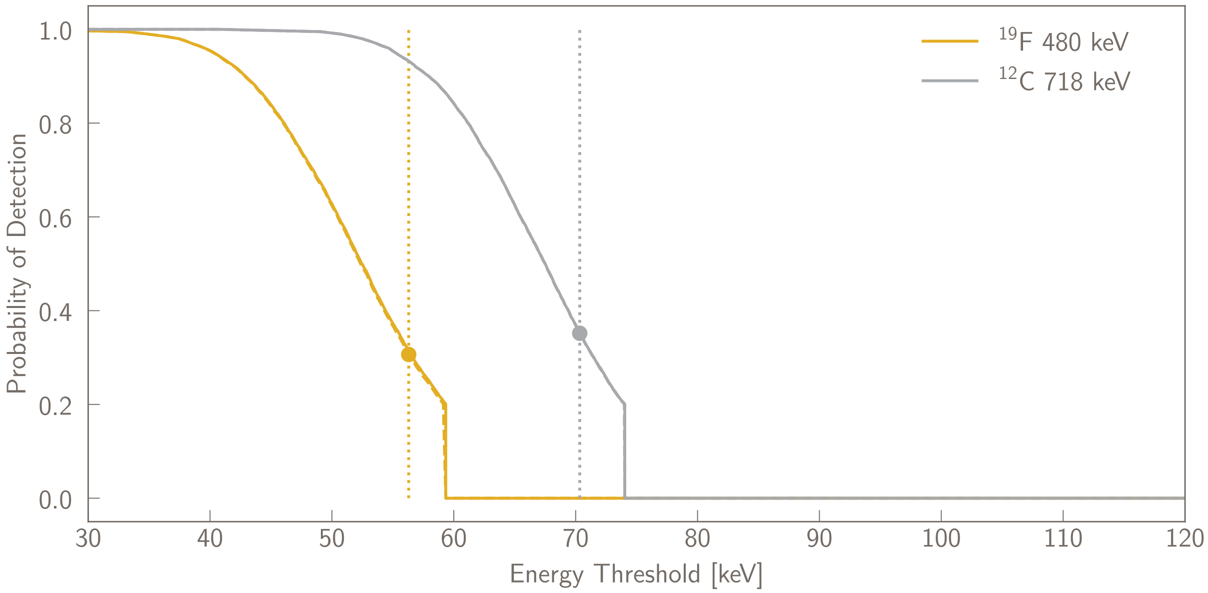

Figure 6.9. Example of what the probability of detection curve would look like after application of a 20% cut factor.

Table 6.4 contains integral data representing the predicted counts throughout the entire detection volume. Integral totals are more useful for observing the relative contributions by ^{19}F versus ^{12}C. Just above the pressure threshold, the efficiency of detection should be small. This is a consequence of the radial pressure gradient as well was the fact that the fluid will only be sensitive to the highest energy recoil ions as the result of direct knock-on collisions. The total number of interactions on each isotope in the MCNPP output file is represented as $N(E_r > 0)$. The number of events which are predicted to have a non-zero detection probability is shown as $N(P > 0)$. The ratio of $\left(\frac{N(P>0)}{N(E_r>0)}\right)$ indicates the fraction of interactions that are actually detectable. The average detection probability of all events, $\bar{P}$, is found from the quotient of the total detection probability, $\sum_{i=1}^{i=N} P_i$, and the total number of detectable events, $N(P > 0)$.

The impact of truncating the detection probability curve is readily apparent in both the radial distribution plots and tabulated integral counts. For a neutron energy of 2.527 MeV, the count distribution (fig. 6.10) resulting from zero truncation is approximately flat across

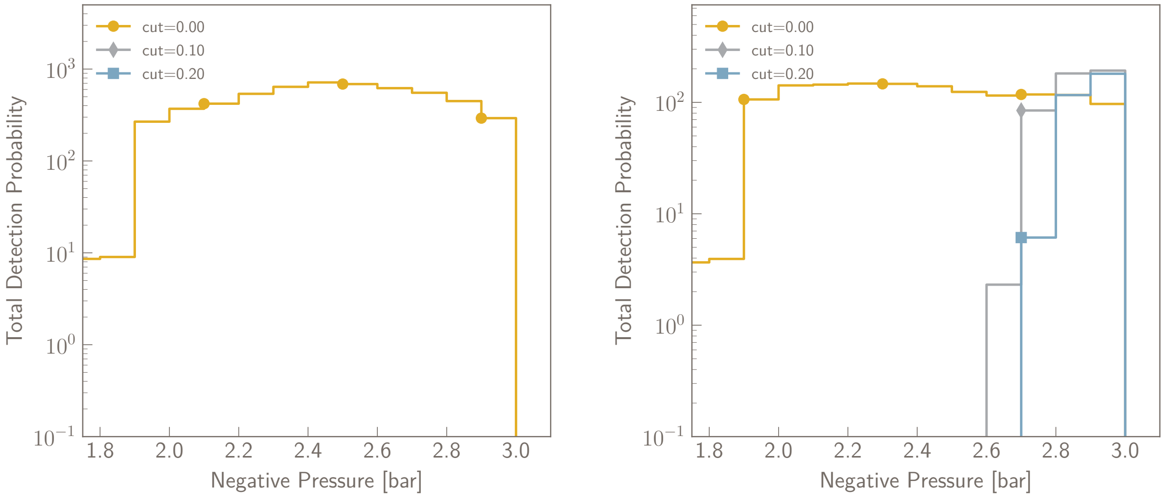

(a) ^{19}F recoils

(b) ^{12}C recoils

Figure 6.10. Summation of the detection probabilities from a MCNPP simulation consisting of a 2.527 MeV planar neutron beam illuminating the 16 cm^3 CTMFD M76. The summation of the detection probabilities is represented as a function of pressure(radial distance), in 0.1 bar increments, for a centerline pressure of 3.0 bar. The (A,N) coefficients used for the DETC curve are taken from the 100 cm dataset in table 7.2.

the detection volume for both isotopes. The sharp drop just below 2.0 bar coincides with the junction of the central bulb and the arm tubing. Over 50% of events have non-zero detection probabilities, yet the average probability between both isotopes is approximately 7e-3. Truncating the last 10% of the probability curve reduces the number of non-zero probability events on ^{12}C by two orders of magnitude and completely eliminates all counts from ^{19}F. Therefore, the 2.527 MeV threshold is defined exclusively by ^{12}C. The data for the 0.754 MeV neutron energy case is more ambiguous. It is clear that both isotopes contribute to the total count rate. The total number of non-zero events and the total probability of all events for ^{19}F is two orders of magnitude larger relative to ^{12}C.

The pressure at which the radial count rate drops to zero represents the threshold predicted by the probabilistic model. The predicted location of the threshold is also dependent on the “A” and “N” coefficients that define the DETC curve, as shown in table 6.5. The variation in the estimated threshold for the 2.527 MeV case is approximately 0.3 bar depend-

Table 6.4. Comparison of the probabilistic model predicted counts, integrated over all pressures in the detection volume, for the MCNPP monoenergetic planar source simulations from fig. 6.10 and fig. 6.11 for different cut factors.

Neutron Energy [MeV]	2.527		0.754	
Isotope	^{19}F	^{12}C	^{19}F	^{12}C
$N(E_r > 0)$	1.30e6	3.59e5	1.61e6	6.43e5
cut=0.00				
$N(P > 0)$	6.43e5	2.48e5	1.04e6	4.81e5
$\sum_{i=1}^{i=N} P_i$	5.72e3	1.47e3	1.30e5	1.54e4
$\bar{P}$	8.89e-3	5.93e-3	1.25e-1	3.21e-2
cut=0.10				
$N(P > 0)$	0.00	3.39e3	8.00e5	8.90e3
$\sum_{i=1}^{i=N} P_i$	0.00	5.65e2	1.33e5	1.06e3
$\bar{P}$	0.00	1.67e-1	1.67e-1	1.19e-1
cut=0.20				
$N(P > 0)$	0.00	1.52e3	3.55e5	2.87e3
$\sum_{i=1}^{i=N} P_i$	0.00	4.11e2	9.33e4	6.82e2
$\bar{P}$	0.00	2.71e-1	2.63e-1	2.38e-1

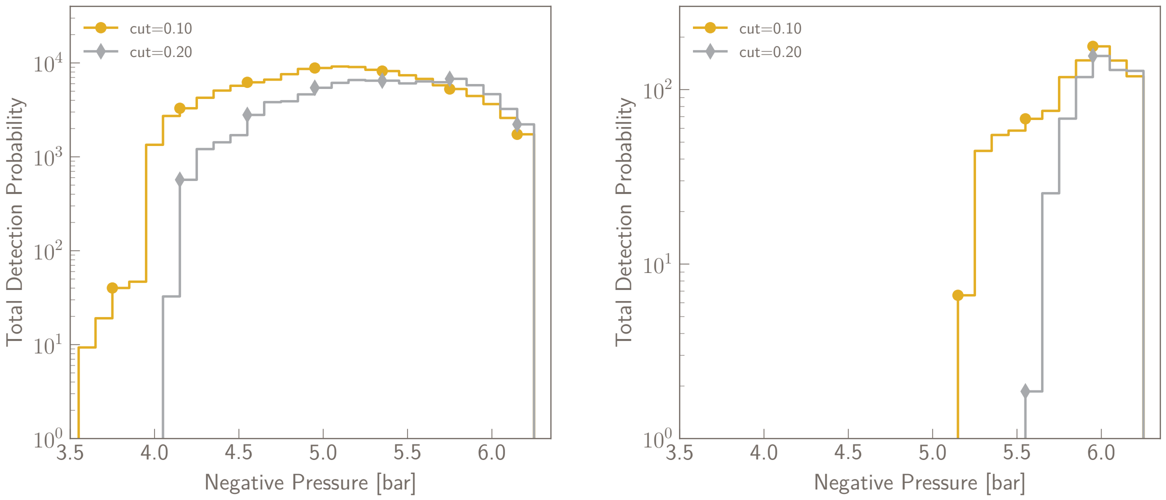

(a) ^{19}F recoils

(b) ^{12}C recoils

Figure 6.11. Summation of the detection probabilities from a MCNPP simulation consisting of a 755 keV planar neutron beam illuminating the 16 cm^3 CTMFD M76. The summation of the detection probabilities is represented as a function of pressure(radial distance), in 0.1 bar increments, for a centerline pressure of 6.25 bar. The (A,N) coefficients used for the DETC curve are taken from the 200 cm dataset in table 7.2.

ing on the cut factor or coefficients used. Archambault et. al estimates the D+D threshold to be approximately 2.8 bar once contamination by D+T neutrons has been subtracted [49], which is in agreement with the 50 and 100 cm cases after applying a cut value of 0.2.

The “A” and “N” coefficients for the 50 cm dataset are not applicable for the 0.754 MeV case. Due to saturation concerns, count rate data could only be recorded up to 4.0 bar. The experimental estimate of the threshold for 0.754 MeV neutrons was 6.336 bar, well outside the calibration pressure range. bar. None of the datasets have experimental data for both sources that fully encompass both predicted thresholds. The importance of restricting application of the DETC to pressures within the calibration range is explained further next chapter. However, the conclusion that can be drawn is that the coefficients that predict the 2.527 MeV threshold the best, i.e. the 50 cm dataset, will likely have the worst prediction for the 0.754 MeV case. The converse trend should also hold in which case the 200 cm coefficients would best predict the 0.754 MeV case.

The fact that the probabilistic model predicts the D+D threshold within 0.3 bar for the worst case is in support of the cut factor's relevancy. The important question is whether the model's predictions are accurate at higher pressures, which does not appear likely considering the corresponding response matrix predicts a non-zero response to neutrons with energies between 100-200 keV as low as 5 bar. Despite the questions raised in section 6.3.1 regarding counting statistics and the relative source intensity between neutron energies, it is difficult to imagine a scenario where the experimental data in fig. 6.4 could be extrapolated to converge at a threshold of 5 bar. Nevertheless, the lack of accuracy at higher pressures is surprising. As will be seen next chapter, the probabilistic model in fact excels at predicting count rates above 5.0 bar.

Table 6.5. Variation in the pressure thresholds to 2.527 MeV and 0.754 MeV neutrons as predicted by the probabilistic model for the dataset-optimized "A" and "N" coefficients found in table 7.2. Values of N/A are shown for cases where there were no non-zero detection probability events.

Neutron Energy [MeV]		2.527		0.754	
Isotope		^{19}F	^{12}C	^{19}F	^{12}C
Distance [cm]	**Cut**	**Pressure Threshold [bar]**			
50	0.1	N/A	2.6	3.75	5.35
100		N/A	2.5	3.65	5.35
200		N/A	2.4	3.55	5.15
50	0.2	N/A	2.7	4.45	N/A
100		N/A	2.6	4.35	N/A
200		N/A	2.5	4.05	5.55

7. DETERMINATION OF THE ENERGY DEPOSITION THRESHOLD FOR CAVITATION

This chapter introduces the criteria used to optimize the deposition energy threshold curve needed to predict the response of TMFD's. A figure of merit is defined to quantify the accuracy of MCNPP-predicted count rates to the data measured in experiments using both the CSDA and probabilistic detection models. Two separate optimization analyses are performed. The first analysis focuses on optimization over the full range of pressures for a single detector in a low fluence field. The second analysis aims toward development of a multi-detector system capable of operating at higher fluence rates, where each detector is optimized for a specific range of pressures.

7.1 Parameterization of the DETC Curve

As previously mentioned, based on the work by Grimes [21], the DETC curve is assumed to follow a power law with the form $E_T = A(p_{neg})^N$. Constraining the DETC curve to a specific functional form is a pivotal assumption, which if incorrect, could undermine the success of this work. The benefit of assuming a continuous function for the DETC curve is a reduction in the computational complicity of the problem. A significant fraction of the work done by Grimes was devoted to development of customized numerical methods necessary to solve for the DETC curve in discretized form.

Functional forms other than the power law were explored in the early stages of this work. Literature on superheated droplet detector threshold measurements (using monoenergetic neutrons) have reported an exponential relationship between temperature and ^{19}F recoil energy [46]. However, the slope of the experimental count rate curve could never be replicated by assuming an exponential of the form $Ae^{(-b*p_{neg})}$. The slope of the predicted count rates was either far too steep or far too gradual. Various order polynomial functions were also explored. A power law yielded the best prediction in all cases. Thus, the optimization in this work is centralized around finding the A,N coefficients that yield the best agreement between experiment and simulation.

It was necessary to come up with a figure of merit (FOM) to judge how well a given A,N combination reproduced the experimental data. Conceptually, the FOM represents the uncertainty weighted percent-difference of the predicted versus experimental count rates ($\dot{C}$) at negative pressure i P_i. The percent-difference at each pressure was weighted with the 1 σ uncertainty of the corresponding measurement to ensure that measurements with more detections events had a greater effect on the FOM. The formal definition of the FOM is defined in eq. (7.1), which shares a resemblance to the L_2 norm. Note that the residual of the percent difference, rather than the residual of the actual count rate is used. This is because there is such a drastic difference in count rates at low pressures versus high pressures. If using the residual of the actual count rates then the FOM value would be almost entirely dominated by how well the A,N curve matched the count rates at higher pressures and would say very little about how well it matched at lower pressures. Using percent difference describes how well the A,N parameters predict the count rate curve as a whole. The weighted sum of the residuals is normalized by the number of experimental pressures in the data set. Doing this allows for comparisons between different sources and or different detectors where dead time or efficiency effects constrain the number of pressures in which it is possible to obtain valid data.

Optimization is performed through minimization of the FOM. Three sets of A,N coefficients are determined: The coefficients which yield the lowest FOM for the measurements made with the ^{252}Cf source, the coefficients which yield the lowest FOM for the measurements made with the ^{241}AmBe source, and then the coefficients which give the best agreement for both sources together. A single set of coefficients that produces good agreement for both spectrums is the most ideal scenario. A common pitfall in any optimization analysis is the tendency to overfit the model to match the training data. Training the model with two distinctly different spectrums acts as a safeguard against this tendency and ensures that the resulting solution is extensible across a wide range of neutron energies.

$$FOM = \frac{1}{N}\sqrt{\sum_{i=1}^{N}\left[\frac{1}{\sigma(P_i)^2}\left(\frac{\dot{C}(P_i)_{mcnp}}{\dot{C}(P_i)_{exp}} - 1\right)^2\right]} \tag{7.1}$$

7.2 Optimization of a Single-Detector System

Experimentation in the initial stages of this work involved the use of only a single detector. At that point in time, knowledge about the relationship between pressure threshold as a function of neutron energy was limited to only the 2.5 and 14.1 MeV statepoints obtained with D+D and D+T accelerators. It was assumed that a negative pressure of somewhere in the range of 8-10 bar was necessary to achieve sensitivity to 100 keV neutrons. Under that assumption, the response of the CTMFD needed to be optimized for pressures spanning the range of approximately 1 bar (14 MeV) to 10 bar (100 keV). Unfortunately, it is rather impractical to take measurements over the entire 1-10 bar range with a single detector and at a single source-to-detector distance. At too close of a distance the detector will likely saturate before 10 bar, while at too far of a distance the detection rate will be so low it is difficult to statistically distinguish from that of background

The speeds required to obtain tension states in the range of 8-10 bar require the CTMFD to be well balanced. Improper balance induces mechanical vibration that can impact the neutron sensitivity in a manner difficult to quantify. At this stage, it was qualitatively determined via experience that the 16cm^3 detector M76, referenced in chapter 6, was particularly well balanced and thus was selected for the single-detector system as a consequence. A drawing showing the various dimensions of the glassware is shown in fig. 7.1. An artist's rendition of a hand portable version of the CTMFD apparatus is shown in fig. 7.2.

In order to reach 10 bar, the source-to-detector distance had to be 300 cm, though this meant data could only recorded down to 3.0 bar. The detector and surrounding room geometry were introduced in fig. 3.5. At this distance, the flux at the detector from the ^{252}Cf and ^{241}AmBe sources was 6.128e-2 and 3.946e-2 n/cm^2/s, respectively, which correspond to a dose rate <10 μRem/hr.

The A,N coefficients for the Cf optimized, AmBe optimized, and both optimized cases are tabulated in table 7.1. Their corresponding count rate predictions using the CSDA and probabilistic detection models are plotted in fig. 7.3 and fig. 7.4, respectively. The error bars in these plots represent the 2σ uncertainty from counting statistics. Predictions that lie outside the uncertainty margin likely can not be attributed to statistical effects but rather

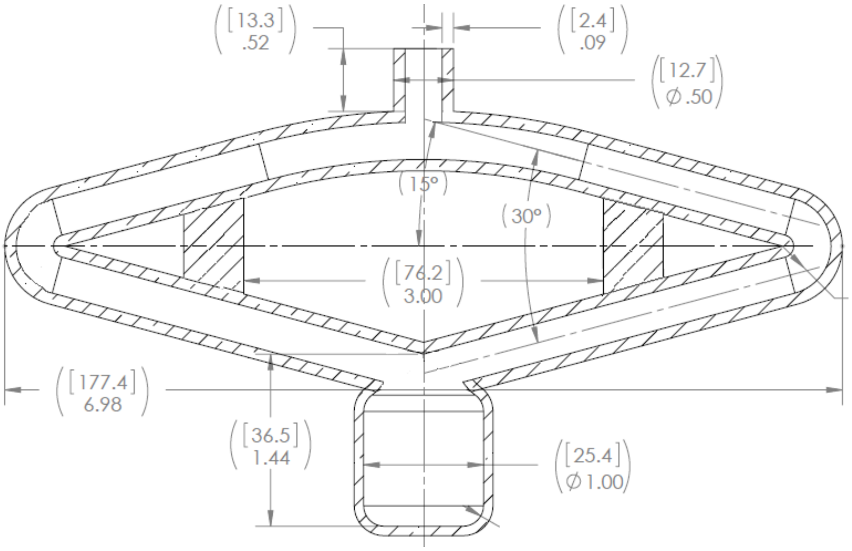

Figure 7.1. Dimensions of the 16 cm^3 CTMFD, “M76”.

Figure 7.2. Rendering of a single detector system for portable spectroscopic and or dosimetric measurements.

are a consequence of inaccuracies in the representation of the DETC curve. Inaccuracy

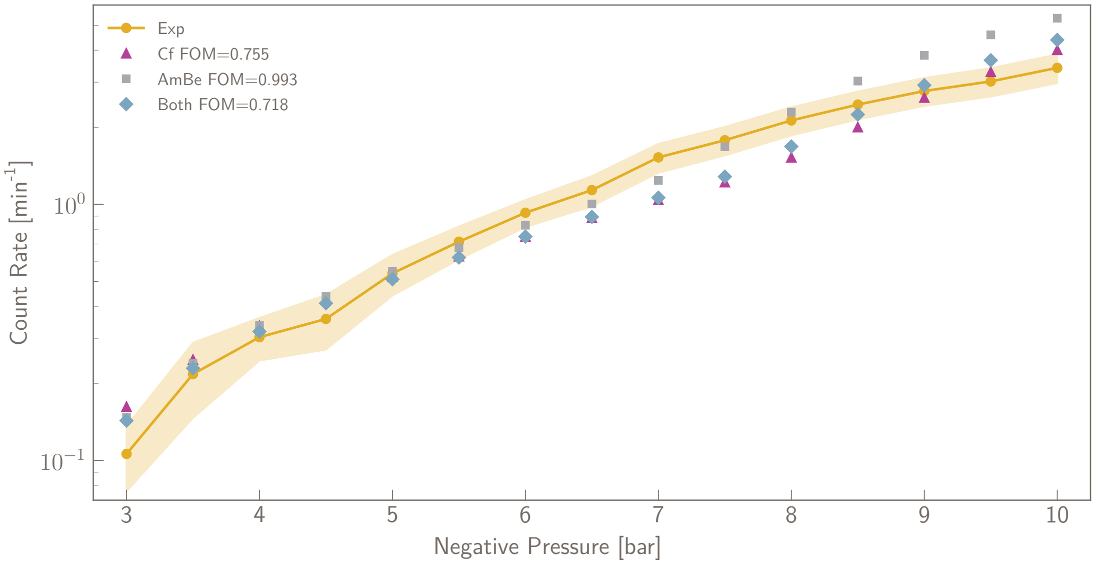

(a) ^{252}Cf

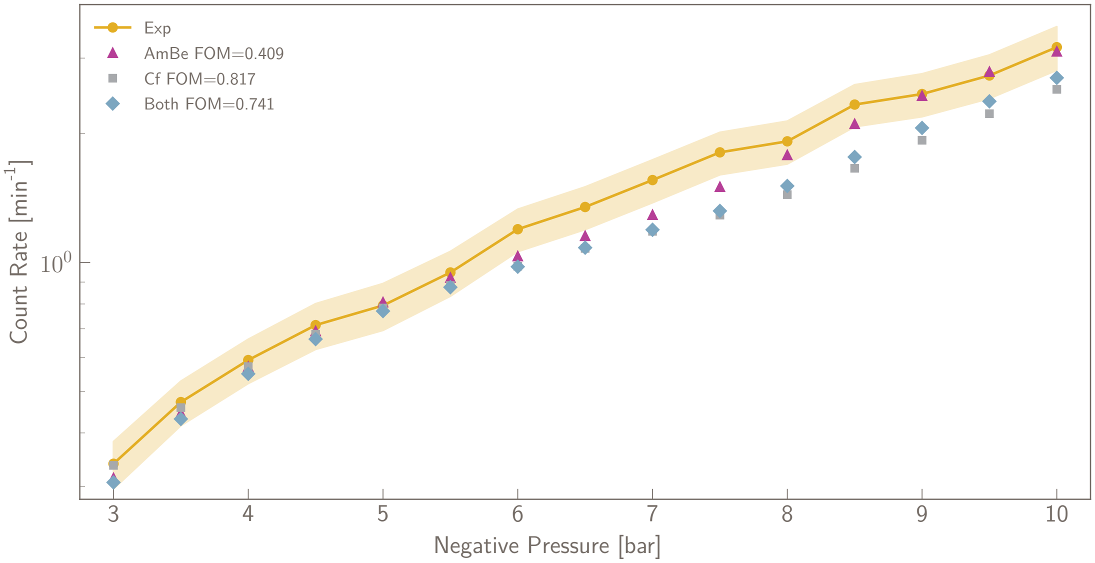

(b) ^{241}AmBe

Figure 7.3. Comparison between the experimentally measured and MCNP predicted count rates, from the CSDA model, in detector M76 at a source-to-detector distance of 300 cm. Results are shown for optimization using ^{252}Cf data only, ^{241}AmBe data only, and both data sets combined.

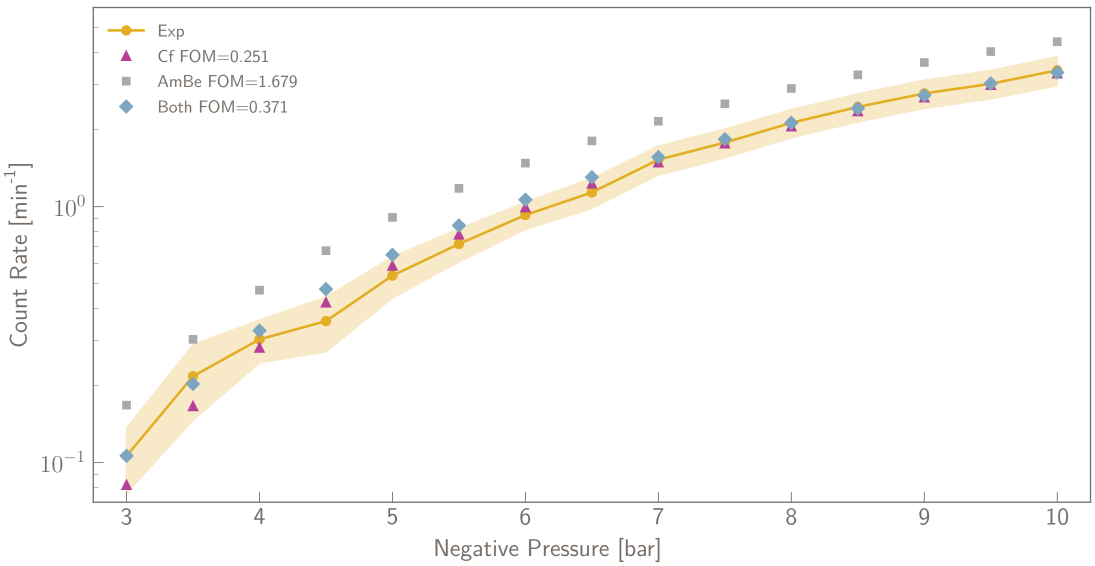

(a) ^{252}Cf

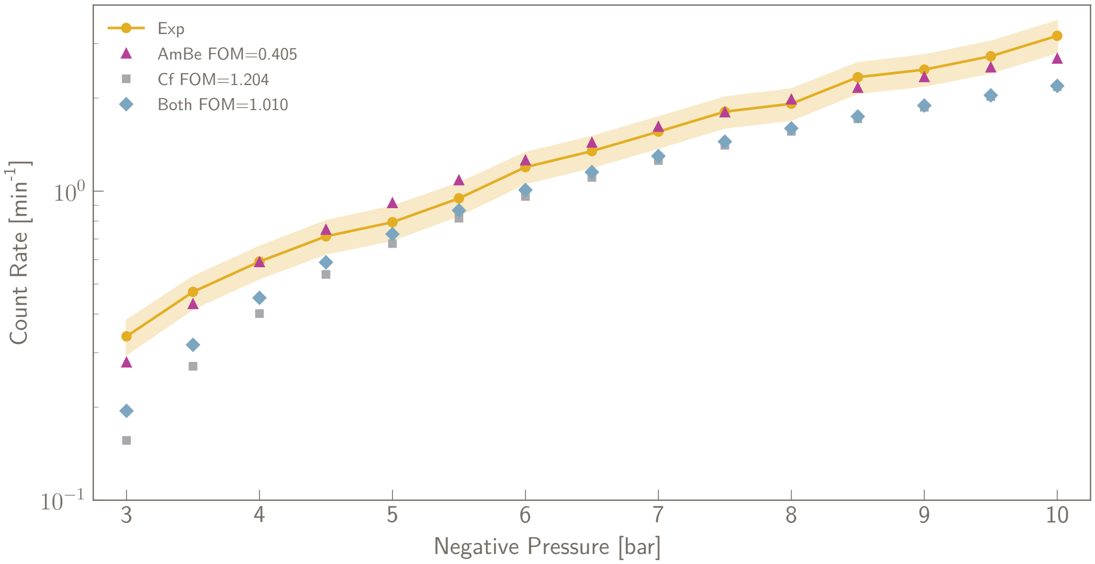

(b) ^{241}AmBe

Figure 7.4. Comparison between the experimentally measured and MCNP predicted count rates, from the probabilistic model, in detector M76 at a source-to-detector distance of 300 cm. Results are shown for optimization using ^{252}Cf data only, ^{241}AmBe data only, and both data sets combined.

Table 7.1. Optimized A,N coefficients for detector M76 at a source-to-detector distance of 300cm.

Source	**A Coeff.**	**N Coeff.**
	CSDA	
Cf	515	-1.62
AmBe	570	-1.70
Both	550	-1.66
	Probabilistic	
Cf	725	-1.80
AmBe	640	-1.80
Both	665	-1.76

in the predictions here will translate to inaccuracy in the detector's response matrix and subsequently propagate to the unfolded spectra.

A point worth noting is the lack of interchangeability between the coefficients that were optimized exclusively with ^{252}Cf or ^{241}AmBe data. Significant discrepancies arise between predictions and experiment from applying the coefficients that best predict the ^{241}AmBe count rates to MCNPP output data simulated with a ^{252}Cf source. This trend will be observed in all of the data presented throughout the remainder of this chapter and perfectly illustrates the pitfalls of over-fitting the solution to the training data. The accuracy of this model should thereby be judged based on the use of the coefficients optimized for both sources.

The accuracy of the coefficients resulting from optimization with data from both sources is disproportionately skewed towards ^{252}Cf. These coefficients consistently under-predict the ^{241}AmBe count rates in both the CSDA and probabilistic models. The same bias between experiment and MCNP predictions noted for the BSS system in section 4.3 is also present in the TMFD data. Recall, an ^{241}AmBe intensity of 3.8x10^4 n/s was necessary to maintain agreement between the ^{241}AmBe and ^{252}Cf calibration factors. When assuming an ^{241}AmBe intensity of 3.8e5 n/s in TMFD simulations, the coefficients for the "both" optimized case produce excellent agreement between experiment and simulation, with no apparent bias towards either source. Despite observing this trend in two detector systems with fundamentally different detection principles, assuming an intensity that is 20% higher than the theoretical maximum yield for a 10 mCi source is not justifiable. The question of intensity will be further addressed at the end of this chapter.

To better illustrate the trends in the predicted versus experimental count rates, the percent difference of the predicted count rate at each pressure is plotted in fig. 7.5. For the CSDA model, the predictions are within ±20% up to 6.0 bar, though after 5.0 bar the error drops sharply from +20% to -20%. While the error in the ^{241}AmBe data remains consistently low, the error in the ^{252}Cf data rises sharply after 8 bar, overestimating the count rate by 30% at 10 bar. The persistent inaccuracy beginning at 5 bar makes sense based on the threshold results in chapter 6. The CSDA model cannot account for the added energy straggling seen with lower neutron energies. On the contrary, the probabilistic detection model excels at pressures above 5.0 bar.

Though the coefficients used in fig. 7.5 do produce the lowest FOM, the FOM does not converge sharply to a distinct minimum. Coefficients which produce accurate predictions for the lower pressures do so at the expense of accuracy at higher pressures. As such, there is a wide range of values which yield reasonably accurate predictions. This ambiguity is illustrated by the heat maps in fig. 7.6. While the optimal FOM is more localized in the CSDA model, the probabilistic model is more accurate overall. That is, the optimal FOM for the CSDA model is notably larger than the optimal FOM for the probabilistic model. The conclusion that was eventually drawn from analysis of this dataset is that a single set of A,N coefficients is insufficient to accurately predict the CTMFD's count rates over the entire range. This conclusion led to the development of the multiple detector system.

7.3 Optimization of a Multiple-Detector System

A system containing multiple detectors was developed to address the difficulties encountered with the single detector system. The additional detectors were designed to have lower detection efficiencies (smaller fluid volumes), thereby allowing the system to operate in much higher fluence fields. The underlying idea behind the concept was that each detector would be calibrated for a select range of pressures. The most efficient (largest volume) detector

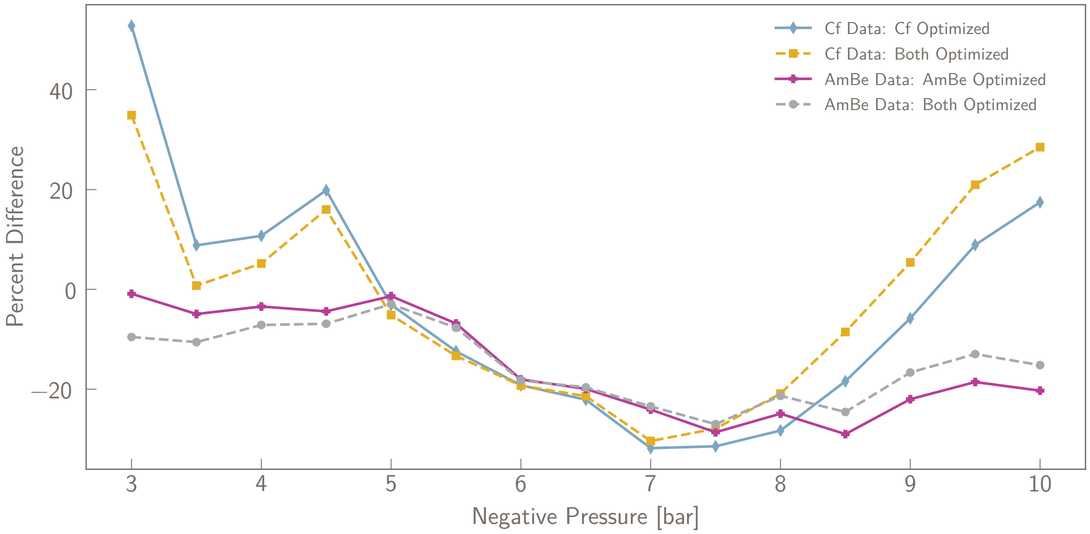

(a) CSDA

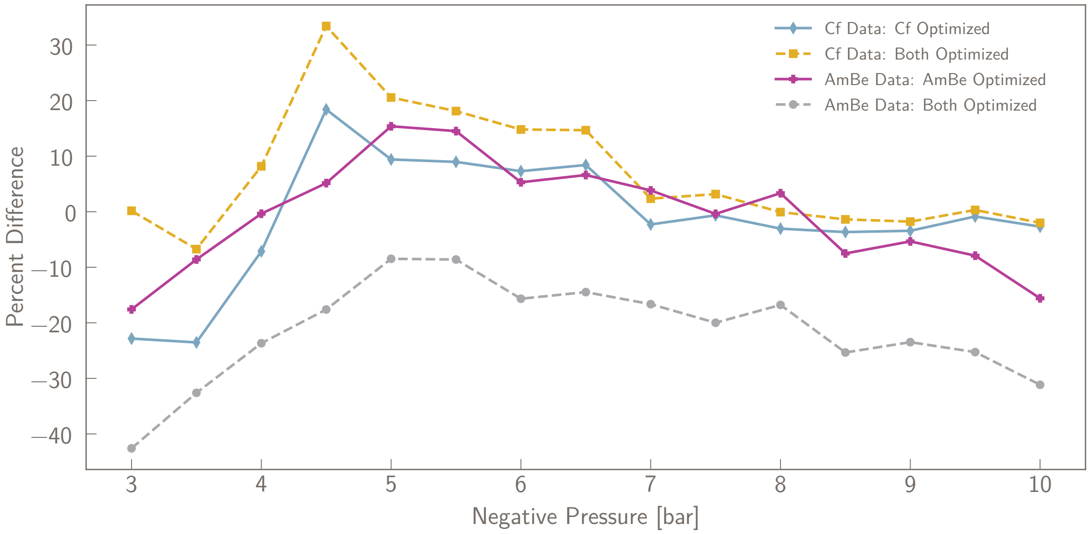

(b) Probabilistic

Figure 7.5. Comparison of the percent difference between the MCNP predicted count rate and the experimental count rate from using the CSDA versus probabilistic detection probability models.

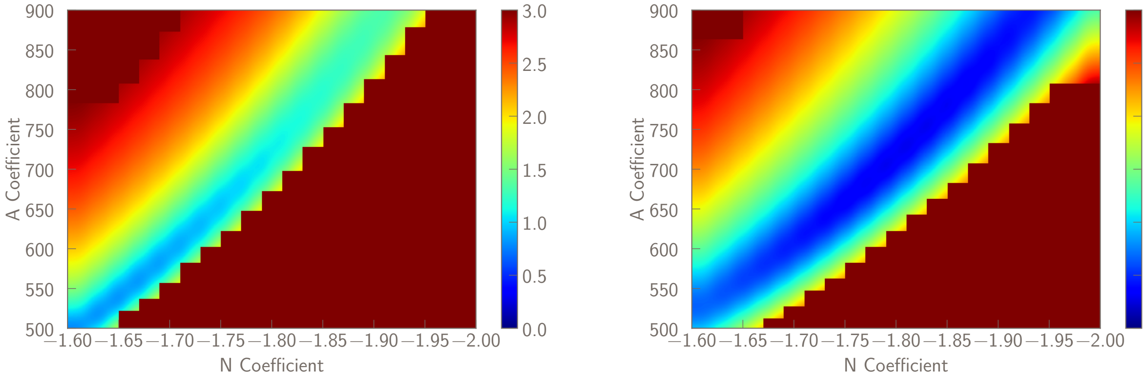

(a) Cf CSDA (b) Cf Probabilistic

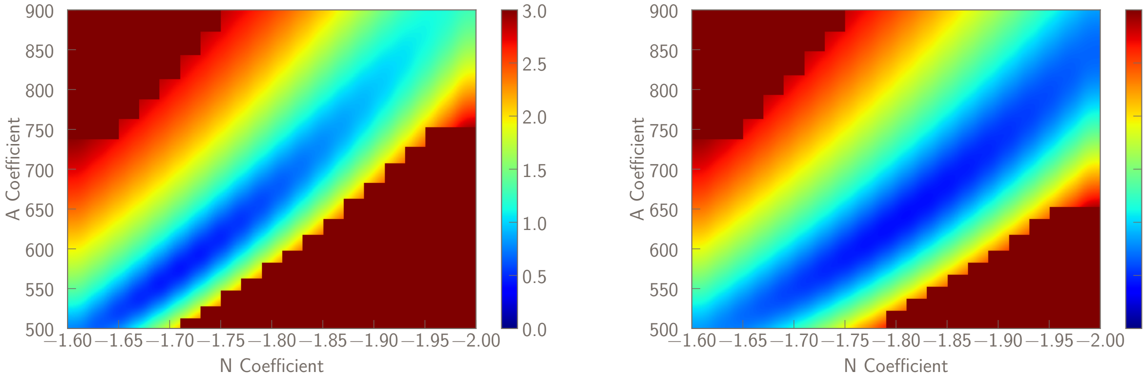

(c) AmBe CSDA (d) AmBe Probabilistic

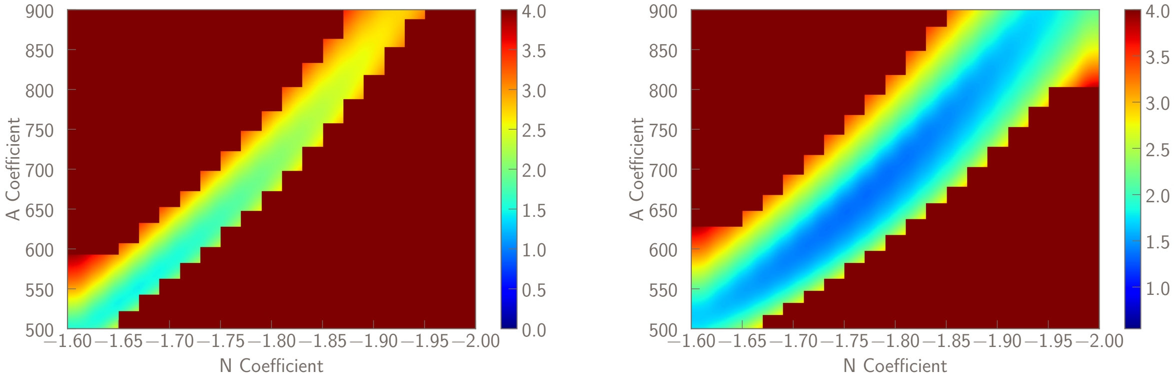

(e) Both CSDA (f) Both Probabilistic

Figure 7.6. Parametric surface of the figure of merit for detector M76 at a distance of 300 cm. The color map scale has been truncated to better accentuate the wide band of solutions with a corresponding low FOM.

would operate at low pressures, e.g. 4 bar and below, while the least efficient (smallest volume) system would operate at higher pressures, e.g. 7-10 bar. A third detector, with an intermediate efficiency, would be responsible for the 4-6 bar range. The fourth detector was included to enable sensitivity to thermal and epithermal neutrons. More information about thermal sensitivity will be discussed in later chapters.

A rendering of the multi-detector system is shown in fig. 7.7. When using multiple detectors to unfold a spectrum, it is required that zero spatial or intensity gradient exists between the different detectors. This requirement is somewhat problematic for this proof-of-concept design due to the different detector heights. For the time being, the position of the source was placed as close as possible to the geometric center of the four detector locations. To reduce the amount of flux asymmetry introduced from neutron scattering in the floor, the detector panel was elevated such that the bottom detector row was approximately 160 cm off the floor.

Figure 7.7. Rendering of the multiple detector system.

Despite taking all available precautions to ensure symmetry in the flux spectrum across the panel, one of the main concerns with adopting a multi-detector approach was whether the DETC curve optimized for one unit would translate to another unit of a different volume. The amount of energy deposition necessary to create a stable vapor cavity is a property of the detection fluid itself and therefore should be independent of the dimensions (volume) of the detector apparatus itself. That is, neglecting 3-D fluid structure interaction induced variability in the realized negative pressure. The coefficients that minimize the FOM in the high efficiency CTMFD should also minimize the FOM in the low efficiency CTMFD. Additionally, the optimized coefficients should be mostly independent of perturbations in the spectrum shape, for example, as the result of increasing the source-to-detector distance. These expectations are, however, theoretical in nature and depend on how representative the simulation model is of the underlying physics that govern the detector's behavior.

The data presented in the subsections below will show that the ideal behavior was not observed in practice. Count rate measurements were taken at multiple distances with both the ^{252}Cf and ^{241}AmBe sources. The resultant optimization analyses found a unique set of A,N coefficients for each distance. The question then arises: how accurate would the coefficients optimized for one distance (e.g. 50 cm) predict the experimental count rates from a dataset at another distance (e.g. 100 cm)? An estimate of the associated error is provided by plotting the count rates predicted by each set of optimized coefficients (for every distance) against experimental measurements.

7.3.1 16cm^3 CTMFD Results

The 16cm^3 detector "M76", used in the single detector system described in the previous section, was adapted to the multi-detector system. Experiments were run at source-to-detector distances of 50, 100, and 200 cm. The A,N coefficients, optimized with data from both sources, for each distance are tabulated in table 7.2 as a function of the cut factor applied to the detection probability distribution. The comparison between the predicted and experimental count rates are shown in figs. 7.8 to 7.10.

The data in table 7.2 table indicates the FOM is improved by applying a cut factor to the detection probability distribution, reaching a minimum with a cut factor of 0.2. This concept was introduced in section 6.5.1 as a mechanism to preserve threshold behavior in the probabilistic model. A physics-based explanation of why the high-energy (transfer) collisions, responsible for the tail of the detection probability curve, do not create a stable vapor cavity is unavailable. However, it's existence is merited from an empirical stand point by the substantial improvements in the probabilistic model's predictions for the count rate as well as the neutron thresholds.

In general, the coefficients representing the DETC reproduce the the count rates for the dataset (distance) they were optimized to very well. Discrepancies are observed in the 100 and 200 cm datasets below 3.0 bar, but not in the 50 cm dataset. In all cases, the simulated count rates are higher than those seen in experiment. The probabilistic model's persistent inability to accurately predict the count rates at low pressures is a trend that should be investigated further.

The amount of error introduced by using A,N coefficients optimized for a different distance can partially be explained by the different pressure ranges in each dataset. For example, the highest pressure in the 50 cm dataset was 4.0 bar for ^{252}Cf and 2.75 bar for ^{241}AmBe, whereas the 200 cm dataset contains data up to 7.5 bar from both sources. Thus, it is expected that the 50 cm coefficients will be inaccurate for pressures outside of the calibration range. The 100 cm dataset contains many pressures that overlap the pressure ranges of the 50 and 200 cm datasets. As a consequence, the amount of error incurred from using the 100 cm coefficients to predict the count rates at other distances is in the range of 10-15%. For a ^{252}Cf spectrum, this is an acceptable margin of error. However, the penalty incurred for a ^{241}AmBe spectrum is outside the typical 20% error margin because the error is compounded with the under-prediction bias persistent throughout all of the ^{241}AmBe measurements in this work.

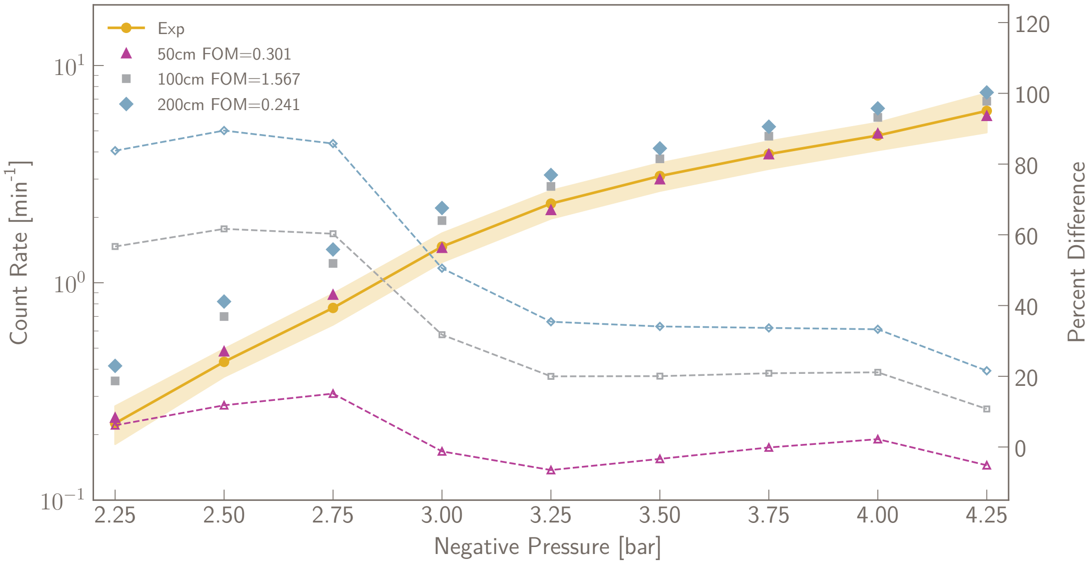

(a) ^{252}Cf 50 cm, probabilistic model

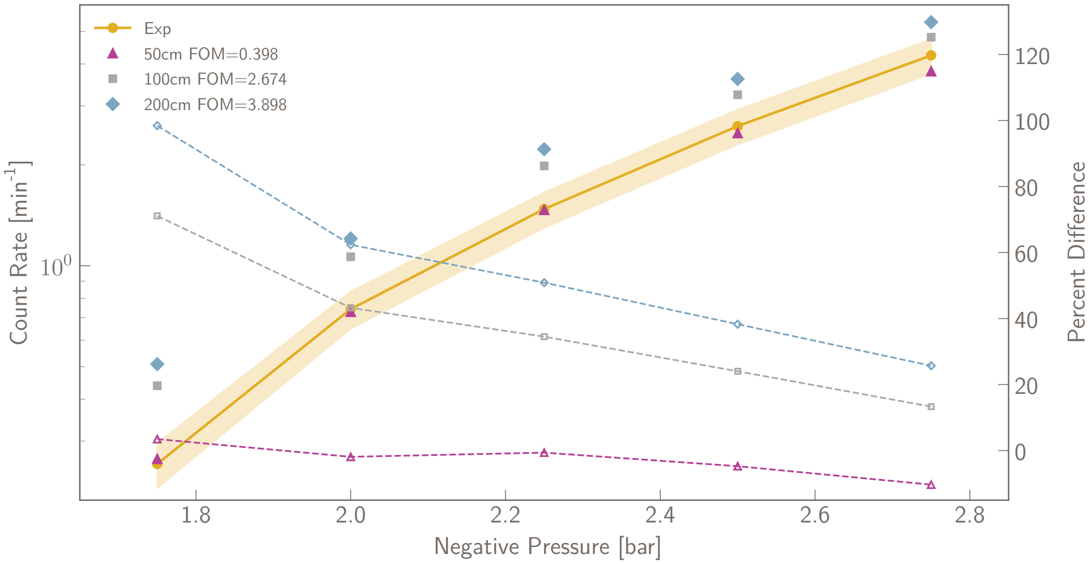

(b) ^{241}AmBe 50 cm, probabilistic model

Figure 7.8. Comparison between the experimentally measured and MCNPP predicted count rates in detector M76 at a source-to-detector distance of 50 cm. Count rate estimates are made using the probabilistic model with a 20% cut factor applied to the detection probability distribution. Predictions resulting from the use of coefficients optimized to the 100 cm and 200 cm datasets are also included for comparison. The dashed lines represent the percent difference between experiment and simulation.

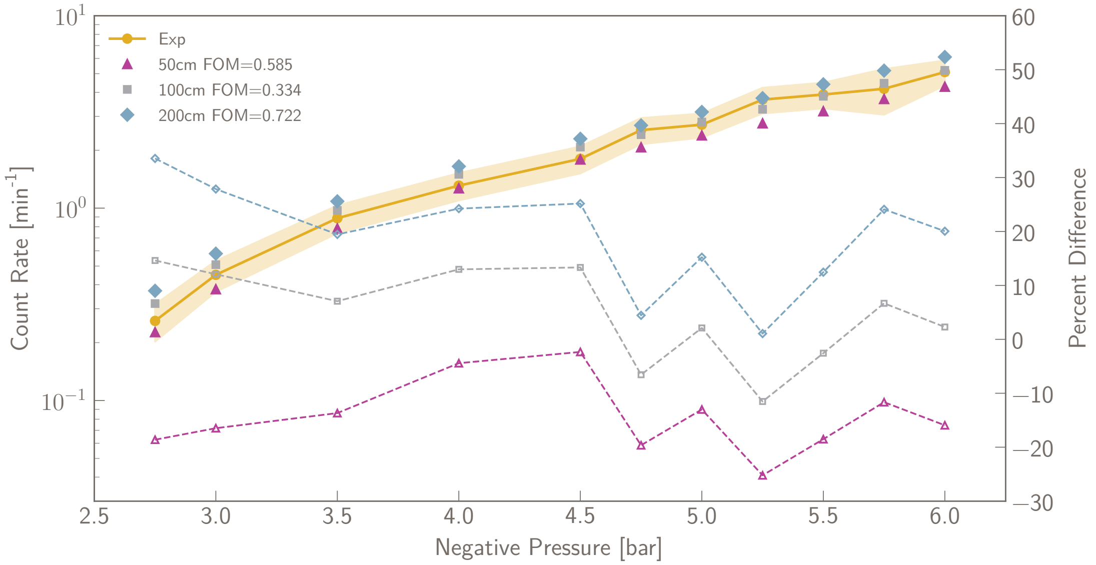

(a) ^{252}Cf 100 cm, probabilistic model

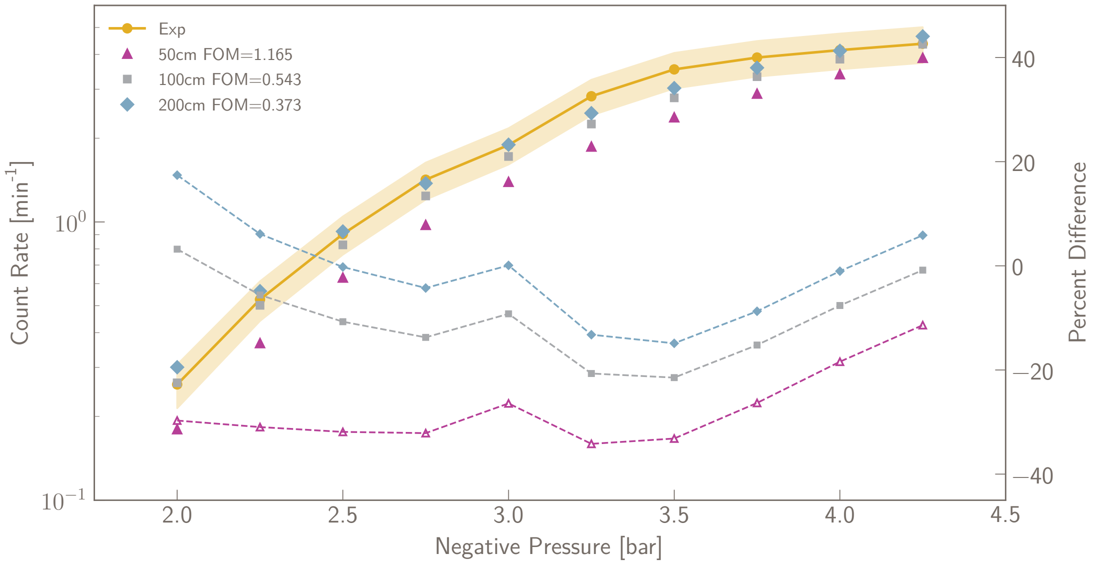

(b) ^{241}AmBe 100 cm, probabilistic model

Figure 7.9. Comparison between the experimentally measured and MCNPP predicted count rates in detector M76 at a source-to-detector distance of 100 cm. Count rate estimates are made using the probabilistic model with a 20% cut factor applied to the detection probability distribution. Predictions resulting from the use of coefficients optimized to the 50 cm and 200 cm datasets are also included for comparison. The dashed lines represent the percent difference between experiment and simulation.

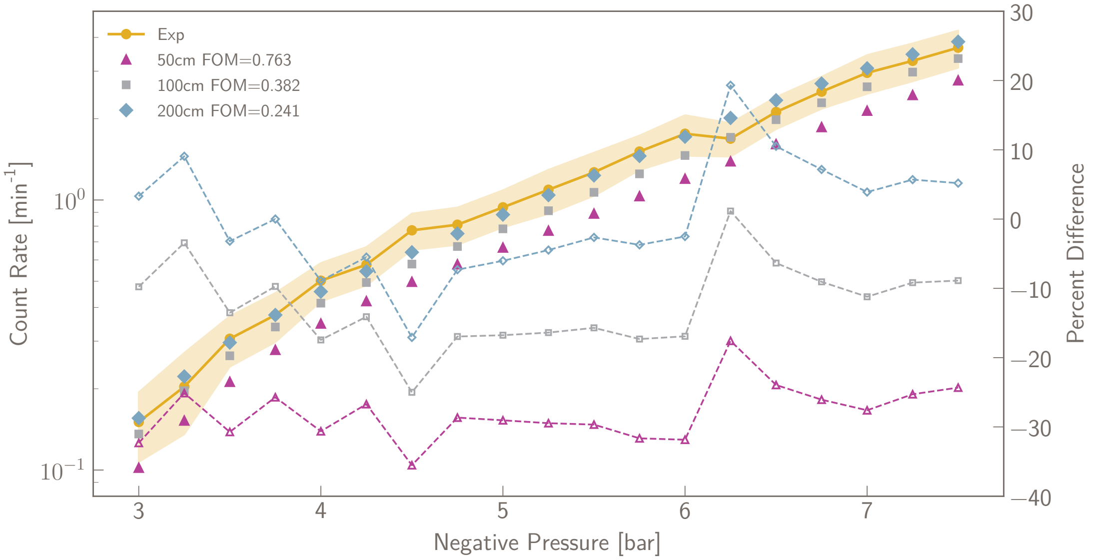

(a) ^{252}Cf 200 cm, probabilistic model

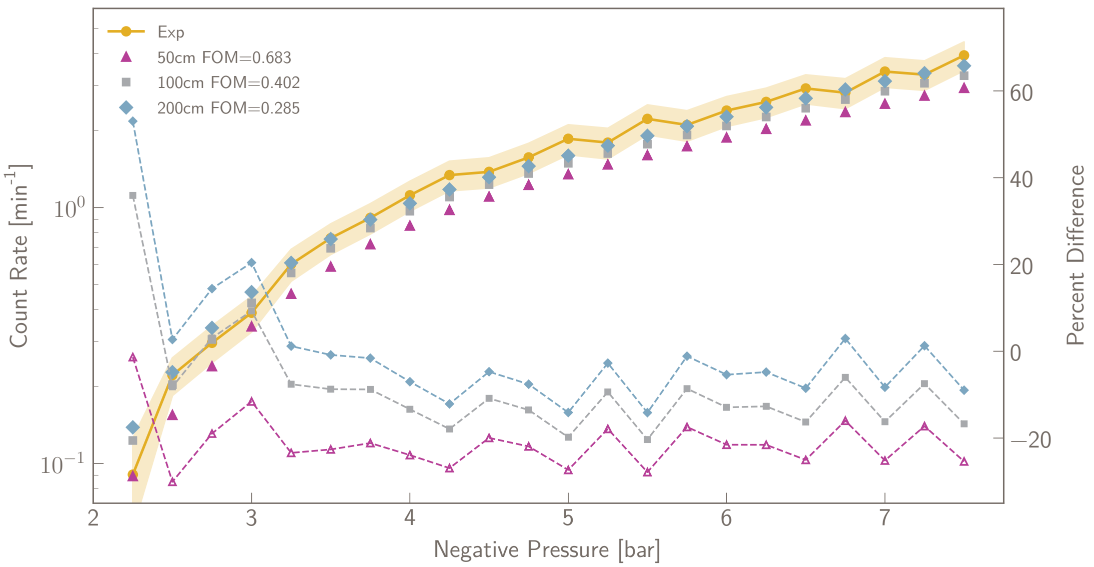

(b) ^{241}AmBe 200 cm, probabilistic model

Figure 7.10. Comparison between the experimentally measured and MCNPP predicted count rates in detector M76 at a source-to-detector distance of 200 cm. Count rate estimates are made using the probabilistic model with a 20% cut factor applied to the detection probability distribution. Predictions resulting from the use of coefficients optimized to the 50 cm and 100 cm datasets are also included for comparison. The dashed lines represent the percent difference between experiment and simulation

Table 7.2. Optimal A,N coefficients for detector “M76” as a function of cut value and source-to-detector distance.

Distance [cm]		50			100			200		
Cf Press [bar]		2.25-4.0			2.75-6.0			3.0-7.0		
AmBe Press [bar]		1.75-2.75			2.0-4.25			2.25-7.5		
Cut	Source	A	N	FOM	A	N	FOM	A	N	FOM
0.00	Cf	910	-1.94	0.489	705	-1.74	0.281	750	-1.82	0.230
	AmBe	860	-1.98	0.515	745	-1.88	0.368	740	-1.86	0.181
	Both	745	-1.78	0.873	620	-1.66	0.550	710	-1.80	0.258
0.10	Cf	760	-1.86	0.263	665	-1.76	0.214	600	-1.72	0.222
	AmBe	755	-1.88	0.177	720	-1.88	0.318	715	-1.86	0.214
	Both	710	-1.80	0.276	640	-1.74	0.349	655	-1.78	0.209
0.15	Cf	755	-1.86	0.242	705	-1.82	0.223	620	-1.76	0.218
	AmBe	740	-1.86	0.177	730	-1.90	0.292	725	-1.88	0.217
	Both	720	-1.82	0.263	660	-1.78	0.320	660	-1.80	0.197
0.20	Cf	750	-1.86	0.213	730	-1.82	0.223	645	-1.80	0.209
	AmBe	750	-1.88	0.181	740	-1.92	0.292	740	-1.90	0.216
	Both	715	-1.82	0.240	685	-1.82	0.316	685	-1.84	0.182

7.3.2 1 cm^3 CTMFD Results

The theoretical intent behind the incorporation of an intermediate size into the multi-CTMFD system was that it could serve as a utility detector. In the case of a low fluence field, the data acquisition time for the smallest volume CTMFD could grow unreasonably long on account of its very low efficiency, in which case its role of recording count rates at high pressures (8-10 bar) would be replaced by the intermediate size. Conversely, for a high fluence field with the potential to saturate the large volume CTMFD, the intermediate size would assume responsibility for recording count rates at the low pressures. Reducing the range of pressures that each volume is responsible for also has the added benefit of decreasing the data acquisition time. However, the degree of flexibility for the intermediate size is contingent on the ability to accurately model the response across the full range of pressures.

A schematic of the dimensions of the intermediate volume CTMFD used in the multi-detector system is shown in fig. 7.11. To maintain compatibility with the motor housing, and all of the associated engineering that went into properly balancing the system, the cross-sectional form factor of the CTMFD was kept consistent with that of the 16cm^3. Reducing the neutron detection efficiency was accomplished by decreasing the size of the central volume, which is composed of the same diameter (10.0 mm OD, 5.6 mm ID) tubing used in the "arms". With these dimensions, the volume of the central region is about 1 cm^3.

Experiments were run at source-to-detector distances of 50, and 100 cm. Since the detector was able to reach 10 bar in the 100 cm dataset, a 200 cm dataset was deemed unnecessary on account of the large time requirement for data acquisition at such low count rates. The A,N coefficients are tabulated in table 7.2 and the comparisons between the predicted and experimental count rates are shown in figs. 7.8 to 7.10. All coefficients were optimized with a 20% cut applied to the detection probability curve as it was again found to minimize the FOM.

The ability to reproduce the count rates under identical conditions was found to be somewhat challenging for this detector. Multiple datasets were discarded on account of erroneous results. Steady loss of the vacuum seal on the detector and subsequent evaporation

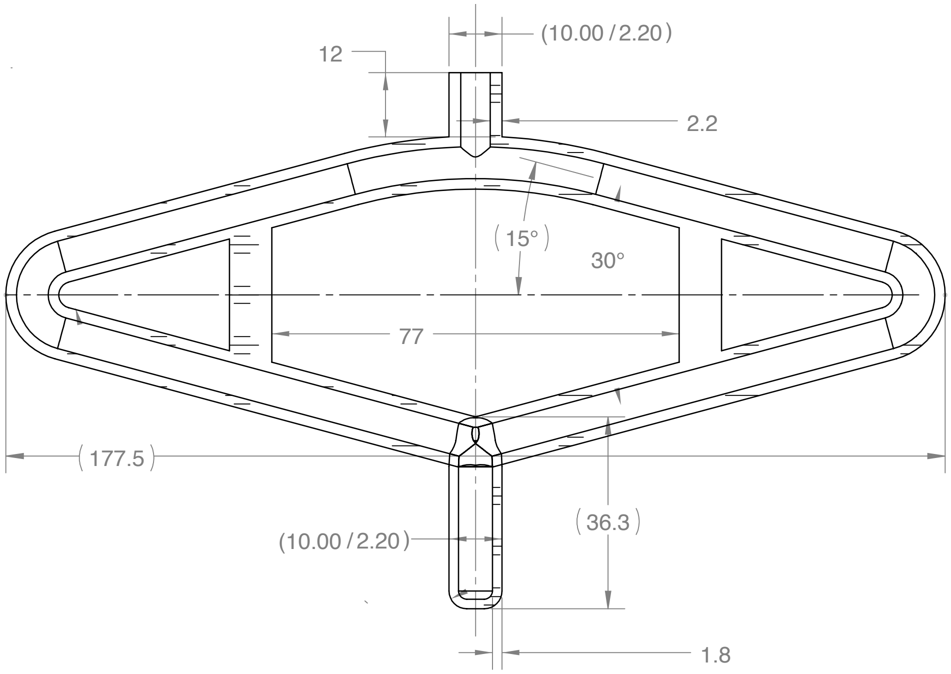

Figure 7.11. Dimensions of the 1 cm^3 CTMFD, "T3".

Table 7.3. Optimal A,N coefficients for detector "T3" as a of function source-to-detector distance.

Distance [cm]		50			100		
Cf Press [bar]		4.0-7.5			4.0-10.0		
AmBe Press [bar]		4.0-6.0			4.0-9.0		
			CSDA				
	Source	A	N	FOM	A	N	FOM
	Cf	530	-1.66	0.683	505	-1.64	0.951
	AmBe	595	-1.78	0.394	585	-1.78	0.736
	Both	510	-1.64	0.525	515	-1.66	0.771
			Probabilistic				
Cut	Source	A	N	FOM	A	N	FOM
	Cf	620	-1.76	0.345	870	-1.98	0.948
0.20	AmBe	510	-1.70	0.446	735	-1.98	0.439
	Both	520	-1.66	0.491	780	-1.94	0.897

of the detection fluid , was responsible for a large fraction of this error. The smaller volume designs were not investigated until the very end of this work and thus sufficient time was

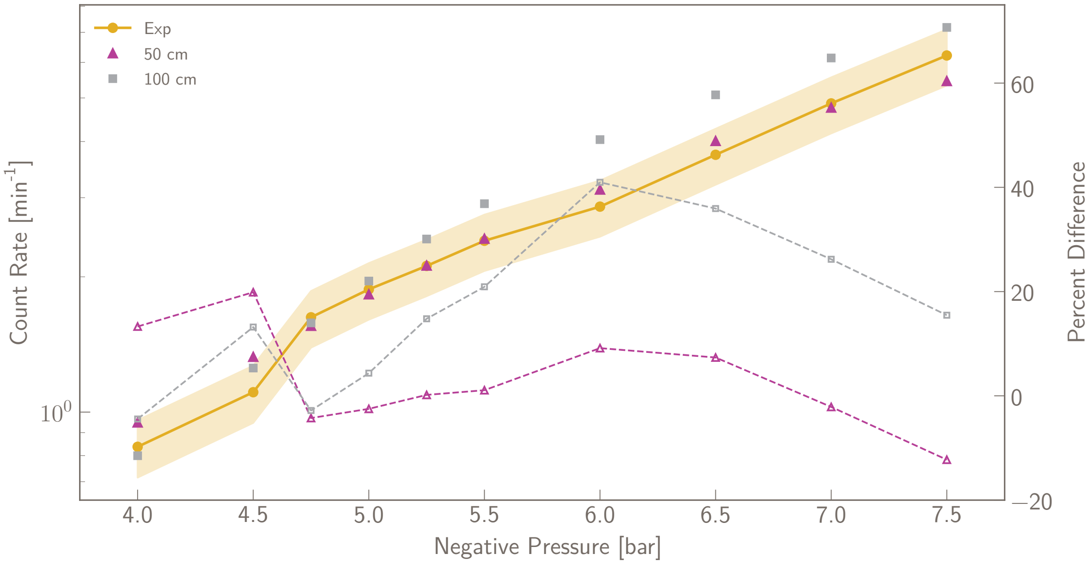

(a) ^{252}Cf 50 cm, probabilistic model

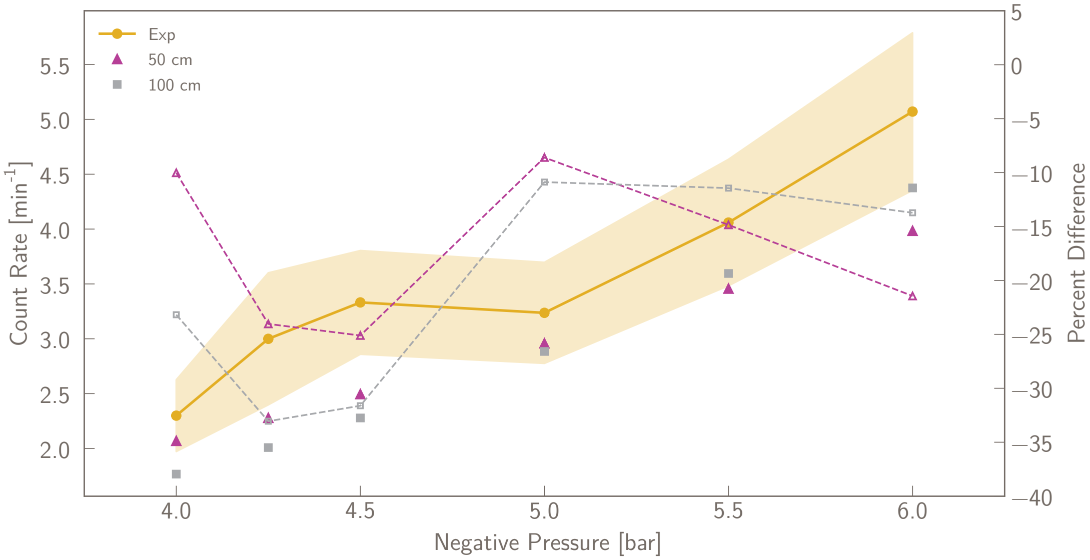

(b) ^{241}AmBe 50 cm, probabilistic model

Figure 7.12. Comparison between the experimentally measured and MCNPP predicted count rates in detector T3 at a source-to-detector distance of 50 cm. Count rate estimates are made using the probabilistic model with a 20% cut factor applied to the detection probability distribution. Predictions resulting from the use of coefficients optimized to the 100 cm dataset are also included for comparison. The dashed lines represent the percent difference between experiment and simulation.

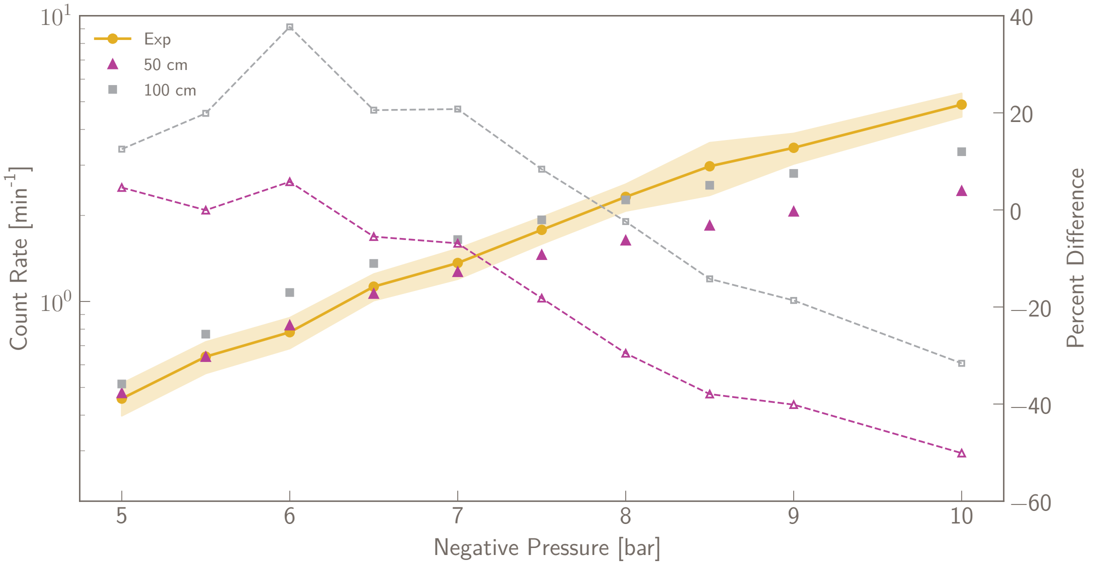

(a) ^{252}Cf 100 cm, probabilistic model

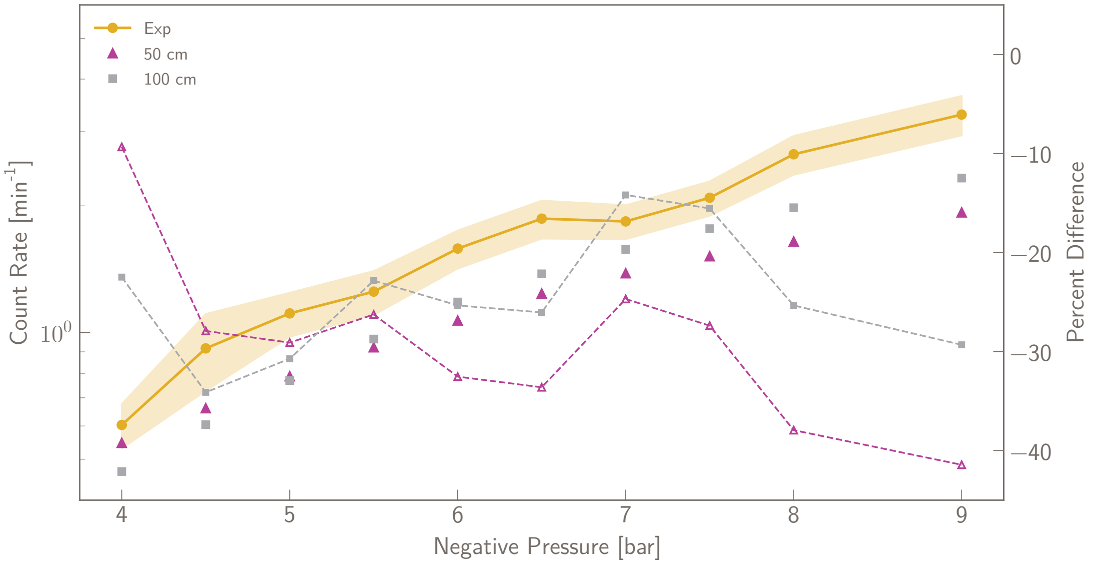

(b) ^{241}AmBe 100 cm, probabilistic model

Figure 7.13. Comparison between the experimentally measured and MCNPP predicted count rates in detector T3 at a source-to-detector distance of 100 cm. Count rate estimates are made using the probabilistic model with a 20% cut factor applied to the detection probability distribution. Predictions resulting from the use of coefficients optimized to the 50 cm dataset are also included for comparison. The dashed lines represent the percent difference between experiment and simulation.

not available to conclusively prove that the detector's sensitivity was not being affected by external mechanical factors. Alternatively, it is also possible that some of the fluctuations in the count rate curves are entirely statistical in nature.

Regardless of which detection probability model is used, the count rate predictions for the T3 detector are less accurate than those for the larger volume detector, M76. For M76, significant error in the count rate predictions arose only when applying A,N coefficients that were optimized to a dataset at a different distance. In contrast, the only T3 dataset that had a prediction error within the typical 20% margin was ^{252}Cf at 50 cm. The negative bias in the predicted count rates for the ^{241}AmBe source is amplified in the T3 results, particularly in the 100 cm dataset, where the percent difference oscillates between -20 and -30%.

The prediction accuracy in the 100 cm dataset is uncomfortably problematic, even for the ^{252}Cf spectrum. The slope of the percent difference line in fig. 7.13a is unusual considering good agreement was found with all ^{252}Cf measurements taken in detector M76. The predictions overestimate the count rate by 20% at pressures below 7 bar. After which, the slope of the predicted rates begin to plateau faster rate than the experimental rates, under-predicting by 30% at 10 bar. The 50 cm coefficients, surprisingly, produce better results up to 7.0 bar. It is not understood why these trends are present in T3 but not M76.

7.3.3 0.4 cm^3 CTMFD Results

A schematic of the dimensions of the smallest volume CTMFD used in the multi-detector system is shown in fig. 7.14. Similar to T3, the central volume is made from the same diameter glass capillary tubing as the central volume. With an inner diameter of only 2 mm, this design represents the minimum neutron detection efficiency achievable without altering the cross-sectional form factor of the glass apparatus. Further reducing the inner diameter would cause the vapor bubble generated from a detection event to remain trapped in the central volume, unable to overcome the increased capillary forces. As it is now, the rate of data acquisition is severely limited by the amount of time required for the vapor bubble to travel up the arm tubing. This time delay is approximately 45 seconds for T1, compared to only 3 seconds for the larger diameter tubing used in M76 and T3. However, field practicality was not the primary motivation behind the capillary design. The T1 design was made as a proof-of-concept to establish an upper-bound estimate for the maximum dose rate that a TMFD spectrometer could operate in before saturating.

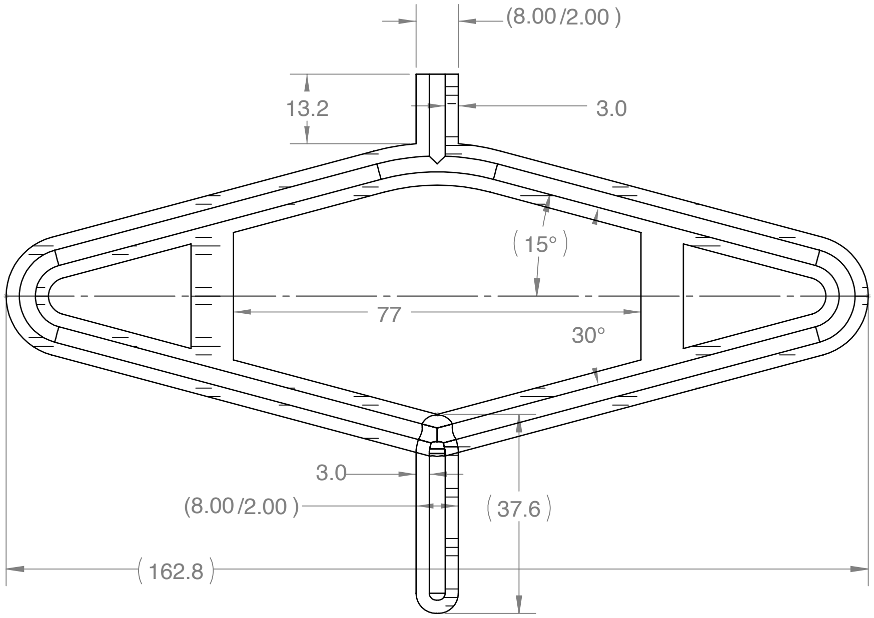

Figure 7.14. Dimensions of the 0.4 cm^3 CTMFD, "T1".

Complications regarding the detector's ability to hold a vacuum seal required an update to the design. A seal is typically maintained by compressing a rubber stopper into the upper spout tubing. However, the diameter of the top spout was found to be too narrow to achieve the amount of compression necessary for an air-tight seal. Loss of the vacuum seal is critically problematic in a capillary design. The small tubing diameter amplifies the effects (on the negative pressure profile) of evaporation of the detection fluid as a result of the corresponding change in the fluid radius (eq. (2.1)). The capillary design was eventually updated to replace the top spout with the same diameter tubing used in the M76 design, which solved the loss of vacuum issue. However, sufficient time was not available to retake all of the experimental data necessary to re-calibrate the A,N coefficients.

The comparison between the predicted and experimental count rates is shown in fig. 7.15. The percent error is within the 20% acceptable margin of error. While the good agreement appears encouraging, the large uncertainty in the accuracy of the experimental count rates means the optimized A,N coefficients likely will not translate to the new T1 design. It is expected that a similarly good agreement will be possible once new experimental calibration data is available.

Table 7.4. Optimal A,N coefficients for detector "T1".

Distance [cm]	50
Cf Press [bar]	6.5-11.0
AmBe Press [bar]	6.0-11.0

CSDA

Source	A	N	FOM
Cf	500	-1.54	1.523
AmBe	505	-1.56	0.790
Both	500	-1.54	0.897

Probabilistic

Cut	Source	A	N	FOM
0.20	Cf	500	-1.58	0.231
	AmBe	700	-1.78	0.285
	Both	515	-1.60	0.371

7.4 Discussion on the Relevancy of the Cut Factor

One potential reason behind the discrepancy is that the true DETC curve is not actually a power law, but some other functional form that closely resembles a power law. This trend seen below the 3-4 bar range implies that the slope of the physical DETC curve is increasing faster than what is represented by the optimized A,N coefficients. The more likely hypothesis, however, is that the cut factor is the dominant source of error.

Recall, from the discussion on SDD literature in section 5.7, that the criteria for an ion nucleating a stable vapor cavity is determined by whether or not the CSDA average energy deposition, E_{dep}, exceeds the energy threshold E_{th}. If true, the probability of detection is calculated using the sigmoidal shape function given by eq. (5.9), which goes to zero when E_{dep}=E_{th}. This behavior is what the cut factor is attempting to reproduce. Without a cut factor, the only way the probabilistic model will return a detection probability of zero is if

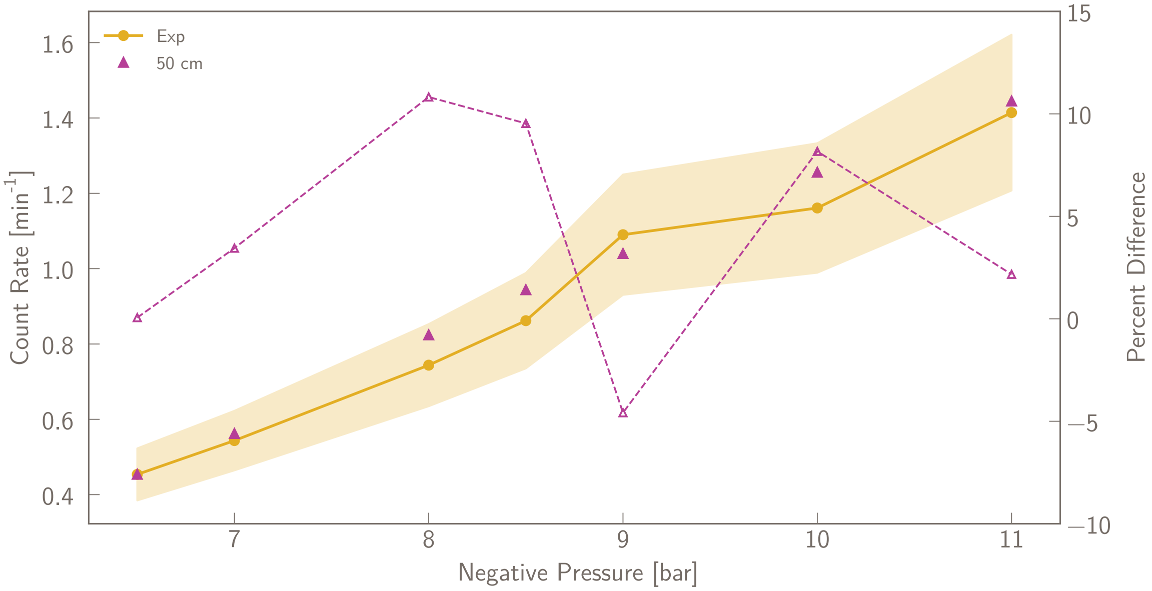

(a) ^{252}Cf 50 cm, probabilistic model

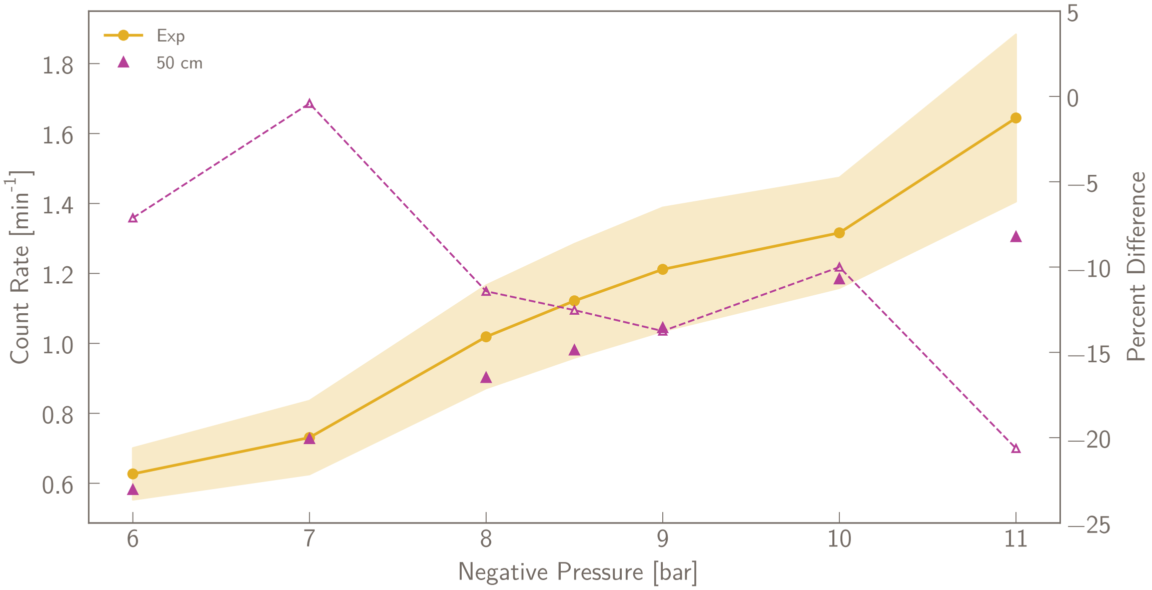

(b) ^{241}AmBe 50 cm, probabilistic model

Figure 7.15. Comparison between the experimentally measured and MCNPP predicted count rates in detector T1 at a source-to-detector distance of 50 cm. Count rate estimates are made using the probabilistic model with a 20% cut factor applied to the detection probability distribution. The dashed lines represent the percent difference between experiment and simulation.

E_{th} is greater than the initial energy of the ion. Thus, it may be relevant to consider where the CSDA average energy deposition falls on the detection probability curve as a point of reference for where the cut factor should be applied.

To illustrate the potential importance of the CSDA energy deposition value, refer back to the detection probability curves (fig. 6.8) representing the pressure thresholds determined with monoenergetic neutron sources. The point on the y-axis (detection probability) at which the dashed vertical line, representing the CSDA energy deposition, intersects the probability curve varies as a function of the particular isotope, it's initial energy, and the critical diameter length. For example, consider the detection probability curves for ^{12}C. The probability when $E_{th} = E_{dep}$ is approximately 0.2 for a 1.743 MeV recoil (6.136 MeV neutron energy), rises to approximately 0.4 for a 0.718 MeV recoil (2.527 MeV neutron energy), and then begins decreasing for recoil energies below 150 keV (527 keV neutron energy). The opposite trend is seen for ^{19}F. Thus, it does not appear coincidental that a cut factor of 0.2 was found to minimize the FOM.

While SDD literature doesn't specify any dependence of the detection probability on the particular isotope, the empirically determined "a" coefficient in eq. (5.9) is reported to have a dependence on energy. Hence, it would make sense to also introduce a coarse energy dependence into the value of the cut factor. Furthermore, considering the results and discussion in section 6.5.1 regarding the relative contributions of ^{12}C versus ^{19}F to the total count rate, it also seems logical that the cut factor should be specific to each particular isotope.

7.5 Discussion on the Uncertainty in the Source Intensities

The persistent negative bias of MCNP predictions compared to experimental data for the ^{241}AmBe source was mentioned throughout this chapter as well as section 4.3. Additionally, it was mentioned in section 7.2 that better agreement between the ^{241}AmBe and ^{252}Cf predictions could be achieved by increasing the assumed intensity of the ^{241}AmBe source. However, in order to maintain consistency with the BSS results, all of the results and analysis are based on an intensity of 2.8x10^4 n/s. This section will briefly discuss what the CTMFD optimization results would look like if the FOM was used to optimize the ^{241}AmBe intensity as well.

It should be noted that the concept behind the cut factor had not been thought of by the time the decision was made to transition from a single detector system to a multi-detector system. To illustrate the logical progression of thought that led to this change, all of the single-detector data shown in section 7.2 is the result of optimization without a cut factor. After conclusion of this project and while composing this section, the single detector 300 cm data was re-optimized with a cut factor applied to see what improvements, if any, were possible. Consistent with the datasets presented in the multi-detector system results, a 20% cut factor was found to minimize the FOM for the 300 cm data.

An ^{241}AmBe intensity of 3.3x10^{4} n/s was found to minimize the FOM for the 300 cm dataset. A comparison is shown in fig. 7.16 between the count rates predicted by the coefficients optimized at the nominal intensity and the intensity-optimized coefficients. Both the ^{252}Cf and ^{241}AmBe predictions improve at the higher intensity. Recall, these coefficients are optimized using data combined from both sources to avoid overfitting to a single spectrum. As such, it is interesting to see an improvement in the ^{252}Cf prediction from an increase in ^{241}AmBe intensity. Figure 7.17 demonstrates how well the re-optimized 300 cm coefficients predict the count rates for the 100 and 200 cm datasets. The 300 cm coefficients display excellent agreement across the other data sets at pressures above 4.5 bar. A fully representative detection model should be extensible to datasets other than the training set. As such, the observed agreement provides additional evidence in support of a higher than assumed source intensity.

Table 7.5 contains data for the optimal A,N coefficient and corresponding FOM as a function of assumed ^{241}AmBe intensity for all four M76 datasets: 50, 100, 200, and 300 cm. The lowest optimal intensity corresponded to the 200 cm dataset with a value of 3.0x10^{4} n/s, while the highest optimal intensity belongs to the 100 cm dataset with a value of 3.4x10^{4} n/s. The average optimal intensity is 3.225x10^{4} n/s. Similar results are found for detector T3.

Despite the evidence from two detector archetypes pointing to an intensity higher than assumed, it does seem rather infallible that the intensity could be greater than or equal to the theoretical maximum yield for the listed activity. Nor does it make sense that the probabilistic model would exhibit an offset bias. The motivation underlying the inclusion of this section should not be construed to assume a case is being made for a different than assumed intensity. Rather, the goal is to document the trends observed in the data for future analyses. Regardless, whether it be the source intensity or the physics of the detection model, identifying the source of the model's bias is considered crucial moving forward.

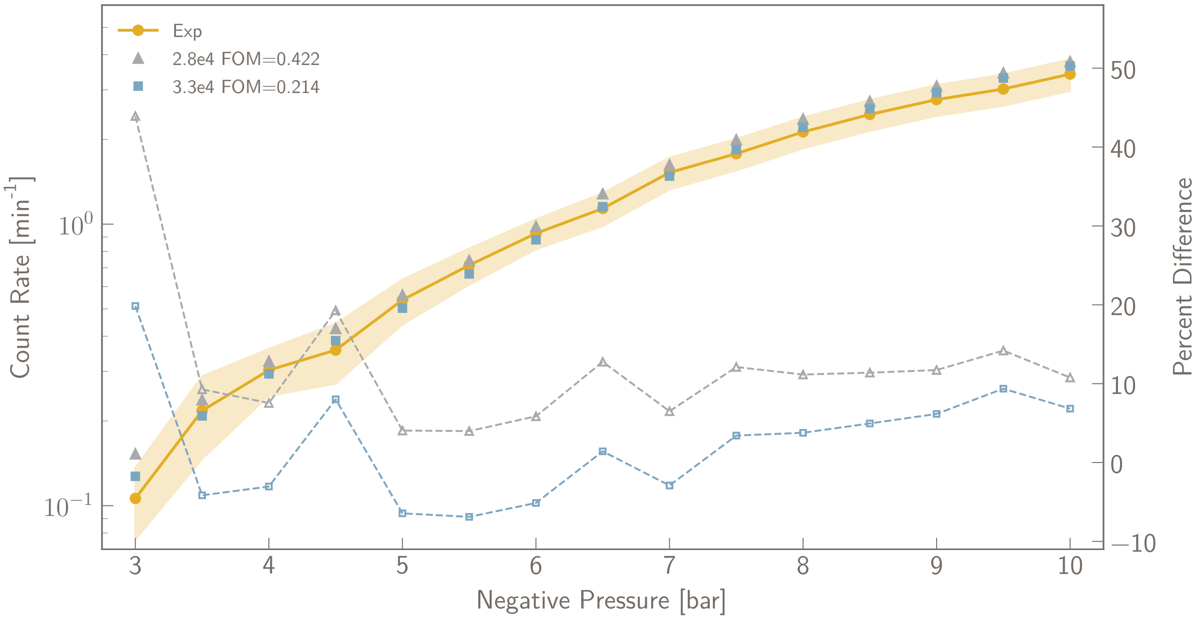

(a) ^{252}Cf

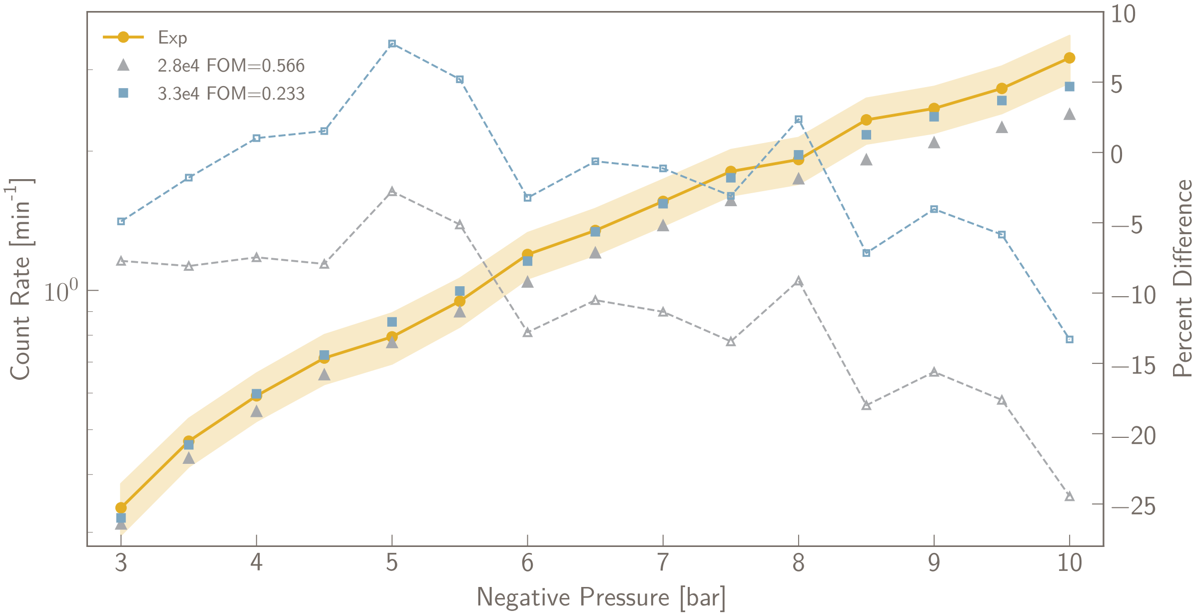

(b) ^{241}AmBe

Figure 7.16. Comparison between the experimentally measured and MCNP predicted count rates, from the probabilistic model, in detector M76 at a source-to-detector distance of 300 cm. Results are shown for optimization using ^{252}Cf data only, ^{241}AmBe data only, and both data sets combined.

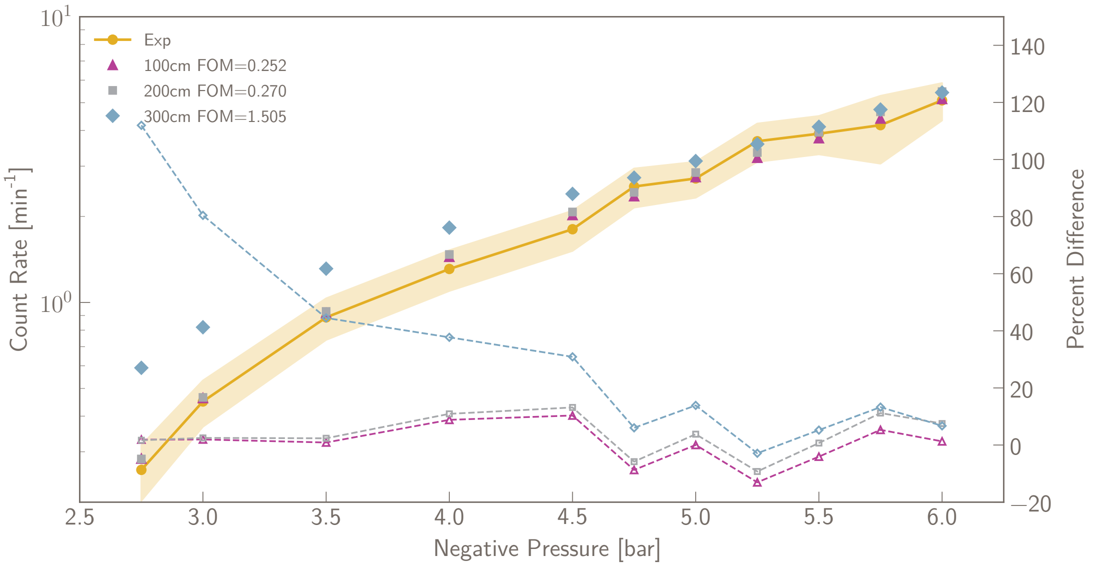

(a) ^{252}Cf 100 cm, probabilistic model

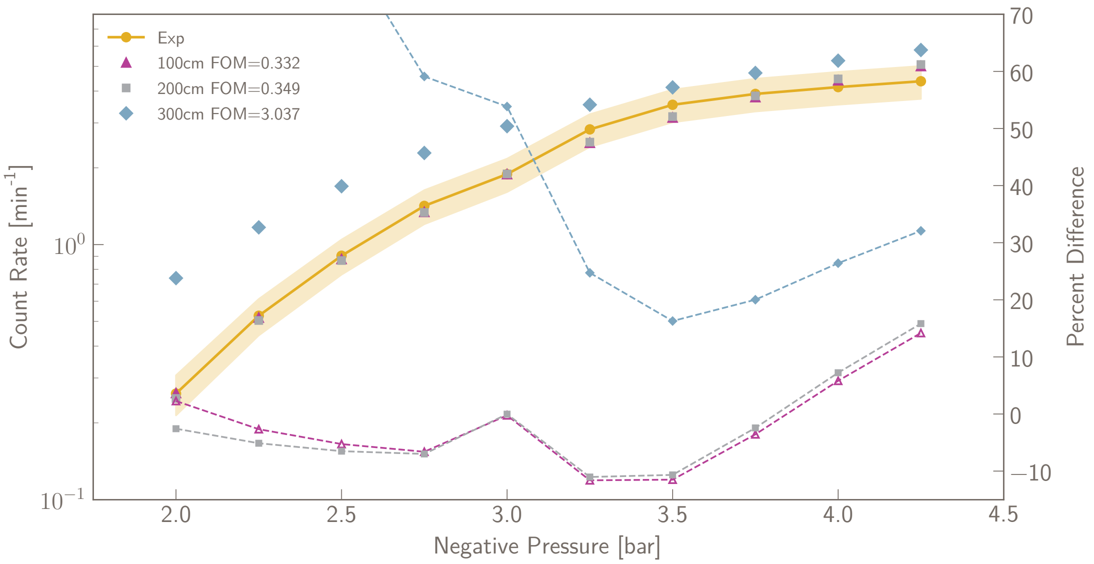

(b) ^{241}AmBe 100 cm, probabilistic model

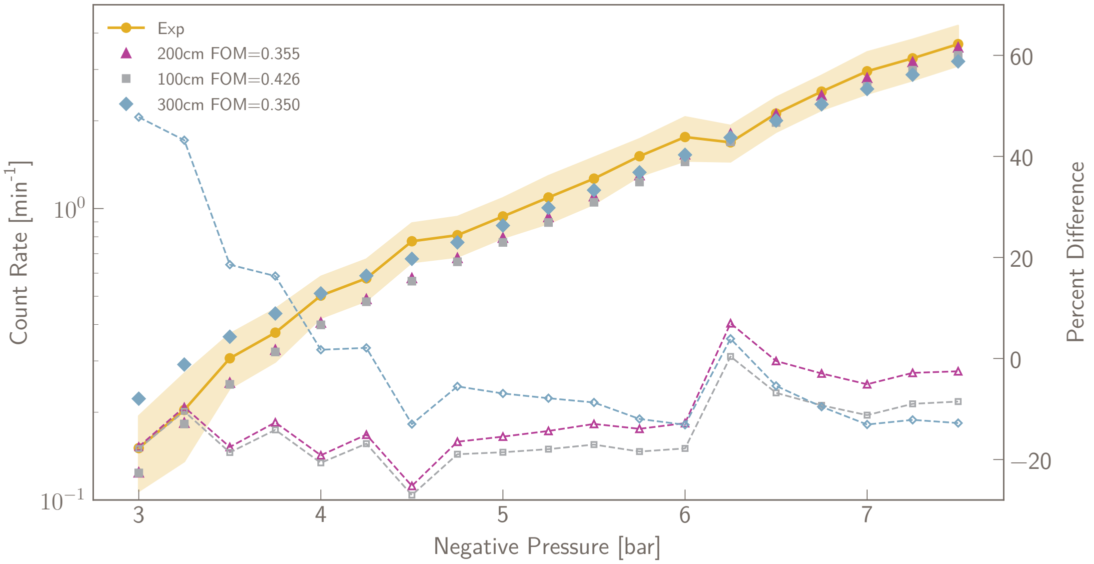

(c) ^{252}Cf 200 cm, probabilistic model

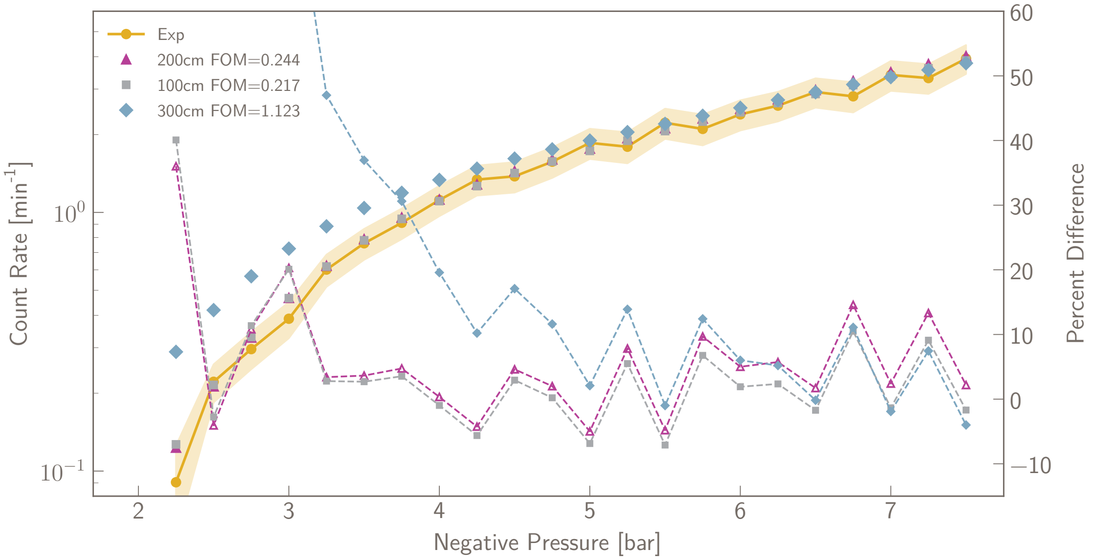

(d) ^{241}AmBe 200 cm, probabilistic model

Figure 7.17. Comparison between the experimentally measured and MCNPP predicted count rates in detector M76 at a source-to-detector distance of 200 cm. Count rate estimates are made using the probabilistic model with a 20% cut factor applied to the detection probability distribution. Predictions resulting from the use of coefficients optimized to the 50 cm and 100 cm datasets are also included for comparison. The dashed lines represent the percent difference between experiment and simulation

Table 7.5. Optimal A,N coefficients for detector “M76” as a function of cut value and source-to-detector distance.

Distance [cm]	50			100			200			300		
Intensity	A	N	FOM	A	N	FOM	A	N	FOM	A	N	FOM
2.2e4	680	-1.78	0.544	640	-1.78	0.571	630	-1.80	0.389	500	-1.66	0.699
2.3e4	695	-1.80	0.489	645	-1.78	0.522	650	-1.82	0.345	500	-1.66	0.638
2.4e4	695	-1.80	0.434	660	-1.80	0.476	655	-1.82	0.304	505	-1.66	0.578
2.5e4	700	-1.80	0.384	665	-1.80	0.434	655	-1.82	0.267	505	-1.66	0.518
2.6e4	700	-1.80	0.330	665	-1.80	0.390	680	-1.84	0.232	505	-1.66	0.462
2.7e4	715	-1.80	0.282	665	-1.80	0.353	680	-1.84	0.204	525	-1.68	0.407
2.8e4	715	-1.82	0.240	685	-1.82	0.316	685	-1.84	0.182	525	-1.68	0.355
2.9e4	730	-1.82	0.206	685	-1.82	0.282	710	-1.86	0.171	530	-1.68	0.305
3.0e4	730	-1.84	0.193	690	-1.82	0.258	710	-1.86	0.169	530	-1.68	0.258
3.1e4	735	-1.84	0.169	690	-1.82	0.234	715	-1.86	0.174	550	-1.70	0.219
3.2e4	735	-1.84	0.167	710	-1.84	0.220	720	-1.86	0.189	535	-1.68	0.186
3.3e4	750	-1.86	0.175	710	-1.84	0.207	725	-1.86	0.210	555	-1.70	0.161
3.4e4	750	-1.86	0.211	710	-1.84	0.211	725	-1.86	0.235	555	-1.70	0.158
3.5e4	755	-1.86	0.230	715	-1.84	0.215	730	-1.86	0.261	560	-1.70	0.160
3.6e4	770	-1.88	0.258	715	-1.84	0.232	735	-1.86	0.289	565	-1.70	0.185
3.7e4	770	-1.88	0.293	735	-1.86	0.249	740	-1.86	0.318	565	-1.70	0.211
3.8e4	775	-1.88	0.333	740	-1.86	0.273	765	-1.88	0.346	585	-1.72	0.247

8. SPECTRUM UNFOLDING RESULTS USING CTMFDS

This chapter describes how response matrices are calculated in MCNPP for the CTMFD. Major features of the response shapes, and how these features provide spectral resolution, are discussed. The response matrices, calculated using the optimal parameters for the DETC curve presented in chapter 7 are used to unfold experimental data measured in the closed-room geometry with both the single-detector and multi-detector system. Explanations for inaccuracies in the unfolded spectra along are provided with relation to the count rate prediction trends discussed in chapter 7.

8.1 Calculation of the CTMFD Response Matrices

Simulation of the CTMFD response matrices is procedurally similar to the ^{6}LiI BSS calculation discussed in section 4.2; i.e. a finite-energy-width plane wave of neutrons illuminating a detector in a vacuum. For each energy in the response matrix, 8 different detector orientations are run to simulate the transient cross sectional area of the detection volume. The first and last subcases consist of the CTMFD's arms oriented perpendicular and parallel, respectively, to the surface normal vector of the plane wave, with each intermediate subcase constituting a rotation of 11.25 degrees. The impact of the surface area effect is dependent on the neutron energy (mean free path) and volume of the CTMFD. At neutron energies of 15 MeV the difference in detector response is negligible for the 16 cm^3 design compared to approximately 15-20% for the 1 and 0.4 cm^3 designs. For neutron energies on the order of 100 keV, response deviations of approximately 15% and 60% were observed for the large and small volumes, respectively. The difference in responses is thus significant and the added complexity necessary to accurately model the CTMFD's response. Though not explicitly stated in prior chapters, this approach was employed in all MCNP simulations related to CTMFDs.

Note that the MCNPP geometry for the response matrix calculations only includes the CTMFD glass apparatus and detection fluid. The acrylic containment, plastic base and motor housing, aluminum lid, control circuitry, etc. are not included in the model. These additional components underwent multiple design revisions throughout the tenure of this work. Thus, it made sense to exclude them from the model rather than having to re-simulate the response for different configurations. To truly have geometrically independent response matrices, the full geometry of the detector should be included in the model. Furthermore, for a multi-detector system design, the “full geometry” must consist of the surrounding detectors to account for attenuation and or scattering by the neighboring units.

The response matrix encompasses energies from 100 keV to 15.3 MeV with uniform energy-bin widths of 100 keV. At the time the decision was made on what the energy structure of the response matrix should consist of, it was not known whether the CTMFD’s energy resolution was fine enough to warrant such narrow bin widths. To be conservative, it made sense to sample the response at energy intervals finer than the anticipated resolution and then combine the bin responses as necessary. With respect to negative pressure, the matrix contains response data for centerline pressures ranging from 1.0 bar to 13.5 bar in 0.25 bar increments. The CTMFD’s response is actually continuous in the pressure parameter space. Discretization of the centerline pressures is an artifact of the computational framework and is also necessary to satisfy the input formatting requirements of the unfolding package. If a finer discretization is desired, e.g. 0.1 bar, the current 0.25 bar contours can be interpolated with a minimal loss of accuracy.

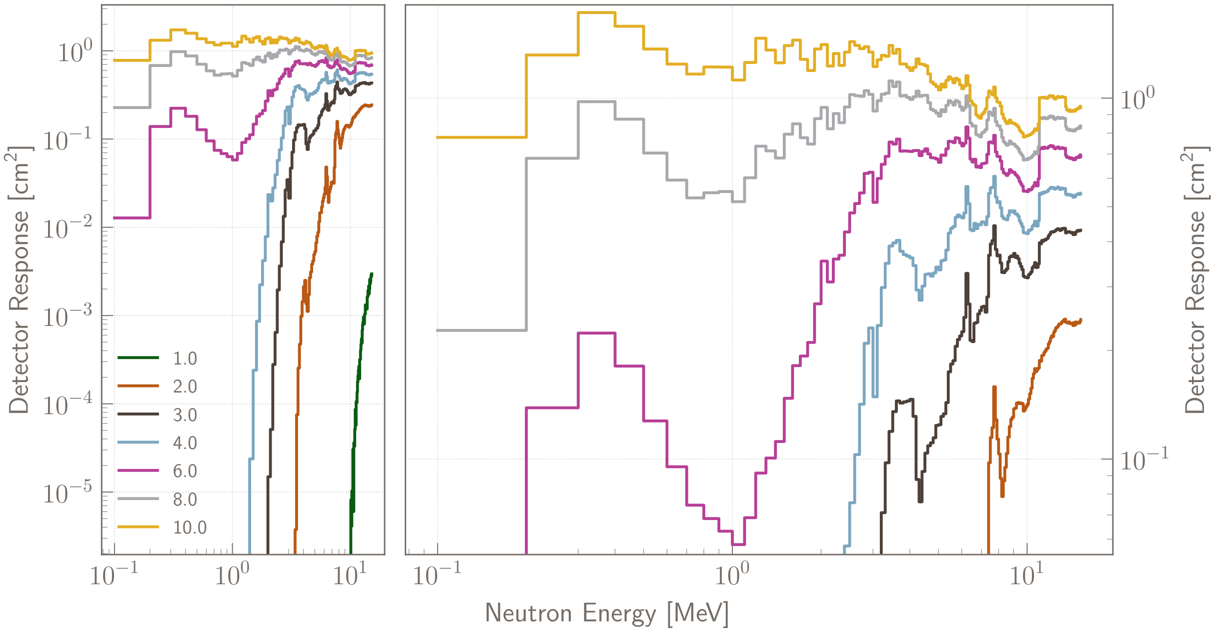

(a) M76

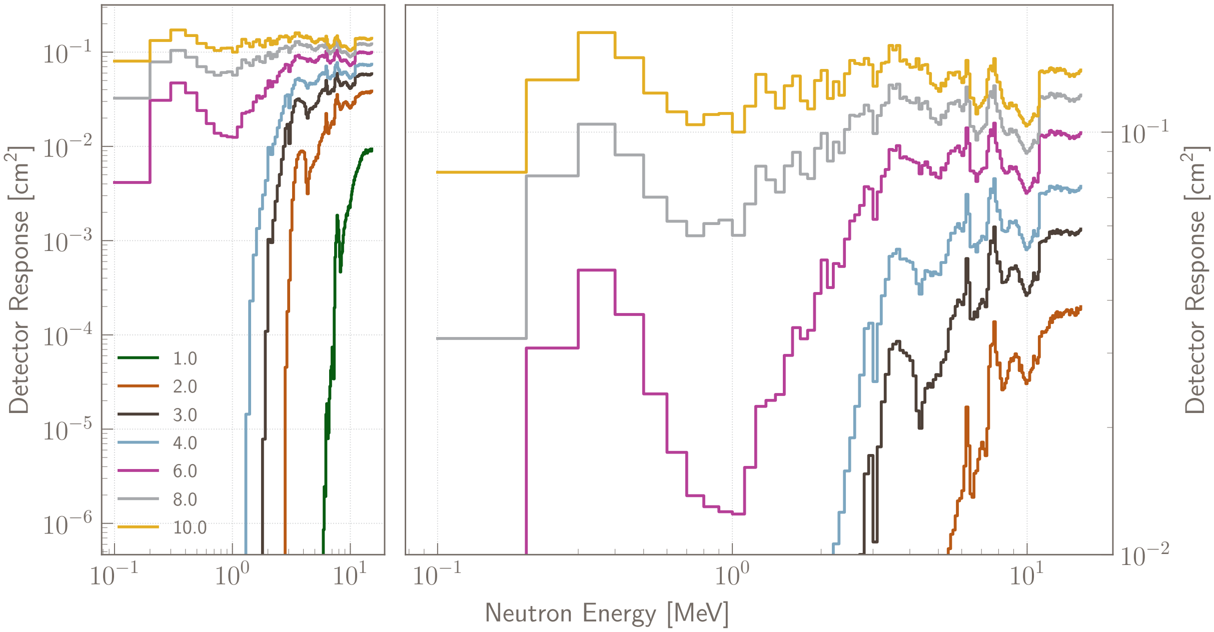

(b) T3

Figure 8.1. MCNPP response matrices, calculated with the probabilistic model, for the different volume detectors introduced in chapter 7: M76, T3, and T1. Values for the optimized "A" and "N" coefficients correspond to the 100 cm dataset in table table 7.2 and 50 cm datasets in table 7.3 and table 7.4, respectively.

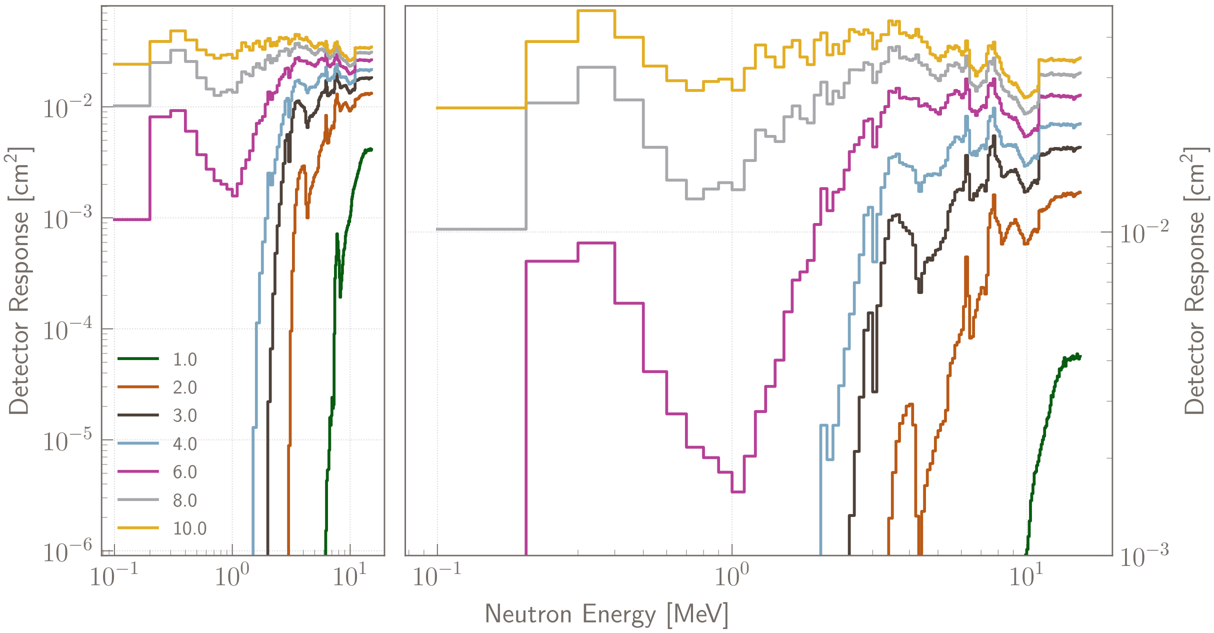

(c) T1

Figure 8.1. MCNPP response matrices, calculated with the probabilistic model, for the different volume detectors introduced in chapter 7: M76, T3, and T1. Values for the optimized "A" and "N" coefficients correspond to the 100 cm dataset in table table 7.2 and 50 cm datasets in table 7.3 and table 7.4, respectively.

Plots of the MCNPP simulated response matrices, calculated using the probabilistic model with a 20% cut value applied to the detection probability distribution, are shown in fig. 8.1 for detectors M76, T3, and T1. To avoid over-conflating the figure with data while still illustrating the structure of the individual responses, only select centerline pressures are shown. The DETC curve used to generate the matrices is parameterized by coefficients optimized with the 100 cm dataset in table table 7.2 for M76 and the 50 cm datasets in table 7.3 and table 7.4 for detectors T3 and T1, respectively. Because the optimized coefficients are not the same for each detector, it is difficult to draw definitive conclusions about the equivalence of individual response structures in one detector to that of another. It is, however, within reason to compare the magnitude of the integral response from one detector to another.

Figure 8.2 contains data on the integral response of detector's M76 and T3, normalized to the integral response of detector T1, as a function of pressure. The non-linear relationship with pressure observed in the response ratios is a consequence of the differences in the central volume shapes and threshold neutron sensitivity. The response ratio is not simply a proportional scale factor of the volume because of the radial pressure gradient. The 16 cm^3 design is seen to have an integral response a factor of 30x higher than the 0.4 cm^3 design, while the 1 cm^3 design plateaus at a factor of 4x. These ratios are of importance for theoretically estimating the max dose rate field a multi-TMFD spectrometer system can operate in.

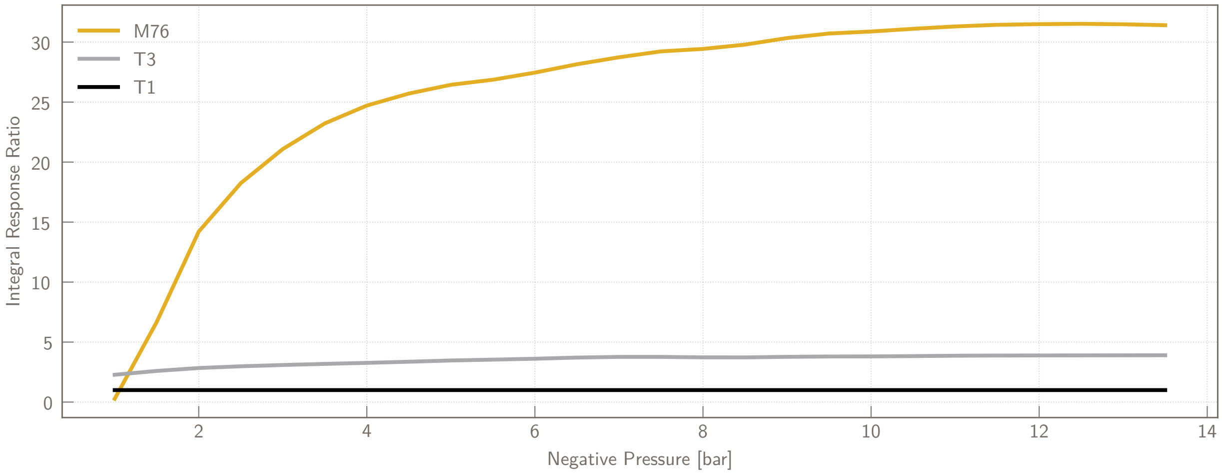

Figure 8.2. Ratio of the CTMFD's integral response as a function of pressure, normalized by the smallest volume detector, T1.

From a visual perspective, the structure of the responses resemble those calculated for fluorocarbons commonly used in SDD detectors, notably the peaks in the response as a result of resonances in the ^{19}F cross section [47], [53]. At first glance, two trends in the TMFD response matrix appeared concerning: the step-like increase in the response at 11 MeV and the high sensitivity to neutrons below 1 MeV (at pressures of 6.0 bar and above). Both trends are present in SDD response matrices, however, which adds further credibility to the probabilistic model developed in this work.

The implications of the differences in the CSDA versus probabilistic models have been discussed at length, but are best illustrated by comparing the response matrices calculated by each model. While a comparison of the matrices generated with the optimized A,N coefficients from each model may also be of interest, distinctions between the two models would be conflated by the effect of the different parameterizations of the DETC curve. A direct comparison is only possible if the same A,N coefficients are used in both models. This comparison is shown in fig. 8.3 for the probabilistic model's coefficients, optimized to the 100 cm dataset (values from table 7.2).

The relative shapes of the response curves from one model to another is depicted in fig. 8.4 through the ratio of the response at each energy $\left(\frac{\mathrm{R_{prob}}}{\mathrm{R_{csda}}}\right)$. The most obvious difference in the responses from each model is the location of the neutron energy thresholds, where the response drops to zero (fig. 8.3) or where the response ratio jumps to infinity (fig. 8.4). Details on each model's threshold predictions were already provided at length in chapter 6, such that further discussion is not necessary. Rather, the purpose of fig. 8.4 is to illustrate the dependence of the response ratio on neutron energy.

At energies greater than 2-3 MeV the 3, 4, and 6 bar response ratio is relatively constant, fluctuating between 0.7-0.8. It is interesting that the two models differ by only 20-30% considering that the CSDA model assigns every detection event a probability of 1.0, while the probabilistic model's average probability is approximately 0.3. Significant differences between the two models are evident for the 2, 8, and 10 bar responses. As mentioned several times throughout this work, the starkest difference of the probabilistic model is seen for the cases of high negative pressure and low neutron energy. The 8 and 10 bar ratio curves confirm this assertion.

8.2 Unfolded Spectrum Results Using the Single-Detector System

The unfolded spectra in this section correspond to the experimental data taken with the single detector system at a source-to-detector distance of 300 cm. The count rates and A,N coefficients (optimized with data from both sources) used to generate the response matrices can be found in fig. 7.3/fig. 7.4 and table 7.1. Each unfolded spectrum is compared against

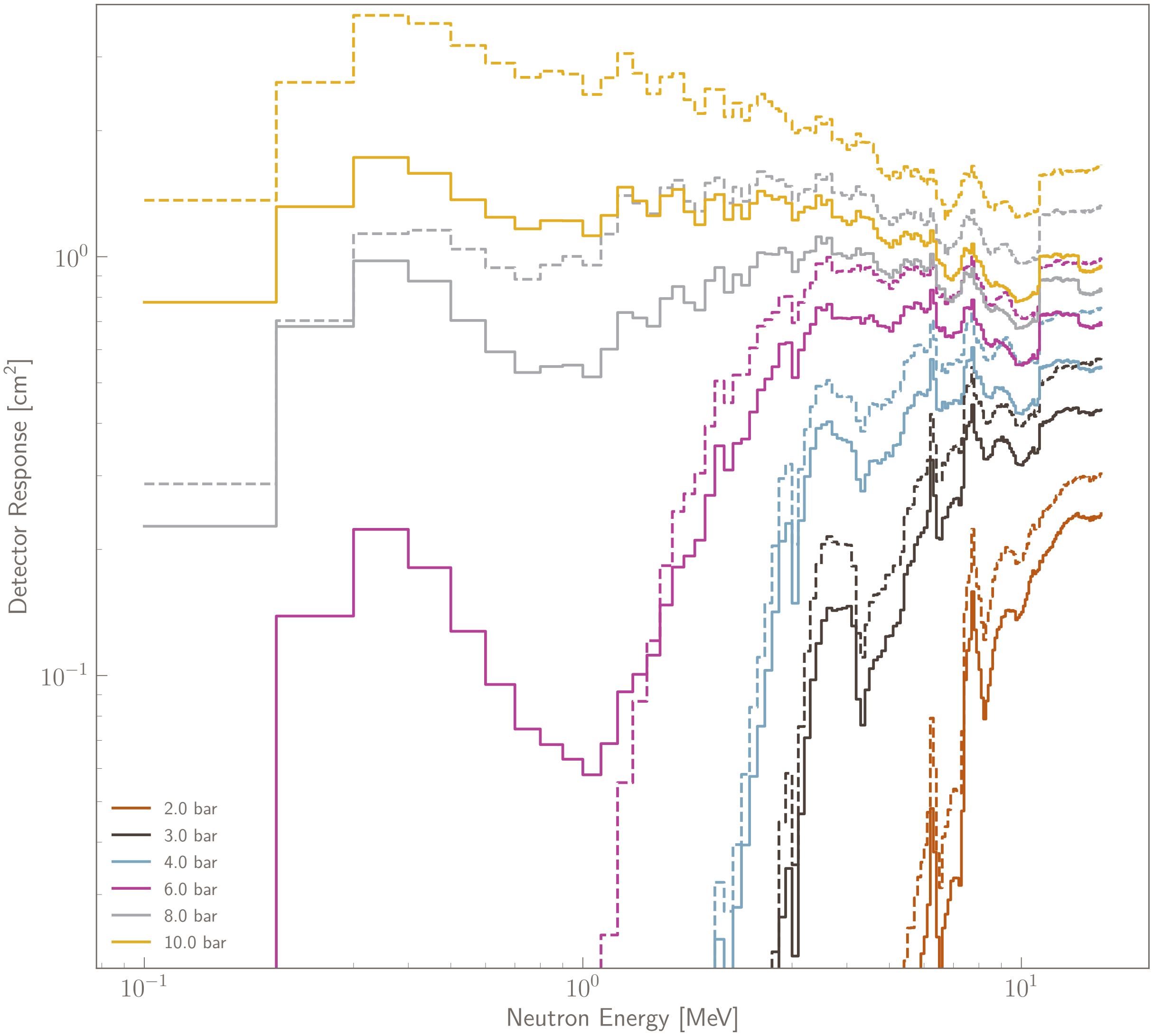

Figure 8.3. Comparison of the M76 response matrices generated using the CSDA (dashed lines) and probabilistic (solid lines) detection models using the same DETC curve, with "A" and "N" coefficient values of 685.0 and -1.82, respectively. The DETC curved parameterized by these coefficients is the result of optimizing the 100 cm dataset (table 7.2) with the probabilistic detection model and a cut value of 0.2.

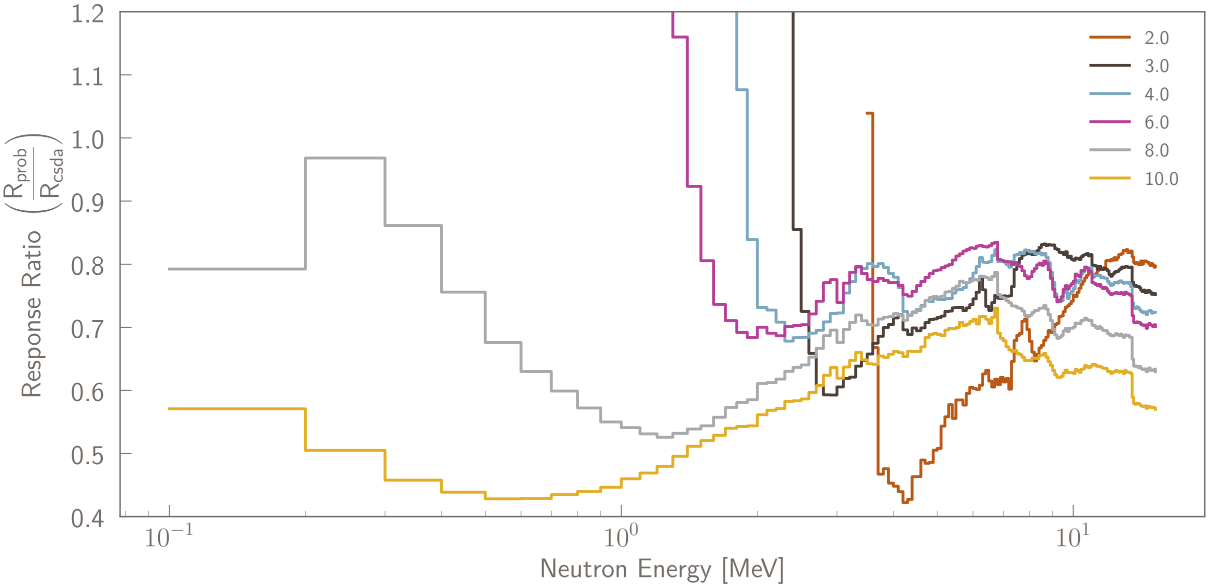

Figure 8.4. Ratios of select M76 response curves generated using the CSDA (dashed lines) and probabilistic (solid lines) detection models using the same DETC curve, with "A" and "N" coefficient values of 685.0 and -1.82, respectively. The DETC curved parameterized by these coefficients is the result of optimizing the 100 cm dataset (table 7.2) with the probabilistic detection model and a cut value of 0.2.

the "true" spectrum as simulated by MCNP. The details of how the fluence spectrum was tallied by MCNP and the geometry in the model are described in section 3.3.

Two different guess spectra templates are used for unfolding, corresponding to the extreme cases for the amount of *a priori* information known about the spectrum. A flat (in lethargy space) spectrum represents a worst case scenario, where zero information is available about the spectrum being measured, thereby necessitating every energy bin be assigned an equal probability. As a best case scenario, the exact spectrum is known. Rather than using the MCNP simulation results as the best-case guess, which would account for all room scatter, a template spectrum of the same source is used instead. These templates are identical to those used for the BSS system in section 4.4.

8.2.1 Spectra Resulting from Response Matrices Calculated with the CSDA Model

The unfolded spectra resulting from the response matrix constructed using the both-source optimized CSDA coefficients is shown in fig. 8.5. Dashed and solid lines represent the guess and unfolded spectra, respectively. Neither the ^{252}Cf nor ^{241}AmBe unfolded spectra agree very well with the MCNP simulation results. In both cases, the unfolded spectra overestimate the fluence from neutron energies of 2-5 MeV. The overestimation in the ^{252}Cf unfolded spectra is compensated for by a significant underestimation of the fluence below 1 MeV. The underlying reasoning behind these trends is implicitly contained in fig. 7.5, which shows the percent difference between the predicted and experimental count rates. Over or under predicting the count rates similarly result in over/under estimation in the CTMFD's response matrix calculations. Over/under estimation in the response matrix is inversely related to over/under estimates of the unfolded spectra; i.e. if the calculated response is too low, the fluence must necessarily be over-inflated to conserve the detector's count rate.

Referring to fig. 7.5a, the large peaks in the ^{252}Cf unfolded spectra can be attributed to the significant under-prediction of the count rates from 6-8 bar. The under-estimation of the fluence below 1 MeV is a combinational effect of two factors. The primary effect is again attributed to errors in the percent difference curves at 9-10 bar and the inverse relationship between response and unfolded fluence. The secondary effect is a consequence of the unfolding algorithm using the χ^2 test as convergence criteria. The scalar count rate, resulting from folding the spectrum with the response matrix, must be conserved (within error) of the measured experimental rate. The integral area between the MCNP and unfolded curves forming the peak (over estimate) at 2-5 MeV must be counterbalanced by the area between the MCNP and unfolded spectra curves below 1 MeV (under estimate). Simply put, neighboring energy bins are negatively correlated. Unlike ^{252}Cf, the percent difference curve for the ^{241}AmBe does not have counterbalancing regions (above 5 bar) of successive under and over prediction. The predicted count rates remain negatively biased up to 10 bar and the unfolded fluence is consequently over estimated across the entire energy spectrum.

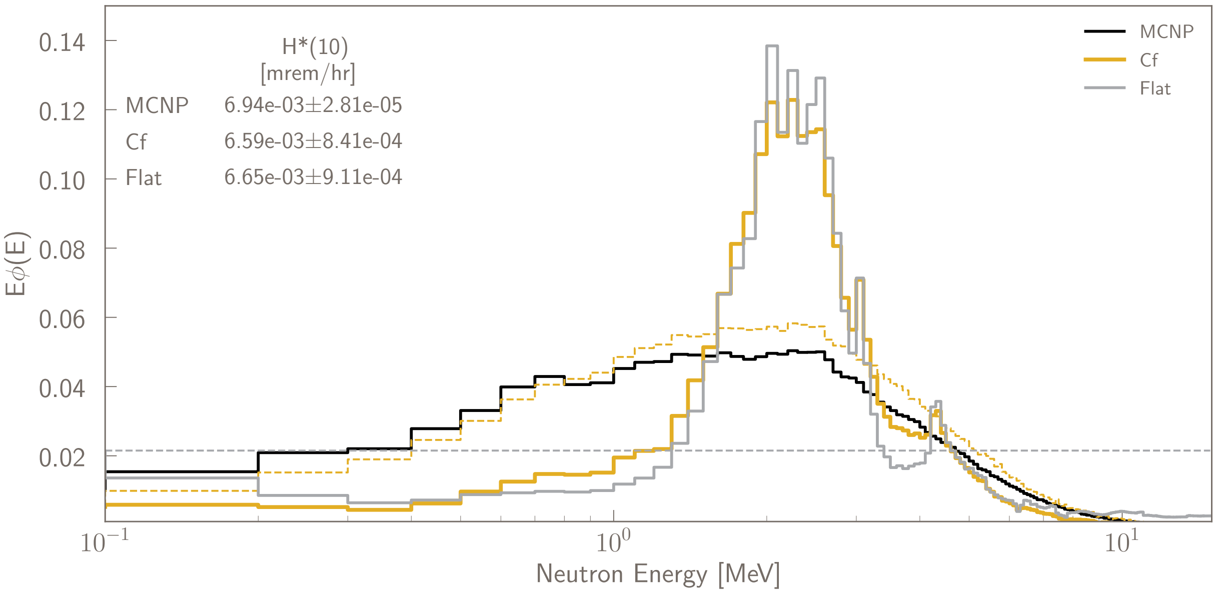

(a) ^{252}Cf

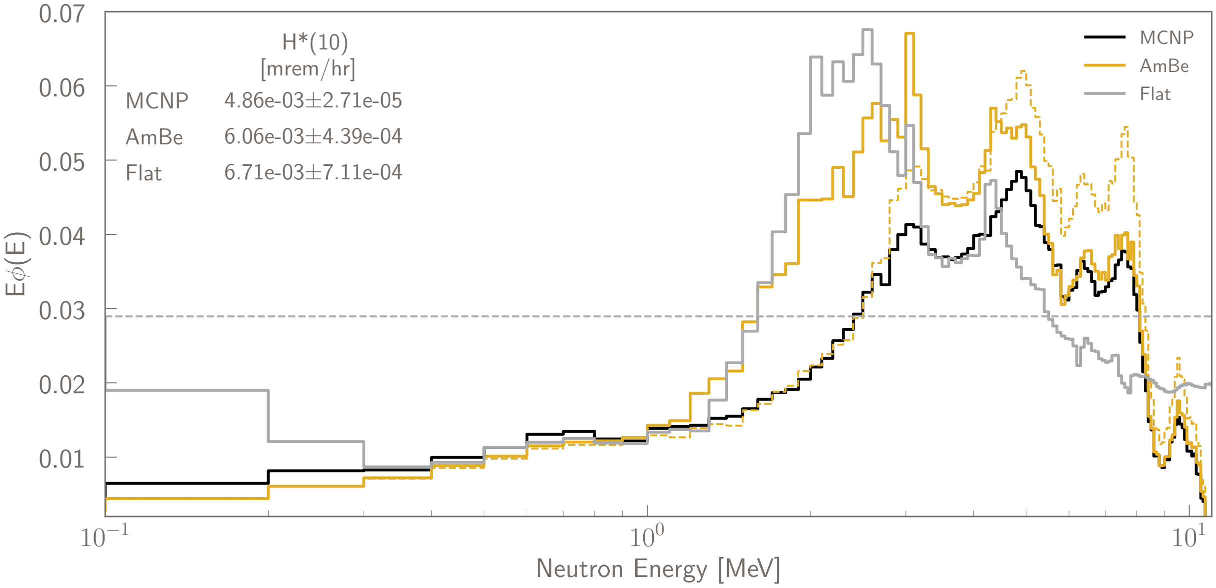

(b) ^{241}AmBe

Figure 8.5. Unfolded spectra resulting from measurements with the single detector system at a source-to-detector distance of 300 cm. The response matrix was constructed using the both-source optimized CSDA coefficients from table 7.2. The dashed and solid lines represent the guess and unfolded spectra, respectively.

Finally, it should be stated that the effects discussed in the paragraph above are not actually mutually exclusive; though, it is useful to describe them as such for the purpose of a qualitative discussion. Nor, do the discussed reasons solely explain the trends in the unfolded spectra. The shape of the guess spectrum and structure of the response curves also seem to influence the location (energy) at which peaks appear. This effect is particularly noticeable when a "flat" guess is used for unfolding. An entire separate chapter could be devoted to further explaining the reasoning behind these results from the perspective of general unfolding theory. This, however, is outside the scope of this work.

8.2.2 Spectra Resulting from Response Matrices Calculated with the Probabilistic Model

The spectra in fig. 8.6 are unfolded with the same experimental data as those in fig. 8.5 but instead use a response matrix calculated with the probabilistic rather than CSDA model. Though the dose rates estimates are similar for both models, large differences exist in the unfolded spectra. While the resemblance between the unfolded and MCNP-simulated spectra is significantly improved for ^{252}Cf, the ^{241}AmBe results are equivalently worse. The discrepancies between the unfolded and MCNP-simulated spectra are consistent with what should be anticipated based on the shape of the percent difference curve in fig. 7.5b and the accompanying discussion in the last section. Specifically, for the ^{241}AmBe spectra, the peaks above 7 MeV are the result of the under prediction in the count rates below 5.0 bar.

To prove the cause and effect of the the under prediction below 5.0 bar, refer to the unfolded spectra in fig. 8.7. These spectra are the result of excluding different portions of the data below 5.0 bar from the unfolding code. The numbers in the figure's legend key represent the lowest pressure data point used in the unfolding deconvolution. For example, the 4.0 curve corresponds to the spectra from unfolding with count rate data from 4.0-10.0 bar (i.e. 3.0 and 3.5 bar are excluded). The amplitude of the high energy peaks decrease with each point excluded. Using the data from 4.5 bar and above, the unfolded spectrum shape matches quite well, despite the count rate predictions containing a 20% bias. This implies that response matrix is close to accurate for the larger negative pressures.

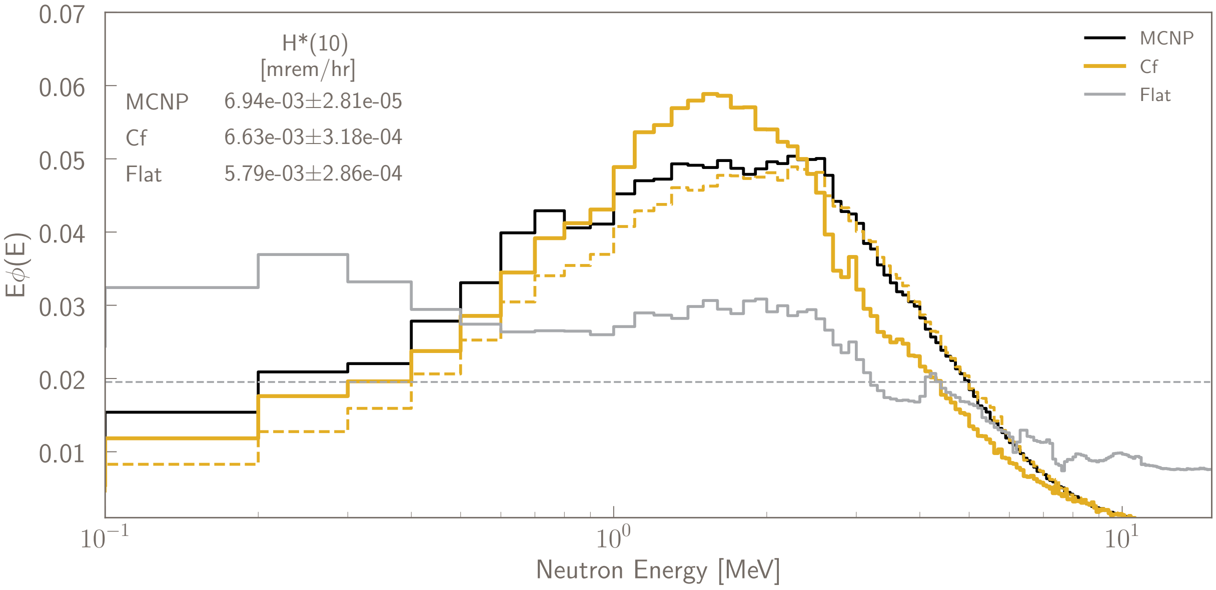

(a) ^{252}Cf

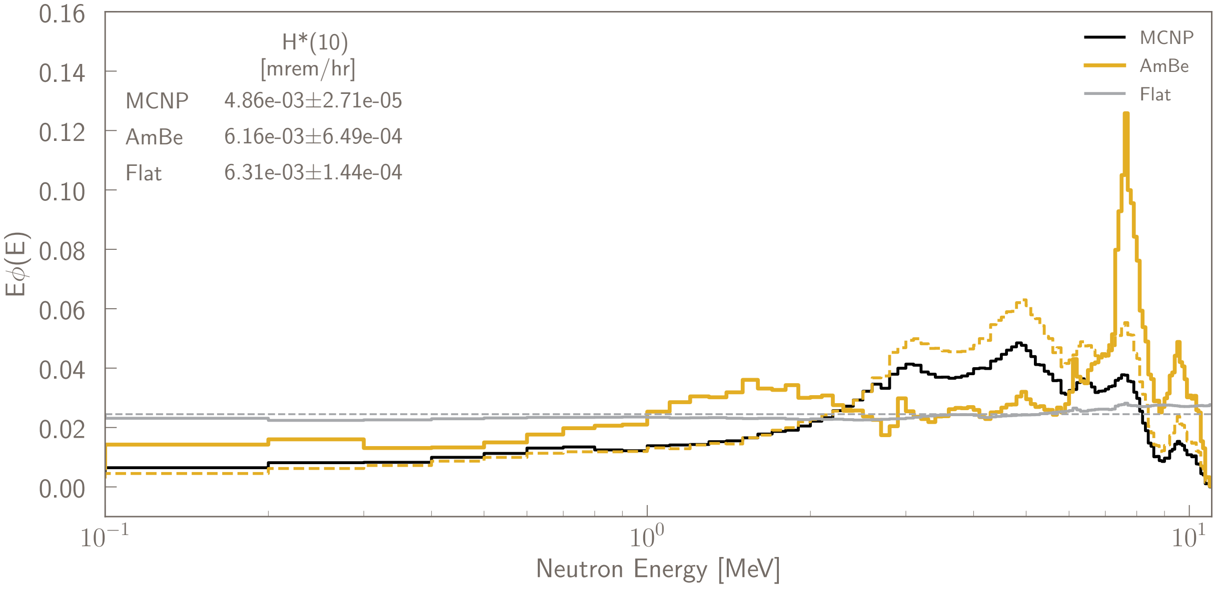

(b) ^{241}AmBe

Figure 8.6. Unfolded spectra resulting from measurements with the single detector system at a source-to-detector distance of 300 cm. The response matrix was constructed using the both-source optimized probabilistic coefficients from table 7.2. The dashed and solid lines represent the guess and unfolded spectra, respectively.

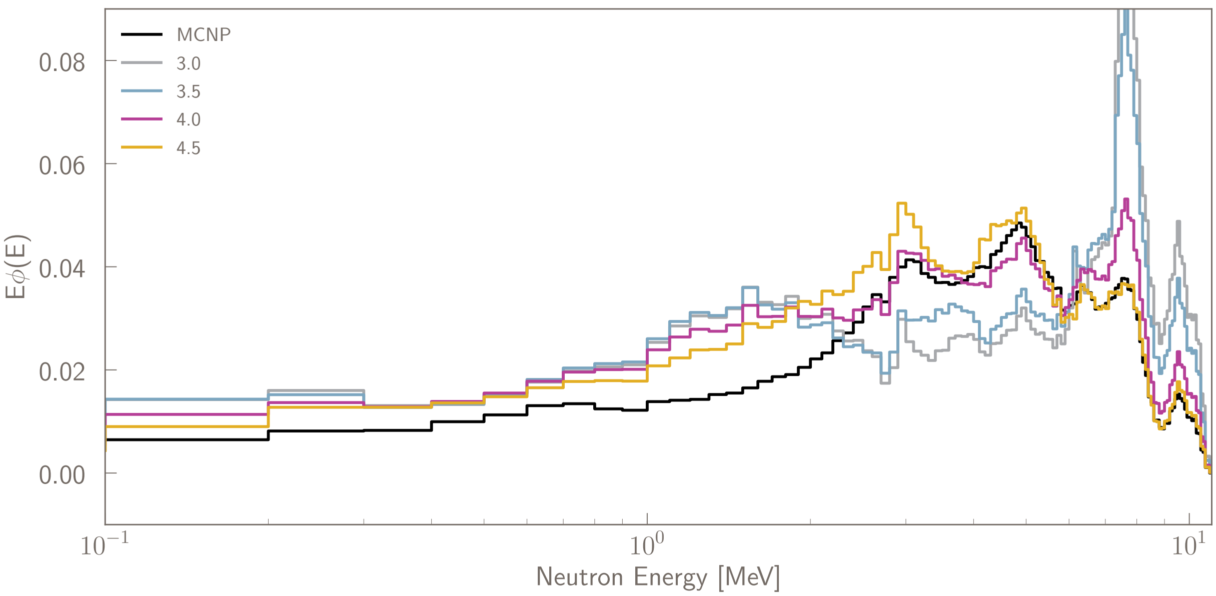

Figure 8.7. Influence on the 300 cm unfolded spectra from excluding (from the unfolding code input) data for pressures below 5.0 bar. The legend keys represent the lowest pressure data point used in the deconvolution.

The improvement agreement seen in fig. 8.7 provides substantiating evidence regarding the correctness of the response matrices calculated in section 8.1, at least for the pressures whose count rates are in agreement with experimental data. This assertion is further corroborated by the unfolded results seen in fig. 8.8. Recall, from section 7.5, that the predicted count rates were found to agree within 20% of experimental data across the entire 3.0-10.0 bar range if the ^{241}AmBe intensity was assumed to be 3.4e4 neutrons/sec. Using the response matrices generated with the ^{241}AmBe intensity optimized coefficients from table 7.5 (A=555, N=-1.70), the ^{241}AmBe and ^{252}Cf spectra agree very well with MCNP when the proper spectrum is used as the guess shape. A similarly good agreement is not seen with a "flat" guess, though the dose estimate is still accurate to within 20%. The full accuracy of these results are, however, dependent on the validity of the assumed source intensity.

8.3 Unfolded Spectrum Results Using the Multiple-Detector System

The single detector system unfolded results in fig. 8.7 and fig. 8.8 demonstrate that the CTMFD can accurately unfold a measured spectrum (with a proper guess shape) with a select subset of pressure response curves. The difficulty with the single detector system, covered extensively in chapter 7, is that the subset of suitable pressures to use for unfolding varies depending on which dataset the A,N coefficients were optimized to. Calibrating the A,N coefficients for accuracy at low pressures came at the cost of accuracy at higher pressures.

From a field operability perspective, where prior knowledge of the neutron spectrum may not be available, the problem lies in determining what pressures the detector needs to record measurements at to best reproduce the spectrum shape. For example, calibrating the detector's response for accuracy at high pressures could incur significant penalties when unfolding the spectrum around a D-T accelerator. Conversely, calibrating for accuracy at low pressures could incur a similarly large penalty when attempting to unfold the spectrum from an ^{241}AmLi source. Therein lies a primary motivation of the multiple detector panel. Compromising the accuracy of the system to specific neutron energies is not necessary if each detector is calibrated, via optimization of the A,N coefficients, for a select subset of pressures that, when used together, span the range of negative pressures necessary to unfold

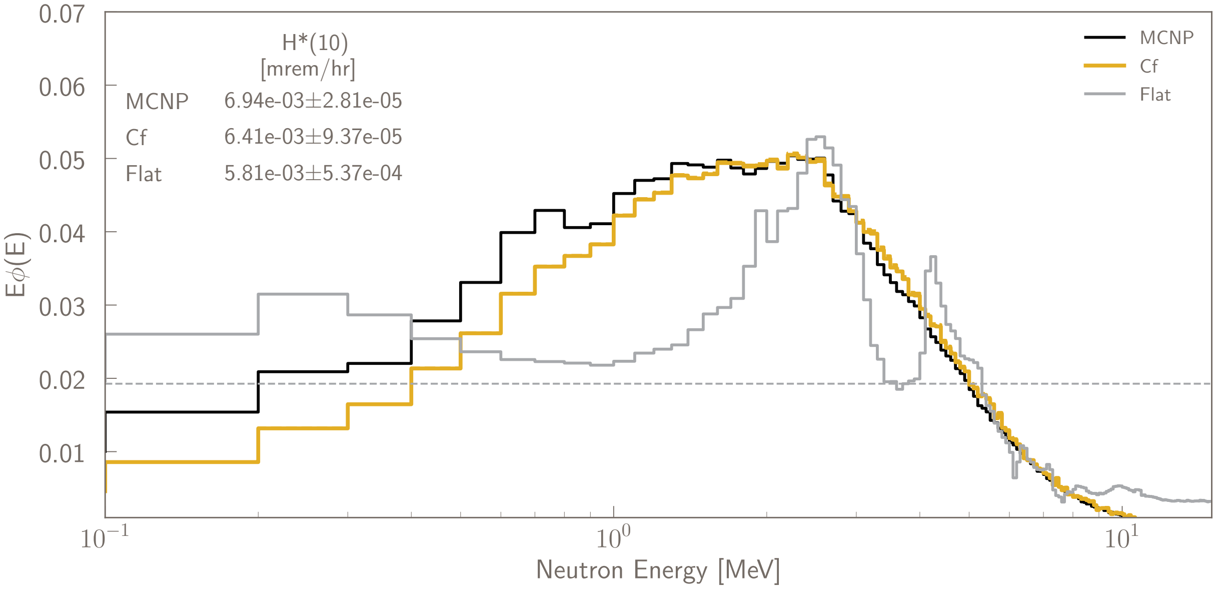

(a) ^{252}Cf

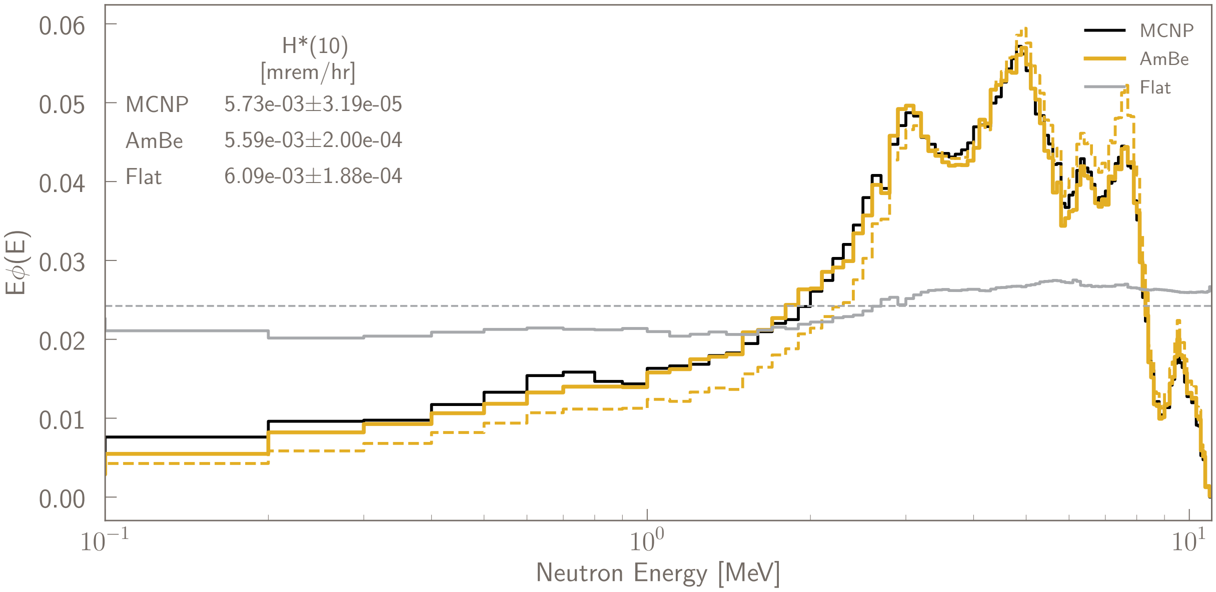

(b) ^{241}AmBe

Figure 8.8. Unfolded spectra resulting from measurements with the single detector system at a source-to-detector distance of 300 cm. The response matrix was constructed using the ^{241}AmBe intensity optimized coefficients from table 7.5. The dashed and solid lines represent the guess and unfolded spectra, respectively.

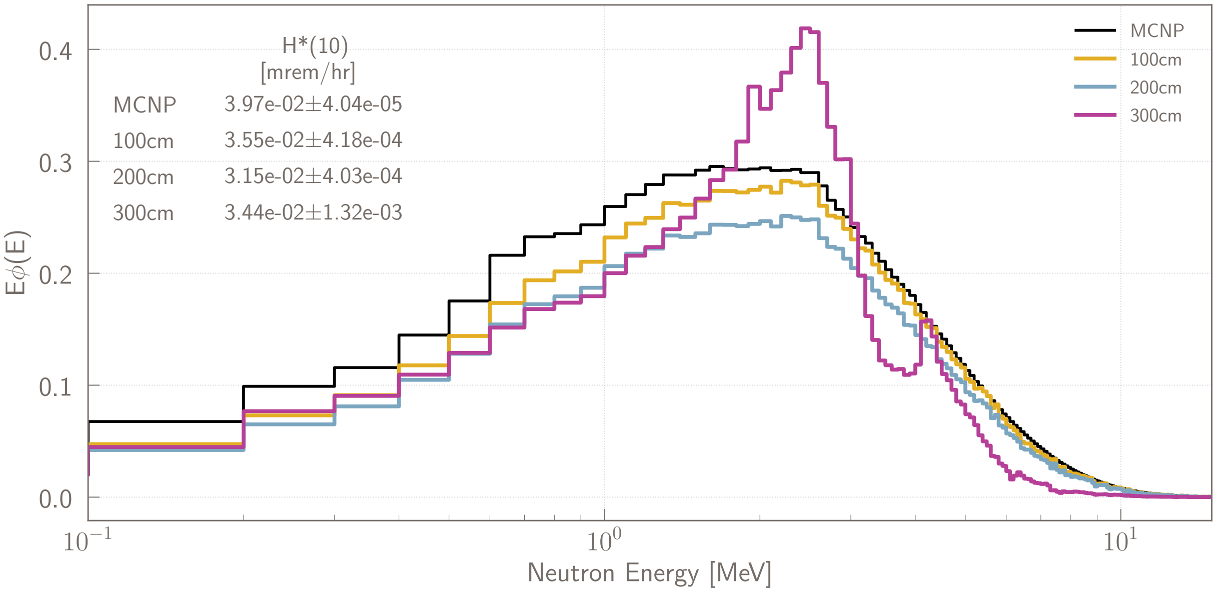

(a) ^{252}Cf

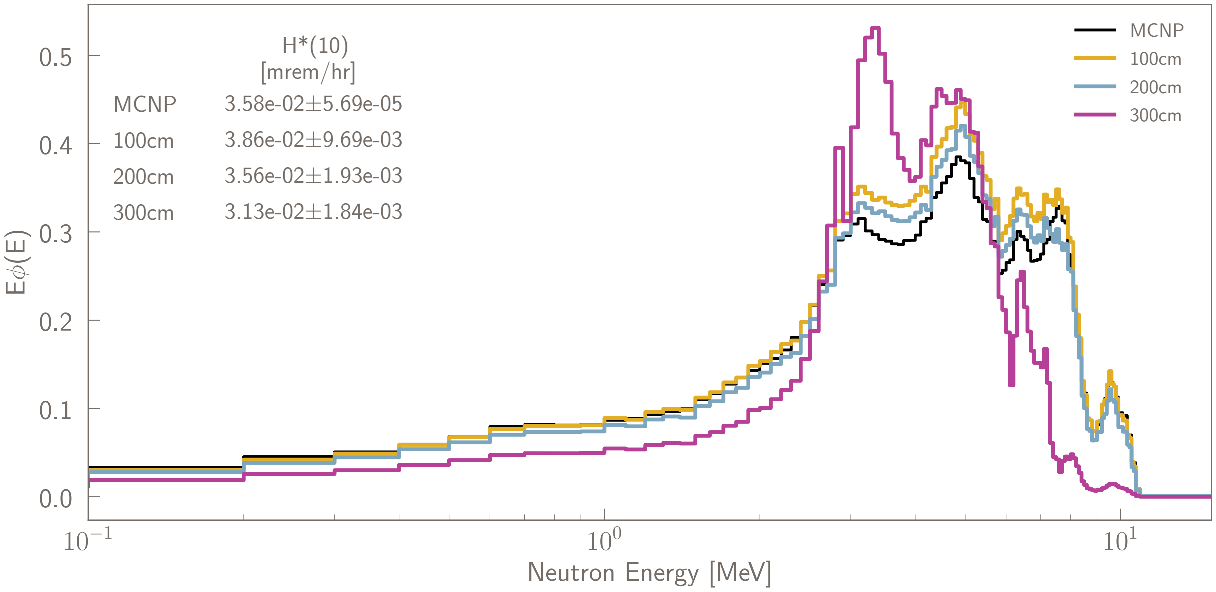

(b) ^{241}AmBe

Figure 8.9. Unfolded spectra using only M76 count rate data from the 100cm dataset and the optimized coefficients from each distance's dataset illustrating extensibility of optimized coefficients to slight perturbations in measured spectra.

the neutron spectrum from 0.1 MeV to 15 MeV. The results in this section demonstrate the proof of concept behind this idea.

Figure 8.10 displays the spectra unfolded using the count rates from the 50 cm dataset for detectors M76 and T3 only. These count rates can be found in fig. 7.8 and fig. 7.12, respectively. The A,N coefficients (table 7.2 and table 7.3) used to build the response matrices for unfolding were optimized to the 50 cm dataset with the probabilistic model and the nominal cut value of 0.2.

Both the ^{252}Cf and ^{241}AmBe unfolded spectra shapes agree very well with MCNP for the best case guess shape. The magnitude of the ^{241}AmBe spectrum is over estimated, though this is not unexpected. If the ^{241}AmBe intensity is assumed to be 3.3x10^4 rather than 2.8x10^4 neutrons/sec, the unfolded results would match MCNP exactly. The ^{241}AmBe and ^{252}Cf unfolded dose rates are within 6% and 3%, respectively, of the dose rate estimates from the spectra unfolded with the BSS system. Though the measurements for each system were taken in a slightly different geometric configuration, the source-to-detector distance was the same. The dose rates being referenced correspond to the "Lit$_{\text{avg}}$" case in table 4.8, where the ^{252}Cf dose rate has been decay corrected to account for the approximate 11 month time difference between experiments.

Figure 8.11 displays the spectra unfolded using the count rates from the 100 cm dataset for detectors M76 and T3 only. These count rates can be found in fig. 7.8 and fig. 7.12, respectively. The A,N coefficients (table 7.2 and table 7.3) used to build the response matrices for unfolding were optimized to the 100 cm dataset with the probabilistic model and the nominal cut value of 0.2.

The spectra unfolded from the 100 cm dataset are noticeably worse compared to the 50 cm dataset The count rates measured at pressures below 5.0 bar or above 7.0 bar in detector T3 were not used during unfolding. If this data were to be included, the unfolding algorithm will not converge with a χ^2 criteria of 1.0. While convergence is possible if the χ^2 criteria is increased to a value of 2.0, the unfolded spectra bear no resemblance to the actual spectra and incorrectly estimate the dose rate by approximately 50%. Excluding the data above 7.0 bar is not unjustifiable when considering the count rate predictions in fig. 7.13. Furthermore, with the specified data excluded, the dose rate estimated by the

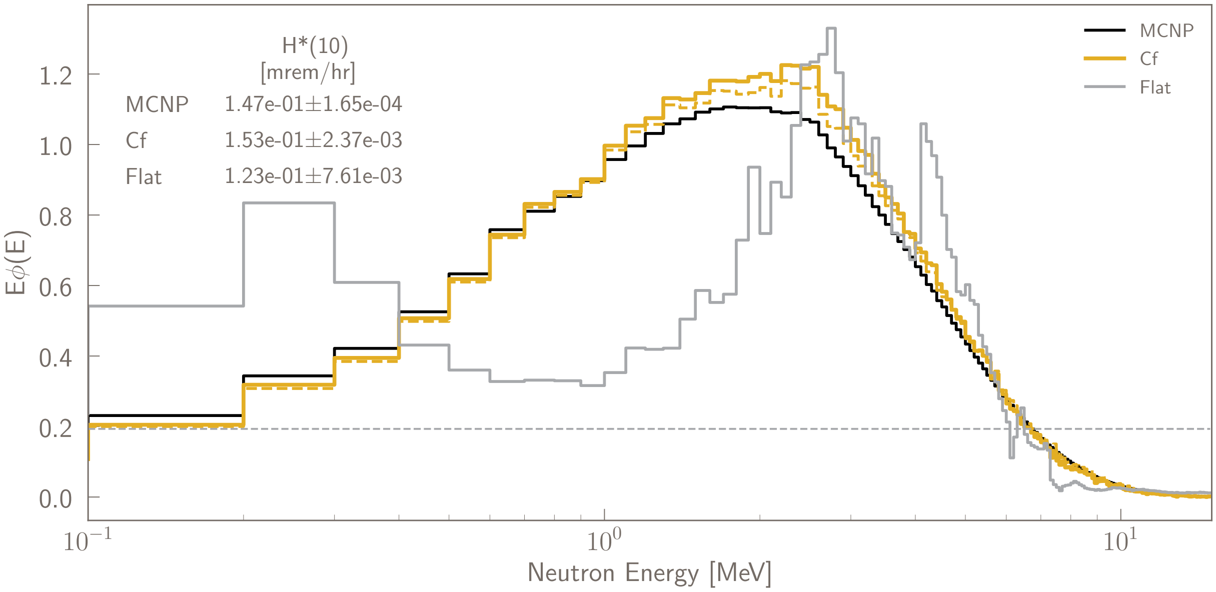

(a) ^{252}Cf

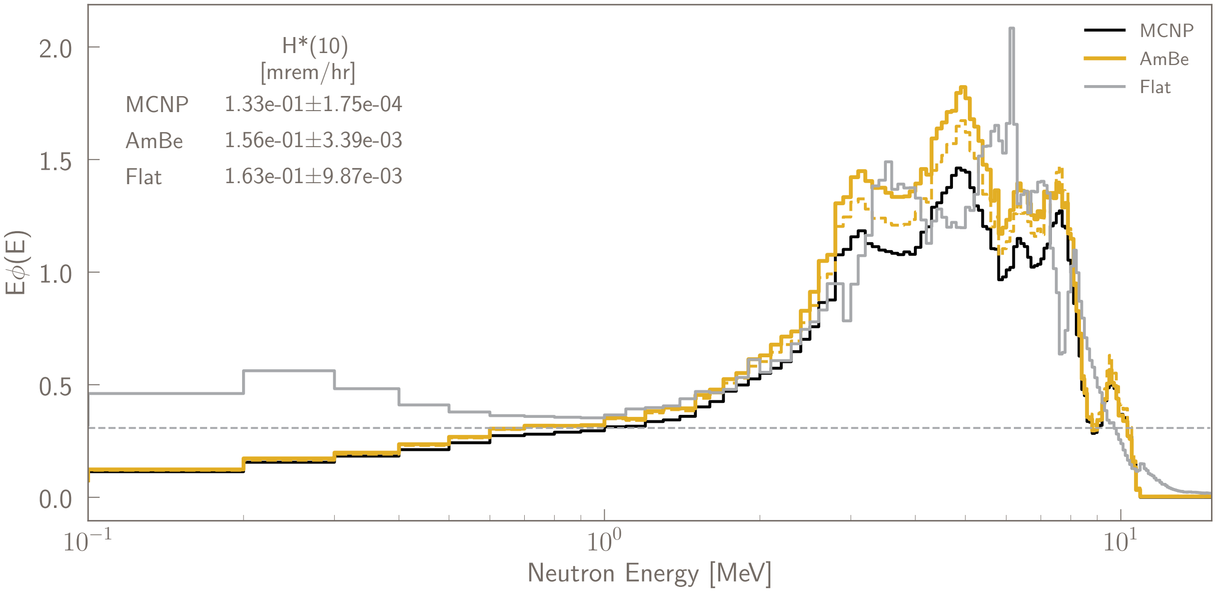

(b) ^{241}AmBe

Figure 8.10. Unfolded spectra from the 50 cm dataset using the response matrices and count rate data for detectors M76 and T3 only.

^{252}Cf unfolded spectrum is accurate within 19% for the best case guess spectrum, and the ^{252}Cf shape is at least preserved. The ^{241}AmBe unfolded spectrum results is considered unusable. The large oscillations seen in the fluence spectrum are indicative of difficulty achieving convergence. Additionally, the uncertainty in the dose rate is 40% of the total, whereas a properly converged solution would typically have an uncertainty 5%.

Figure 8.12 demonstrates the effect on the unfolded spectra from using the T3 50 cm optimized response matrix with the count rates from the 100 cm dataset. Note that, the accuracy of the M76 response matrix is not being called into question, and thus is left unchanged. For the case of ^{252}Cf, the unfolded results are actually improved from using the 50 cm response matrix. As shown in fig. 7.13, the A,N coefficients optimized to the 50 cm dataset predict the ^{252}Cf experimental count rates better at pressures of 7.0 bar and below; hence, the improvement in the unfolded results. The 50 cm optimized A,N coefficients under-predict the 100 cm ^{241}AmBe count rates by approximately 30% and yield worse results after unfolding. The conflicting trends observed with the ^{252}Cf and ^{241}AmBe results unfortunately raise questions about the validity of the 100 cm dataset for detector T3, whether it be the experimental data or the MCNP simulations. Since the maximum pressure recorded in the 50 cm dataset was 7.5 bar, it is not recommended that T3 be used outside this range until further validation work can be done.

Figure 8.13 displays the spectra unfolded using the count rates from the 50 cm dataset for all three detectors in the panel: M76, T3, and T1. These count rates can be found in fig. 7.8, fig. 7.12, and fig. 7.15, respectively. The optimized A,N coefficients (table 7.2, table 7.3, and table 7.4) used to build the response matrices for unfolding were optimized to the 50 cm dataset with the probabilistic model and the nominal cut value of 0.2. Without further verification of the accuracy of the T1 detector, it is not recommended that it be used for unfolding.

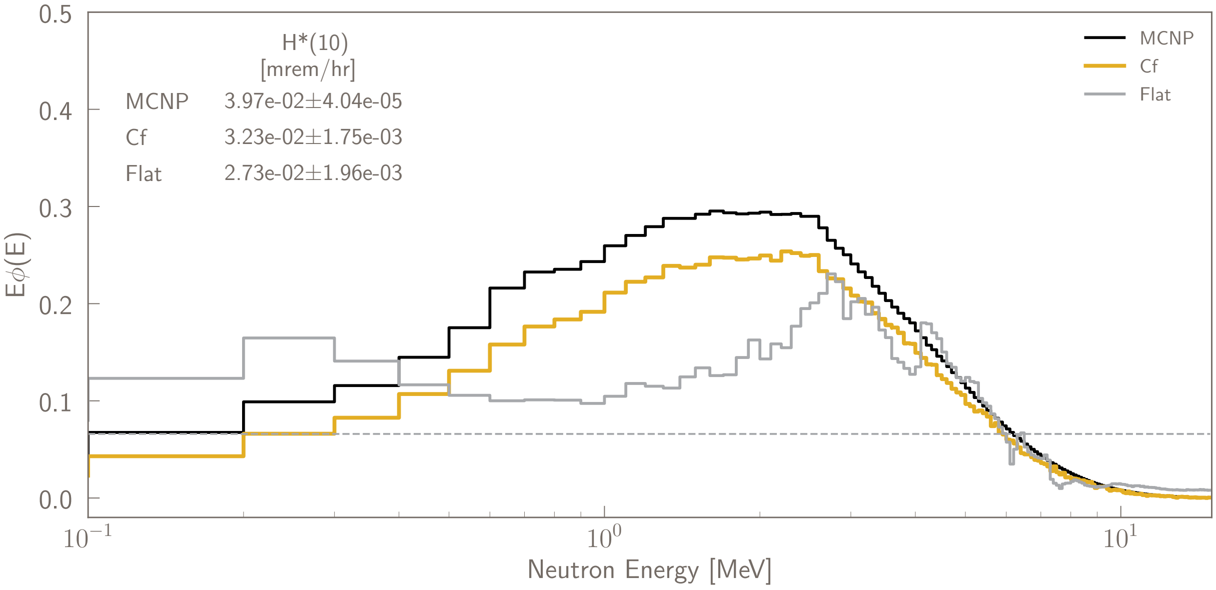

(a) ^{252}Cf

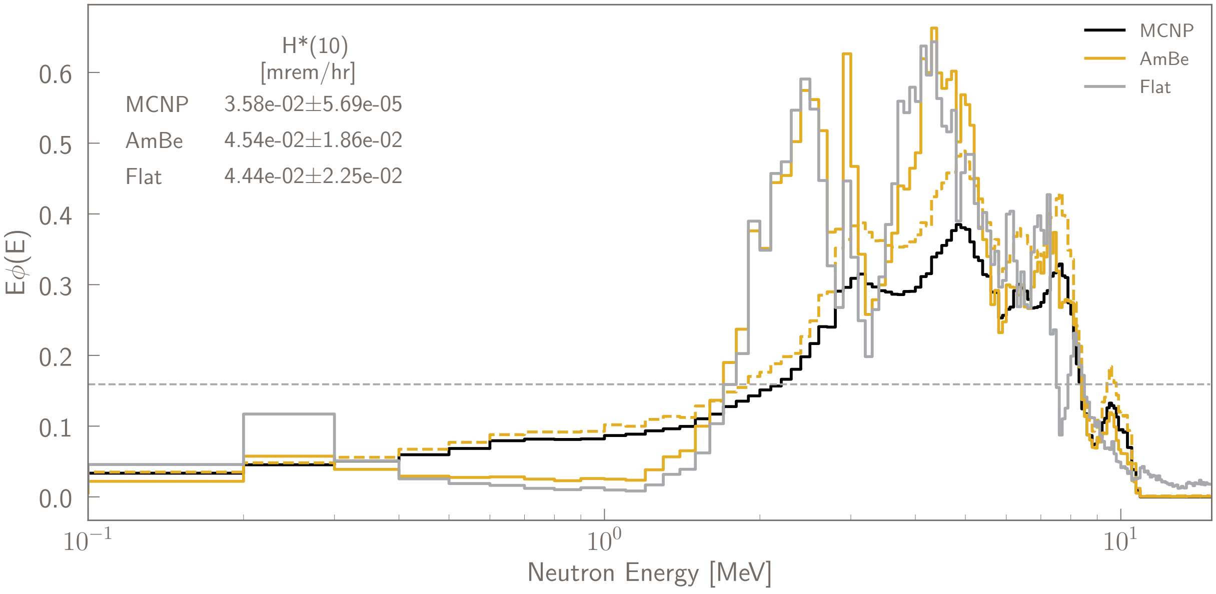

(b) ^{241}AmBe

Figure 8.11. Unfolded spectra from the 100 cm dataset using the response matrices and count rate data for detectors M76 and T3 only.

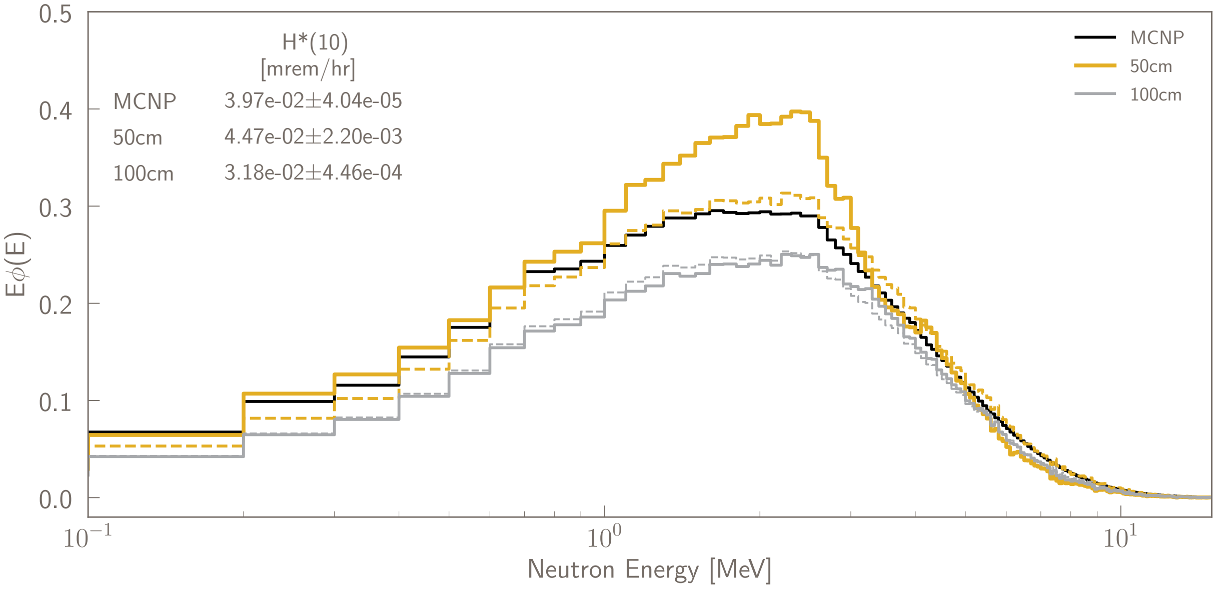

(a) ^{252}Cf

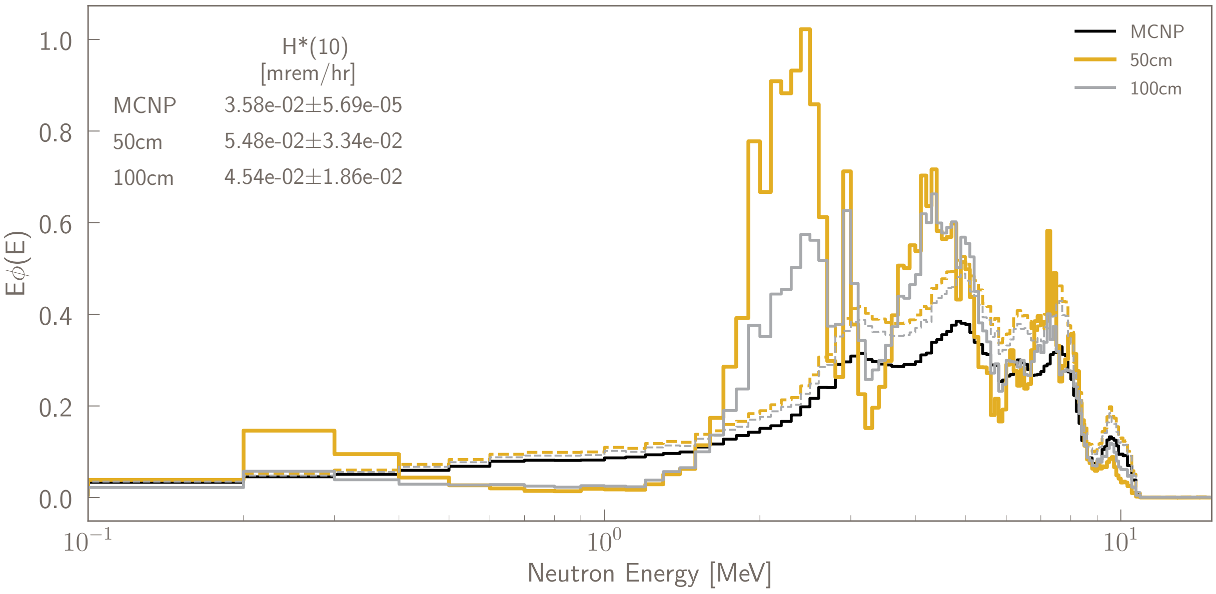

(b) ^{241}AmBe

Figure 8.12. Unfolded spectra demonstrating the effect of using a response matrix for unfolding that was optimized on data from a different distance . The above cases correspond to 100 cm experimental data from detectors M76 and T3 deconvolved with 50 cm and 100 cm optimized response matrices.

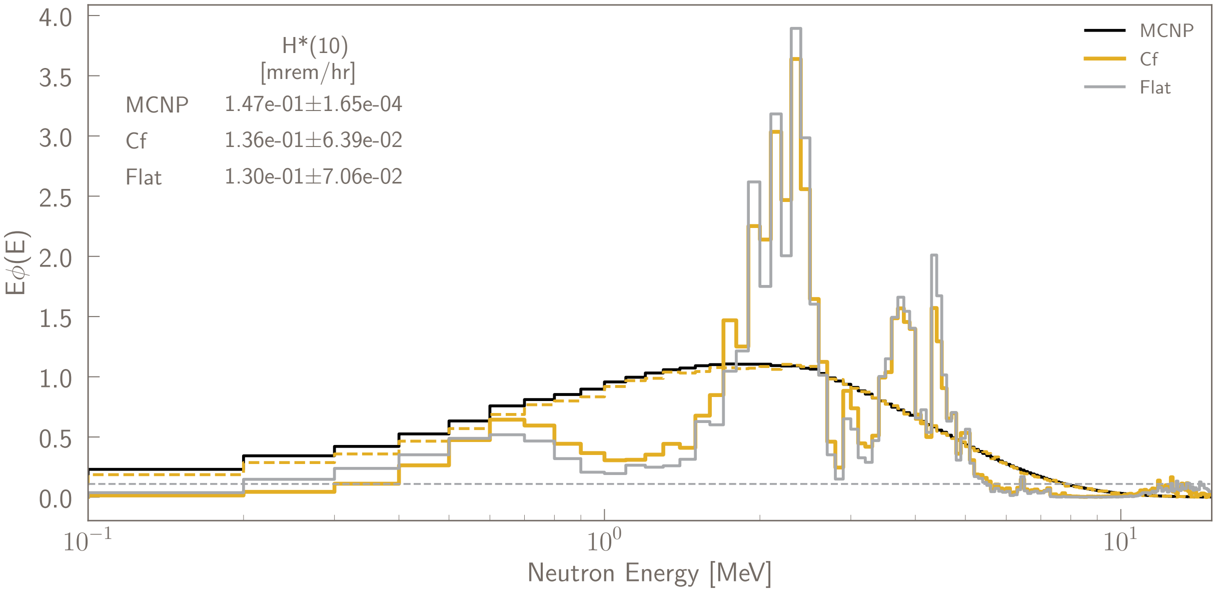

(a) ^{252}Cf

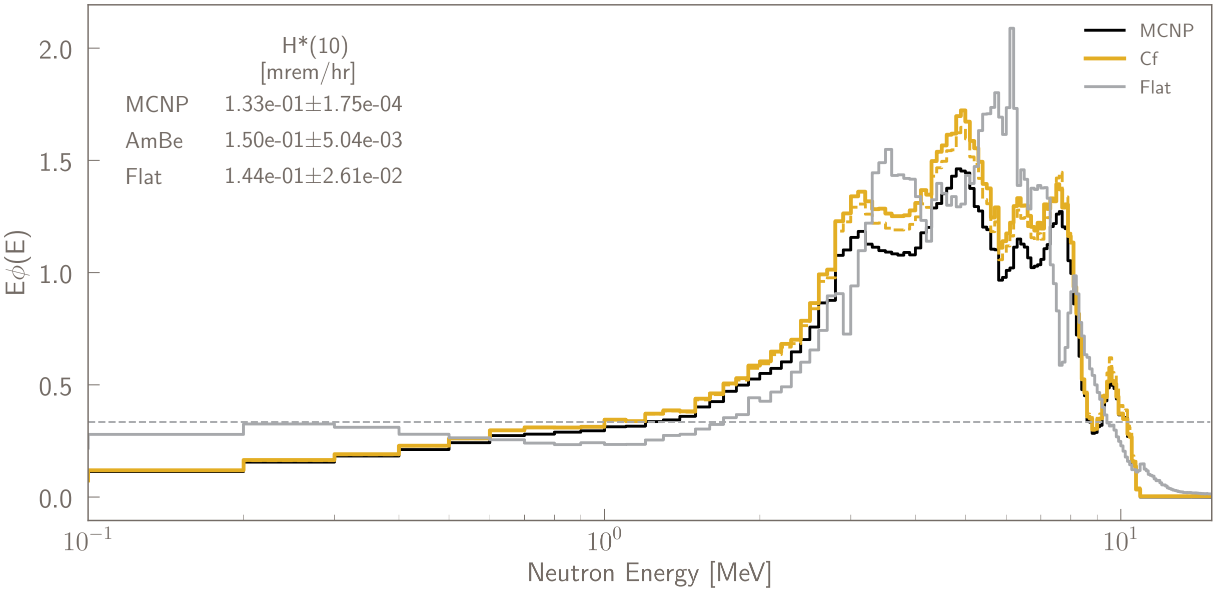

(b) ^{241}AmBe

Figure 8.13. Unfolded spectra from the 50 cm dataset using the response matrices and count rate data for all three detectors M76, T3, and T1.

9. MONITORING OF THERMAL AND EPITHERMAL NEUTRONS USING BORATED FLUIDS

This chapter discusses experiments related to expanding TMFD neutron sensitivity to epithermal and thermal energies via the addition of boron into the detection fluid. A proof-of-concept experiment using CTMFD's and a heavily moderated source was designed and modeled in MCNP to demonstrate that a statistically significant step-increase in the detector's count rate can be achieved in borated detectors. Importantly, the resulting increase is not observed when a strong thermal neutron poison is present, indicating that the elevated count rate is solely the result of (n,α) events as opposed to a shift in the fast neutron sensitivity. The pressure detection threshold for the (n,α) reaction, estimated from experimental data, is analyzed using the probabilistic modeling framework introduced in chapter 5. Finally, the chapter concludes with a brief discussion on the application of thermally sensitive CTMFDs in the context of the spectro-dosimetric detector panel described in chapter 7.

9.1 Motivation for Thermal Sensitivity in TMFDs

Enablement of thermal sensitivity in TMFDs is a topic that has been explored for several years by various other colleagues, as the capability has relevancy in other detection applications unrelated to dosimetry, such as special nuclear monitoring. The reasoning behind the idea of borating the detection fluid is rooted in prior experience with detection of dissolved alpha-emitting nuclei, such as ^{238}U. The work eventually led to the idea of dissolving ^{235}U into the detection fluid, which at that time was acetone, whereby detection events are initiated from the recoiling fission products. The proliferation concerns of having a fissile material inside the detector make such an idea impractical, however.

While there are numerous isotopes with absorption reactions, the challenge lies in finding a detection fluid or combination of detection fluid and additive that meets the following criteria:

- The absorption reaction must produce daughter nuclei with enough energy and high enough LET to induce nucleation at a reasonable negative pressure.

- The macroscopic cross section must be large enough to achieve an efficiency commensurate with alternative modern detection technologies. Alternatively, the cross section must not be so large that the TMFD becomes easily paralyzed.
- The detection fluid or additive combination must be chemically compatible such that spurious nucleation and false positives are negligible.
- The detection fluid or additive should have a negligible effect on the fast neutron sensitivity, or the change in the fast neutron sensitivity must be quantifiable.

9.2 Thermal Detection Fluid Compositions and Cross Section Estimates

With consideration of the traits for an idea detector described above in section 9.1, a tertiary combination of DFP $C_5F_{10}H_2$, TriMethylBorate $C_3H_9BO_3$, and Methanol CH_4O was devised for the detection fluid. The possibility exists to vary the relative proportions of the mixture components depending on the desired ratio of fast versus thermal sensitivity, though the range of combinations is constrained by chemical compatibility considerations due to TriMethylBorate's (TMB) tendency to oxidize in the presence of water or the humidity in the air. Crystalline precipitates form as a result of the decomposition reaction, which can lead to spurious nucleation induced false positives. Methanol, which is a solvent for TMB, is added to act as a "garbage collector" for any precipitates.

Three different mixture compositions were devised to characterize the relative trend in the detector's count rate as a function of TMB content. The first mixture tested had a composition (by weight) of 90% DFP, 8% TMB, and 2% Methanol, which we will refer to in shorthand notation as DFPTMBM 90-08-02 or just 90-08-02 throughout the remainder of the document. The alternative candidate mixtures had compositions of 80-16-04 and 60-32-08, equating to a doubling of the weight percent TMB. The atomic compositions, mean free path for thermal neutrons, and mixture density are shown in table 9.1. The mean free path ranges between 0.626-2.036 cm for the 60-32-08 and 90-08-02 mixtures. As a point of reference, the mean free path of 0.025 eV neutrons in BF_3 gas at 1 atmosphere is approximately 10 cm. Note that the short interaction path length in DFPTMBM solutions is achieved with natural boron. If an even higher thermal efficiency is desired, the TMB could be specially enriched to higher ^{10}B concentrations.

Table 9.1. Atomic composition of the different DFP-TMB-M mixtures tested for thermal neutron detection. The ^{10}B atom density is used to calculate the mean free path for thermal (0.025 eV) neutrons.

Isotope	**Mixture Composition**		
	90-08-02	80-16-04	60-32-08
C	1.815E+22	1.768E+22	1.680E+22
H	1.447E+22	2.049E+22	3.018E+22
O	2.562E+21	4.771E+21	8.341E+21
F	3.118E+22	2.581E+22	1.692E+22
^{10}B	1.278E+20	2.379E+20	4.159E+20
^{11}B	5.446E+20	1.014E+21	1.773E+21
density $\left[\frac{\mathbf{g}}{\mathbf{cm^3}}\right]$	1.450	1.35	1.18
mean free path [cm]	2.036	1.094	0.626

9.3 Description of the Experimental Geometry and Basis for Experimentation

Experiments investigating thermal neutron sensitivity in CTMFDs required a softer spectral fluence than could be obtained using bare sources in the enclosed room geometry. Since CTMFD's currently do not have the capability to distinguish a detection initiated by fast versus thermal neutrons on a single event-by-event basis, the most ideal spectrum for characterizing the thermal neutron detection efficiency would be one that has a negligible fast component. Completely removing the entire fast component from an isotope source's spectrum using only moderation is impractical for a scoping study. Thus, any hypothetically measured detector response manifests as the summation of the fast and thermal count rates. While a less desirable option, the possibility also exists to remove the thermal component of the spectrum to characterize the detector's response solely to fast neutrons using a neutron poison. The thermal response can then be deduced by differencing the detector responses with and without the absorptive shielding present.

A specialty thermal neutron shielding material SWX-238 Flexi-Boron (FB), a flexible boron-doped silicone rubber manufactured by Shieldwerx™, was selected as the neutron poison on account of its usefulness for shielding irregular shapes and ability to adhere to straight or curved surfaces. The atomic composition of FB is shown in table 9.2, where it can be seen that the material is heavily hydrogenated thus will have an inherent moderating effect on the fast spectrum as well. The manufacturer-provided data in fig. 9.1 implies that FB's moderating impact on the fast neutron spectrum should be negligible. For example, the thickness of material required to reduce 90% of a 1 MeV beam of neutrons to epithermal energies is approximately 2.5 inches which equates to a factor of 20 greater than the 1/8" thick sheet used during experimentation. In contrast, the thickness to reduce the intensity of thermal neutrons by 90% is only 0.048 inches. The above logic forms the foundation for the underlying assumption that the detector's thermal response can be extracted from count rate differencing.

Table 9.2. Atomic composition of the Shieldwerx™ Flexi-Boron thermal neutron shielding material.

Element	**Weight %**	**Atomic Density** $\left[\frac{\text{atoms}}{\text{cm}^3}\right]$
B	27.55	2.51E+22
Si	26.85	9.41E+21
O	23.57	1.45E+22
C	18.69	1.53E+22
H	2.76	2.70E+22
Zn	0.26	3.87E+19
N	0.16	1.10E+20
Fe	0.16	2.86E+19
Material Density $\left[\frac{\text{g}}{\text{cm}^3}\right]$	1.64	

A ^{252}Cf source was selected for experimentation to be representative of the fission neutron spectrum one might encounter at a power plant or industrial work environment. At the time of experimentation the source intensity was 6.5x10^4 n/s. A large amount of moderator is necessary to reduce the source intensity to a range ideal to the CTMFD. Rather than stacking a large number paraffin blocks for moderation and risk introducing artifacts in the data from

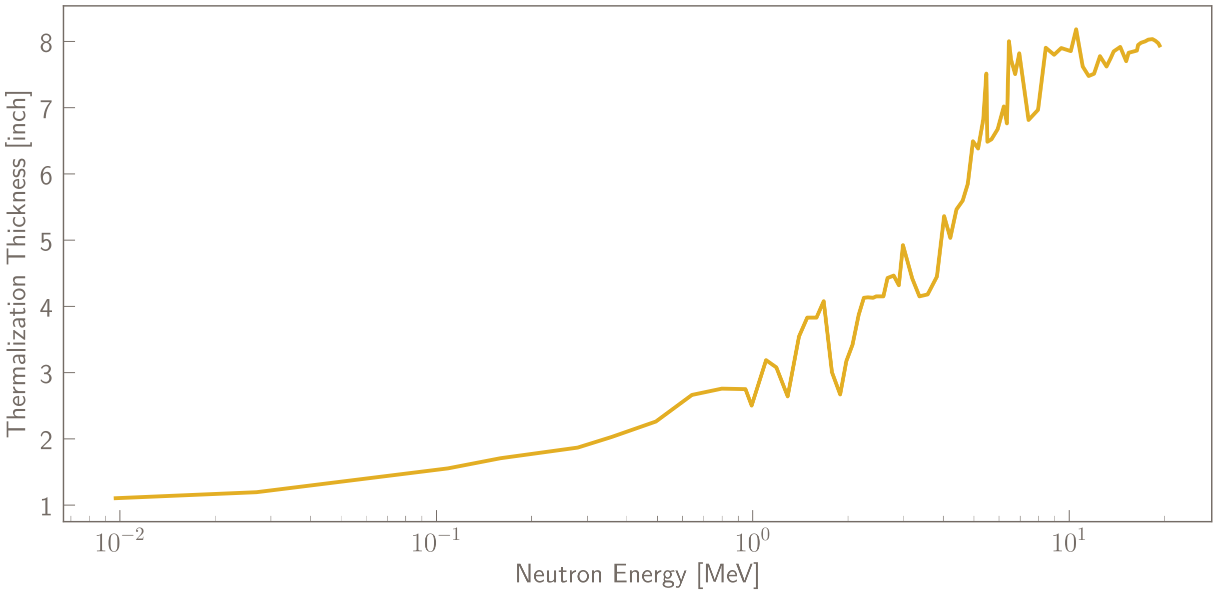

Figure 9.1. Required thickness of Flexi-Boron shielding to reduce 90% of incident fast flux to thermal energies, i.e. the exit epithermal flux is 10% of incident neutron flux.

neutron streamlining, the source was placed within a drop tube at the symmetrical origin of an approximately 0.35 m^3 block of ice. As shown by the schematic in fig. 9.2, the shortest path length that a neutron could travel from the source to the 3 cm^3 detector would require passage through 25 cm of moderation.

9.3.1 MCNP Modeling of the Moderating Geometry

An MCNP model was constructed to assess the effect of the as-described moderating geometry had on the raw ^{252}Cf spectrum. While not shown in fig. 9.2, the simulation geometry also contains the concrete floor and soil beneath to best represent contributions from albedo. The simulated flux spectrum though the detector bulb is shown in fig. 9.3. For quantitative comparison, the ratio of the thermal component of the flux to that of the fast is compared. The neutron energy defining the thermal cutoff is set at 1x10^{-4} MeV. At this neutron energy, the (n,α) reaction rate is approximately two orders of magnitude less than

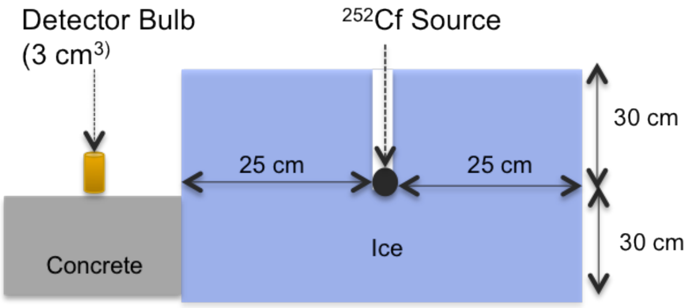

Figure 9.2. Schematic of the moderating geometry used for thermal neutron sensitivity experiments in the CTMFD where the source to detector total distance is 45 cm.

at thermal energies. The energy cutoff for fast energies is set at 0.1 MeV to coincide with the CTMFD's response matrix. Thus, inclusion of epithermal energies would only dilute the ratio because they contribute very little to the count rate.

Table 9.3 contains data for the integral fast and thermal flux totals and predicted (n,α) reaction rate inside the detector sensitive volume. It can be seen that the ice moderation increases the thermal-to-fast metric by a factor of 14. The fast fluence is decreased by a factor of 20. However, past 15 cm of shielding the ratio begins showing diminishing returns as the the absorption cross section for water becomes of significance.

Table 9.3. Integral flux totals and reaction rates predicted by MCNP for the geometry in fig. 9.2.

E [meV]	No FB	With FB	Unmoderated
$\phi_{Th}(E < 10^{-4})$	0.201	0.038	0.276
$\phi_{Th}(E > 10^{-1})$	0.150	0.149	2.867
ϕ_{Th}/ϕ_F	1.342	0.257	0.096
$\dot{C}$ [cpm]	4.769	0.633	4.381

9.4 Count Rate Measurements in Highly Moderated Spectra

At the time of experimentation the CTMFD detector system described in section 7.2 and much of the engineering related to quality-control had not yet been developed. Rather than

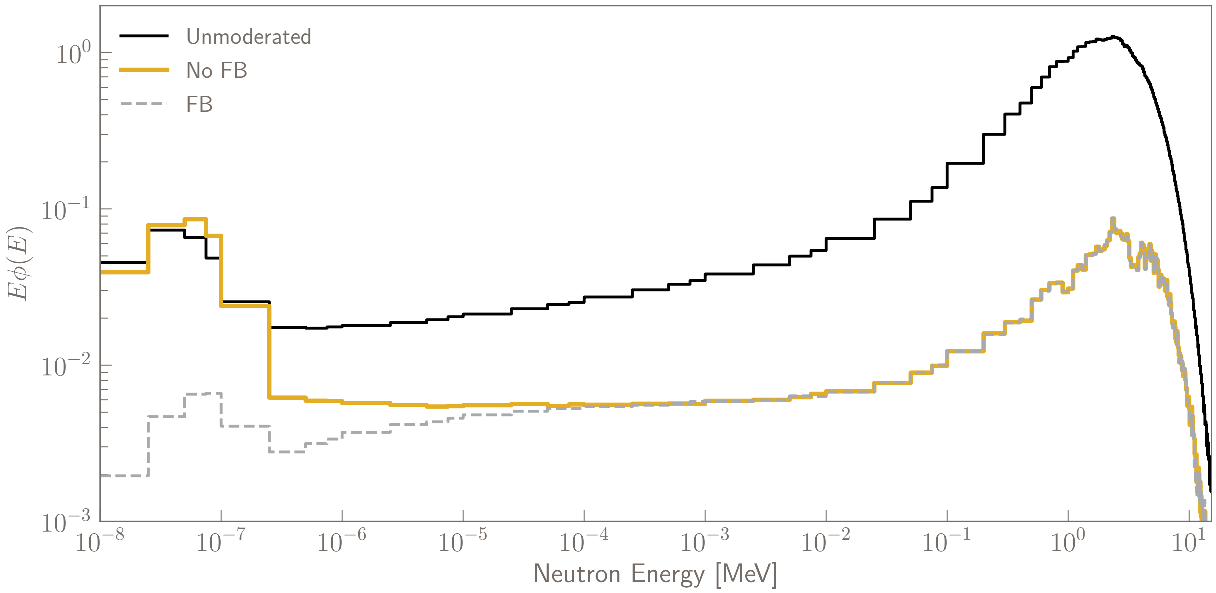

Figure 9.3. Moderated flux spectra used throughout the thermal sensitivity experiments. The gold and gray curves represent the moderated spectrum with and without the FlexiBoron thermal neutron absorber. Though not actually used during experimentation, the black curve is included as a reference point for an unmoderated ^{252}Cf spectrum

the currently employed direct current motors, CTMFD's were driven by alternating current motors. The high heat output of the alternating current motors introduced issues with temperature stability, whereby the sensitivity of the detector was transiently coupled with changes in the detection fluid temperature. The efficiency of the detector increases as the detection fluid's temperature rises. With the AC motor system, the fluid temperature could change as much as 7 °C between detection intervals. A method was later implemented to compensate for temperature fluctuations. The results are also biased because the detectors did not operate under a vacuum so all results are shifted by approximately 0.6 bar. As such, it would not be appropriate to assume the experimental results described in this section will accurately translate to the thermal detector in the panel system described in section 7.3.

Figure 9.4 contains count rate data for three detection fluids: 100-00-00, 90-08-02, and 90-00-10; i.e. pure DFP, borated DFP, and DFP with methanol. The 100-00-00 and 90-00-10 count rates closely overlap, indicating that the presence of methanol has very little effect on the fast sensitivity. The difference in the detection rates between the borated and non-borated detectors is readily apparent. The 90-08-02 count rates sharply increase between 4.5-4.75 bar and almost plateau by 5.0 bar. Similar step-like increases in the observed count rates are seen when alpha-emitting isotopes like ^{241}Am are dissolved into the detection fluid. Decay events are detected with near 100% efficiency just above the pressure threshold and undetectable just below. Experimental count rates do exhibit a finite slope across the threshold however on account of the pressure gradient in the bulb. The described behavior closely resembles the trend in fig. 9.4 and thereby indicates that the (n,α) reaction is detectable.

Further evidence in support of the above assertion is found in the experimental results for cases with and without FlexiBoron. The count rates shown in fig. 9.5 correspond to detection fluid compositions of 80-16-04 and 60-32-08. A comparison to the count rates from fig. 9.4 would not be valid because the source-to-detector distance had to be increased by approximately 50% to prevent saturation. The decrease in count rates when FlexiBoron is present confirms that the elevated count rates are the result of (n,α) detections.

9.5 Comments on the Energy Deposition Thresholds Implied from Experiments with Neutrons versus Alphas

Following the confirmatory evidence that CTMFD's can detect thermal neutrons, efforts were undertaken to validate the experimental data with the MCNP simulation results from section 9.3.1. Multiplication of the macroscopic absorption cross section for the DFPTMBM 90-08-02 detection fluid with the fluence results in fig. 9.3 yields a theoretical (n,α) detection rate of 4.77 counts per minute. Referring back to fig. 9.4, the experimental (n,α) count rate is approximately 3.84 cpm at 5 bar which is 20% lower than predicted by MCNP; whereas at 6 bar the difference is only 7.5%. At a centerline pressure of 6 bar the entire central volume is above the identified threshold pressure of 4.5 bar compared to only 50% of the volume at a centerline pressure of 5 bar. As a consequence, it would be expected that the experimental count rates at 5 and 6 bar would be proportional to the increase in sensitive volume. Such a trend is not observed in practice.

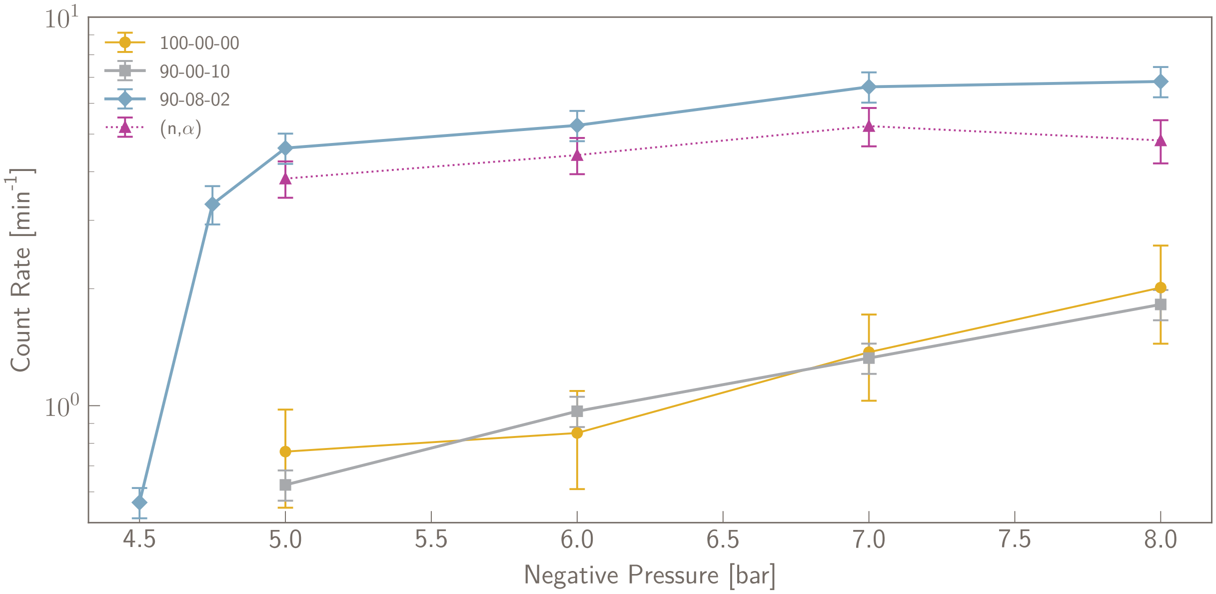

Figure 9.4. Count rates measured outside of the ice fridge moderator. The difference in the count rates between the borated (90-08-02) and non-borated (90-00-10) detection fluid mixtures represent the rate of (n,α) events. To demonstrate that the addition of methanol has little effect on the fast neutron sensitivity, the count rates recorded with pure DFP (100-00-00) are also shown.

The exact cause of the disagreement between experiment and simulation is unknown. Numerous assumptions exist in both experiment and simulation where it would not be unreasonable to assign several percent uncertainty as a result of each assumption. For example, it is expected that the thermal region of the flux spectrum in fig. 9.3 will inherently be less accurate than the fast region [37]. However, this section will limit its discussion to one area that is particularly problematic: that is, the best approximation for the deposition energy threshold for cavitation from the optimization analyses in chapter 7 conflicts with the experimentally measured α detection pressure thresholds. Additionally, the thermal (n,α) threshold is also in conflict with measured thresholds for dissolved α-emitting actinides.

For instance, consider the 100 cm optimized A,N coefficients from table 7.2. At a centerline pressure of 4.5 bar, the parameterized DETC curve implies an energy deposition of approximately 35 keV is necessary for detection. Note that when referencing the 4.5

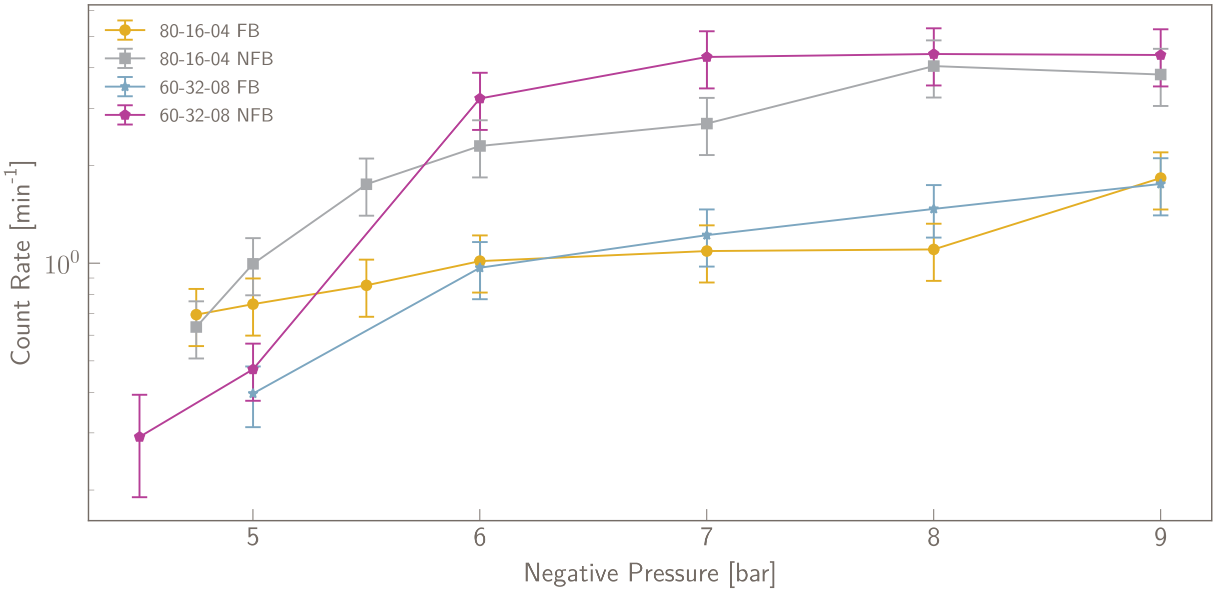

Figure 9.5. Count rates measured outside of the ice fridge moderator with and without a cylindrical thermal neutron shield around the acrylic containment.

bar detector centerline pressure, the fluid is actually experiencing 5.12 bar of tension because pulling a vacuum on the detector adds an additional 0.62 bar. This offset needs to be accounted for when calculating the deposition energy necessary for cavitation. Neutron threshold experiments with SDDs have shown that the deposition energy threshold for cavitation, calculated from experiments with monoenergetic neutrons, are in close agreement with α-recoil thresholds in the ^{241}Am decay chain [46]. Results with α-emitting actinides in TMFDs imply thresholds much higher than 35 keV.

Experiments with ^{222}Rn in DFP have identified the pressure detection threshold for ^{218}Po, one of the daughter products in the decay chain, to also be 4.5 bar. The difference between the reaction Q value of 6.115 MeV and an alpha energy of 6.002 MeV equates to a ^{214}Pb recoil kinetic energy of approximately 113 keV. The ^{214}Pb recoil can be assumed to deposit all of its energy in the 1035 A critical diameter because its range is smaller than the diameter. The 6 MeV α-particle will deposit on average an additional 10 keV inside a critical diameter. If assumed the daughter products are born with momentum vectors in the same direction, the length scale for energy deposition is represented by the critical diameter length and the total energy deposition inside the cavity equates to 123 keV. Since the ^{222}Rn nucleus has essentially zero momentum prior to decay, it is more realistic to assume the products travel in opposite directions, in which case the length scale for energy deposition would be 518 A, half of the critical diameter, and the combined energy deposited is approximately 86 keV.

Application of the probabilistic modeling framework to the ^{214}Pb recoil ion case also implies the pressure detection threshold should be lower. Consider the half-diameter case in fig. 9.7, since the range of both recoils is greater than the deposition length scale, energy straggling necessitates that the detection probability cannot be binary, despite the fact that it contradicts experimental observations. The detection probability for the full-diameter case exhibits a more step-like response. However, the Pb ion's 113 keV energy deposition still far exceeds the 35 keV prediction implied by the results with neutrons.

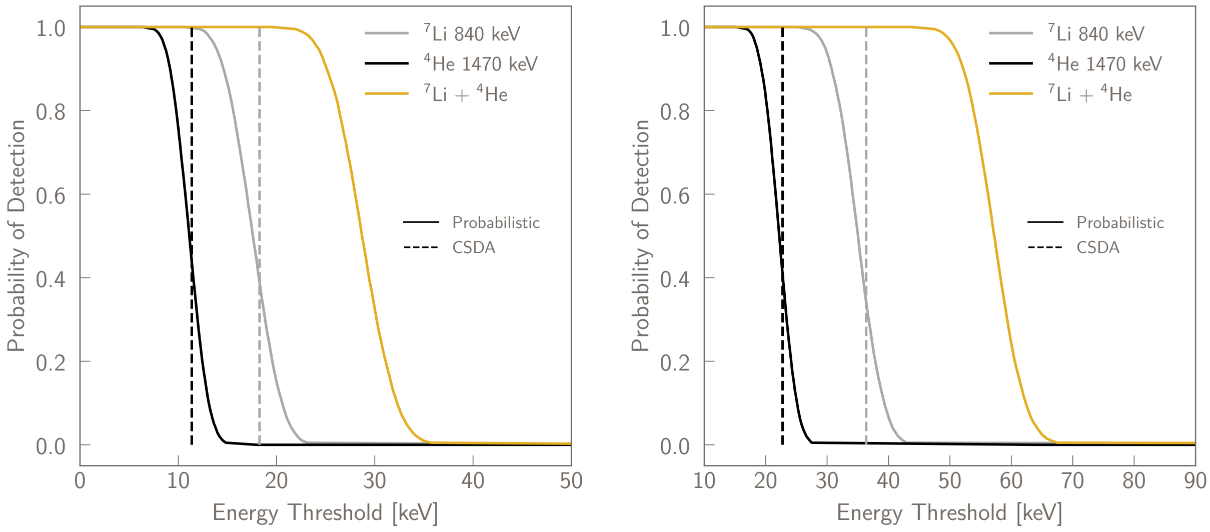

(a) 518 Angstroms

(b) 1035 Angstroms

Figure 9.6. Detection probability estimates from the probabilistic model for the ^{7}Li and ^{4}He reaction products following a ^{10}B thermal capture event. The gold line represents the summation of the energy deposition by both recoil products over a given length scale. The subfigures correspond to the probability if the deposition length scale for each ion is assumed to be a full critical diameter or half of a diameter.

Detection probability curves for the ^{7}Li and ^{4}He reaction products are shown in fig. 9.6. While still ambiguous, the threshold implied by the reaction products energy deposition is closer in agreement with the results for neutrons than ^{214}Pb. For the half diameter case, the combined energy deposition of ^{7}Li and ^{4}He does not exceed 35 keV. Whereas, for the full diameter length scale, the ^{7}Li ion is shown to be capable of depositing the necessary 35 keV for detection approximately 50% of the time. The slope of the detection probability curve suggests that the effect of energy straggling is not significant. The energies corresponding to a 90% and 10% detection probability are 31 keV and 39 keV, respectively, which approximately equate to centerline pressures of 4.25 and 4.75 bar. Thus, unlike results with dissolved actinides, it appears plausible that the step-like response of the count rates in fig. 9.4 is accounted for to some degree by the probabilistic model's handling of energy straggling.

9.6 Estimation of the Dosimetric Response for Neutrons Below 100 keV

Given the ambiguity in the energy threshold predictions for neutron and dissolved actinides and thermal (n,α) events, the decision was made not to simulate the TMFD's response to neutrons below 100 keV. Recall, the underlying motivation for this work was to adapt TMFD's to function as a dosimeter. The weighting factor for thermal and epithermal neutrons relative to fast energies is too small to justify the time and effort necessary to address the discrepancies reported in the prior section. Considering the moderated spectrum in fig. 9.3 as an example, neutrons with energies below 100 keV constitute over 50% of the total fluence but only 5% of the dose.

It is worth mentioning that, even if the CTMFD's response below 100 keV could be adequately simulated, it would not be possible to extract spectroscopic information the way the multi-detector panel in section 7.3 is currently configured. With only one thermal count rate, the response matrix would only contain a single bin with a non-zero response below 100 keV. More than one response function is necessary to deconvolve the spectrum shape and thus would require the addition of a fifth detector unit to the panel. Additionally, the response function of the fifth unit would have to sufficiently differ from the dedicated thermal unit already present, such as from the addition of polyethylene around the detector. The corresponding weight increase would be counterproductive to the system's practicality and is in essence equivalent to a Bonner spectrometer.

Without attempting to resolve the ambient energy spectrum, the solution adopted to incorporate the dose from neutrons below 100 keV involved calibrating the thermal unit as if it were a rate meter to determine the count rate per unit dose. Cognizant of the discussion in section 1.2 regarding the problems with calibrating rate meters to a specific energy spectrum, the calibration constant is computed from the average of the dose conversion constants from experiments with two different spectra. The sources were selected under the premise that averaging the results from two different spectra attempts to mitigate the pitfalls of over fitting.

Two experiments were performed, firstly, with the ^{252}Cf source encapsulated inside a 5 inch HDPE sphere at a distance of 100 cm, and secondly, with the ^{239}PuBe source placed within a 2" diameter, 0.04" thick, aluminum drop tube placed at the center of an 11 inch right circular cylinder volume of paraffin wax (height of 13 inches) at a distance of 200 cm. MCNP simulations indicated the corresponding dose rates from neutrons with energies less than 100 keV to be 0.7μRem/hr and 10 μRem/hr.

The count rates obtained with the borated and non-borated 1.6 cm^3 detectors are shown in fig. 9.8. The excess detection rate was calculated for each experiment at a negative pressure of 5 bar. Unfortunately, due to dead-time issues, the highest measurable negative pressure for the moderated Pu-Be case was 4.75 bar; therefore, the live time detection rate was linearly extrapolated to 5.0 bar. The result was a calibration factor of 0.214 μRem/hr per CPM and 0.219 μRem/hr per CPM, respectively.

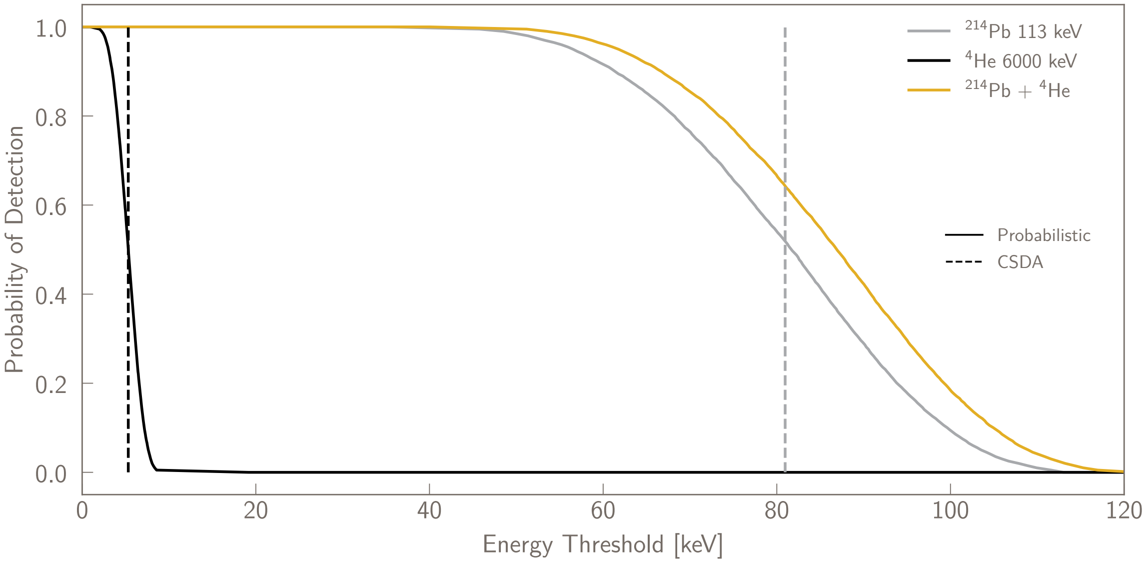

(a) 518 Angstroms

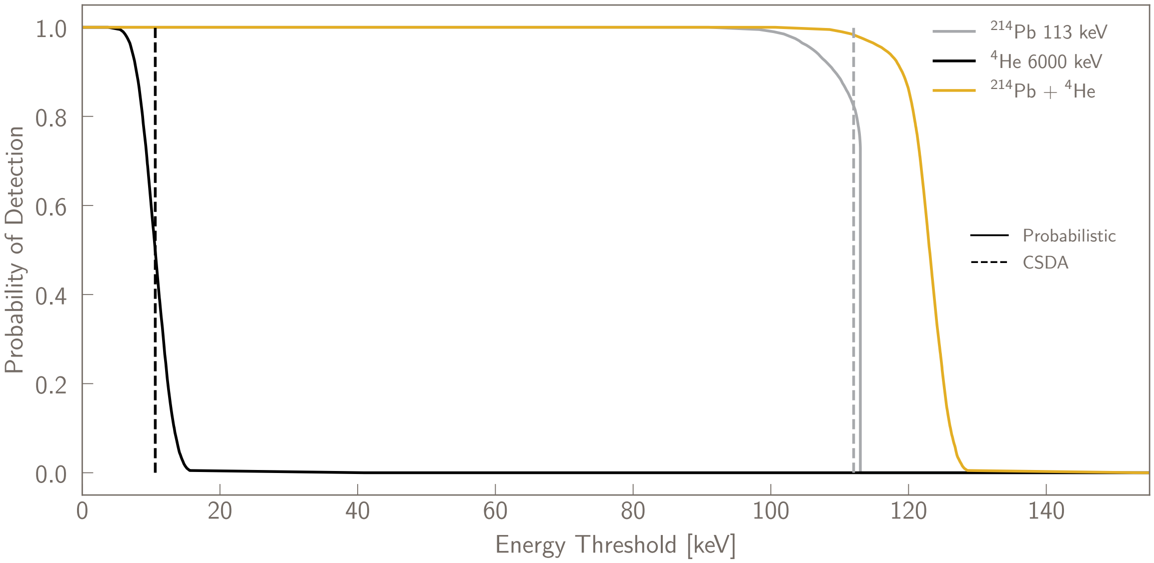

(b) 1035 Angstroms

Figure 9.7. Detection probability estimates from the probabilistic model for the ^{214}Pb and ^{4}He reaction products following a ^{218}Po α decay. The gold line represents the summation of the energy deposition by both recoil products over a given length scale. The subfigures correspond to the probability if the deposition length scale for each ion is assumed to be a full critical diameter or half of a diameter.

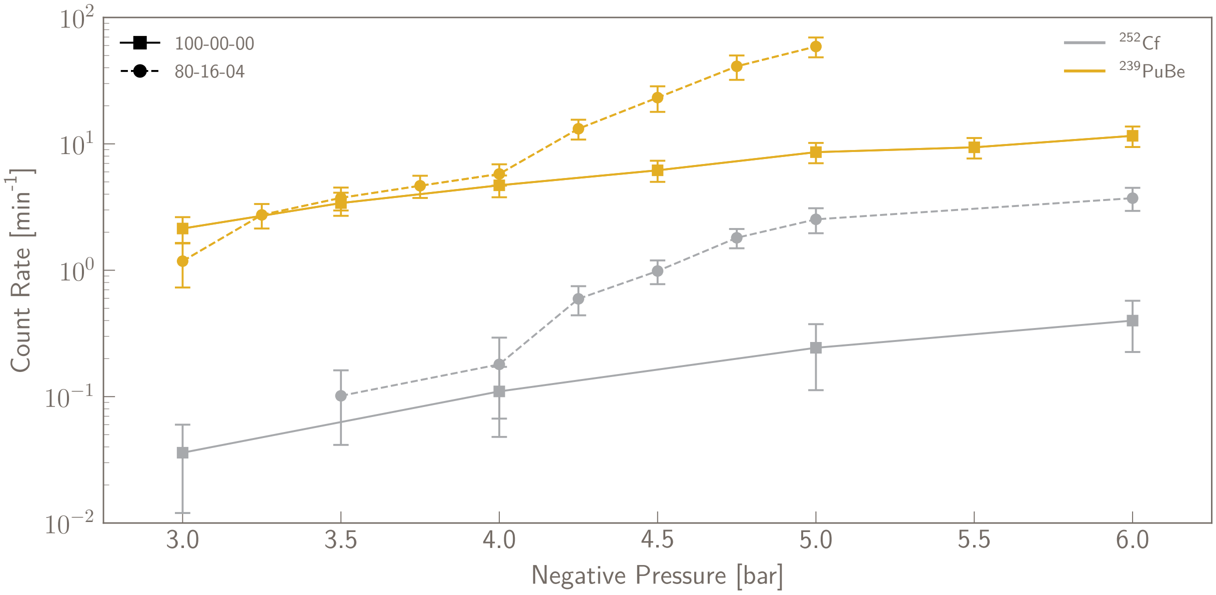

Figure 9.8. Detection rates for the borated (dashed line) and non-borated (solid line) detectors used to calibrate the thermal dose conversion factor for the spectrodosimetric panel described in chapter 7. The moderated neutron sources in this dataset consist of ^{252}Cf at 100 cm in a 5 inch sphere of HDPE and the ^{239}PuBe in an 11 inch diameter paraffin right circular cylinder.

10. EVALUATION OF H*(10) CAPABILITIES IN TMFD SENSORS AT OAK RIDGE NATIONAL LAB

This chapter discusses work related to a Department of Energy research grant with Oak Ridge National Laboratory (ORNL) to evaluate the accuracy of TMFDs as an H*(10) dosimeter by comparison with results from a LiI Bonner Sphere spectrometer. The evaluation consisted of measurements with a series of unknown sources with the TMFD system by the Purdue MFRL staff, followed by independent data acquisition and analysis by the ORNL staff. The results of the evaluation, published in a technical report by the ORNL staff, are discussed and critiqued. After which, the raw data is used in a secondary follow-up analysis.

10.1 Summary of the Experiments at ORNL

As part of the specification of the Department of Energy grant, the accuracy of the TMFD systems H*(10) dose estimates were to be tested in a one-to-one, independent comparison with a bonner sphere spectrometer system. Analogous to operation in a real-world environment, experiments with the CTMFD system were performed without prior knowledge of the neutron spectrum or intensity of the radiation field being measured. The source configurations, shown in table 10.1, were selected entirely by the ORNL staff, based only on guidance regarding what dose rate is most appropriate for the CTMFD system.

Table 10.1. Source configurations for the experiments at ORNL.

Configuration	Source	Activity [n/s]	Moderation
1	^{252}Cf	232871	None
2		232871	Lead
3		120016	Lead
4		232871	Polyethylene
5		120016	Polyethylene
6		232871	Steel
7		120016	Steel

The count rate measurements and unfolding analysis were not performed congruently for the CTMFDs. The unfolding-related analyses were performed by the MFRL staff upon return to Purdue. The dose rates estimated from the CTMFD measurements were submitted to the ORNL staff before the details in table 10.1 were made available. Once received, the ORNL staff independently replicated the experiments with the BSS system. Unfolding of the data was done through a supplemental LabVIEW user-interface supplied by Sagamore-Adams LLC. The program is essentially a user-friendly wrapper around the UMG software package, which was designed to simplify and standardize the advanced input options needed by the MAXED unfolding code. The details of the experiments, raw data, BSS unfolding analyses, and dose rate comparisons with the CTMFD were then compiled by Bell [54] into a technical report.

All measurements were performed at ORNL in Building 3500, 2nd floor, room D001. The details of the source configurations and detector geometry are taken from the technical report. The geometry of the room is shown in fig. 10.1. The source source-to-detector distance was 126 cm for both systems. A Ludlum 42-41L Prescilla detector connected to a Ludlum 2363 neutron/gamma dose rate meter was set on a tripod on the opposite side of the table at the same distance from the source as was the BSS/CTMFD cart to act as a flux monitor. The idea of the flux monitor was to provide a time stream of dose rate data throughout all experiments to verify that an external experiment in another room was not contaminating the CTMFD/BSS measurements.

The Ludlum 42-41L computes dose through a straight conversion from cpm to mrem/hr based on a specified calibration factor. The response of the detector does not perfectly follow the H*(10) dose curve, and thus some degree of error is expected for spectrums that differ from the spectrum the detector was calibrated to. Calibration is accomplished by exposing the meter to a NIST-traceable ^{252}Cf source at a distance such that the dose rate is 20 mRem/h, a value well within the 0.1–1000 mRem/h range of the meter. The conversion factor at the time of the ORNL measurements was 200 cpm/(mRem/h). Note that, the manufacturer recommends a calibration value of 350 cpm/mRem/hr, based on an ^{241}AmBe spectrum, a factor of 1.75 higher than when calibrated with ^{252}Cf. The dose rate was recorded by accumulating counts during 60-second intervals. Since the measured dose rates were close to the lower operational limit of the detector, the uncertainty in the dose rates are high as a

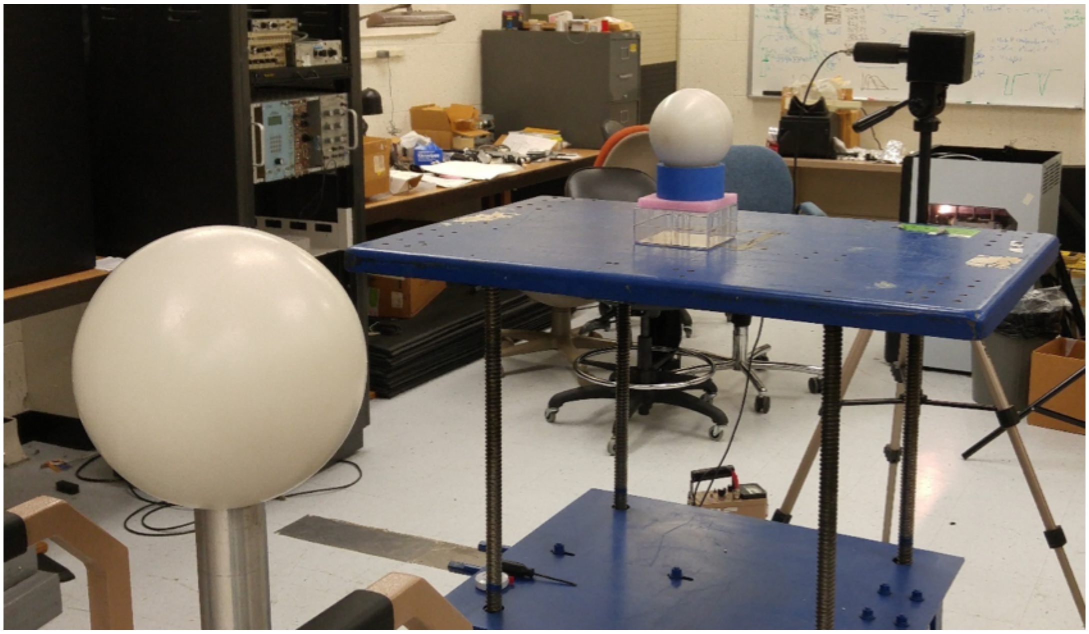

Figure 10.1. Geometry of ORNL building 3500 room DOO1 where the measurements were taken, shown for the BSS. The source/moderator combination rested on the blue cart in the center of the picture. A Ludlum 42-41L, located on a tripod in the upper right of the picture, was used as a flux intensity monitor.

result of poor counting statistics. Nevertheless, the meter was still able to successfully verify that the CTMFD and BSS measurements were not contaminated by external sources.

The source moderators were chosen for their effect on the neutron spectrum. The polyethylene and steel moderators were realized as four concentric spheres with a 4.8” outermost diameter with a total of 1.83” of material between the center and outer edges. The ^{252}Cf sources were placed within the innermost sphere. The shells are stepped at the equator so that no unobstructed line-of-sight paths between center and outside of the assembly exist. The lead moderator was constructed from an 8” × 8” × 6” × 1” thick rectangular shell supported by 4” of lead and covered by 1” of lead plate. The source was placed on plastic foam in the center of the moderator. Images of the moderators are shown in fig. 10.2.

Measurement of the seven sources with the CTMFDs took place over a period of approximately 5 days from 8/27/2018-8/31/2018 using the same multi-detector panel system described in section 7.3, which contains three detectors for measurement of fast neutrons and one borated detector to estimate the thermal dose rate. Plots of the count rates for

(a) Polyethylene and steel spherical moderating shells.

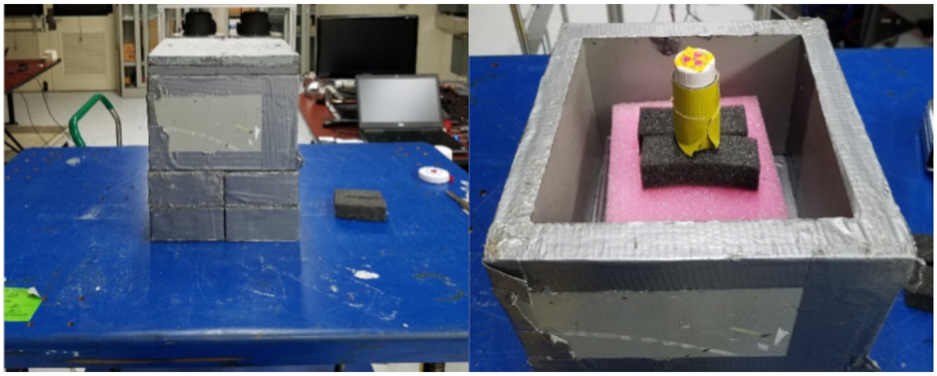

(b) Lead moderator

Figure 10.2. Polyethylene, steel, and lead moderators used in the experiments at ORNL.

each CTMFD and each source are shown in fig. 10.5. Though data was acquired with the capillary volume detector, T1, it was ultimately not used in the unfolding analysis due to the same issues described in section 7.3.3. At the present time, a well-defined procedure does not exist for what pressures the detectors need to be operated at for unfolding. A trained or experienced operator is considered necessary to understand the nuances of the detector's efficiency and response as a function of the neutron spectrum shape. Given that information about the source spectrum being measured was not available, it was decided that a predetermined procedure would not be created.

Each CTMFD would sweep its respective pressure range in as fine of increments as would be possible to obtain adequate counting statistics for all seven sources in a five day time window. This roughly equated to one measurement each day of about 8-12 hours during the day and one overnight measurement of approximately 12-16 hours. The pressures were swept in a cyclic manner, obtaining approximately 50 detections at each pressure before changing to the next, typically in increments of 0.5 bar or 1.0 bar. Operating in this manner, as opposed to a single long count at each pressure, allowed for adjustments mid-experiment by the operator as deemed appropriate. In the count rate curves of fig. 10.5 the average count rate of each specific set is shown as a scatter plot to verify that the multiple measurements were normally distributed. Note, however, that the data input into the unfolding algorithm is actually the summation of all measurement sets, such as would be the case with a single long counting window. The purpose of the summation is to reduce the magnitude of the statistical counting uncertainty.

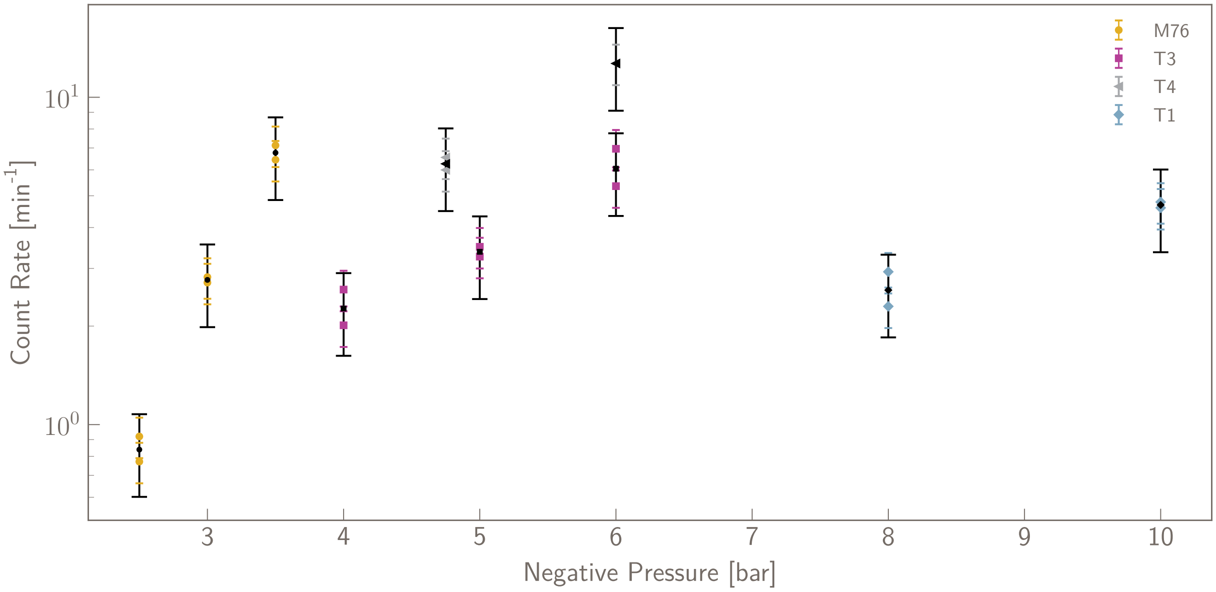

(a) Source 1: Bare Cf

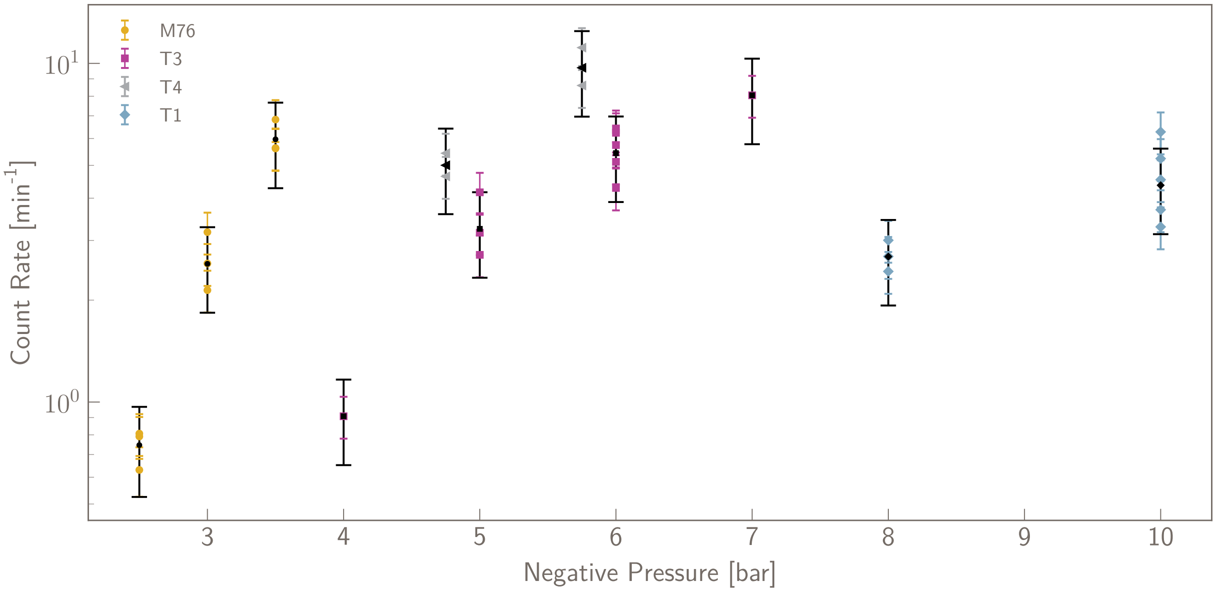

(b) Source 2: Cf in lead

Figure 10.3. Count rates for the four CTMFD's in the multi-detector system. The colored markers represent the average from each individual measurement. The black markers represent the average across all measurement sets, shown with two sigma error bars.

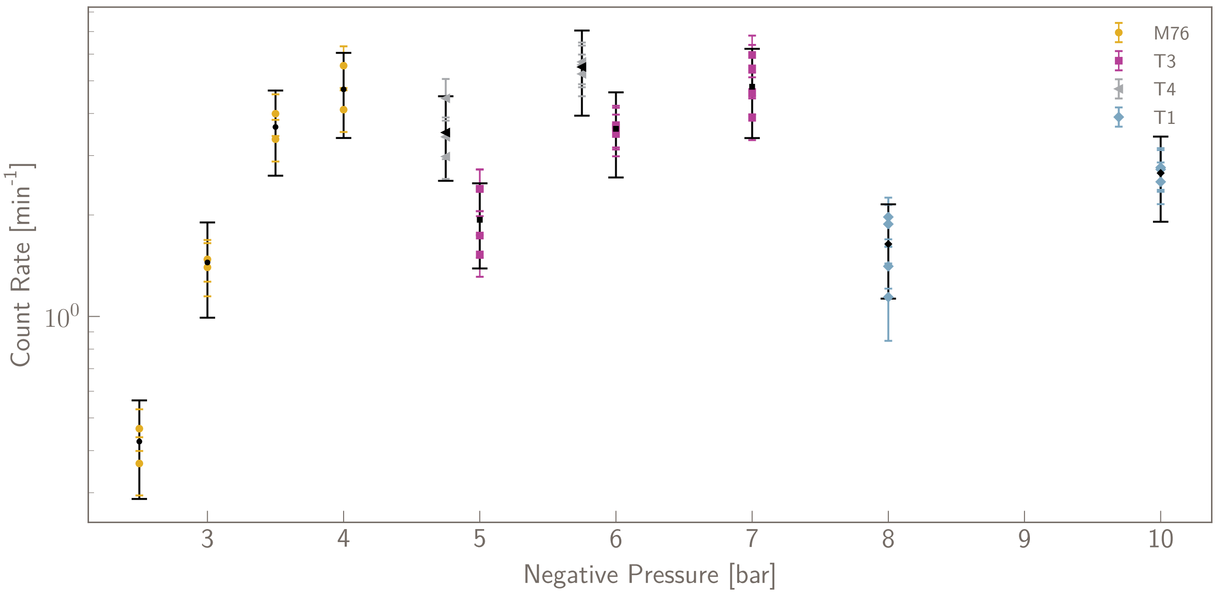

(a) Source 3: Cf in lead

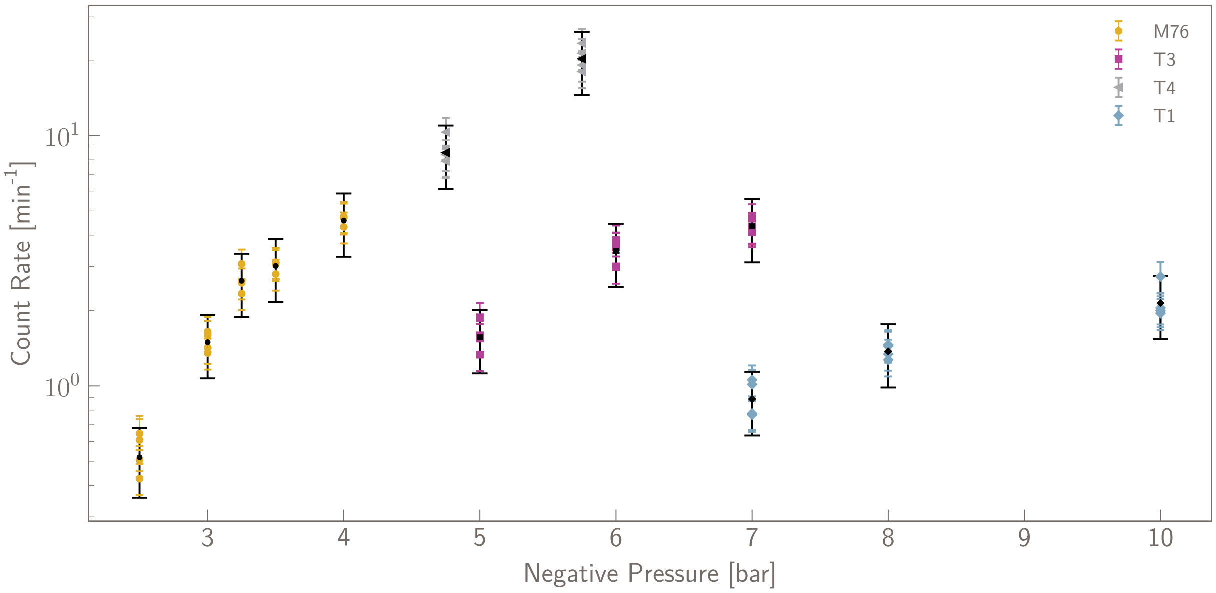

(b) Source 4: Cf in polyethylene

Figure 10.4. Count rates for the four CTMFD's in the multi-detector system. The colored markers represent the average from each individual measurement. The black markers represent the average across all measurement sets, shown with two sigma error bars.

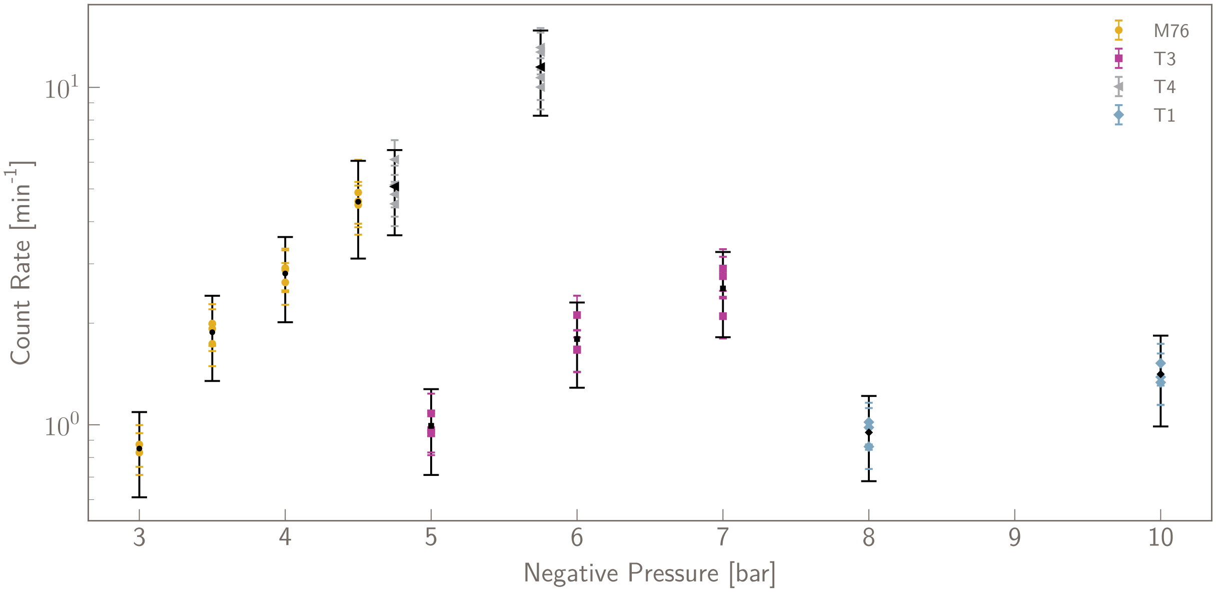

(a) Source 5: Cf in polyethylene

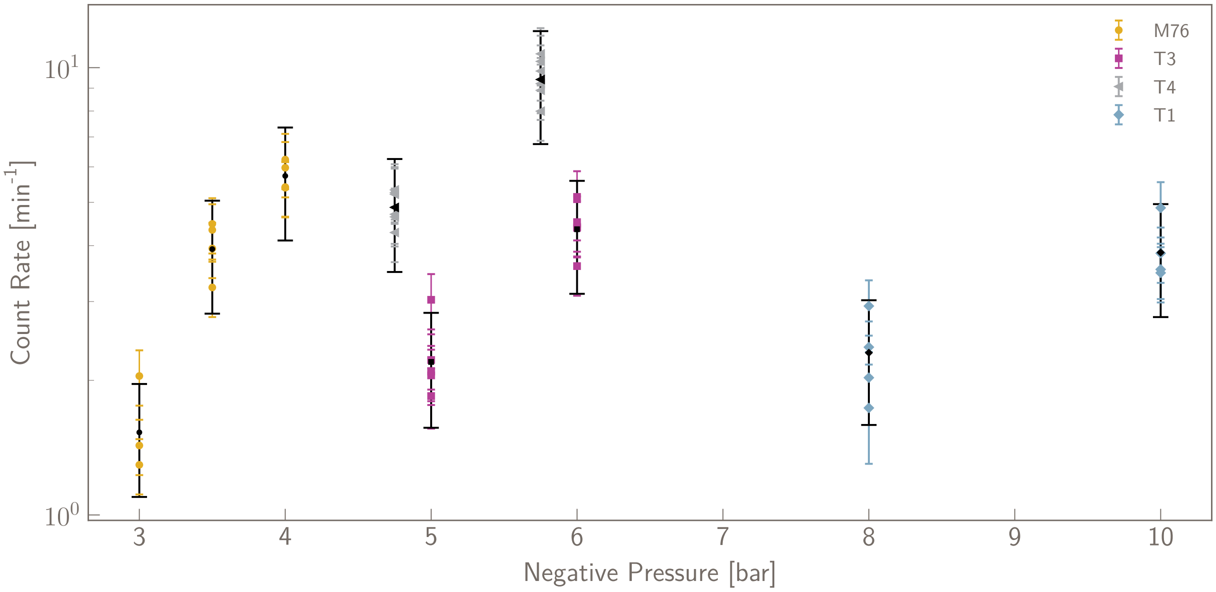

(b) Source 6: Cf in steel

Figure 10.5. Count rates for the four CTMFD's in the multi-detector system. The colored markers represent the average from each individual measurement. The black markers represent the average across all measurement sets, shown with two sigma error bars.

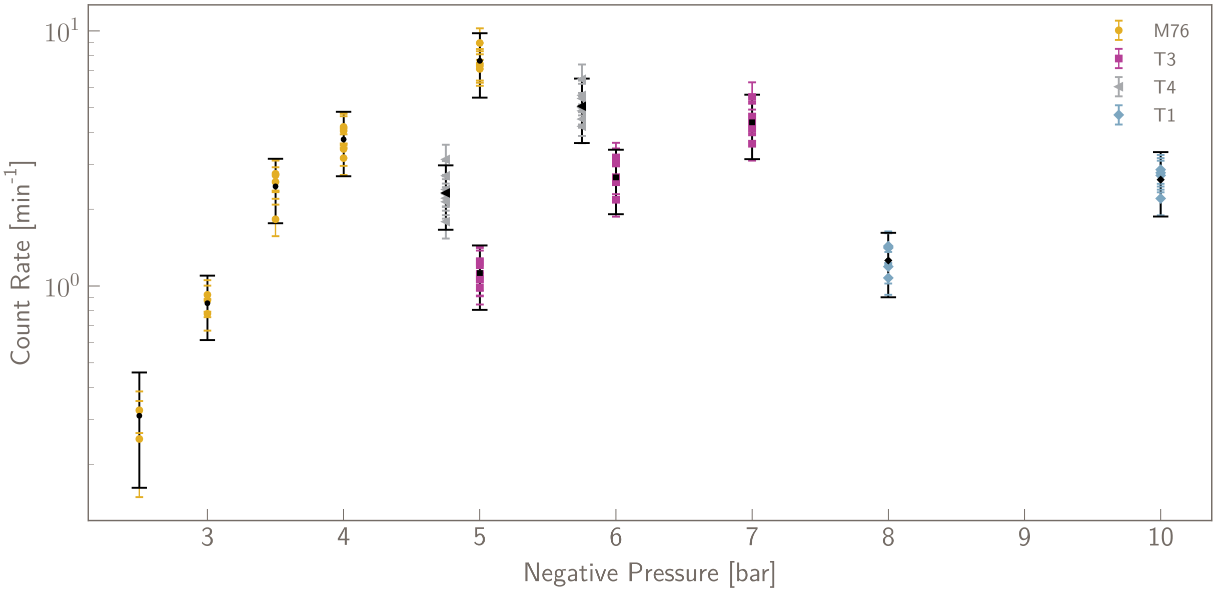

(c) Source 7: Cf in steel

Figure 10.5. Count rates for the four CTMFD's in the multi-detector system. The colored markers represent the average from each individual measurement. The black markers represent the average across all measurement sets, shown with two sigma error bars.

Replication of the experiment for the BSS was accomplished by the ORNL staff intermittently over the time frame of 9/8/2018-9/12/2018. Data acquisition was a 24-hour per day activity. With the exception of the 2" and sometimes the 3" spheres, each ball was exposed for a nominal 4 hours. This had been calculated to generate at least 1000 counts during each exposure to make the statistical uncertainty no worse than 3%. The count rates for the different sphere sizes for each source are shown in table 10.2.

Table 10.2. Count rate data recorded by the ORNL staff with the BSS.

(a) Source 1

Ball [inches]	Counts	Count Time [s]	Count Rate [s^{-1}]
2	1400	21678.15	0.0646
3	1871	14071.00	0.1330
5	4566	16013.24	0.2851
8	4089	14404.39	0.2839
10	3053	14519.47	0.2103
12	2209	15266.34	0.1447

(b) Source 2

Ball [inches]	Counts	Count Time [s]	Count Rate [s^{-1}]
2	1917	27095.04	0.0708
3	2153	15255.04	0.1411
5	4392	14876.62	0.2952
8	3887	12887.19	0.3016
10	2798	12393.05	0.2258
12	1738	11901.01	0.1460

(c) Source 3

Ball [inches]	Counts	Count Time [s]	Count Rate [s^{-1}]
2	971	22611.97	0.0429
3	1152	13380.10	0.0861
5	2584	14626.21	0.1767
8	2183	12955.83	0.1685
10	1921	14597.98	0.1316
12	1310	15025.66	0.0872

Table 10.2. Count rate data recorded by the ORNL staff with the BSS.

(d) Source 4

Ball [inches]	Counts	Count Time [s]	Count Rate [s^{-1}]
2	3269	21678.15	0.1213
3	2325	14071.00	0.1794
5	3579	16013.24	0.2307
8	2727	14404.39	0.1866
10	2002	14519.47	0.1349
12	954	15266.34	0.0903

(e) Source 5

Ball [inches]	Counts	Count Time [s]	Count Rate [s^{-1}]
2	2009	21678.45	0.0709
3	2893	14071.00	0.1109
5	2205	16013.21	0.1423
8	1609	14404.39	0.1115
10	1193	14519.47	0.0828
12	724	15266.34	0.0544

(f) Source 6

Ball [inches]	Counts	Count Time [s]	Count Rate [s^{-1}]
2	2984	42639.89	0.0700
3	2149	14461.81	0.1486
5	4136	14304.00	0.2891
8	3699	14247.41	0.2596
10	2267	13147.09	0.1724
12	1485	13105.09	0.1133

Table 10.2. Count rate data recorded by the ORNL staff with the BSS.
(g) Source 7

Ball [inches]	Counts	Count Time [s]	Count Rate [s^{-1}]
2	1270	28701.13	0.0442
3	2561	27435.47	0.0933
5	2636	14458.01	0.1823
8	2405	14893.95	0.1615
10	1470	13050.00	0.1126
12	849	12141.18	0.0699

10.2 Suggestions Regarding the Equivalence of the Dose Rates Measured with the CTMFD and BSS

The effective dose rates from the ORNL technical report are shown in table 10.3. The procedure for comparing the CTMFD's dose rate to that of the BSS was determined largely by the staff at ORNL. Slight differences exist between the manner in which the ORNL and MFRL staff arrived at the effective dose rates from their respective detector systems. After first explaining the underlying reasons behind the differences, the BSS and CTMFD dose rates will be re-computed with equivalent analysis procedures. As a point of preface, the topics described herein should not be interpreted as a critique of the employed analysis methods, but rather an expansion of prior work in the interest of an equivalent comparison.

Table 10.3. Comparison of the dose rates published in the ORNL technical report from the BSS and CTMFD unfolded spectra as well as the Ludlum 42-41L .

Source	Dose Rate $\left[\frac{\text{mRem}}{\text{hr}}\right]$		
	BSS	CTMFD	Ludlum 42-41L
1	0.228 ±6.98E-03	0.271 ±4.98E-03	0.190 ±2.65E-02
2	0.239 ±7.22E-03	0.245 ±8.63E-03	0.214 ±2.79E-02
3	0.137 ±8.58E-03	0.146 ±8.63E-03	0.117 ±2.13E-02
4	0.138 ±9.33E-02	0.139 ±8.63E-03	0.167 ±2.70E-02
5	0.082 ±8.53E-03	0.082 ±8.63E-03	0.095 ±2.08E-02
6	0.195 ±8.35E-03	0.182 ±8.63E-03	0.184 ±2.72E-02
7	0.124 ±5.27E-03	0.114 ±8.63E-03	0.106 ±2.14E-02

10.2.1 Correlation of the Dose Rates

ORNL's Bell performed a regression analysis of the dose rates from the different detectors. The fits were computed by the effective variance method of Tellinghuisen because there is uncertainty in both the x and y values [55]. In all cases, the data are well-represented by a straight line with no or small offset, implying that the difference in dose rates between the detectors can be approximated by a simple scale factor. It should be noted that the regression fit between the Ludlum 42-41L and CTMFD data, reported by Bell in figure 5 [54], appears to contain an error. The uncertainty of the CTMFD is overrepresented, such that the proportionality of the dose rates appears closer to unity than is actually the case. To correct for this, the regression fits were recomputed using orthogonal distance regression or total variance method and the software package ODRPACK [56]. For the case of a linear fit $y = a * x + b$, the two methods are equivalent. The results are shown in fig. 10.6. These results will be expanded on in the updated analysis to discuss the covariance of the regression fit coefficients.

10.2.2 Compensation for Background Radiation

One, albeit minor, procedural discrepancy is the exclusion of the count rates from background radiation in the BSS count rate data used for unfolding. The LabVIEW program supplied to ORNL contains the ability to subtract background count rates before unfolding, a feature useful for comparison with MCNP simulations, and contained non-zero default values. The default background count rates resulted in a reduction of the unfolded dose rate of approximately 5%. The CTMFD dose rates calculated by the MFRL staff did not account for contributions from background, i.e. background subtraction was not performed. In consideration of how a dosimeter would operate in the field, it does not make sense, nor is it likely possible, to distinguish what constitutes background radiation. The effective dose rate at any location is simply the summation of the dose rates from all sources. As such, the updated analyses procedure will not account for background contributions.

10.2.3 Calibration of the Bonner Sphere Spectrometer Response Matrix

The largest component of the observed differences in the dose rates is an artifact of the response matrix transmitted with the BSS unfolding software. As originally transmitted, the LabVIEW program contained the response matrix as directly calculated from MCNP (fig. 4.3). That is, without adjustment by the calibration scale factor discussed in section 4.3. To further explore the discrepancy between the BSS and Ludlum dose rates, Bell unfolded the BSS count rate data with a separate unfolding code, BUNKIUT18. The code was originally written at the Naval Research Laboratory; the response matrix was calculated, using the ANISN discrete ordinate code for neutron transport, by Hertel and Davidson at the University of Texas, Austin [57].

BUNKIUT18 does not have the ability to propagate counting statistics through the computation as does MAXED/IQU. Therefore, an additional procedure was introduced for estimation of the uncertainty to ensure an equivalent comparison. The dose rate and uncertainty in the dose rates seen in table 10.3 are different than the output of the LabVIEW program, which computes the uncertainty by propagating the uncertainty in the counting statistics with the (user-specified) uncertainty in the default/guess spectrum. Rather, the tabulated values represent the average of the dose rates resulting from unfolding with each of the six guess spectra shapes supplied with the software; the variance is taken as the standard deviation of the seven dose rates, added in quadrature, and then averaged. Similarly, unfolding with BUNKIUT18 used a Maxwellian distribution, and a flat distribution as the starting spectrum guess, averaged the dose rates together, and computed the variance from the sample standard deviation.

A comparison of the dose rates estimated by the two unfolding packages and response matrices is given in table 10.4. The uncertainty-weighed regression fit in fig. 10.6c indicates that the unfolded results are highly correlated, and the choice of unfolding codes is of no consequence. Furthermore, given the different computational methods used (i.e. discrete ordinate versus monte-carlo), the correlated agreement adds validity to the response matrix calculated in this work. This agreement, however, does not imply accuracy or precision, but instead is an example of code verification. Following the discussion in section 4.3, which is based on the results in literature from Alevra et. al [36] and Mares and Schraube [32], the unfolded results should be recalculated with the BSS response matrix scaled by the aforementioned calibration factor.

Table 10.4. Comparison of the BSS effective dose rates calculated by ORNL with the MAXED and BUNKIUT18 unfolding codes. The MAXED results use the (uncalibrated) response matrix calculated at Purdue University, while the BUNKIUT18 results use the response matrix calculated at University of Texas, Austin.

Source	Dose Rate $\left[\frac{\text{mRem}}{\text{hr}}\right]$	
	MAXED/Purdue	BUNKIUT18/Texas
1	0.1613 ±5.57E-03	0.1841 ±7.23E-03
2	0.1709 ±6.64E-03	0.1902 ±3.07E-03
3	0.0922 ±3.27E-03	0.1101 ±3.39E-03
4	0.0923 ±3.72E-03	0.1082 ±4.39E-03
5	0.0498 ±5.33E-03	0.0636 ±1.91E-03
6	0.1361 ±7.42E-03	0.1547 ±5.16E-03
7	0.0809 ±3.49E-03	0.0971 ±2.13E-03

10.2.4 Choice of Guess Spectrum and Default Uncertainty

The final procedural discrepancy relates to the sensitivity of the output dose rate to the guess spectrum used in unfolding and subsequent estimation of the uncertainty. As mentioned earlier, the BSS dose rates reported by Bell [54] were the result of averaging the individual dose rates corresponding to the 7 different guess spectra. Conversely, the dose rates supplied by the MFRL staff at Purdue were the result of unfolding solely with a ^{252}Cf guess spectrum, due to the fact that it yielded the best agreement with the CMTFD's count rate data. Though both approaches undoubtedly have their own merit, the averaging method allows for a more detailed comparison between the BSS and CTMFD systems, and therefore will be adopted in the proceeding analysis.

Tangentially related to the starting guess spectrum, is the ability to assign uncertainty in the guess spectrum and propagate it throughout unfolding. The reported dose rate estimates from the LabVIEW program supplied to ORNL and those computed at Purdue MFRL had

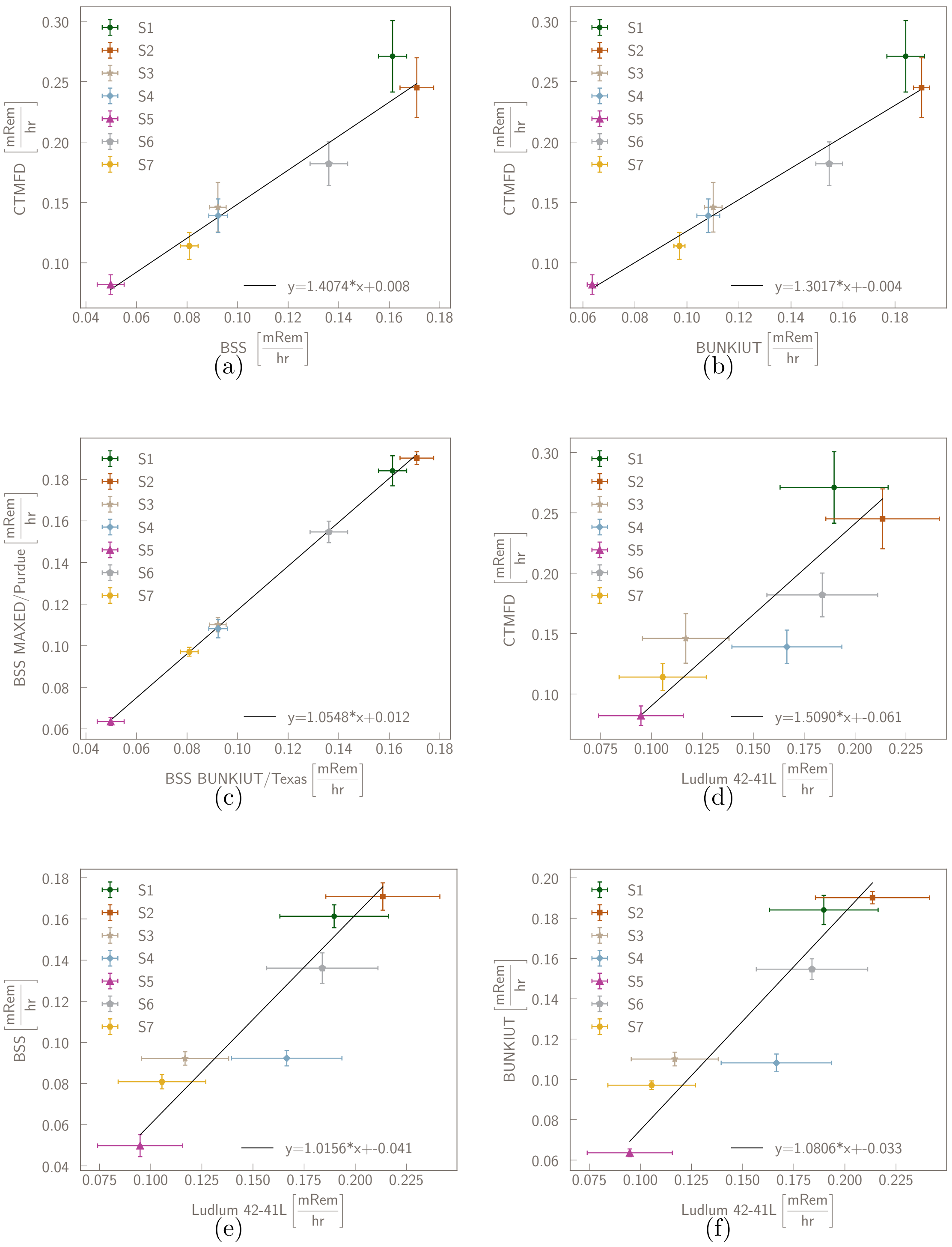

Figure 10.6. Correlations between the dose rates measured by the Ludlum 42-41L, CTMFD, and BSS, including results from both unfolding codes MAXED (Purdue response matrix) and BUNKIUT (Texas response matrix).

uncertainty built into the guess spectrum. Though it was kept consistent between the BSS and CTMFD analyses, this default uncertainty was set arbitrarily to act as a placeholder of sorts. Due to the fact that IQU/MAXED distinguishes between the uncertainty propagated from counting statistics and the uncertainty propagated from the guess spectrum, it made sense to include the option to give the end user freedom to specify whatever value deemed appropriate. The contribution could always be removed in post processing with relative ease.

After further consideration, the decision was made to remove the default spectrum uncertainty from the results in the proceeding analysis. IQU requires the user to specify the energy binning and the amount of uncertainty in that bin (as a percentage). As an example, if the user created one energy bin for every energy bin in the response matrix and specified the uncertainty as 20%, the uncertainty propagated after unfolding would closely approximate 20% of the output flux. However, if a coarse energy bin structure was defined and each bin assigned a value of 20%, the propagated uncertainty would not total 20% as before. Rather, the uncertainty would be less than 20% as a consequence of the integrated bin structure. The implication of this dependence is that some amount of *a priori* information must be known to justify the energy bin structure and or the percent uncertainty.

An example of when it would be appropriate to assume uncertainty in the guess spectrum might consist of dose verification measurements relating to unfolding the spectrum of an isotope source with a known spectrum shape but inherent uncertainty in activity. However, in a situation such as the experiments conducted at ORNL where zero prior knowledge exists, it would be a logical fallacy to impose a higher degree of certainty than is known about the source's spectrum shape or intensity. Importantly, addition of unjustified uncertainty in the guess spectrum artificially inflates the total uncertainty in the dose rate. As a consequence, the orthogonal distance regression analyses in fig. 10.6 would misrepresent the slope of the trend line, implying a greater degree of correlation than is actually present.

10.3 Unfolded Spectra and Dose Rate Comparisons After Homogenization of the Analysis Procedures

The dose rates measured by the CTMFD were recomputed using the guess spectrum averaging method described in the prior section. The response matrices used to produce the unfolded results in this section are slightly different than those used to generate the data in table 10.3; that is, the dose rates originally submitted to ORNL. Time constraints in the period leading up to the ORNL evaluation did not allow for the same degree of rigor as presented in the optimization analyses in chapter 7, though the original response matrices were the best available at that time. The response matrices used in this analysis were adopted to be consistent with the optimized A,N coefficients shown in table 7.2 and table 7.3. Adoption of the new response matrices also has the added benefit of further testing the validity of the optimization analyses in chapter 7 with an independent data set. This change has a minimal effect on the predicted dose rates. However, the new matrices do appear to produce a stable unfolded spectrum more consistently than the original matrices.

The guess spectrum averaging analysis methodology used by Bell [54] was implemented with both the CTMFD and BSS count rate data. Three new guess spectrums were added to the original array of seven supplied with the LabVIEW software. The original seven guess spectra included ^{252}Cf unshielded, D_2O, ^{241}AmBe, ^{241}AmLi, ^{241}AmB, and flat. The intention behind the after-the-fact addition is to provide a one-to-one comparison of the two detectors unfolded output. The new spectra consisted of a simplistic model, excluding all of the room geometry, of the different moderator geometries used in source configurations 2-7. The effects of the different moderating materials on a bare ^{252}Cf spectrum are illustrated in fig. 10.7. Information about the relative change in intensity from attenuation is lost in the normalization process. This loss of information is inconsequential for the default spectra. Since the intensity of the source being measured is not known beforehand, the unfolding algorithm is directed to scale the default spectrum by a value that minimizes the starting χ^2 value.

10.3.1 Comparison of the Dose Rates

The guess spectrum dependent dose rates for all seven sources are shown in table 10.5. Each table also contains the averaged dose rate, standard deviation, as well as the difference between the maximum and minimum dose rate across all nine guess spectra. After multiplying the BSS response matrix by the calibration factor, the average dose rate is within

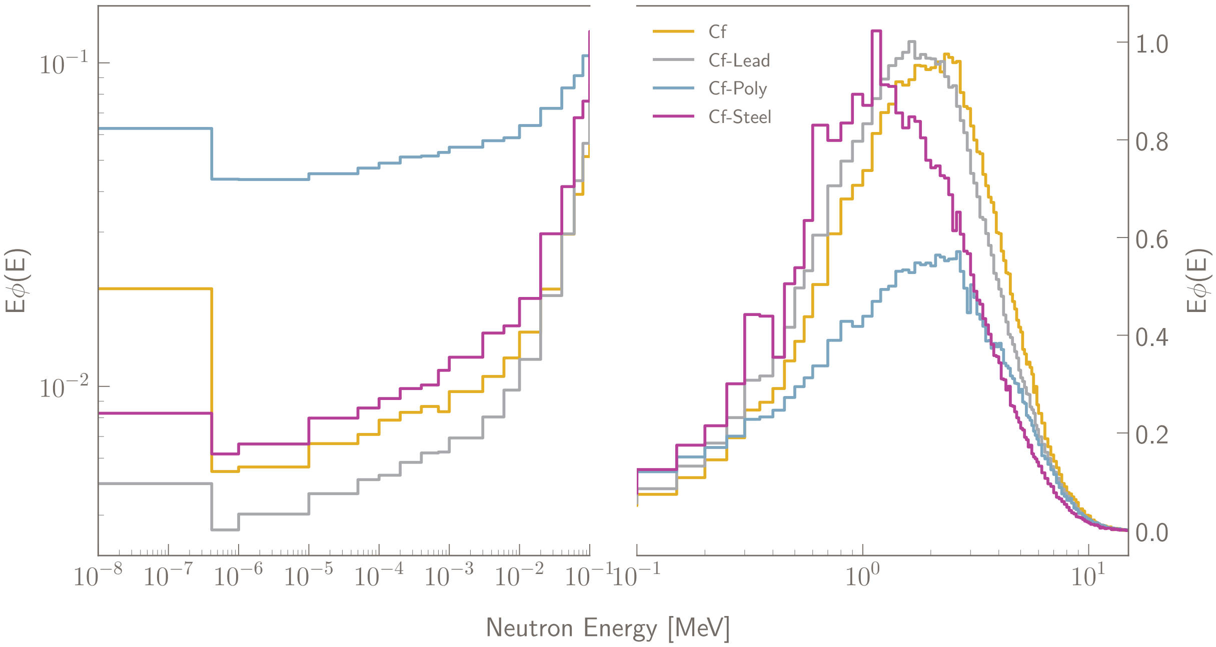

Figure 10.7. Guess spectrums corresponding to the moderation geometries chosen by ORNL. The spectrums are normalized to better illustrate the effect of moderation relative to a bare ^{252}Cf spectrum.

20% of that predicted by the CTMFD system for all cases. The uncertainty in the dose rate is larger for the CTMFD than the BSS. Each bonner sphere received approximately 1000 counts. For comparison, the maximum number of detection events in a single CTMFD at a single pressure was 300. The uncertainty in the individual pressure measurements is what ultimately bounds the final uncertainty after unfolding. Considering that the BSS' data acquisition window was significantly longer than the CTMFD's, it is not surprising that the BSS has a lower uncertainty.

The "Max-Min" statistic seen in table 10.5 is indicative of how well the unfolding system handles an input guess spectrum that is unrepresentative of the true spectrum. For example, the use of an ^{241}AmBe or flat spectrum when unfolding measurements of a bare ^{252}Cf source. The BSS significantly outperforms the CTMFD in this category. Particularly for source configurations one and two, where the CTMFD's range is seven to ten times larger than that of the BSS, which equates to 50% of the averaged dose rate. Such a large range may be unacceptable for field applications. Unfortunately, other than the flat guess, there does not appear to be guess spectrum that is consistently inaccurate, which implies that the CTMFD system may be limited to applications where a reasonable amount of *a priori* is available.

Results for correlation of the dose rates between the CTMFD, BSS, and Ludlum systems are shown in fig. 10.8. The BSS and CTMFD dose rates are seen to be highly correlated, with a trend line slope of 0.98. Though orthogonal distance regression accounts for uncertainty in both x and y dimensions, there is still uncertainty present in the regression fit coefficients. The standard deviation of the fit coefficients correspond to the diagonal elements of the covariance matrix, scaled by the residual variance. From the concept of a confidence interval, an estimate can be made for the range of values the slope coefficient could take at a desired level of confidence. Using a confidence level of 95%, the slope of the correlation line will be contained by the interval of 0.834-1.126. The 95% confidence interval of the intercept coefficient was similarly calculated to be -0.032-0.011.

Though the BSS and CTMFD are now in better agreement, scaling the BSS response matrix by the calibration factor worsened the correlation fit with the Ludlum 42-41L system, to which a 41% disagreement is now present. The 95% confidence interval of the slope and intercept coefficients were calculated to be 0.782-2.041 and -0.132-0.054, respectively. The very large confidence interval is on account of the relatively poor fit of the regression line and large standard deviations present in the Ludlum measurements.

Table 10.5. Unfolded dose rates for the CTMFD and BSS as a function of the initial guess spectrum. The uncertainty in each dose rate corresponds to propagation of the uncertainty in the counting statistics by the program IQU. The guess spectrum matching the actual source configuration is emphasized in bold.

(a) Source 1: Bare Cf

	CTMFD			BSS		
Guess Spectrum	Guess χ^2	Dose Rate $\left[\frac{\text{mRem}}{\text{hr}}\right]$	σ $\left[\frac{\text{mRem}}{\text{hr}}\right]$	Guess χ^2	Dose Rate $\left[\frac{\text{mRem}}{\text{hr}}\right]$	σ $\left[\frac{\text{mRem}}{\text{hr}}\right]$
Cf	3.86	0.244	1.15E-2	126.34	0.248	7.60E-3
Cf-Lead	2.31	0.273	9.08E-3	159.28	0.247	1.02E-2
Cf-Poly	5.57	0.238	1.35E-2	124.96	0.235	6.71E-3
Cf-Steel	1.55	0.332	1.17E-2	92.69	0.246	1.08E-2
D2O	5.76	0.222	1.33E-2	887.15	0.232	1.88E-2
AmBe	28.34	0.176	3.35E-2	352.52	0.246	1.35E-2
AmLi	34.43	0.296	3.85E-2	229.44	0.249	1.74E-2
AmB	2.01	0.212	1.09E-2	344.46	0.234	1.39E-2
Flat	38.64	0.181	3.18E-2	1130.89	0.244	1.67E-2
Average		0.242			0.242	
Std. Dev.		7.410e-03			4.485e-03	
Max - Min		0.156			0.017	

Table 10.5. Unfolded dose rates for the CTMFD and BSS as a function of the initial guess spectrum. The uncertainty in each dose rate corresponds to propagation of the uncertainty in the counting statistics by the program IQU. The guess spectrum matching the actual source configuration is emphasized in bold.

(b) Source 2: Cf in lead

	CTMFD			BSS		
Guess Spectrum	Guess χ^2	Dose Rate $\left[\frac{\text{mRem}}{\text{hr}}\right]$	σ $\left[\frac{\text{mRem}}{\text{hr}}\right]$	Guess χ^2	Dose Rate $\left[\frac{\text{mRem}}{\text{hr}}\right]$	σ $\left[\frac{\text{mRem}}{\text{hr}}\right]$
Cf	6.00	0.232	9.59e-03	162.88	0.261	7.86e-03
Cf-Lead	3.25	0.254	8.08e-03	209.12	0.259	1.01e-02
Cf-Poly	8.55	0.227	1.07e-02	119.91	0.250	1.03e-02
Cf-Steel	2.26	0.291	1.43e-02	127.79	0.259	1.06e-02
D2O	8.96	0.212	1.05e-02	821.73	0.246	2.17e-02
AmBe	49.60	0.179	2.52e-02	400.81	0.259	2.29e-02
AmLi	46.19	0.241	2.59e-02	218.12	0.260	1.92e-02
AmB	1.98	0.200	9.29e-03	398.99	0.247	1.88e-02
Flat	64.18	0.180	2.25e-02	1053.85	0.257	2.22e-02
Average		0.224			0.255	
Std. Dev.		5.540e-03			5.651e-03	
Max - Min		0.111			0.015	

Table 10.5. Unfolded dose rates for the CTMFD and BSS as a function of the initial guess spectrum. The uncertainty in each dose rate corresponds to propagation of the uncertainty in the counting statistics by the program IQU. The guess spectrum matching the actual source configuration is emphasized in bold.

(c) Source 3: Cf in lead

	CTMFD			BSS		
Guess Spectrum	Guess χ^2	Dose Rate $\left[\frac{\text{mRem}}{\text{hr}}\right]$	σ $\left[\frac{\text{mRem}}{\text{hr}}\right]$	Guess χ^2	Dose Rate $\left[\frac{\text{mRem}}{\text{hr}}\right]$	σ $\left[\frac{\text{mRem}}{\text{hr}}\right]$
Cf	5.61	0.147	8.57e-03	96.57	0.150	9.34e-03
Cf-Lead	3.04	0.156	6.18e-03	118.73	0.149	1.09e-02
Cf-Poly	7.45	0.144	8.78e-03	56.34	0.142	4.54e-03
Cf-Steel	2.20	0.170	1.14e-02	73.71	0.149	1.12e-02
D2O	7.85	0.134	8.90e-03	489.25	0.139	1.40e-02
AmBe	47.64	0.125	2.63e-02	234.14	0.149	1.06e-02
AmLi	36.58	0.137	1.96e-02	134.06	0.150	1.58e-02
AmB	3.70	0.135	2.10e-02	230.48	0.141	1.07e-02
Flat	61.32	0.118	1.82e-02	629.94	0.147	1.32e-02
Average		0.141			0.146	
Std. Dev.		5.264e-03			3.851e-03	
Max - Min		0.052			0.011	

Table 10.5. Unfolded dose rates for the CTMFD and BSS as a function of the initial guess spectrum. The uncertainty in each dose rate corresponds to propagation of the uncertainty in the counting statistics by the program IQU. The guess spectrum matching the actual source configuration is emphasized in bold.

(d) Source 4: Cf in polyethylene

	CTMFD			BSS		
Guess Spectrum	Guess χ^2	Dose Rate $\left[\frac{\text{mRem}}{\text{hr}}\right]$	σ $\left[\frac{\text{mRem}}{\text{hr}}\right]$	Guess χ^2	Dose Rate $\left[\frac{\text{mRem}}{\text{hr}}\right]$	σ $\left[\frac{\text{mRem}}{\text{hr}}\right]$
Cf	2.97	0.137	1.53e-02	602.84	0.151	1.02e-02
Cf-Lead	1.09	0.140	2.26e-03	640.63	0.150	1.08e-02
Cf-Poly	4.07	0.132	1.26e-02	84.29	0.144	5.59e-03
Cf-Steel	2.47	0.155	1.16e-02	532.37	0.150	1.09e-02
D2O	4.51	0.125	1.80e-02	176.44	0.135	1.11e-02
AmBe	46.26	0.121	5.39e-02	828.58	0.151	1.03e-02
AmLi	71.10	0.124	2.08e-02	334.40	0.152	1.57e-02
AmB	9.25	0.135	6.90e-02	832.16	0.143	8.64e-03
Flat	63.70	0.113	3.17e-02	254.39	0.146	1.03e-02
Average		0.131			0.147	
Std. Dev.		1.109e-02			3.562e-03	
Max - Min		0.042			0.016	

Table 10.5. Unfolded dose rates for the CTMFD and BSS as a function of the initial guess spectrum. The uncertainty in each dose rate corresponds to propagation of the uncertainty in the counting statistics by the program IQU. The guess spectrum matching the actual source configuration is emphasized in bold.

(e) Source 5: Cf in polyethylene

	CTMFD			BSS		
Guess Spectrum	Guess χ^2	Dose Rate $\left[\frac{\text{mRem}}{\text{hr}}\right]$	σ $\left[\frac{\text{mRem}}{\text{hr}}\right]$	Guess χ^2	Dose Rate $\left[\frac{\text{mRem}}{\text{hr}}\right]$	σ $\left[\frac{\text{mRem}}{\text{hr}}\right]$
Cf	1.14	0.075	1.43e-03	472.54	0.090	7.89e-03
Cf-Lead	0.64	0.085	1.10e-02	500.56	0.090	8.20e-03
Cf-Poly	1.44	0.075	2.22e-03	54.18	0.087	3.95e-03
Cf-Steel	3.12	0.091	5.79e-03	405.40	0.090	8.36e-03
D2O	1.59	0.070	2.28e-03	118.88	0.080	5.97e-03
AmBe	23.04	0.062	9.20e-03	660.20	0.090	6.90e-03
AmLi	56.73	0.073	1.06e-02	215.87	0.090	1.19e-02
AmB	1.75	0.065	6.34e-03	667.73	0.085	6.06e-03
Flat	23.86	0.064	6.94e-03	171.70	0.086	5.32e-03
Average		0.073			0.088	
Std. Dev.		2.358e-03			2.499e-03	
Max - Min		0.029			0.010	

Table 10.5. Unfolded dose rates for the CTMFD and BSS as a function of the initial guess spectrum. The uncertainty in each dose rate corresponds to propagation of the uncertainty in the counting statistics by the program IQU. The guess spectrum matching the actual source configuration is emphasized in bold.

(f) Source 6: Cf in steel

	CTMFD			BSS		
Guess Spectrum	Guess χ^2	Dose Rate $\left[\frac{\text{mRem}}{\text{hr}}\right]$	σ $\left[\frac{\text{mRem}}{\text{hr}}\right]$	Guess χ^2	Dose Rate $\left[\frac{\text{mRem}}{\text{hr}}\right]$	σ $\left[\frac{\text{mRem}}{\text{hr}}\right]$
Cf	7.61	0.189	1.79e-02	336.63	0.212	9.07e-03
Cf-Lead	4.07	0.197	1.26e-02	395.93	0.213	8.74e-03
Cf-Poly	8.61	0.184	1.70e-02	51.52	0.201	7.79e-03
Cf-Steel	1.52	0.223	1.01e-02	255.86	0.213	7.45e-03
D2O	9.17	0.179	2.72e-02	649.63	0.198	2.31e-02
AmBe	44.69	0.161	5.23e-02	645.05	0.209	1.46e-02
AmLi	69.98	0.199	2.12e-02	124.08	0.213	1.53e-02
AmB	5.20	0.179	5.82e-02	641.60	0.200	1.69e-02
Flat	50.20	0.155	2.85e-02	905.37	0.205	1.81e-02
Average		0.185			0.207	
Std. Dev.		1.054e-02			4.808e-03	
Max - Min		0.068			0.014	

Table 10.5. Unfolded dose rates for the CTMFD and BSS as a function of the initial guess spectrum. The uncertainty in each dose rate corresponds to propagation of the uncertainty in the counting statistics by the program IQU. The guess spectrum matching the actual source configuration is emphasized in bold.

(g) Source 7: Cf in steel

	CTMFD			BSS		
Guess Spectrum	Guess χ^2	Dose Rate $\left[\frac{\text{mRem}}{\text{hr}}\right]$	σ $\left[\frac{\text{mRem}}{\text{hr}}\right]$	Guess χ^2	Dose Rate $\left[\frac{\text{mRem}}{\text{hr}}\right]$	σ $\left[\frac{\text{mRem}}{\text{hr}}\right]$
Cf	13.30	0.131	1.78e-02	206.56	0.135	5.74e-03
Cf-Lead	7.87	0.133	1.50e-02	233.97	0.135	5.86e-03
Cf-Poly	15.22	0.127	1.68e-02	27.95	0.127	4.53e-03
Cf-Steel	3.65	0.138	1.51e-02	142.12	0.135	5.26e-03
D2O	15.98	0.118	1.57e-02	400.10	0.123	1.13e-02
AmBe	67.57	0.115	3.09e-02	423.46	0.132	1.06e-02
AmLi	77.26	0.118	1.77e-02	70.78	0.134	9.77e-03
AmB	11.11	0.128	3.53e-02	425.76	0.126	1.10e-02
Flat	82.91	0.108	2.11e-02	538.77	0.129	1.04e-02
Average		0.124			0.131	
Std. Dev.		7.253e-03			2.894e-03	
Max - Min		0.030			0.011	

10.3.2 Comparison of the Unfolded Spectra

Comparisons of the unfolded spectra between the BSS and CTMFD system are shown in fig. 10.9. The starting guess spectrum is chosen to match the corresponding source/moderator configuration from table 10.1. Since an MCNP simulated spectrum is not available as an absolute reference for accuracy, the portion of the BSS unfolded spectrum above 100

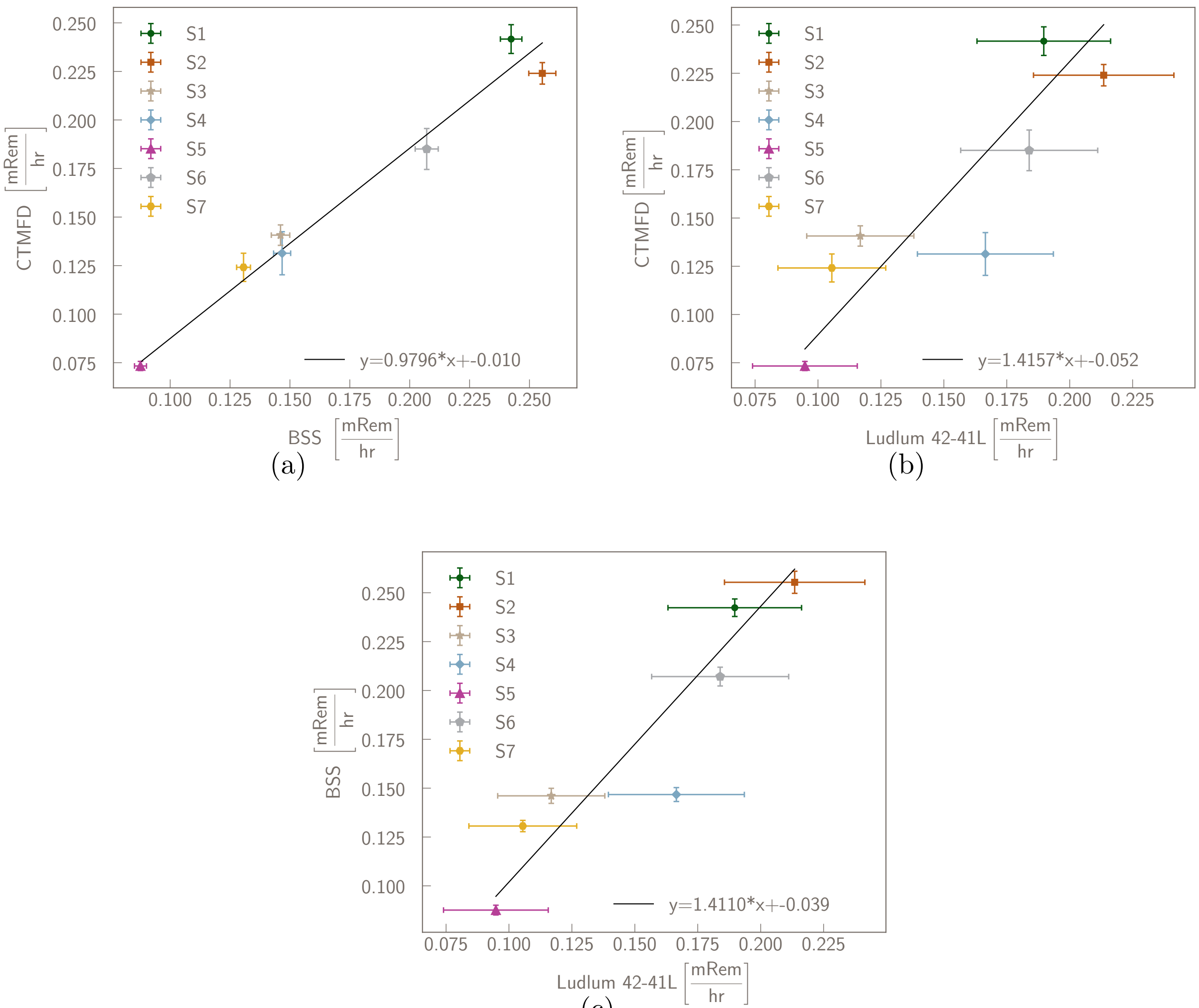

(a) (b)

(c)

Figure 10.8. Updated correlation fits, calculated using orthogonal distance regression, between the dose rates measured by the Ludlum 42-41L, CTMFD, and BSS after homogenizing the analysis methods for the CTMFD and BSS data.

keV is overlaid with that of the CTMFD. Good agreement overall is seen across the seven sources. The CTMFD's unfolded spectra for sources 1 and 7 display resonance artifacts in the range of 2-4 MeV. Similar trends were seen in chapter 8 for the data unfolded at MFRL and thus are likely attributed to inaccuracy in the calculated response matrix.

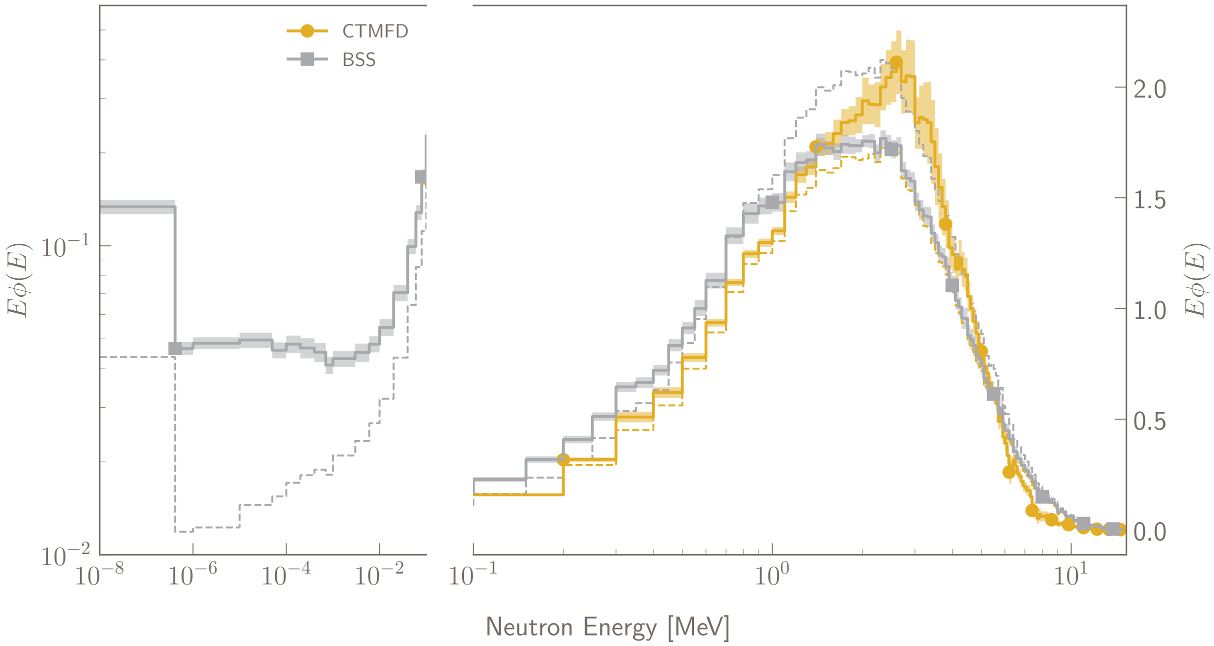

(a) Source 1: Bare Cf

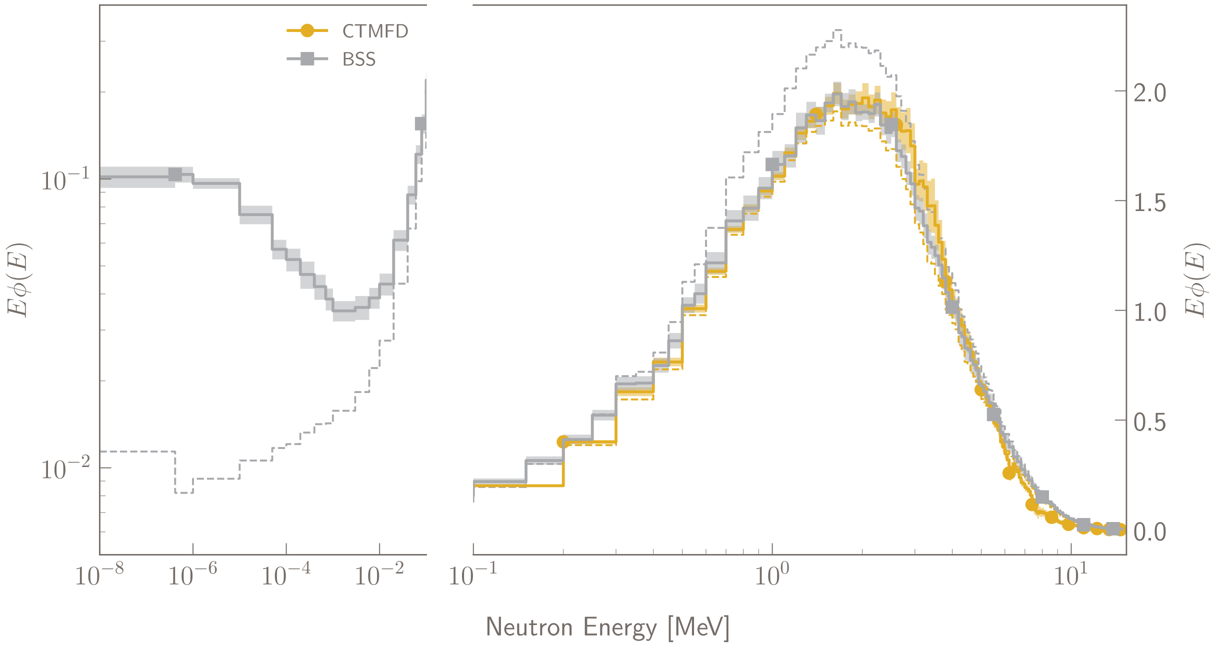

(b) Source 2: Cf in lead

Figure 10.9. Comparison of the CTMFD and BSS unfolded spectra using the guess spectrum that matches the source/moderator configuration of the measurement.

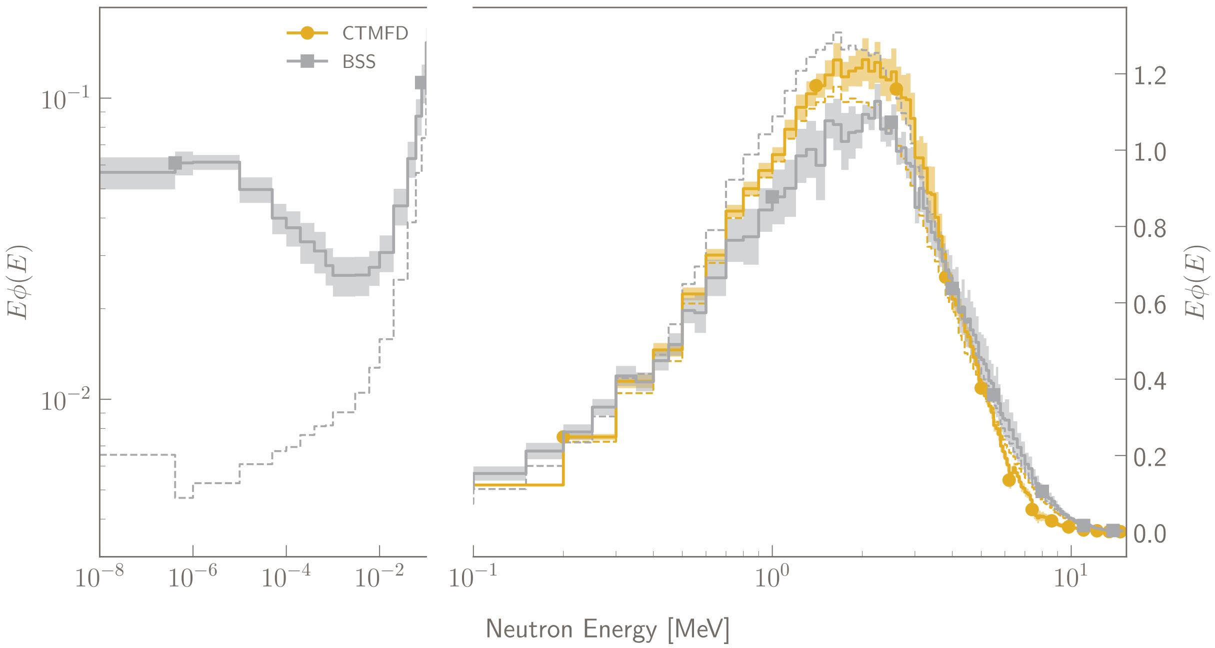

(c) Source 3: Cf in lead

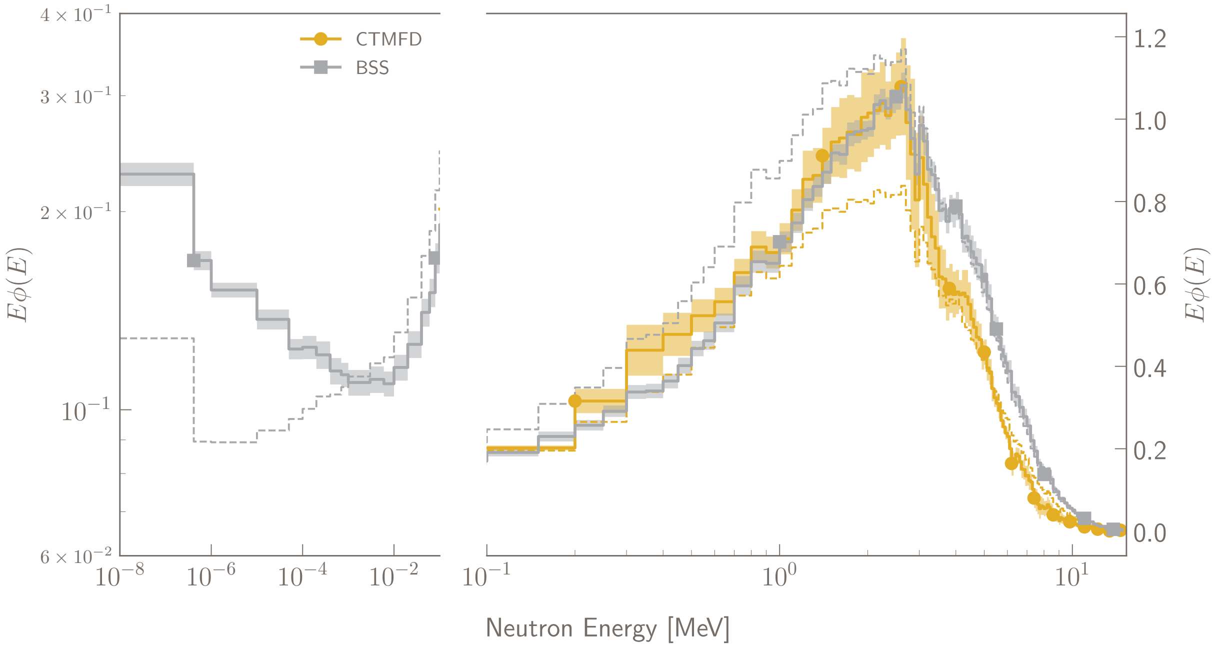

(d) Source 4: Cf in polyethylene

Figure 10.9. Comparison of the CTMFD and BSS unfolded spectra using the guess spectrum that matches the source/moderator configuration of the measurement.

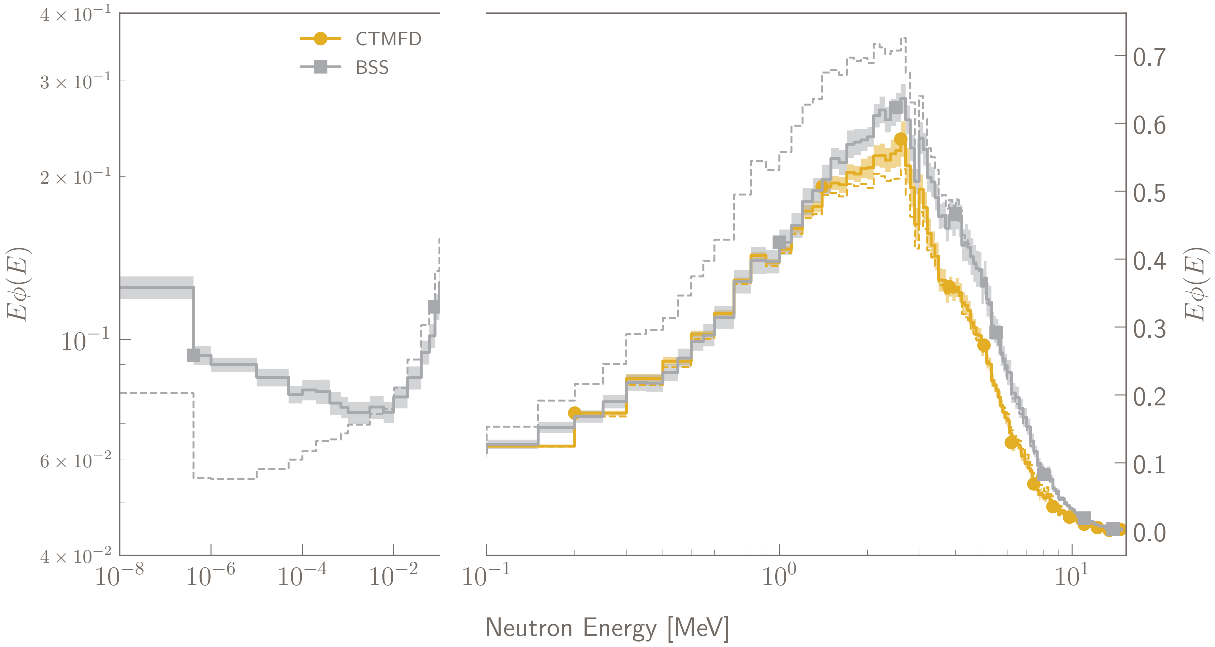

(e) Source 5: Cf in polyethylene

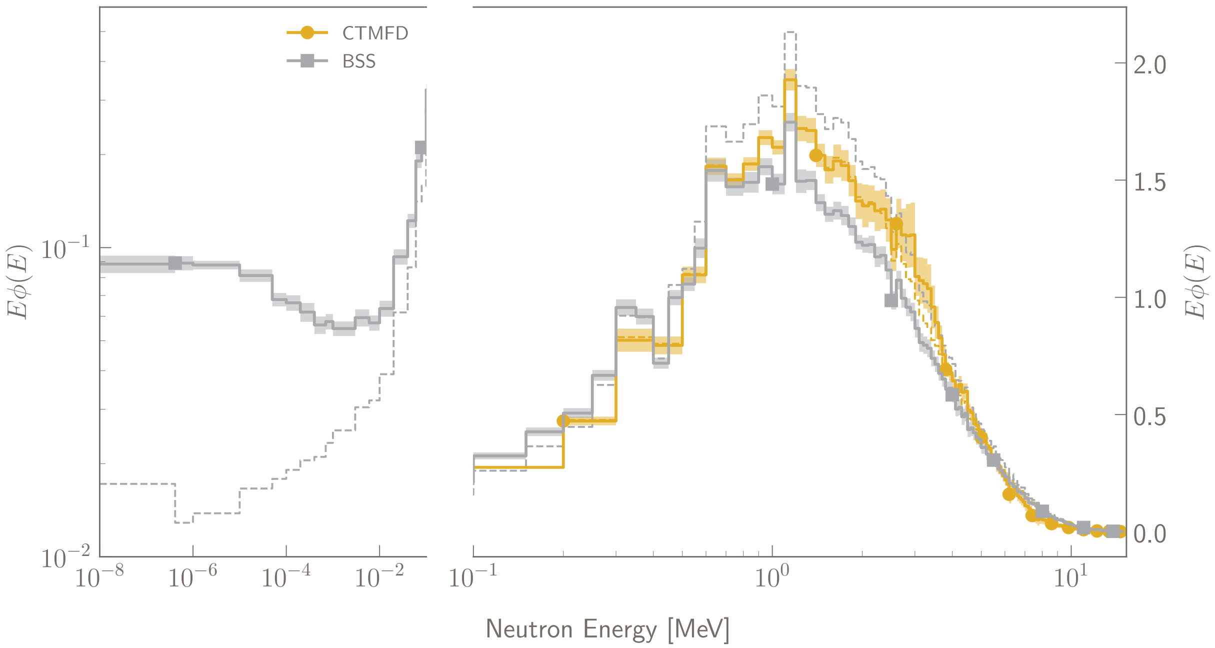

(f) Source 6: Cf in steel

Figure 10.9. Comparison of the CTMFD and BSS unfolded spectra using the guess spectrum that matches the source/moderator configuration of the measurement.

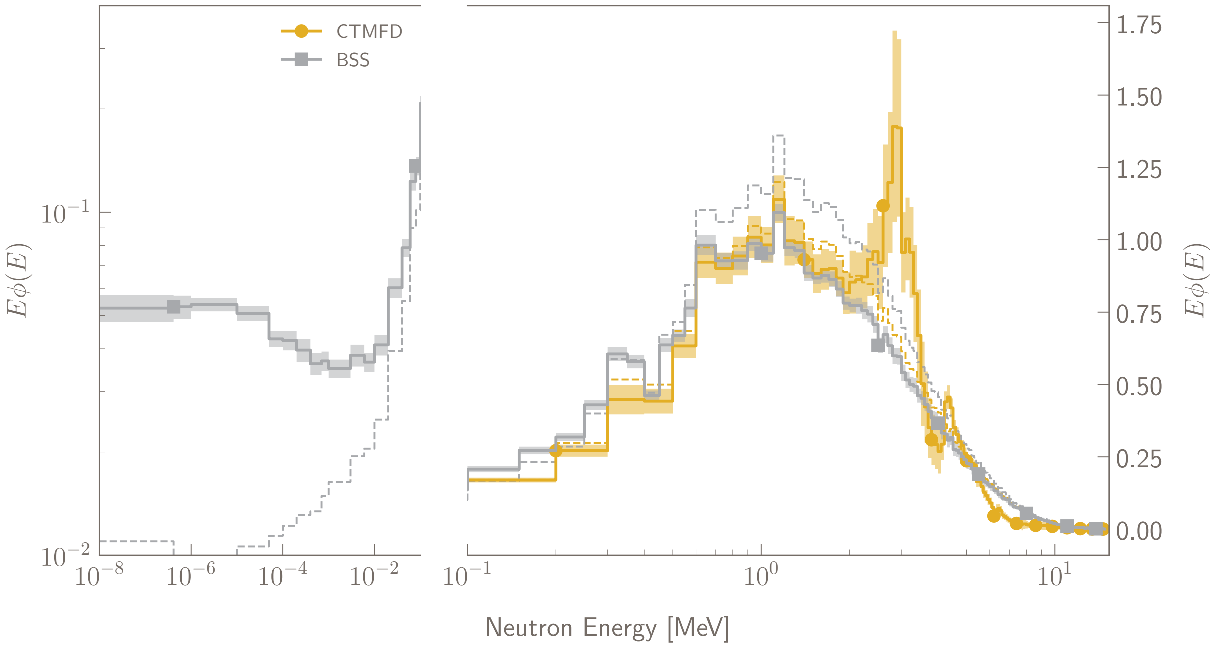

(g) Source 7: Cf in steel

Figure 10.9. Comparison of the CTMFD and BSS unfolded spectra using the guess spectrum that matches the source/moderator configuration of the measurement.

The Ludlum 42-41L system is calibrated by NIST traceable ^{252}Cf sources; thus, it would be expected that the Ludlum measurements would be accurate for the ^{252}Cf-based configurations used at ORNL. Almost all configurations produced dose fields at the lower operational limit of the system, which is listed as 0.1 mRem/hr. At such low dose rates it is difficult to infer whether the Ludlum measurements should be taken as the absolute standard for accuracy. Analysis of raw time-stream of dose rates output by the Ludlum confirms that the data is Poissonian as expected, effectively ruling out the possibility that the detector was behaving erratically. When also considering how the Ludlum is calibrated, little justification exists to support the assertion that the detector has an inherent offset bias in it's dose calibration either.

If the Ludlum 42-41L is assumed to be the standard of accuracy, then the BSS response matrix as computed by MCNP does not need scaling by a calibration constant. A result that contradicts the findings of Alevra et. al [36] and Mares and Schraube [32]. The assumption would similarly invalidate the CTMFD's response matrix and the underlying detection model. With so many conflicting trends in the data across detectors, further conclusions cannot be drawn until confidence can be established in a reference standard of accuracy.

11. SUMMARY AND CONCLUSIONS

The content in this dissertation encompasses the research pathways undertaken in pursuit of enabling spectroscopic functionality in CTMFD's for applications pertaining to ambient dose monitoring. Dosimetry through spectroscopy is an inherently challenging approach irregardless of detector architecture. The underlying justification for the added complexity pertains to the application of fluence-to-dose weighting coefficients and the degree of conservatism that must be assumed in the absence of spectral information.

The ability of the CTMFD to ascertain spectral information emanates from it's ability to tailor its sensitivity as a function of operating pressure. Quantification the detector's response as a function of pressure is predicted on establishing the amount of energy which must be deposited by a recoil ion to initiate a critically-sized vapor cavity. The research pathways undertaken to establish this relationship is summarized herein.

11.1 Bonner Spectrometers as a Baseline Reference of Accuracy

A ^{6}LiI-based Bonner Spectrometer was acquired to serve as a baseline reference for comparison against the performance of TMFDs. A response matrix for the BSS was simulated using MCNP and found to be in close agreement with values published in literature for the same spectrometer set. However, MCNP simulations intended to verify experimental data taken with ^{252}Cf and ^{241}AmBe sources revealed a discrepancy between the simulated and measured count rates. Attempts to systematically isolate the source of the discrepancy through additional analyses and experimentation were unsuccessful, partially on account of the uncertainty inherent in the intensity of the available isotope sources, particularly the ^{241}AmBe source. The general agreement between the shapes of the simulated response functions and normalized count rates for each Bonner sphere with data published in literature implies that the BSS response matrix should be scaled by a calibration constant. The validity of this assumption still remains an open question. Nevertheless, using the assumed calibration constant, the BSS experimentally measured dose rate was within ±15% of theoretical benchmark simulated in MCNP.

11.2 TMFD Detection Model and Threshold Prediction

One of the primary contributions of this study involved the incorporation of the stochastic nature of ion deposition. The prior body of knowledge for TMFDs, originating from work related to single atom spectroscopy and detection thresholds, was built using the continuous slowing down assumption for ion energy deposition as a deterministic criteria for detection. While the CSDA estimate is accurate on average, detection threshold experiments with monoenergetic neutron sources found the deterministic approach yielded non-physical estimates for the deposition energy threshold for cavitation. As a consequence, it was necessary to devise a new approach to map the effects of energy straggling to a probability that an ion will deposit an amount of energy greater than or equal to the threshold energy for cavitation. Future extensions of this work should prioritize additional experimentation with monoenergetic sources. While the probabilistic approach did improve count rate predictions, the accuracy of the thresholds predicted by the model remains in question.

11.3 Estimation of the Deposition Energy Threshold for Cavitation

Building upon results from prior work with single atom spectroscopy in heptane, the DETC curve was assumed to have a power law functional form. In conjunction with MCNP simulations, a series of experiments were conducted with ^{252}Cf and ^{241}AmBe sources to find the optimal set of coefficients parameterizing the DETC curve which demonstrate the best agreement between simulated and experimentally measured count rates. Optimization was performed for a single detector over the range of 3-10 bar and for a panel of detectors with different sensitivities. The concept behind the detector panel arose out of difficulty finding a coefficient set that accurately predicted count rates of the entire pressure range. The probabilistic method demonstrated better agreement with experimental count rates than the CSDA method with the exception of pressures below 4-5 bar. As a consequence of the limited range of accuracy, each detector in the panel was designed to be calibrated for a select subset of negative pressures.

The experimental data used to calibrate the panel configuration comprised datasets from multiple distances. Calibrate the system with data at multiple distances served two purposes:

it extends the applicable range of pressures spanning the calibration space and demonstrates the sensitivity of the calibration to slight perturbations in the fluence spectrum resulting from varying contributions from albedo. Simulated count rates displayed markedly better agreement to experimental data for the 16 cm^3 detector as compared to the 1 cm^3 and 0.4 cm^3 detectors. The count rates simulated using one of the optimized coefficients exhibited good accuracy for the dataset they were optimized with, approximately within 10% of experimental measurements for ^{252}Cf and 20% for ^{241}AmBe. Coefficients optimized to one distance exhibited limited extensibility when applied to a dataset from a different distance. Errors as large as 30% were observed when applying, for example, the 50 cm coefficients to the 200 cm dataset despite the fact that the actual threshold energies for cavitation differ by only 6-9% over the applicable pressure range.

11.4 Spectrum Unfolding with TMFDS

Response matrices were computed using a DETC curve parameterized by coefficients which minimized the difference between experiment and simulation. Detector responses are computed in 0.25 bar increments to give the system operator flexibility with respect to operating pressure. The energy structure of the CTMFD response matrix consists of equally spaced bins 100 keV wide spanning energies from 100 keV to 15 MeV. With such fine energy spacing, the unfolding problem constitutes a mathematically under-determined system of equations, meaning the converged solution is not unique. This class of unfolding problem is known algorithmically as few-channel unfolding and is characterized by a strong dependence on the supplied *a priori* information. Future work should investigate what influence the binning structure has with respect to the accuracy of *a priori* provided.

Unfolding with the single detector system produced mixed results. This particular case illustrates a practical lower bound of sensitivity for the 16 cm^3 detector, representing a dose equivalent rate of less than 10 μRem/hr. Unfolded dose rates were within 5% and 25% of MCNP simulations for ^{252}Cf and ^{241}AmBe, respectively. Excluding count rates below 4.5 bar when performing unfolding improved ^{241}AmBe results to be commensurate with ^{252}Cf. Improvements in the unfolded results reiterate the importance of restricting the set of pressures used during unfolding to those where agreement is observed between simulated and experimental count rates.

A similar lack of parity between the ^{252}Cf and ^{241}AmBe unfolded spectra was observed for with measurements acquired using the panel configuration. Unfolding was performed using count rates from only the 16 cm^3 detector M76 as well as a combination of count rates from the 1 cm^3 detector T3. The latter case demonstrates, as a proof of concept, that detectors with varying sensitivities can be combined to extend the maximum measurable fluence rate. The dose rate resulting from unfolding with only count rates from M76 was within 10% of MCNP predictions. Utilizing response matrices computed from coefficients optimized to a different distance reduced the accuracy to within 20% of MCNP.

Dose rates resulting from unfolding with count rates from both M76 and T3 were within 5% and 17% of MCNP for ^{252}Cf and ^{241}AmBe, respectively. Conjoining measurements from both detectors was successful only when using the 50 cm response matrix for T3. It was found that the 50 cm response matrix for T3 could be paired with the 100 cm response matrix for M76 with a few important caveats. The pressure ranges encompassing each calibration set overlaps between 4-6 bar. However, the DETC energies parameterized bsfy the two coefficient sets differ by approximately 3% at 4 bar and 12% at 6 bar. As a consequence, strong oscillations were occasionally observed in unfolded spectra when attempting to unfold with overlapping pressures. Finally, it should be mentioned that once the accuracy of the simulated count rates in T3 become commensurate with those seen for M76, the restrictions on interoperability with multiple detectors can be lifted.

11.5 Thermal Neutron Sensitivity in TMFDs

The sensitivity of CTMFDs can be extended below 100 keV via the addition of boron to the detection fluid. A series of experiments with heavily moderated sources were conducted using borated and non-borated detection fluids, where a sharp divergence in count rates was noted beginning at 4.5 bar. Count rates for the borated fluid began to plateau above 5 bar. The shape of the borated count rate curve is representative of behavior typical for a threshold-type reaction and is consistent with past experiments using actinides dissolved in the detection fluid.

In contrast to the relative success with simulating the CTMFD's response to fast neutrons, the measured count rates could not be replicated through MCNP simulations for unknown reasons. The pressure at which the detector becomes sensitive to the thermal (n,α) reaction is not consistent with thresholds determined with dissolved actinides. The optimized coefficients which define the DETC curve imply a threshold of 35 keV at 4.5 bar, which reasonably explains the sensitivity to the thermal (n,α) reaction, where the ^{7}Li recoil deposits slightly more than 35 keV on average. The same detection model cannot explain the threshold behavior observed with actinides in any capacity. As such, it is not possible to simulate the CTMFDs response to neutrons below 100 keV at the present time.

Spectral information below 100 keV cannot be resolved unless the detector response can be quantified as a function of energy. However, the effective dose rate of neutrons below 100 keV can be approximated to some degree by calibrating the borated CTMFD to operate as a rate meter.

11.6 Evaluation of TMFDs vs BSS at ORNL

Measurements with the CTMFD system were performed for seven sources, all of which were chosen by ORNL staff, without prior knowledge of the neutron spectra or intensities. Details of the source configurations were revealed only after the unfolded spectra's dose rates had been reported. The seven source configurations were selected based on their practical relevance to the workplace and were composed of ^{252}Cf sources of differing intensities moderated by lead, steel, or polyethylene. Identical experiments were conducted by ORNL staff with the bonner spectrometer system. Details of the comparison were compiled in a technical report composed by ORNL staff.

Further analyses were conducted after publication of the technical report to maintain consistency with the BSS calibration factor reported in chapter 4 and DETC parameterization coefficients tabulated in chapter 7. In attempt to further evaluate the performance of the two systems, the final estimate for the dose rate represents the mean unfolded dose rate from nine guess spectra in contrast to the dose rate resulting from unfolding with the guess spectra which had the lowest initial χ^2. Furthermore, the reported uncertainty represents the sample variance from the nine guess spectra rather than propagation of statistical measurement uncertainty.

After multiplying the BSS response matrix by the calibration factor, the average dose rate is within 20% of that predicted by the CTMFD system for all cases. An uncertainty weighted linear regression fit yielded a slope of 0.98, indicating that the unfolded dose rates from each system are highly correlated. In contrast, use of the BSS calibration factor worsened agreement with the Ludlum 42-41L rate meter, which took measurements simultaneously during the CTMFD and BSS experiments to ensure any external sources in the building were not contaminating the data. Considering the Ludlum rate meter was calibrated using NIST-traceable ^{252}Cf sources and the fact that the steel, lead, and polyethylene-moderated spectra do not significantly differ from a bare source, it is difficult to distinguish which result defines the baseline reference of accuracy.

11.7 Meeting/Exceeding Objectives and Goals of Dissertation

This section clarifies that the afore-mentioned objectives and goals mentioned earlier in section 1.4 have been met and/or exceeded.

Objective 1: Establishment of a baseline reference of accuracy using a conventional Bonner sphere spectrometer

> The response matrix for a ^{6}LiI bonner spectrometer was simulated in MCNP. Measurements of the detectors response to isotope sources were performed and later validated with MCNP. The measurement data was successfully unfolded and found in agreement with MCNP.

Objective 2: Development of a simulation model for TMFDs extensible beyond pure hydrocarbons

> The capability for multi-atom spectroscopy was developed for Decaflouropentane using MCNP and SRIM. A correlation mapping count rates to recoil ion energy deposition

inside a critical diameter was found and a new probabilistic detection model was implemented.

Objective 3: Development of a geometrically independent response matrix for TMFDs using monte-carlo-based monoenergetic neutron sources from 100 keV to 14 MeV

> The response matrix of a CTMFD was simulated using the found correlation between count rate and energy deposition. The response matrix is independent of geometry and can be used to unfold arbitrary spectrums.

Objective 4: Successfully unfold neutron spectra from data taken with TMFDs

> Data was taken with both a single detector system and a multi-detector system and modeled in MCNP. The spectra and corresponding $H^*(10)$ dose rate, resulting from unfolding with the simulated CTMFD response matrix, were in good agreement with MCNP. A list template of common isotope source spectra was created to serve as *a priori* information for unfolding.

Objective 5: Extend TMFDs for also enabling sensitivity to neutrons below 100 keV

> CTMFDs were made sensitive to thermal neutrons by adding boron to the detection fluid. The threshold pressure where the detector becomes sensitive to thermal events was identified. A correlation between detection rate and equivalent dose from neutrons below 100 keV was established with MCNP.

Objective 6: Independently evaluate the CTMFD's capability against the reference Bonner sphere spectrometer

> Measurements of 7 different unknown sources were taken at ORNL. The measurements were unfolded and the corresponding spectra and dose rates were to transmitted to ORNL staff, who repeated the measurements with a ^{6}LiI BSS. The BSS dose rates were unfolded using the response matrix computed in MCNP and compared against the CTMFD in a technical report. The CTMFD and BSS unfolded dose rates are highly correlated.

12. Recommendations for Future Work

This chapter briefly lists recommendations to address remaining open questions and expand on the work described in prior chapters.

- Address the normalization issue for the Bonner spectrometer system described in the chapter 4 to better establish the reference standard for the sources used to calibrate the CTMFDs.

- Repeat the calibration procedure utilized for the 16 cm^3 detector for the 0.4 and 1 cm^3 detectors across the entire negative pressure to enable spectroscopy in higher fluence rate fields.

- Acquire additional data with monoenergetic sources. The accelerator facility should be modeled in MCNP such that the simulation model can be benchmarked against experimental data. Specific attention should be directed towards lower neutron energies and their corresponding negative pressure thresholds due. Establishing the lower energy bound the response matrix is important.

- Further diversify the spectra used in the calibration procedure described in chapter 7 to find the coefficients parameterizing the DETC curve. An ^{241}AmLi spectrum could prove beneficial.

- Establish a more suitable thermal reference spectrum to calibrate the response of borated CTMFDs. A purely thermal neutron detector such as BF_3 or ^{3}He with a known response function should first be used to validate a MCNP simulation model. Once verified, repeat the experiment with borated CTMFDs. Finally, using the verified simulation model, assess whether the CTMFD's detection model (i.e. DETC curve) agrees with the observed thermal threshold and measured response.

REFERENCES

[1] "10 cfr 835 occupational radiation protection," Code of Federal Regulations, Standard, Jan. 2016.

[2] "The 2007 recommendations of the international commission on radiological protection. icrp publication 103," *Annals of the ICRP*, vol. 37, no. 2-4, pp. 9–34, 2007. DOI: 10.1016/j.icrp.2007.10.003. [Online]. Available: https://doi.org/10.1016/j.icrp.2007.10.003.

[3] I. O. Andersson and J. Braun, "Neutron rem-counter with uniform sensitivity from 0.025ev to 10mev," *Proc. IAEA Symp. on Neutron Dosimetry, Vienna, 1963*, vol. 2, pp. 87–95, 1963. [Online]. Available: https://ci.nii.ac.jp/naid/10016124603/en/.

[4] D. Hankins, "Modified-sphere neutron detector," Los Alamos National Laboratory (LANL), Los Alamos, NM, Tech. Rep., Jan. 1966. DOI: LA-3595.

[5] J. W. Leake, "An improved spherical dose equivalent neutron detector," *Nuclear Instruments and Methods*, vol. 63, no. 3, pp. 329–332, 1968, ISSN: 0029-554X. DOI: https://doi.org/10.1016/0029-554X(68)90590-9. [Online]. Available: http://www.sciencedirect.com/science/article/pii/0029554X68905909.

[6] R. H. Olsher, H.-H. Hsu, A. Beverding, J. H. Kleck, W. H. Casson, D. G. Vasilik, and R. T. Devine, "Wendi: An improved neutron rem meter.," *Health Physics*, vol. 79, no. 2, 2000.

[7] T. Oakes, S. Bellinger, W. Miller, E. Myers, R. Fronk, B. Cooper, T. Sobering, P. Scott, P. Ugorowski, D. McGregor, J. Shultis, and A. Caruso, "An accurate and portable solid state neutron rem meter," *Nuclear Instruments and Methods in Physics Research Section A: Accelerators, Spectrometers, Detectors and Associated Equipment*, vol. 719, pp. 6–12, Aug. 2013, ISSN: 0168-9002. DOI: 10.1016/J.NIMA.2013.03.060. [Online]. Available: https://www.sciencedirect.com/science/article/pii/S0168900213003707.

[8] Physikalisch-Technische Bundesanstal, *Nemus: An extended bonner sphere spectrometer (neutron multisphere spectrometer)*, https://www.ptb.de/cms/en/ptb/fachabteilungen/abt6/fb-64/643-neutron-spectrometry/nemus.html.

[9] G. F. Knoll, *Radiation Detection and Measurement*, 4th ed. John Wiley & Sons, 2010, p. 860, ISBN: 0470131489.

[10] A. Alevra and D. Thomas, "Neutron spectrometry in mixed fields: multisphere spectrometers," *Radiation Protection Dosimetry*, vol. 107, no. 1-3, pp. 37–72, Nov. 2003, ISSN: 0144-8420. DOI: 10.1093/oxfordjournals.rpd.a006388. [Online]. Available: https://doi.org/10.1093/oxfordjournals.rpd.a006388.

[11] H. Tagziria and W. Hansen, “Neutron spectrometry in mixed fields: proportional counter spectrometers,” *Radiation Protection Dosimetry*, vol. 107, no. 1-3, pp. 73–93, Nov. 2003, ISSN: 0144-8420. DOI: 10.1093/oxfordjournals.rpd.a006389. [Online]. Available: https://doi.org/10.1093/oxfordjournals.rpd.a006389.

[12] H. Klein, “Neutron spectrometry in mixed fields: NE213/BC501A liquid scintillation spectrometers,” *Radiation Protection Dosimetry*, vol. 107, no. 1-3, pp. 95–109, Nov. 2003, ISSN: 0144-8420. DOI: 10.1093/oxfordjournals.rpd.a006391. [Online]. Available: https://doi.org/10.1093/oxfordjournals.rpd.a006391.

[13] N. V. Kornilov and V. A. Khriatchkov, “Neutron spectroscopy with fast waveform digitizer,” *Nuclear Instruments and Methods in Physics Research Section A: Accelerators, Spectrometers, Detectors and Associated Equipment*, vol. 497, no. 2, pp. 467–478, 2003, ISSN: 0168-9002. DOI: https://doi.org/10.1016/S0168-9002(02)01790-4. [Online]. Available: https://www.sciencedirect.com/science/article/pii/S0168900202017904.

[14] S. Marrone and D. Cano-Ott, “Pulse shape analysis of liquid scintillators for neutron studies,” *Nuclear Instruments and Methods in Physics Research Section A: Accelerators, Spectrometers, Detectors and Associated Equipment*, vol. 490, no. 1, pp. 299–307, 2002, ISSN: 0168-9002. DOI: https://doi.org/10.1016/S0168-9002(02)01063-X. [Online]. Available: https://www.sciencedirect.com/science/article/pii/S016890020201063X.

[15] C. Heimbach, *Nist calibration of a neutron spectrometer rospec*, Dec. 2006.

[16] F. d’Errico, “Radiation dosimetry and spectrometry with superheated emulsions,” *Nuclear Instruments and Methods in Physics Research Section B: Beam Interactions with Materials and Atoms*, vol. 184, no. 1, pp. 229–254, 2001, Advanced Topics in Solid State Dosimetry, ISSN: 0168-583X. DOI: https://doi.org/10.1016/S0168-583X(01)00730-3. [Online]. Available: https://www.sciencedirect.com/science/article/pii/S0168583X01007303.

[17] F. d’Errico and M. Matzke, “Neutron spectrometry in mixed fields: superheated drop (bubble) detectors,” *Radiation Protection Dosimetry*, vol. 107, no. 1-3, pp. 111–124, Nov. 2003, ISSN: 0144-8420. DOI: 10.1093/oxfordjournals.rpd.a006380. [Online]. Available: https://doi.org/10.1093/oxfordjournals.rpd.a006380.

[18] F. d’Errico, W. Alberts, G. Curzio, S. Guldbakke, H. Kluge, and M. Matzke, “Active Neutron Spectrometry with Superheated Drop (Bubble) Detectors,” *Radiation Protection Dosimetry*, vol. 61, no. 1-3, pp. 159–162, Aug. 1995, ISSN: 0144-8420. DOI: 10.1093/oxfordjournals.rpd.a082774. [Online]. Available: https://doi.org/10.1093/oxfordjournals.rpd.a082774.

[19] P. F. Scholander, E. D. Bradstreet, E. A. Hemmingsen, and H. T. Hammel, “Sap Pressure in Vascular Plants: Negative hydrostatic pressure can be measured in plants,” *Science*, vol. 148, no. 3668, pp. 339–346, Apr. 1965, ISSN: 0036-8075. DOI: 10.1126/science.148.3668.339. [Online]. Available: http://www.ncbi.nlm.nih.gov/pubmed/17832103%20http://www.sciencemag.org/cgi/doi/10.1126/science.148.3668.339.

[20] F. Seitz, “On the theory of the bubble chamber,” *The Physics of Fluids*, vol. 1, no. 1, pp. 2–13, 1958. DOI: 10.1063/1.1724333. eprint: http://aip.scitation.org/doi/pdf/10.1063/1.1724333. [Online]. Available: http://aip.scitation.org/doi/abs/10.1063/1.1724333.

[21] T. F. Grimes, “Nucleation and Detection in Tension Metastable Fluid Detectors,” Doctoral Thesis, Purdue University, 2015.

[22] “ISO 8529 Reference neutron radiations - Part 1: Characteristics and methods of production,” International Organization for Standardization, Standard, Feb. 2001.

[23] “ISO 8529 Reference neutron radiations - Part 2: Calibration fundamentals of radiation protection devices related to the basic quantities characterizing the radiation field,” International Organization for Standardization, Standard, Aug. 2000.

[24] N. J. Roberts and L. N. Jones, “The Content of 250Cf and 248Cm in 252Cf Neutron Sources and The Effect on the Neutron Emission Rate,” *Radiation Protection Dosimetry*, vol. 126, no. 1-4, pp. 83–88, 2007. DOI: 10.1093/rpd/ncm017. [Online]. Available: https://academic.oup.com/rpd/article/126/1-4/83/1605472.

[25] J. Kim, H. Park, and K.-O. Choi, “Measurement of the 250Cf component in a 252Cf neutron source at KRISS,” *Radiation Protection Dosimetry*, vol. 161, no. 1-4, pp. 171–175, 2014. DOI: 10.1093/rpd/nct327. [Online]. Available: https://academic.oup.com/rpd/article/161/1-4/171/1608523.

[26] R. Radev and T. Mclean, “Neutron Sources for Standard-Based Testing LLNL-TR-664160,” Lawrence Livermore National Laboratory, Tech. Rep., 2014. [Online]. Available: https://e-reports-ext.llnl.gov/pdf/785407.pdf.

[27] W. B. Wilson, R. T. Perry, and E. F. Shores, “Sources 4c : A code for calculating ([alpha],n), spontaneous fission, and delayed neutron sources and spectra.,” Jan. 2002. [Online]. Available: https://www.osti.gov/biblio/976142.

[28] J. Marsh, D. Thomas, and M. Burke, "High resolution measurements of neutron energy spectra from AmBe and AmB neutron sources," *Nuclear Instruments and Methods in Physics Research Section A: Accelerators, Spectrometers, Detectors and Associated Equipment*, vol. 366, no. 2-3, pp. 340–348, Dec. 1995, ISSN: 0168-9002. DOI: 10.1016/0168-9002(95)00613-3. [Online]. Available: https://www.sciencedirect.com/science/article/pii/0168900295006133.

[29] L. D. Schulte, "Actinide beryllium neutron source with reduced dispersion characteristics. background information on ambe source fabrication," Mar. 2011. [Online]. Available: https://www.osti.gov/biblio/1055279.

[30] E. A. Lorch, "Neutron spectra of 214am/b, 241am/be, 241am/f, 242cm/be, 238pu/13c and 252cf isotopic neutron sources," *The International Journal of Applied Radiation and Isotopes*, vol. 24, no. 10, pp. 585–591, 1973, ISSN: 0020-708X. DOI: https://doi.org/10.1016/0020-708X(73)90127-0. [Online]. Available: https://www.sciencedirect.com/science/article/pii/0020708X73901270.

[31] L. Sarchiapone and D. Zafiropoulos, "Neutron spectrometry using LNL bonner spheres and FLUKA," in *AIP Conference Proceedings*, vol. 1530, American Institute of Physics, Jul. 2013, pp. 163–170. DOI: 10.1063/1.4812919. [Online]. Available: http://aip.scitation.org/doi/abs/10.1063/1.4812919.

[32] V. Mares and H. Schraube, "Evaluation of the response matrix of a Bonner sphere spectrometer with LiI detector from thermal energy to 100 MeV," *Nuclear Instruments and Methods in Physics Research Section A: Accelerators, Spectrometers, Detectors and Associated Equipment*, vol. 337, no. 2-3, pp. 461–473, Jan. 1994, ISSN: 0168-9002. DOI: 10.1016/0168-9002(94)91116-9. [Online]. Available: https://www.sciencedirect.com/science/article/pii/0168900294911169.

[33] M. Lacerda, R. Méndez-Villafañe, A. Lorente, S. Ibañez, E. Gallego, and H. Vega-Carrillo, "A new response matrix for a 6 LiI scintillator BSS system," *Nuclear Instruments and Methods in Physics Research Section A: Accelerators, Spectrometers, Detectors and Associated Equipment*, vol. 868, pp. 122–128, Oct. 2017, ISSN: 01689002. DOI: 10.1016/j.nima.2017.06.057. [Online]. Available: http://linkinghub.elsevier.com/retrieve/pii/S0168900217307118.

[34] A. Lorente A, A. Martin Martin, E. Gallego, E. Acuña, H. Vega-Carrillo, D. I, J. Gutierrez Villanueva, and M. Iñiguez, "Calculation of response matrix of a bss with 6lii scintillator," *Revista Mexicana de Física*, vol. 54, Feb. 2008.

[35] H. Mazrou, Z. Idiri, T. Sidahmed, and M. Allab, "MCNP5 evaluation of a response matrix of a Bonner Sphere Spectrometer with a high efficiency 6LiI (Eu) detector from 0.01 eV to 20 MeV neutrons," *Journal of Radioanalytical and Nuclear Chemistry*, vol. 284, no. 2, pp. 253–263, May 2010, ISSN: 0236-5731. DOI: 10.1007/s10967-010-0493-9. [Online]. Available: http://link.springer.com/10.1007/s10967-010-0493-9.

[36] A. Alevra, M. Cosack, J. Hunt, D. Thomas, and H. Schraube, "Experimental Determination of the Response of Four Bonner Sphere Sets to Monoenergetic Neutrons (II)," *Radiation Protection Dosimetry*, vol. 40, no. 2, pp. 91–102, Feb. 1992, ISSN: 1742-3406. DOI: 10.1093/oxfordjournals.rpd.a081196. [Online]. Available: https://academic.oup.com/rpd/article/40/2/91/1600638/Experimental-Determination-of-the-Response-of-Four.

[37] D. T. Seagraves and T. D. Mclean, "252cf-based neutron measurements and monte carlo calculations for dhs-dndo in support of ansi standard n42.34," Nov. 2014. DOI: 10.2172/1164467. [Online]. Available: https://www.osti.gov/biblio/1164467.

[38] M. Reginatto and P. Goldhagen, "Maxed, a computer code for the deconvolution of multisphere neutron spectrometer data using the maximum entropy method," *Health Physics*, vol. 5, no. 77, Nov. 1999. DOI: 10.1097/00004032-199911000-00012.

[39] M. Reginatto and P. Goldhagen, "Spectrum unfolding, sensitivity analysis and propagation of uncertainties with the maximum entropy deconvolution code maxed," *Nuclear Instruments and Methods in Physics Research Section A: Accelerators, Spectrometers, Detectors and Associated Equipment*, vol. 476, no. 1, pp. 242–246, 2002, Int. Workshop on Neutron Field Spectrometry in Science, Technology and Radiation Protection, ISSN: 0168-9002. DOI: https://doi.org/10.1016/S0168-9002(01)01439-5. [Online]. Available: http://www.sciencedirect.com/science/article/pii/S0168900201014395.

[40] E. Padovani, S. A. Pozzi, S. D. Clarke, and E. C. Miller, *MCNPX-PoliMi Users Manual*, 2012.

[41] DuPont, *Technical datasheet*, https://miller-stephenson.com/wp-content/uploads/2016/09/Vertrel-XF-PDF.pdf, 2008.

[42] L. D. Landau, "On the Energy Loss of Fast Particles by Ionization," *J. Phys.(USSR)*, vol. 8, no. 4, pp. 201–205, 1944.

[43] P. Vavilov, "Ionization losses of high-energy heavy particles," *Soviet Phys. JETP*, vol. 5, Nov. 1957.

[44] K. S. R. Groom D. E., "Passage of particles through matter," *The European Physical Journal C - Particles and Fields*, vol. 15, no. 1, pp. 163–173, Mar. 2000, ISSN: 1434-6052. DOI: 10.1007/BF02683419. [Online]. Available: https://doi.org/10.1007/BF02683419.

[45] F. D'Errico, "Fundamental Properties of Superheated Drop (Bubble) Detectors," *Radiation Protection Dosimetry*, vol. 84, no. 1-4, pp. 55–62, Aug. 1999, ISSN: 0144-8420. DOI: 10.1093/oxfordjournals.rpd.a032796. eprint: http://oup.prod.sis.lan/rpd/article-pdf/84/1-4/55/9924398/55.pdf. [Online]. Available: https://doi.org/10.1093/oxfordjournals.rpd.a032796.

[46] F. Aubin, M. Auger, M.-H. Genest, V. Zacek, S. Archambault, E. Behnke, T. M. Undagoitia, L. Rauch, C. Leroy, P.-G. Rancoita, D. Twerenbold, M. Cirelli, E. D. Nobile, and P. Panci, "New insights into particle detection with superheated liquids," *New J. Phys*, vol. 13, 2011. [Online]. Available: http://iopscience.iop.org/1367-2630/13/4/043006.

[47] M. Barnabé-Heider, M. Di Marco, P. Doane, M. Genest, R. Gornea, R. Guénette, C. Leroy, L. Lessard, J. Martin, U. Wichoski, V. Zacek, K. Clark, C. Krauss, A. Noble, E. Behnke, W. Feighery, I. Levine, C. Muthusi, S. Kanagalingam, and R. Noulty, "Response of Superheated Droplet Detectors of the PICASSO Dark Matter Search Experiment," *Nuclear Instruments and Methods in Physics Research Section A: Accelerators, Spectrometers, Detectors and Associated Equipment*, vol. 555, no. 1, pp. 184–204, 2005. DOI: https://doi.org/10.1016/j.nima.2005.09.015. [Online]. Available: http://www.sciencedirect.com/science/article/pii/S0168900205018255.

[48] H. M.J. and J. Rich, "Radiation-induced nucleation in superheated liquid droplet neutron detectors," *Nuclear Instruments and Methods in Physics Research Section A: Accelerators, Spectrometers, Detectors and Associated Equipment*, vol. 336, no. 1, pp. 220–225, 1993, ISSN: 0168-9002. DOI: https://doi.org/10.1016/0168-9002(93)91101-R. [Online]. Available: http://www.sciencedirect.com/science/article/pii/016890029391101R.

[49] B. Archambault, A. Hagen, T. F. Grimes, and R. Taleyarkhan, "Development of a centrifugal tensioned metastable fluid detector array to detect snm using active neutron interrogation," Oct. 2017. DOI: 10.1109/NSSMIC.2017.8532869.

[50] R. Finlay, C. Brient, D. Carter, A. Marcinkowski, S. Mellema, G. Randers-Pehrson, and J. Rapaport, "The ohio university beam swinger facility," *Nuclear Instruments and Methods in Physics Research*, vol. 198, pp. 197–206, Jul. 1982. DOI: 10.1016/0167-5087(82)90256-3.

[51] M. Drosg, "Sources of variable energy monoenergetic neutrons for fusion-related applications," *Nuclear Science and Engineering*, vol. 106, no. 3, pp. 279–295, 1990. DOI: 10.13182/NSE90-A29056. [Online]. Available: https://doi.org/10.13182/NSE90-A29056.

[52] International Atomic Energy Agency, *Drosg-2000: Neutron source reactions data files with computer codes for 56 monoenergetic neutron source reactions (iaea-nds–87(rev5))*, https://www-nds.iaea.org/public/libraries/drosg2000/, 2000.

[53] M. B. Smith, H. R. Andrews, H. Ing, and M. R. Koslowsky, “Response of the bubble detector to neutrons of various energies,” *Radiation Protection Dosimetry*, vol. 164, no. 3, pp. 203–209, 2015. DOI: 10.1093/rpd/ncu288.

[54] Z. W. Bell and G. W. Wright, “Report of Bonner Sphere Set Measurements at ORNL,” Oak Ridge National Laboratory, Oak Ridge, TN, Tech. Rep., 2018, pp. 1–29.

[55] J. Tellinghuisen, “Least-squares analysis of data with uncertainty in y and x: Algorithms in excel and kaleidagraph,” *Journal of Chemical Education*, vol. 95, no. 6, pp. 970–977, 2018. DOI: 10.1021/acs.jchemed.8b00069.

[56] J. W. Zwolak, P. T. Boggs, and L. T. Watson, “Algorithm 869: Odrpack95: A weighted orthogonal distance regression code with bound constraints,” *ACM Trans. Math. Softw.*, vol. 33, no. 4, Aug. 2007, ISSN: 0098-3500. DOI: 10.1145/1268776.1268782.

[57] D. J. Hertel N.E, “The response of bonner spheres to neutrons from thermal energies to 17.3 mev,” *Nuclear Instruments and Methods in Physics Research Section A: Accelerators, Spectrometers, Detectors and Associated Equipment*, vol. 238, no. 2, pp. 509–516, 1985, ISSN: 0168-9002. DOI: https://doi.org/10.1016/0168-9002(85)90494-2.

A. APPENDIX: SIMULATION DATABASE

This section discusses how to use the included Python coding framework developed throughout this work for spectroscopy in CTMFDs. All relevant computer code is organized in Jupyter Notebooks for ease of presentation. Furthermore, the code has been refactored to convert all path and file references relative a root project folder such that it is possible to utilize the computational framework developed in this work in future research. A general procedure to develop a response matrix for any arbitrary CTMFD is outlined below.

First, acquire experimental data with the specified detector using multiple neutron sources with as diverse spectra as possible. Review the discussion in chapter 7 regarding pressure ranges and saturation effects. There is not a fixed procedure for how many detection events should be recorded at each pressure or what pressures measurements should be recorded at. However, based the on experience acquired throughout this project, it proved beneficial to take data at 0.5 bar increments. When the slope of the count rate curve is steep, such as with high intensity sources or at low negative pressures, a 0.25 bar interval is recommended.

The next step constitutes the application of a detection model to MCNPX PoliMi simulation data with the intention of minimizing the difference between the detection model's predicted count rate and the experimentally measured count rate. As discussed in chapter 7 and chapter 8, large residuals in the predicted and simulated count rates will propagate through computation of the response matrix and manifest as inaccuracies in the resulting unfolded spectrum. Thus, when optimizing the detection model, the objective function should be based on count rate residuals as opposed to residuals of the unfolded spectrum.

Develop a MCNPX-PoliMi model of the experimental geometry, such as the file "PanelTemplateT3 bare AmBe HSroom 100cm.txt" located in the path root/PoliMi_Raw_Data/MCNP_geom_templates/PanelGeom/. Use the code in "Panel_HSR_inpgen.ipynb" to rotate the detector orientation and create a batch file that will run all simulations. Once the simulations are complete, use "Create_Recoils_DataFrame.ipynb" to convert the PoliMi DAT files into a Pandas DataFrame with a structure designed to compatible with the stochastic method's count prediction functions. The code also pre-calculates the local negative pressure at each event location and CSDA energy deposition along the critical diameter length scale.

Using the DataFrame of ion recoils, use “PredictCounts&OptimizeL2.ipynb” in root/ThresholdOptimization to generate the counts predicted from MCNP data. For each specified negative pressure, the function returns a 2D array, where each index represents the counts predicted from a specific set of A,N coefficients. Using code from the same notebook, convert the raw predicted MCNP counts to physical count rates and find the A,N coefficient set that yields the lowest figure of merit with experimental data. This coefficient set parameterizes the energy deposition threshold for cavitation curve that is ultimately used to build a response matrix.

Develop MCNPX PoliMi input decks of the CTMFD for response matrix generation. The current work used the glass apparatus only in a vacuum, but future work should include the rest of the detector housing (motor enclosure, etc.) and any other detectors (for a panel configuration). The notebook “ResponseMat_inpFile_Generator.ipynb” in root/ResponseMatrix can be used to generate the entire set of input decks and batch files from one of the template input decks such as “M76_RM_template.txt”. The code allows the energy bin structure to be customized but assumes the number of particle histories simulated in each case to be constant. For each neutron energy, the orientation of the CTMFD’s arms relative to the fluence normal vector is varied to simulate rotation. The code in “Concatenate_Files.ipynb” combines the DAT files from each orientation into a single DataFrame for each neutron energy and assigns a unique nps number to each recorded history.

Almost identical to the script used for threshold optimization, the code in “Create_Recoils_DataFrame.ipynb” performs the required data formatting and precalculations for each neutron energy simulated. Once finished, use the optimized A,N coefficient set and “BuildResponseMatrix.ipynb” to construct response matrices using the stochastic and or CSDA models for detection. The data saved to disk represents the summation of individual detection probabilities for each event histories in the DataFrame. Use equation eq. (4.1) to normalize the matrix into the proper units. The normalization factors for the detectors discussed in this work can be found in /root/Modules in the file “MainMods.py” under the variable “rm_scalefactors”.

PUBLICATIONS

R.P. Taleyarkhan, B. Archambault, A. Sansone, T.F. Grimes, A. Hagen, Neutron spectroscopy & H*10 dosimetry with tensioned metastable fluid detectors, Nuclear Instruments and Methods in Physics Research Section A: Accelerators, Spectrometers, Detectors and Associated Equipment, Volume 959, 2020.

A. A. Sansone, R. P. Taleyarkhan. "Intensification of Chemically Assisted Melt–Water Explosive Interactions." ASME. J. Heat Transfer. April 2017; 139(4): 042004. https://doi.org/10.1115/1.4035353.

A. Sansone, J. A. Webster, B. C. Archambault, and R. P. Taleyarkhan, "Tensioned Mestastable Fluid Detectors for High Efficiency Thermal and Fast Neutron Sensitivity," In Proceedings of the 24th International Conference on Nuclear Engineering. 2016, pp. 1–7.

R. P. Taleyarkhan, B. C. Archambault, A. Sansone,and A. Hagen, "Femto-to-Macro-Scale Interdisciplinary Sensing with Tensioned Metastable Fluid Detectors". In IEEE Sensors Demonstrations. Orlando, FL: IEEE. 2016.

R. P. Taleyarkhan, J. A. Webster, A. Sansone, B. C. Archambault, R. Reames, and C. D. West, "Metastable Liquid Cavitation Control (With Memory) Apparatus, Methodology, and Results: For Radiation Detection, Reactor Safety, and Other Industrial Applications." ASME. ASME J of Nuclear Rad Sci. January 2017; 3(1): 011004. https://doi.org/10.1115/1.4034975.

A. Sansone, R.P. Taleyarkhan, "Intensification of Chemically Assisted Melt-Water Explosive Interactions". In Proceedings of NURETH-16 International Topical Meeting on Nuclear Reactor Thermal Hydraulics, September 2015.

A. Sansone, R.P. Taleyarkhan, "Prevention and Intensification of Melt-Water Explosive Interactions". In Proceedings of HEFAT-14 10th International Conference on Heat Transfer, Fluid Mechanics and Thermodynamics, July 2014.

T. F. Grimes, B. C. Archambault, J. A. Webster, A. Sansone, and R. P. Taleyarkhan, "Gamma-blind Transformational Nuclear Particle Sensors." In Homeland Security (HST), 2012 IEEE Conference on Technologies for, pp. 417-422. IEEE, 2012.

Zielinski, S. M., Sansone, A. A., Ziolkowski, M., and Taleyarkhan, R. P. (March 30, 2011). ”Prevention and Intensification of Melt-Water Explosive Interactions.” ASME. J. Heat Transfer. July 2011; 133(7): 071201. https://doi.org/10.1115/1.4003531.